5-2018

Highly Excited States of Small Molecules and Negative Atomic Ions

Matthew T. Eiles
Purdue University

HIGHLY EXCITED STATES OF SMALL MOLECULES AND NEGATIVE ATOMIC IONS

A Dissertation

Submitted to the Faculty

of

Purdue University

by

Matthew T. Eiles

In Partial Fulfillment of the

Requirements for the Degree

of

Doctor of Philosophy

May 2018

Purdue University

West Lafayette, Indiana

THE PURDUE UNIVERSITY GRADUATE SCHOOL
STATEMENT OF APPROVAL

Dr. Chris H. Greene, Chair

Department of Physics and Astronomy

Dr. Francis Robicheaux

Department of Physics and Astronomy

Dr. Adam Wasserman

Department of Chemistry

Dr. Chen-Lung Hung

Department of Physics and Astronomy

Approved by:

Dr. John P. Finley

Head of the School Graduate Program

To my parents, who taught me how to learn

ACKNOWLEDGMENTS

The years spent in pursuit of a Ph.D. provide abundant opportunities for countless people to inspire, influence, and shape the student. This is fortunate: it would be an insurmountable challenge to finish it otherwise. It is equally impossible to acknowledge all these influences properly, either due to my negligence or my inability to convey sufficient gratitude – words are futile devices.

Certainly, none of this would have been possible without my advisor, Chris Greene. I owe him a great debt for offering me a position in the AMO group, for his ever-patient mentoring and teaching, and for embarking on all these exciting research projects with me. I am fortunate to have caught a glimpse of the beauty and wonder of physics through his apparently infinite knowledge of atomic and molecular physics and broad range of interests. His door was always open when I needed new ideas, help with a calculation, or quick feedback on a manuscript. He is an inspiration as a mentor, academic, and scientist. Jesús Pérez-Ríos has also been a wonderful mentor and friend, and his enthusiasm and dedication continue to encourage me. Over innumerable lunches and coffee breaks, he taught me an immense amount about science, research, and life. In his words, "Thanks a lot!!!!!!" Francis Robicheaux, through many lunch discussions, has taught me a great amount about how to think critically and clearly about physics. He's also been a dedicated and insightful committee member, and always apologized for calling me an idiot. Thanks also to the rest of my committee, Chen-Lung Hung and Adam Wasserman, for their support. Thanks to Panos Giannakeas for all the encouragement, advice, insight, humor, and

also for teaching me "*Ceci n'est pas une goodbye*." Thanks to Tyler Sutherland and Hyunwoo Lee for all the lively office conversations, which occasionally strayed into something relevant to physics, and for being good friends. It was wonderful to be surrounded by so many excellent colleagues in the AMO group: Su Ju Wang, Yijue Ding, Bin Yan, Rachel Wooten, Teri Price, Changchun Zhong, and Xiao Wang. I owe a lot to the wonderful administrative and custodial staff in the physics department. Sandy Formica and Bill Fornes stand out for their warmth and genuine interest in my success. Special thanks also to Manuel Flores-Rojas, a great friend who always found time to chat with me.

I was warmly welcomed to Germany on two occasions in the past few years, both times thanks to Peter Schmelcher and his group in Hamburg, in particular Christian Fey and Frederic Hummel. Their warm hospitality made my visits very productive and enjoyable. I am also grateful to Tilman Pfau's group, particularly Florian Meinert, Herwig Ott's group, especially Oliver Thomas, and Jan-Michael Rost and Alex Eisfeld at MPI-PKS for their hospitality.

My life would be far poorer without my friends at Purdue: Charlie, Danielle, Nate, Lauren, Matt, Erin, Ingrid, Stephen, Elizabeth, Brendan (special thanks for the grill!), Ian, Brian, Jared, Zach, Julien, Farshid, Peter, Mri, Valentyn, and all the folks at RPC. Purdue would have been a dull and lonely place without all of you. Several professors and teachers helped to develop my interest in physics (mostly, at the start, by teaching me that math can be pretty fun), especially Ken Kidoguchi, Steve Simonds, Tim Pennings, and Peter Gonthier. Like the chicken man, Pete's influence is everywhere, and extends far beyond his teaching and advising. I'm grateful for his friendship. I am very grateful for my Mom and Dad, who sacrificed so much to prepare, teach, love, support, and encourage me all along. They also do their best to keep my head from getting too big – thank you! Thanks also to my

wonderful siblings: Madeleine, Mark, Mike, and Pete. Finally, I owe an incredible debt to my lovely wife, Emily, for putting up with so many very long nights and late evenings at the office, and enduring our separation while I got to travel to conferences and workshops. Her love carried me through it all, and she reminds me that "it's not so impossible."

This work was supported financially by the National Science Foundation and the Department of Energy. Many of these calculations were performed using the computing cluster at the Purdue Rosen Center for Advanced Computing. I am grateful to the Gordon and Betty Moore foundation for a stipend to support me at KITP, and to the Gi-Ryd program, ICPEAC, and Purdue University for conference and workshop travel support.

TABLE OF CONTENTS

Page

Page

LIST OF FIGURES

Figure Page

LIST OF TABLES

PUBLICATIONS

5. **M. T. Eiles**, H. Lee, J. Pérez-Ríos, and C. H. Greene, *Anisotropic blockade using long-range Rydberg molecules*, Phys. Rev. A **95**, 052708 (2017). *Figure chosen for Kaleidescope feature* [1]

4. **M. T. Eiles** and C. H. Greene, *Hamiltonian for the inclusion of spin effects in long-range Rydberg molecules*, Phys. Rev. A **95**, 042515 (2017). [2]

3. J. Pérez-Ríos, **M. T. Eiles**, and C. H. Greene, *Mapping trilobite state signatures in atomic hydrogen*, J. Phys. B: At., Mol., and Opt. **49**, 14LT01 (2016). *(2016 Highlight and IOP select collection; figure chosen for journal cover image)* [3]

2. **M. T. Eiles**, J. Pérez-Ríos, F. Robicheaux, and C. H. Greene, *Ultracold molecular Rydberg physics in a high density environment*, J. Phys. B: At., Mol., and Opt. **49**, 114005 (2016). *(2016 Highlight; figure chosen for journal cover image)* [4]

1. **M. T. Eiles** and C. H. Greene, *Ultracold long-range Rydberg molecules with complex multichannel spectra*, Phys. Rev. Lett. **115**, 193201 (2015). [5]

ABSTRACT

Eiles, Matthew T. PhD, Purdue University, May 2018. Highly Excited States of Small Molecules and Negative Atomic Ions. Major Professor: Chris H. Greene.

Excited states of atoms and molecules exhibit a rich array of diverse phenomena. This dissertation examines two exotic states of atoms at such excited levels: Rydberg molecules and atomic negative ions. Rydberg molecules are formed by a Rydberg atom and one or more ground state atoms, and can be highly polar due to their unusual electronic wave functions and enormous bond lengths. This dissertation expands the theory of these molecules by studying the formation and structure of polyatomic molecules, multichannel Rydberg molecules formed from divalent atoms, and spin effects and relativistic interactions. It also details intermolecular forces between Rydberg molecules, their manipulation via external fields, and their dependence on the intricacies of electron-atom scattering. This electron-atom interaction is also the main component of the latter portion of this thesis, which studies doubly excited states of alkali negative ions in very polarizable and nearly degenerate atomic states. Photodetachment of these states reveals electron correlation and long-range forces stemming from their high excitation.

1. INTRODUCTION

Undoubtedly, the most useful window through which the properties of ions, atoms, and molecules can be studied is the spectrum of their excited states. The light absorbed and emitted by transitions between excited states of different atoms first led Balmer, Rydberg, Ritz, and Bohr to develop empirical formulae and the "old quantum theory" to describe these observations [6–8]. Their efforts led directly to the revolutionary development of quantum mechanics in the 1920s. Rydberg's key contribution was his famous empirical formula relating atomic energy levels, which has since grown into a vibrant field of its own: the study of Rydberg atoms. Although early spectroscopic studies began with excited electronic states in atoms, where the highly attractive Coulomb force supports an infinite number of excited bound states, the utility of exploring microscopic systems via spectroscopy is not limited to these levels below the dissociation threshold. Resonances, transitory quasi-bound states lying at continuum energies, provide another remarkably clear and precise signature of the properties of a given complex [9, 10]. Resonances dominate the excitation spectrum in such diverse scenarios as autoionization in multi-electron atoms, photoionization of molecular Rydberg states, or negative ion photodetachment. In this latter process, these resonances are particularly critical as nearly all atomic negative ions lack any excited bound states. Resonance features are therefore the only way to probe and understand the fascinating behavior of these systems [11].

Various physical processes, for example electron impact, light absorption, or collisions with other atoms, molecules, or ions, can spark a transition to a highly excited

state. Of these methods, light absorption has become the premier probe of fundamental properties of matter since the advent of high resolution lasers, which made it possible to excite atoms or molecules in a highly controlled and precise fashion. The ability of experiment to study excited systems incredibly accurately sparked rapid advancements in the ability of theory to interpret these measurements and predict new phenomena, and the interplay between these two approaches has unraveled many of the fascinating properties of Rydberg atoms and atomic negative ions.

Rydberg atoms possess many exaggerated features – enormous size, long lifetimes, and huge long-range interactions, to name a few – and as a result have exploded in popularity over the last thirty years [12,13]. They can possess very regular and simple spectra, as in the alkali atoms, or complex and rich – but still theoretically tractable – spectra like those observed in alkaline and open shell atoms. These spectra have been successfully interpreted using advanced theoretical tools such as multichannel quantum defect theory (MQDT) and eigenchannel R-matrix theory [10, 14–17]. Furthermore, Rydberg atoms provide a pristine environment for highly accurate quantum metrology and manipulation [18]. They reveal a wealth of information about the myriad effects of external fields on quantum systems, the transition between quantum and classical physics, and the universal properties of many different atomic species [10, 19–23]. Recent applications of Rydberg atoms have shown that the Rydberg blockade stemming from their enormous long-range forces can lead to bizarre nonlinear phenomena such as polariton formation and bound states of photons [24–26]. Laser cooling and trapping have introduced many applications in quantum information and communication [27–30].

Rydberg atoms have also been studied in ultracold gases following the successful Bose-Einstein condensation of multiple atomic species [31–36]. Excited Rydberg states of many molecules, such as H_2, were studied prior to the advent of ultracold

physics [37, 38], but these new nano and microkelvin environments have made it possible to study molecules *composed of* one or more Rydberg atoms. These exotic molecules were predicted to have huge bond lengths and very weak binding energies; these properties have since been verified experimentally [39–42]. One of these molecules – the *"trilobite"* molecule – is a major focus of this thesis. They share many of the properties of the constituent Rydberg atom, and therefore a detailed understanding of the electron-ion interaction and the quantum defect theory of the Coulomb potential is required. However, they are also highly sensitive to the electron-neutral interaction which determines the scattering phase shifts used in the Fermi pseudopotential; this describes the interaction between a Rydberg atom and a neutral atom or atoms located inside the electronic wave function in an accurate yet conceptually simple manner. Rydberg molecules therefore probe both Rydberg physics and ultracold scattering physics, providing myriad opportunities for rich studies.

Although at first glance they seem quite unrelated, excited atomic negative ions share many underlying commonalities with Rydberg atoms and molecules, and can be treated with many of the same theoretical techniques. One encounters in both systems two-electron correlation and exchange as well as the effects of level degeneracy ubiquitous in highly excited states. Some important distinctions are of course also present. Electronic correlation effects are typically far more important in negative ions, since the overpowering Coulomb force dominating Rydberg physics is not present. Furthermore, the electron-neutral interaction crucial in the formation of Rydberg molecules is only between the Rydberg electron and a ground state atom, whereas in doubly excited states of negative ions one can imagine the negative ion as an electron attached to a Rydberg atom, albeit one of relatively low n. In either case the absence of strong Coulomb forces allows electron correlation, enhanced when the system is excited, to play a major role. Furthermore, since all doubly excited nega-

tive ion states in alkali atoms lie above the ionization threshold, autoionization plays a dominant role. Some of the most famous studies of autodetaching states were the joint theoretical and experimental efforts to understand the simplest atomic anion, H^- [43–46]. At photon energies very close to threshold the very slow ejected electron remains highly entangled and correlated with the core; these effects are manifested in remarkable near-threshold effects and rich resonance physics [47–49]. Some atomic negative ions, notably La^- and Os^-, have at least one bound excited states and are promising candidates for laser cooling [50, 51], but only the ground state of an alkali anion is stable [11].

This thesis is devoted to studying both of these excited systems through the perspective of few-body atomic physics. Chapter 2 outlines the key theoretical concepts and techniques utilized throughout this thesis to describe Rydberg atoms, Rydberg molecules, and atomic negative ions. These tools range from remarkably simple, yet accurate, models such as the Fermi pseudopotential to other far more general computational tools such as the eigenchannel R-matrix method. A pedagogical viewpoint is adopted here to underscore the wide generality of these techniques to the diverse topics covered here.

Following this, Chapter 3 reviews long-range Rydberg molecules. It emphasizes the key properties of the simplest class of Rydberg molecules in order to give a general picture of these unique few-body systems. This picture is then expanded in following chapters. The current state of experimental and theoretical efforts in this field is reviewed both in this chapter and in the more specific introductions to later chapters.

The properties of polyatomic Rydberg molecules are elucidated in chapter 4. A theoretical framework is developed which robustly generalizes to any number of constituent atoms in an arbitrary molecular shape, taking advantage of the mathematics

of point-group symmetries where applicable, and identifying the effects of disorder-induced asymmetries in the molecular structure. We find that the level spacings, degeneracies, and adiabatic/diabatic level crossing properties of these systems are determined by hybridized trilobite or butterfly orbitals reflecting the molecular geometry [52, 53]. Following this, we develop a few-body approach which relies on static line broadening theory and uses this same compact treatment of polyatomic Rydberg molecules to treat the spectroscopy of a single hydrogen Rydberg excitation immersed in a high density background of other hydrogen atoms. This system exhibits two unique spectral signatures: its lineshape depends on the Rydberg quantum number and is independent of the density, and it is dominated by sharply peaked features reflecting the oscillatory structure of the potential energy landscape. Finally, the theoretical description of polyatomic molecules is extended beyond the hybridized trilobite and butterfly orbitals to include more realistic details like the non-degenerate states with low angular momentum and couplings to other principal quantum numbers. This generalization of the theory is appropriate for describing more realistic molecular states and is easily adopted to studying external field effects and to include electronic and nuclear spin.

In chapter 5, a generalized class of Rydberg molecules is predicted which consist of multichannel Rydberg atoms. Such molecules exhibit favorable properties for laser excitation because states exist where the quantum defect varies strongly with the principal quantum number. The resulting occurrence of near degeneracies with states of high orbital angular momentum promotes the admixture of low l into the high l deeply bound 'trilobite' molecule states, thereby circumventing the usual difficulty posed by electric dipole selection rules. A specific example in calcium is given to demonstrate these possibilities. These multichannel states also exhibit multi-scale binding possibilities that could present novel options for quantum manipulation. The

spin-orbit splitting of silicon is shown to give rise to perturbed Rydberg series that, for highly excited states, exhibit these unusual behaviors.

Chapter 6 presents a full picture of these molecules including all relevant spin degrees of freedom in the heavy alkali atoms Rb and Cs. This includes the Rydberg fine structure, the hyperfine structure of the ground state atom, and the relativistic spin-orbit splitting of the electron-atom scattering, which we find influences the potential energy curves and dipole moments of Rydberg molecules quite strongly. This chapter provides a foundation for future theoretical studies interested in studying these molecules at spectroscopic accuracy, corrects some invalid assumptions common in the literature, and identifies topics for future effort, particularly the sensitivity of this model to convergence issues and uncertainty in the low-energy phase shifts.

In Chapter 7 we propose an experiment to demonstrate a novel blockade mechanism caused by long-range anisotropic interactions in an ultracold dipolar gas composed of "butterfly" Rydberg molecules. We study the intermolecular interaction between Rydberg molecules and find that, like the interaction between bare Rydberg atoms, it leads to a Rydberg blockade phenomenon when the interaction exceeds the bandwidth of the photoassociation laser. Due to the polar nature of these butterfly molecules this interaction is highly anisotropic, leading to a geometry-dependent blockade radius. When the molecules are prepared in a quasi-one-dimensional (Q1D) trap, the interaction's strength can be tuned via a weak external field. The molecular density thus depends strongly on the angle between the trap axis and the field.

Chapter 8 moves away from Rydberg molecules and presents the results of our study of negative ion photodetachment in highly excited states of the potassium negative ion, K^-. In particular, we explore partial cross sections corresponding to a residual neutral state with a high level of angular excitation. Recent experimental investigations of these partial cross sections showed interesting behavior which was

interpreted as stemming from the enormous polarizabilities of the residual atom. These polarizabilities are greatly enlarged by the mixing of nearly degenerate high angular momentum states, and can even be negative, causing the neutral atom to strongly repulse the detached electron. However, we find evidence that a better interpretation of these effects is to treat the nearly-degenerate channels as exactly degenerate. In this case, as in the hydrogen anion, the degenerate states hybridize and exhibit a linear Stark shift. This leads to a dipole potential. We show that this assumption qualitatively explains the observed partial cross sections and agrees with a full R-matrix eigenchannel calculation. We make predictions for partial cross sections at higher energies, where qualitative differences between these alternative models should become apparent. Results for Na^- photodetachment in a similar energy regime are included to reinforce these findings.

Chapter 9 describes two ongoing extensions of the topics detailed in previous chapters, focusing on modifications to the concept of Rydberg molecules by replacing one or both of the constituent atoms. In the first case, the perturber atom is replaced by a "ghost" atom: the effect of a real atom on the Rydberg wave function is mimicked by a sequence of electric and magnetic field pulses, causing the Rydberg wave function to form precisely the same trilobite chemical bond as we study elsewhere, but here it extends out into empty space. In the second case, both constituent atoms are replaced by different alkali species to search for more diverse physics present in these species, particularly in heteronuclear combinations thereof. Chapter 10 concludes and describes directions for future study.

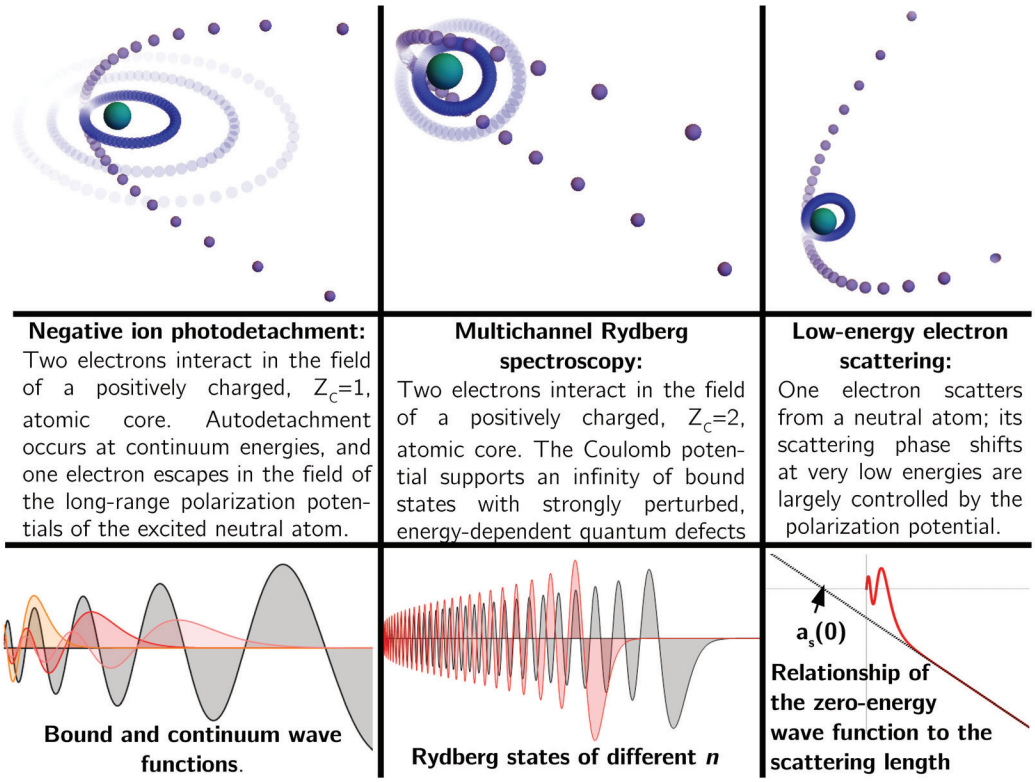

Figure 1.1. Chapter 2 describes the theory of these three different types of interactions, which are the fundamental components of the systems studied in this thesis.

2. THEORETICAL TECHNIQUES

At first glance, the AMO theorist's task is almost trivial: solve the Schrödinger equation for the wave function, and then use this wave function to calculate relevant observables following standard formulae. The theorist simply needs to insert the appropriate Hamiltonian into a partial differential equation solver, then go home for the night while the computer churns, eager to return the next morning to write up some results. This naive view is quickly betrayed by the reality of the complexity of physical phenomena. The primary, sometimes insurmountable, problem is dimension: an N-particle wave function must describe 3N spatial degrees of freedom. Particle spins expand this Hilbert space even further. The theorist must then solve partial differential equations, often involving boundary conditions at infinity, in a many-dimensional space impenetrable to calculation, let alone visualization or even tabulation due to this exponential growth in complexity.

The driving insight behind all the theoretical tools used throughout this thesis is that this vast configuration space can be separated, on firm physical grounds, into various distinct regions where certain interactions dominate and others can be ignored. This concept is the common thread uniting such disparate concepts as multichannel quantum defect theory (MQDT), the R-matrix eigenchannel method, frame transformations, and the Fermi pseudopotential. Every project undertaken in this thesis relies on one or more of these concepts to make the problem tractable.

Separation of configuration space into regions has several important implications. From a phenomenological perspective, after identifying small regions where the

physics may be extremely difficult to solve, one can often parameterize the physics throughout the rest of space using only a few quantities determined by the physics in this complex region. Thus, in the standard formulation of MQDT, the small region of space in which an electron interacts with an atomic or ionic complex determines a few parameters that are very insensitive to the energy of the electron, and which then effortlessly describe the highly energy-dependent physics of the electron at large distances. For example, the quantum defects of each Rydberg channel depend only on the interactions happening in the region around the atomic core, typically spanning a few tens of atomic units at most. Once calculated, they give the electronic energies and give the wave function everywhere outside of the small atomic core region for the infinite number of Rydberg states, thousands of atomic units in size.

Another difficulty regarding the spatial dimensions of problems in atomic and molecular physics is that calculations often involve infinitely large regions of space. When a particle is at positive energy its wave function extends over all space and must be calculated and then later integrated over this entire region to describe scattering properties. Bound state problems can often be treated with relatively brute-force methods due to the L^2 integrability of basis functions with closed boundary conditions at infinity, since typically this outer limit can be approximated as a finite distance very accurately. A large enough basis in this regard can come close to approximating a complete set of states, and finite integrals can be done routinely. Scattering problems, however, must by necessity deal with wave functions that are non-zero at infinity. These must be handled with a broader range of approaches. One interesting solution is the *complex rotation* method, which is a fascinating mathematical approach [54]. In this method, a scaling of the coordinates $r \rightarrow re^{i\theta}$ shifts positive energies into negative energies, thus turning resonance states into bound states. This means that L^2 trial functions can be used for the calculation. Stabi-

lization techniques are also possible, where the use of basis functions not satisfying correct boundary conditions (in this case they are typically box-quantized in a region of size L) can nevertheless be used to calculate resonance properties by varying the size of the box and searching for stabilization points; these can be proved to occur at resonances of the exact system [55, 56].

For investigations seeking to identify not only resonance positions but also dynamical properties such as partial and total cross sections, energy-dependent phase shifts, or angular distribution parameters, the theoretical techniques detailed in this chapter are essential tools. They emphasize the concept of spatial separability discussed earlier, and the physical concepts deployed in deriving these methods form the essential basis for every other topic described here. The eigenchannel R-matrix approach, coupled with multichannel quantum defect theory, is the foundational theory for describing Rydberg states or doubly excited electron interactions in negative ion systems. It is built on the concept, discussed above, that an excited electron only interacts with other core electrons over a range of just a few atomic units; outside of this "R-matrix volume" the electron wave function can be found analytically by solving the appropriate radial Schrödinger equation with the long-range potential r^{-b} relevant to the system, or just by matching to numerical solutions of the single-electron case at large enough distances. For Rydberg atoms, $b = 1$ and the asymptotic solutions are Couloumb wave functions; for the hydrogen anion or for purely centrifugal potentials $b = 2$ and the solutions are spherical Bessel functions (although for the former case, for a sufficiently attractive dipole potential these functions are of complex order and argument, and possess interesting qualities); for other, non-degenerate, atomic anions $b = 4$ and the solutions are Mathieu functions. By separating configuration space in this manner, the challenging two electron calculation can be performed over just a small region of configuration space. This provides

the scattering parameters needed to tether the long-range wave functions, either those of MQDT or a numerical calculation, which describe the system throughout the rest of space. These methods have found incredible success over the years, and a very useful review which forms the foundation of much of this chapter is found in [10].

Similarly, the Fermi pseudopotential was first derived by Fermi to describe the interaction between a Rydberg electron and a neutral atom enveloped within the Rydberg wave function [57]. Again, due to the enormous size of the Rydberg electron relative to the interaction region, this would be an enormously difficult problem for standard techniques. Turning the problem around, the small scale of the interaction region allows its effects to be simply parameterized, and Fermi's resulting model potential was able to explain a series of experimental results. The key insight of Fermi's derivation is that the electron, moving with very little kinetic energy in its Rydberg orbit, is essentially a very low-energy scatterer off of the neutral perturber. Their interaction is therefore determined by a scattering length (or volume, for higher partial waves), derived by effective range theory. Furthermore, the exact interaction can be replaced by a delta function potential proportional to the energy dependent scattering length in such a way that guarantees that the long-range physics will be correct, even though the potential seems to be a shockingly simplistic picture of a real atom-electron interaction. This same idea has since been utilized often in the ultracold regime to describe atom-atom scattering, where the long de Broglie wavelength of very cold scatterers reduces the complicated physics of the atom-atom interaction to a contact interaction providing the correct scattering length is used.

In the remainder of this chapter, we derive these concepts in considerable detail, as they are the essential background for the theory used in the specific projects undertaken in this thesis. Other, related techniques such as the frame transformation

and details of our applications of MQDT, will be described in later chapters when they become relevant.

2.1 Two-electron systems: the eigenchannel R-matrix method

This section endeavours to describe the eigenchannel R-matrix theory used to treat two-electron systems throughout this thesis. This analysis will demonstrate some details of the R-matrix calculation and discuss analytical and numerical aspects of the long-range solutions which, along with the short-range R-matrix solutions, fully characterize the wave function.

2.1.1 The Hamiltonian, its eigenspectrum, and emergent long-range potentials

We begin by defining the Hamiltonian and describing how long-range potentials emerge. Although the R-matrix concept is general to many applications, we specialize to the "two-electron" systems such as alkaline-earth atoms and alkali negative ions. The deeply bound core electrons are treated using independent-electron model potentials, and otherwise play no role. These potentials describe polarization and screening effects, and are characterized by parameters which are fit by comparing the calculated energies to experimental energies.

The two-electron Hamiltonian is straightforward to describe. Upon removing the trivial center of mass motion and assuming an infinitely massive nucleus, we have

$$H = -\frac{1}{2}\nabla_1^2 - \frac{1}{2}\nabla_2^2 + V_{l_1}(r_1) + V_{l_2}(r_2) + \frac{1}{r_{12}}. \tag{2.1}$$

Here, 1,2 label the two electrons, r_i is the position of electron i, $V_l(r)$ is the model potential for each partial wave l, and $r_{12} = \sqrt{r_1^2 + r_2^2 - 2r_1 r_2 \cos\theta_{12}}$ is the distance

between the two electrons. Atomic units are used here and throughout the following, unless otherwise specified. Spin-orbit physics can be included at this stage by adding the potential suggested by the Dirac equation [58],

$$V_{so}^{slj}(r) = \frac{(g-1)\alpha^2}{2}\frac{1}{r}\frac{dV}{dr}\left(1-\frac{(g-1)\alpha^2}{2}V(r)\right)^{-2} s\cdot l, \tag{2.2}$$

where α is the fine-structure constant and g is the electron g-factor. For simplicity, we ignore spin-orbit coupling in this chapter. However, in chapter 5 the frame transformation and MQDT for the Coulomb field are used to treat spin-orbit effects, and in chapter 6 we include spin-orbit effects parameterically through spin-dependent quantum defects and phase shifts.

The specific form of $V_l(r)$ depends on the system. For negative ions, $V_l(r)$ is fit so that the eigenspectrum matches experimental values for the atomic energy levels; for Rydberg states it is fit to match the energy levels of the positive ion. For the hydrogen negative ion or Rydberg states of the helium atom $V_l(r)$ is simply

$$V_l(r) = -\frac{Z}{r} + \frac{l(l+1)}{2r^2}, \tag{2.3}$$

where $Z = 1$ for H^- and $Z = 2$ for He. The model potentials for more complex atoms can be found in Refs. [10, 48, 59]. For typically have a form similar to [48]

$$V_l(r) = -\frac{1}{r}\left(Z_C + (Z-Z_C)e^{-a_1 r} + a_2 r e^{-a_3 r}\right) - \frac{\alpha_c}{2r^4}\left(1-e^{-(r/r_c)^3}\right)^2, \tag{2.4}$$

where r_c, a_1, a_2, a_3 are fit parameters for each l, $Z_C = 1$, and α_c and Z are the polarizability of the core and charge of the nucleus, respectively. The potentials for hydrogen and potassium [48, 59] are compared in Fig. 2.1.

As discussed above, the R-matrix approach is based on the concept that both electrons only interact within a finite volume. As one electron escapes beyond the radius of the R-matrix volume, r_0, its wave function is given numerically by solving

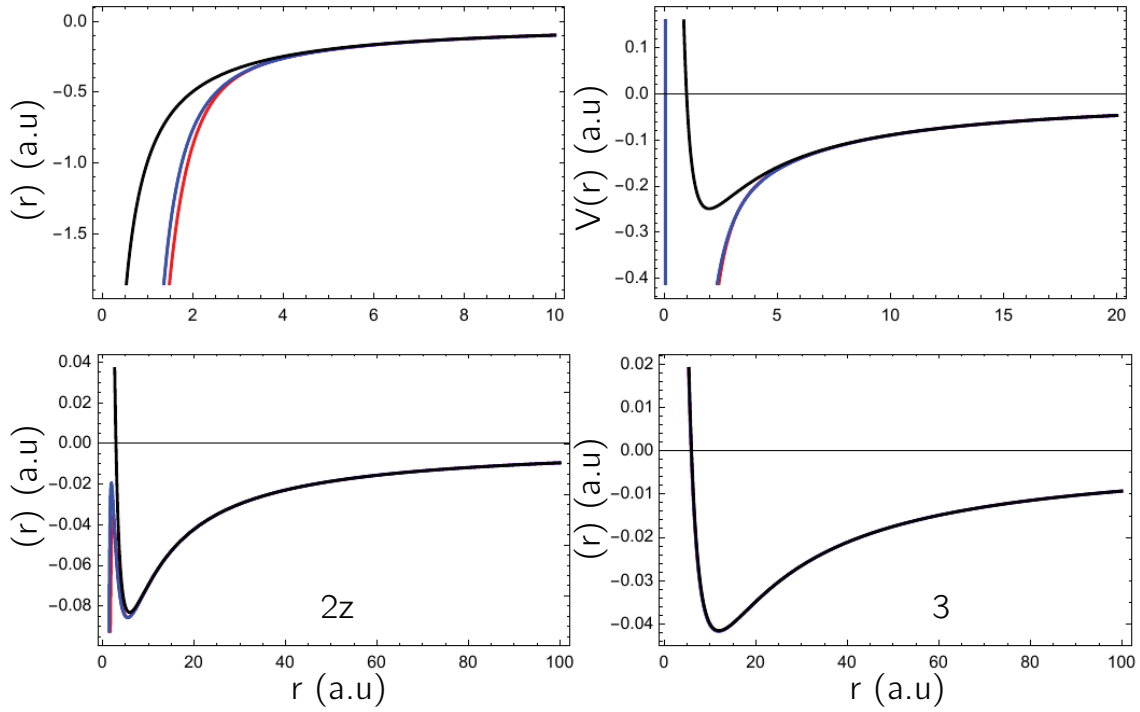

Figure 2.1. Potential energy curves. The black curve is valid for hydrogen, while the red and blue curves represent the model potentials for potassium from [48] and [59], respectively. At large distances, and for large l, these potentials are identical. The two different model potentials give essentially identical one-electron energies.

the coupled channel equations or by analytical methods such as MQDT. The radius r_0 is defined by the boundary condition $\Psi(r_1, r_2) = 0$ if both r_1 and r_2 are greater than r_0. Typically, r_0 must be large enough that the excited states of the residual atom or ionic core which are relevant at the energies under consideration are contained within this volume. Within the R-matrix volume, the full two-electron problem must be solved. Years of R-matrix studies have shown that its success relies on the accuracy

of the one-electron wave functions $u_{nl}(r)$ satisfying the radial Schrödinger equation for a single electron,

$$-\frac{1}{2}\frac{d^2}{dr^2} + \frac{l(l+1)}{2r^2} + V_l(r) - \quad _{nl} \quad u_{nl}(r) = 0, \tag{2.5}$$

subject to box boundary conditions, $u_{nl}(0) = 0$ and $u_{nl}(r_0) = 0$. This is true independently of the choice of model potential $V_l(r)$. This stems from the fact that the electronic wave function phases are guaranteed to be correct if the energies are, and thus the electron-electron interaction $1/r_{12}$, which depends sensitively on the relative electron phases, will be accurate. One can choose from a variety of numerical methods to solve Eq. 2.5: a simple three-point stencil on a square root mesh [60] or more complicated and sophisticated Numerov or predictor-corrector methods are common choices. These methods may struggle to accurately describe the highly oscillatory excited orbitals. These inaccuracies are reflected in the overlap matrix elements, which should vanish for exact wave functions but can substantially differ from zero in these numerical implementations. We have therefore implemented a B-spline method, which can give results to nearly arbitrary precision simply by increasing the number of splines and their order. Details are given in Appendix D, and the typical results of this calculation are exemplified in Fig. 8.2, which compares calculated eigenenergies of the potassium atom with the quantum defect formula. With these one-electron orbitals we construct a properly symmetrized and normalized two-electron basis set [10]:

$$\begin{aligned} y_{i=\{n_1,l_1,l_2\}n_2}(r_1,\vec{r}_2) = & \frac{1}{\sqrt{2(1+\delta_{n_1,n_2}\delta_{l_1,l_2})}} \frac{u_{n_1l_1}(r_1)}{r_1} Y_{l_1l_2LM}(\Omega_1\Omega_2) \frac{u_{n_2l_2}(r_2)}{r_2} \\ & + (-1)^{l_1+l_2-L+S} \frac{u_{n_2l_2}(r_1)}{r_1} \frac{u_{n_1l_1}(r_2)}{r_2} Y_{l_1l_2LM}(\Omega_2,\Omega_1) \ . \end{aligned} \tag{2.6}$$

Typically we obtain $\sim$ 100 closed-type functions, vanishing when either r_1 or r_2 equal r_0, for each of 10-15 partial waves, and since these obey closed boundary

conditions these form a complete and orthonormal set within the R-matrix volume. The fact that Eq. 2.6 provides a very accurate and efficient basis for the two-electron Hamiltonian is a major advantage of the R-matrix method, and of course hinges on the fact that the region of two-electron interactions can be restricted to a finite volume. For this reason, processes like double ionization are significantly more challenging, although these methods can be modified to study them (see e.g. [61]). In addition to the closed-type functions we also include two open-type functions for each partial wave to provide the flexibility to describe the continuum wave function of the escaping electron, which must have non-zero amplitude at the R-matrix radius. These one-electron functions are neither mutually orthogonal nor orthogonal to the closed-type.

Most integrals required to form matrix elements of H require integrating over the coordinates of a single electron and are trivial to calculate using the numerical wave functions provided by the B-spline routines. The greatest computational hurdle is in calculating the matrix elements of $1/r_{12}$. This is facilitated using the expansion into Legendre polynomials P_k

$$\frac{1}{r_{12}} = \frac{1}{\sqrt{r_1^2 + r_2^2 - 2r_1 r_2 \cos\theta_{12}}} = \sum_{k=0} \frac{r_<^k}{r_>^{k+1}} P_k(\cos\theta_{12}). \tag{2.7}$$

Matrix elements in the two-electron basis thus involve integrals of the form

$$\begin{aligned} &n_1 l_1 n_2 l_2 LM|\frac{1}{r_{12}}|n_1 l_1 n_2 l_2 L\ M \qquad (2.8)\\ &= \sum_k \mathrm{d}r_1 \mathrm{d}r_2 u_{n_1 l_1}(r_1) u_{n_2 l_2}(r_2) \frac{r_<^k}{r_>^{k+1}} u_{n_1 l_1}(r_1) u_{n_2 l_2}(r_2)\ \ l_1 l_2 LM|P_k(\cos\theta_{12})|l_1 l_2 L\ M \quad , \end{aligned}$$

a two-dimensional radial integral multiplying a four-dimensional angular integral. This latter factor is obtained analytically and defines important selection rules that

eliminate many terms in the radial integral. The evaluation of the angular integral begins with the identity relating Legendre polynomials to Spherical Harmonics:

$$\begin{aligned} A = &\ l_1 l_2 LM|P_k(\cos\theta_{12})|l_1 l_2 L\ M \\ = &\ l_1 l_2 LM\ \frac{4\pi}{2k+1} \sum_q (-1)^q Y_k^q(\Omega_1) Y_k^{-q}(\Omega_2)\ l_1 l_2 L\ M\ . \end{aligned} \tag{2.9}$$

The coupled angular momentum states are then decoupled, each contributing a Wigner 3J symbol:

$$A = \frac{4\pi}{2k+1} \sum_{\substack{m_1 m_2 \\ m_1 m_2 q}} C^{LM}_{l_1 m_1, l_2 m_2} C^{L\ M}_{l_1 m_1, l_2 m_2} (-1)^q\ l_1 m_1 | kq | l_1 m_1 \quad l_2 m_2 | k-q | l_2 m_2\ . \tag{2.10}$$

These one-electron matrix elements are evaluated using the standard integral over three spherical harmonics:

$$\begin{aligned} lm|kq|l\ m &= \int Y^*_{lm}(\Omega) Y_{kq}(\Omega) Y_{l\ m}\ (\Omega) \mathrm{d}\Omega \\ &= \overline{(2l+1)(2l\ +1)}(-1)^m \begin{pmatrix} l & k & l \\ 0 & 0 & 0 \end{pmatrix} \begin{pmatrix} l & k & l \\ -m & q & m \end{pmatrix} \end{aligned} \tag{2.11}$$

Inserting Eq. 2.11 into Eq. 2.10, converting the Wigner 3J symbols into Clebsch-Gordan coefficients, and manipulating these coefficients gives

$$\begin{aligned} A = &\sum_{\substack{m_1 m_2 \\ m_1 m_2 q}} \overline{(2l_1+1)(2l_2+1)} \begin{pmatrix} l_1 & k & l_1 \\ 0 & 0 & 0 \end{pmatrix} \begin{pmatrix} l_2 & k & l_2 \\ 0 & 0 & 0 \end{pmatrix} (-1)^{l_1+l_2} \\ &\times C^{LM}_{l_1 m_1, l_2 m_2} C^{L\ M}_{l_1 m_1, l_2 m_2} C^{l_1 m_1}_{l_1 m_1, kq} C^{l_2 m_2}_{kq, l_2 m_2} (-1)^{k+l_2-l_2}. \end{aligned} \tag{2.12}$$

This summation is given in Eq. 9.8 of [62]:

$$\begin{aligned} &C^{jm}_{j_{12} m_{12} j_3 m_3} C^{j_{12} m_{12}}_{j_1 m_1 j_2 m_2} C^{j\ m}_{j_1 m_1 j_{23} m_{23}} C^{j_{23} m_{23}}_{j_2 m_2 j_3 m_3} \\ &\quad = \delta_{jj}\ \delta_{mm}\ (-1)^{j_1+j_2+j_3+j} \quad \overline{(2j_{12}+1)(2j_{23}+1)} \begin{Bmatrix} j_1 & j_2 & j_{12} \\ j_3 & j & j_{23} \end{Bmatrix}. \end{aligned} \tag{2.13}$$

This yields

$$\begin{aligned} l_1 l_2 LM|P_k(\cos\theta_{12})|l_1 l_2 L\, M &= \sqrt{(2l_1+1)(2l_1+1)(2l_2+1)(2l_2+1)} \\ &\times \begin{pmatrix} l_1 & k & l_1 \\ 0 & 0 & 0 \end{pmatrix} \begin{pmatrix} l_2 & k & l_2 \\ 0 & 0 & 0 \end{pmatrix} (-1)^{l_1+l_1+L} \delta_{L,L}\, \delta_{M,M} \\ &\times \begin{Bmatrix} l_1 & L & l_2 \\ l_2 & k & l_1 \end{Bmatrix}. \end{aligned} \tag{2.14}$$

This equation is the mathematical expression of angular momentum conservation. Moreover, these Wigner 3J symbols constrain k to be within $\min(l_1+l_1, l_2+l_2)$ and $\max(|l_1-l_1|, |l_2-l_2|)$, also a reflection of angular momentum conservation. This greatly reduces the computational effort expended on these integrals. Finally, since these 3J symbol have zeros on the bottom row, l_1+l_1+k and l_2+k+l_2 must be even integers.

Unlike the angular integrals, the radial integral must be evaluated numerically:

$$\int_0^\infty \int_0^\infty u_{n_1 l_1}(r_1) u_{n_1 l_1}(r_1) \frac{r_<^k}{r_>^{k+1}} u_{n_2 l_2}(r_2) u_{n_2 l_2}(r_2) \mathrm{d}r_1 \mathrm{d}r_2, \tag{2.15}$$

where $r_> = \max(r_1, r_2)$ and $r_< = \min(r_1, r_2)$. By separating the integration over the coordinate r_2 into two regions, $0 \le r_2 \le r_1$ and $r_1 \le r_2 \le \infty$, this cusp can be integrated over as follows:

$$\begin{aligned} \int_0^\infty u_{n_1 l_1}(x_1) u_{n_1 l_1}(x_1) \; \frac{1}{x_2^{2k+2}} \int_0^{x_1^2} u_{n_2 l_2}(x_2) u_{n_2 l_2}(x_2) x_2^{2k} 2x_2 \mathrm{d}x_2 \\ + x_1^{2k} \int_{x_1^2}^\infty u_{n_2 l_2}(x_2) u_{n_2 l_2}(x_2) x_2^{-2k-2} 2x_2 \mathrm{d}x_2 \;\; 2x_1 \mathrm{d}x_1, \end{aligned} \tag{2.16}$$

where a square root mesh defined by $r_i = x_i^2$ has been used.

At this point, Eq. 2.1 may be diagonalized within the basis defined in Eq. 2.6, excluding all open-type functions. For processes such as photoabsorption or photoionization of an atom or negative ion photodetachment it must be diagonalized

in both the initial and final states, denoted in the usual fashion with term notation ${}^{2S+1}L^{\pi}$. The initial and final state eigenvectors are used to calculate transition dipole matrix elements. For negative ions the lowest eigenenergy in the initial state provides the electron affinity; for neutral atoms it should give the atomic ground state. In the final state the eigenenergies should all exceed the first atomic bound state for negative ions, reflecting the absence of excited states in alkali negative ions, while for neutral atoms these states should match excited atomic states.

So far our attention has been focused on the interaction between both electrons in the field of the atomic core, and how to calculate the box eigenstates and energies of the Hamiltonian. To be able to describe the behavior of one of these electrons when it leaves the R-matrix region – whether an electron in a far-flung Rydberg orbit, an electron ejected from an ionic complex through photodetachment, or the scattering electron approaching a neutral atom from infinity – the long-range potentials that extend outside of the R-matrix box and nature of the wave function in this region must be described. Outside of the R-matrix box the wave function can be expanded into channel functions:

$$\Psi(r_1, \vec{r}_2) = \sum_{l_1, l_2} \frac{f_{n_2 l_2}(r_2)}{r_2} \frac{u_{n_1 l_1}(r_1)}{r_1} Y^{LM}_{l_1 l_2}(\Omega_1, \Omega_2), \quad r_2 \geq r_0, \tag{2.17}$$

where r_2 is the radial coordinate of the outgoing electron, and it must be remembered that $\Psi(r_1, \vec{r}_2) = 0$ if r_1 and $r_2 \geq 0$. Antisymmetrization of this wave function, and those in related formulae, is implied. This wave function represents an expansion into the complete set of target states, or *channels*, described by the good angular momentum quantum numbers l_1, l_2, and L, and the radial target eigenfunctions $\frac{u_{n_1 l_1}(r_1)}{r_1}$. These are the bound state wave functions of the electron which does not

leave the R-matrix volume. To make this dependence on channel functions more explicit, Eq. 2.17 is often written instead as

$$\psi_\mu(r_1, \vec{r}_2) = \sum_i^N \frac{1}{r_2}\Phi_i(\omega)G_{i\mu}(r_2), \;\; r_2 \geq r_0, \tag{2.18}$$

where ω is the set of all coordinates except the fragmentation coordinate r_2, Φ_i is the i^{th} channel function, and $G_{i\mu}(r_2)$ is the radial equation of the outgoing electron in the i^{th} channel. By comparison with Eq. 2.17, $\Phi_i(\omega) = \frac{u_{n_1 l_1}(r_1)}{r_1} Y^{LM}_{l_1 l_2}(\Omega_1, \Omega_2)$ if all the channel quantum numbers are collapsed into a single index i. Quite generally, after imposing boundary conditions at the origin but prior to imposing boundary conditions at infinity, an N-channel Schrödinger equation must have N independent solutions; μ labels these linearly independent solutions, and hence we must write the radial wave function as a matrix to include its dependence on channel and its linear independence.

These unknown radial functions are found by setting up the coupled-channel equations. These are constructed by acting on Eq. 2.17 with the Hamiltonian of Eq. 2.1, and then projecting onto the channel wave functions and neglecting exchange terms. Outside of the R-matrix box the μ^{th} linearly independent radial wave function satisfies the full set of coupled channel equations without exchange,

$$\sum_{j=1}^N \left[-\frac{1}{2}\frac{d^2}{dr_2^2} + \frac{l_{2i}(l_{2i}+1)}{2r_2^2} - (E - \;\;_i) \right] \delta_{ij} + \sum_{\lambda=1}^{\infty} \frac{d_{ij}^\lambda}{r_2^{\lambda+1}} \;\; G_{j\mu}(r_2) = 0, \;\; r_2 \geq r_0. \tag{2.19}$$

E is the total energy, $\;\;_i$ is the energy of the inner electron in the i^{th} channel, and d_{ij}^λ are multipole moments:

$$d_{ij}^\lambda = \;\; \Phi_i(\omega)|r_1^\lambda P_\lambda[\cos(\hat{r}_1 \cdot \hat{r}_2)]|\Phi_j(\omega) \;\; . \tag{2.20}$$

Restricting $\lambda \leq 3$ is typically sufficient. We will later use these equations to obtain the wave functions $G_{j\mu}(r_2)$, but for now we show how this set of coupled equations leads to the characteristic long-range potentials expected for Rydberg or negative ion systems. At long range $V_l(r) \to -\frac{Z-N+1}{r}$, where Z is the nuclear charge and N is the total number of electrons. For the systems considered here, $V_l(r) \to -\frac{Z_C}{r}$ where $Z_C = 1$ for atomic negative ions and $Z_C = 2$ for Rydberg states. We can expand the $1/r_{12}$ potential using the first two terms of the Legendre polynomial expansion:

$$\frac{1}{r_{12}} \approx \frac{1}{r_2} + \frac{r_1 \cos\theta_{12}}{r_2^2} + \mathcal{O}\ \ (r_1/r_2)^2\ \ . \tag{2.21}$$

For simplicity, let us take for example a two-channel system. These channels are described by l_0, l_1, the angular momenta of the outer electron in each channel, and $_0, \epsilon_1$, the channel thresholds. Eq. 2.19 in this limit becomes:

$$0 = \begin{pmatrix} -\frac{1}{2}\frac{d^2}{dr_2^2} - \frac{(Z_C-1)}{r_2} + \frac{l_0(l_0+1)}{r_2^2} - (E - \ _0) & \frac{q}{r_2^2} \\ \frac{q}{r_2^2} & -\frac{1}{2}\frac{d^2}{dr_2^2} - \frac{(Z_C-1)}{r_2} + \frac{l_1(l_1+1)}{r_2^2} - (E - \ _1) \end{pmatrix} \cdot \begin{pmatrix} G_{1\mu}(r_2) \\ G_{2\mu}(r_2) \end{pmatrix}, \tag{2.22}$$

where q is a dipole matrix element implied by Eq. 2.20. Since the Coulomb potential in the diagonal terms dominates the centrifugal term and the off-diagonal elements, we can separate these weaker terms as follows:

$$\begin{aligned} 0 = &\begin{pmatrix} -\frac{1}{2}\frac{d^2}{dr_2^2} - \frac{(Z_C-1)}{r_2} & 0 \\ 0 & -\frac{1}{2}\frac{d^2}{dr_2^2} - \frac{(Z_C-1)}{r_2} \end{pmatrix} \begin{pmatrix} G_{1\mu}(r_2) \\ G_{2\mu}(r_2) \end{pmatrix} \\ &+ \begin{pmatrix} \frac{l_0(l_0+1)}{r_2^2} - (E - \ _0) & \frac{q}{r_2^2} \\ \frac{q}{r_2^2} & \frac{l_1(l_1+1)}{r_2^2} - (E - \ _1) \end{pmatrix} \begin{pmatrix} G_{1\mu}(r_2) \\ G_{2\mu}(r_2) \end{pmatrix}. \end{aligned} \tag{2.23}$$

We can decouple this equation adiabatically by diagonalizing this second matrix, composed of coupling potential terms $\propto r^{-2}$ [63]. Doing so and expanding the eigenvalues to lowest non-trivial order, we find:

$$\begin{pmatrix} \frac{l_0(l_0+1)}{r_2^2} - (E - \ _0) & \frac{q}{r_2^2} \\ \frac{q}{r_2^2} & \frac{l_1(l_1+1)}{r_2^2} - (E - \ _1) \end{pmatrix} \tag{2.24}$$
$$\approx \begin{pmatrix} \frac{l_0(l_0+1)}{r_2^2} - (E - \ _0) + \frac{q^2}{(\ _1 - \ _0) r_2^4} & 0 \\ 0 & \frac{l_1(l_1+1)}{r_2^2} - (E - \ _1) - \frac{q^2}{(\ _1 - \ _0) r_2^4} \end{pmatrix}.$$

From this, we obtain two decoupled differential equations for the radial functions in each channel, and see that the off-diagonal elements were converted into polarization potentials, $V \sim -\frac{\alpha}{2r^4}$. If $Z_C = 1$, as in electron-atom scattering and negative ion photodetachment, this polarization potential is the only long-range force. For $Z_C = 2$, the polarization potential can be treated perturbatively and leads to the quantum defects of non-penetrating Rydberg states, as in Eq. 2.76.

This simplistic two-channel derivation showed how polarization potentials arise in atom-electron scattering, negative ion photodetachment, and contribute to the quantum defects of Rydberg states. As a side note, if the energies $_0$ and $_1$ are degenerate, then the arbitrary energy scale in Eq. 2.23 can be ignored and the r^{-2} factors out. We thus obtain two decoupled dipole potential radial Schrödinger equations, which have some fascinating properties that will be discussed alongside the polarization potential in chapter 8. As a final note, the generalization of the preceding discussion to an arbitrary number of channels leads to the channel polarizability α. In second-order perturbation theory this is defined

$$\alpha_{n_1,l_1,l_2} = 2 \sum_{n_1,l_1,l_2} \frac{|\langle n_1 l_1 l_2 LM | r_1 \cos\theta_{12} | n_1 l_1 l_2 LM \rangle|^2}{_{n_1 l_1} - \ _{n_1 l_1}} \tag{2.25}$$

Using this expression, the adiabatic long-range solutions to the coupled channel equations become uncoupled radial Schrödinger equations

$$-\frac{1}{2}\frac{d^2}{dr^2} + \frac{l(l+1)}{2r^2} - \frac{\alpha}{2r^4} - \frac{k^2}{2} \quad u_l(r) = 0. \tag{2.26}$$

These channel polarizabilities are very important in negative ions and in the electron-atom interaction, especially at very low energies where this potential has a strong effect over very large distances. Tables 2.1 and 2.2 show the calculated and experimental ground state polarizabilities for the alkali atoms of relevance to this thesis, and table 8.1 presents some excited state polarizabilities in potassium, showing in particular how they grow extremely large for excited states.

Having uncovered how these long-range potentials emerge, we can return to the Hamiltonian of Eq. 2.1. We have already seen how to obtain its eigenspectrum within a confined volume, which might give physically relevant energies for a few deeply bound states but so far does not have any clear relevance to higher excited states, let alone scattering or detachment/ionization physics, since the basis used restricted both electrons to lie within the R-matrix volume. As the next section shows, this is actually exactly what is needed to efficiently calculate these states, since the electrons only interact within the R-matrix volume. Outside of this volume the outer electron is only affected by the potentials developed above. In the most complicated case, where the multipole moments are strong enough that these potentials extend far outside the R-matrix volume, the coupled channel equations of Eq. 2.19 must be solved numerically. In simpler cases where these potentials drop off rapidly, as is typically the case for Rydberg atoms, quantum defect theory can be used to analytically construct the wave functions outside of the R-matrix volume. To connect these two regions all that is needed is the logarithmic derivative, defined

$$-b = \frac{\partial \ln(\Psi)}{\partial r}. \tag{2.27}$$

Having developed a complete, orthogonal, and physically motivated basis set above within this R-matrix volume, our next goal is to show that this logarithmic derivative can be calculated variationally using this basis.

2.1.2 Streamlined R-matrix calculation

Rather than immediately trying to compute b, we start instead with an identity for the energy, obeyed by the exact wave function Ψ:

$$E = \frac{\int_V \Psi^* \left[-\frac{1}{2}\nabla^2\Psi + U\Psi \right] \mathrm{d}V}{\int_V \Psi^*\Psi \mathrm{d}V}, \tag{2.28}$$

where V is a finite volume, taken to be the R-matrix volume. Using Green's theorem,

$$\Psi^*\nabla^2\Psi \mathrm{d}V = \nabla(\Psi^*\nabla\Psi) - \nabla\Psi^*\nabla\Psi \mathrm{d}V, \tag{2.29}$$

we obtain

$$E = \frac{\int_V \left[\frac{1}{2}\nabla\Psi^* \cdot \nabla\Psi + \Psi^* U \Psi \right] \mathrm{d}V - \frac{1}{2}\int_S \Psi^* \frac{\partial\Psi}{\partial n} \mathrm{d}a}{\int_V |\Psi|^2 \mathrm{d}V}. \tag{2.30}$$

Making b constant on the surface of the R-matrix sphere will eventually lead to the property that it is an eigenvalue of the R-matrix. Using $-b|\Psi|^2 = \Psi^* \frac{\partial\Psi}{\partial n}$, we find

$$E = \frac{\int_V \left[\frac{1}{2}\nabla\Psi^* \cdot \nabla\Psi + \Psi^* U \Psi \right] \mathrm{d}V + \frac{b}{2}\int_S \Psi^*\Psi \mathrm{d}a}{\int_V |\Psi|^2 \mathrm{d}V}. \tag{2.31}$$

Rearrangement of the above gives an equation for b:

$$b = 2\frac{\int_V \left[E\Psi^*\Psi - \frac{1}{2}\nabla\Psi^* \cdot \nabla\Psi - \Psi^* U \Psi \right] \mathrm{d}V}{\int_V \Psi^* \delta(r - r_0)\Psi}. \tag{2.32}$$

Notice that the denominator is just another way of writing the surface integral, and the numerator can be turned into $\Psi^*(E - \hat{H})\Psi$ since

$$\begin{aligned} -\frac{1}{2}\nabla\Psi^* \cdot \nabla\Psi - \Psi^* U \Psi &= -\frac{1}{2}\nabla(\Psi^*\nabla\Psi) + \frac{1}{2}\Psi^*\nabla^2\Psi - \Psi^* U \Psi \\ &= -\frac{1}{2}\nabla(\Psi^*\nabla\Psi) - \Psi^* H \Psi. \end{aligned} \tag{2.33}$$

Upon insertion into the volume integral, this first term can be represented using the Bloch operator, $L = \frac{1}{2r}\delta(r - r_0)\frac{\partial}{\partial r}r$. We therefore define $\hat{H} = H + L$, and obtain

$$b = 2\frac{\int_V \Psi^*(E - \hat{H})\Psi \mathrm{d}V}{\int_V \Psi^*\delta(r - r_0)\Psi \mathrm{d}V}, \tag{2.34}$$

To show that this implies a variational principle for b, we compute δb by setting $\Psi \to \Psi + \delta\Psi$, where $\delta\Psi$ is the first-order difference from the exact wave function. We start by writing Eq. 2.32 as $b = N/D$, and then using the product rule to evaluate δb:

$$\delta b = \frac{1}{D}\left(\delta N - b\delta D\right). \tag{2.35}$$

These terms are:

$$\delta D = 2 \int_V \Psi^*\delta(r - r_0)\delta\Psi \mathrm{d}V \tag{2.36}$$

$$\delta N = 2 \left[2 \int_V \Psi^* E\delta\Psi - \int_V \nabla\Psi^* \cdot \nabla\delta\Psi \mathrm{d}V - \int_V 2\Psi^* U\delta\Psi \mathrm{d}V \right]. \tag{2.37}$$

Applying Green's theorem again to the middle term of δN yields

$$\delta b = \frac{2}{D}\left[2 \int_V \Psi^*(E - H)\delta\Psi + \int_S \delta\Psi\frac{\partial\Psi^*}{\partial n}\mathrm{d}a - b\int_V \Psi^*\delta(r - r_0)\delta\Psi \mathrm{d}V \right]. \tag{2.38}$$

By the definition of b, the last two terms are equal and opposite, and the first term vanishes since Ψ is the exact wave function which satisfies the Schrödinger equation, $H\Psi = E\Psi$. We therefore find that the first-order variation in b vanishes, thus proving the variational nature of this solution.

To explicitly solve for this variational solution we expand the wave function into a convenient basis of complete orthonormal states y_k: $\Psi = \sum_{k=1}^{n} y_k C_k$. The two-

electron basis states of Eq. 2.6 are an obvious choice. Inserting this expansion into Eq. 2.34 and projecting onto state y_k gives the matrix equation:

$$\Gamma C = b\Lambda C; \tag{2.39}$$

$$\Gamma_{kk} = 2 \int_V y_k(E - \hat{H})y_k \, \mathrm{d}V, \; \Lambda_{kk} = \int_S y_k y_k \, \mathrm{d}a. \tag{2.40}$$

Upon solving this generalized eigenvalue problem, we get a set of N eigenvalues b_β and eigenvectors C_β, where N is the number of open or *weakly* closed channels that were included in the basis and are non-zero at the R-matrix boundary. The open channels are evidently those in which the electron is energetically free to escape to infinity. *Weakly* closed channels, in contrast, are still closed as $r \to \infty$ but have non-zero amplitude at r_0. There are also in principal an infinite number of strongly closed channels which, although they contribute heavily to the two-electron dynamics within the R-matrix box, have no amplitude at the box radius and thus do not contribute to additional logarithmic derivatives. A large number of these *strongly* closed channels must be included in the calculation since this forms the complete basis within the R-matrix volume.

The fact that this $n \times n$ matrix equation has only N eigenvalues must be true on physical grounds since the logarithmic derivatives must vanish for every strongly closed channel where there is no wave function at the reaction surface. The rank of Λ, clearly a highly singular matrix, is what guarantees the reduction from the expected n eigenvalues based on the dimension of our matrices, if they were non-singular, to just N eigenvalues. This can be formally proved [64], but setting up the problem in the streamlined version, as we will do shortly, shows clearly that the number of non-zero eigenvalues must correspond directly to the number of open (n_o) and weakly closed (n_c) channels, so that $N = n_o + n_c$. In the equations immediately following we refer to both weakly closed and open channels as open since we are only discussing

their behavior at $r = r_0$, although this will change in section 2.1.3 and chapter 5 since there the only relevant states are those with non-zero amplitude at $r = r_0$, but the different boundary conditions obeyed by weakly closed and open channels must still be treated. In these later cases, closed channels will refer to the n_c weakly closed channels, which still add to the n_o open channels so that $N = n_o + n_c$.

Since it seems remarkably wasteful to solve the $n \times n$ matrix equation 2.39 at each energy only to obtain N eigenvalues, it is preferable to seek out a solution which is better suited to these singular matrices. This is known as the streamlined R-matrix method [65]. We first express the matrix elements of Γ as the sum of an overlap matrix, the Hamiltonian matrix, and the Bloch operator matrix:

$$\Gamma_{kk} = 2(E\mathcal{O}_{kk} - H_{kk} - L_{kk}). \tag{2.41}$$

Next, we partition both Γ and Λ into closed/closed, open/closed, closed/open, and open/open partitions, of which only the open-open partition of Λ is nonzero since most surface terms vanish due to the large number of closed channels. This gives two coupled matrix equations:

$$\Gamma_{cc}C_c + \Gamma_{co}C_o = 0 \tag{2.42}$$

$$\implies C_c = -\Gamma_{cc}^{-1}\Gamma_{co}C_o \tag{2.43}$$

$$\Gamma_{oc}C_c + \Gamma_{oo}C_o = \Lambda_{oo}C_o b. \tag{2.44}$$

$$\implies (-\Gamma_{oc}\Gamma_{cc}^{-1}\Gamma_{co} + \Gamma_{oo})C_o = \Lambda_{oo}C_o b. \tag{2.45}$$

This final matrix equation has dimension equal to that of the open/weakly closed channels, $N \times N$. We write $\Omega = \Gamma_{oo} - \Gamma_{oc}\Gamma_{cc}^{-1}\Gamma_{co}$. Because the Bloch matrix L_{cc} is zero,

and the closed-closed portion of the overlap matrix is I, we can analytically invert Γ_{cc} as a function of E once we move to the representation where H_{cc} is diagonal:

$$H_{cc}^{kk} = \sum_{\lambda,\lambda} X_{k\lambda}^{\dagger} E_{\lambda\lambda} X_{\lambda\, k} \tag{2.46}$$

$$= \sum_{\lambda} X_{k\lambda}^{\dagger} E_{\lambda} X_{\lambda k}\,, \tag{2.47}$$

since $E_{\lambda\lambda}$ is the diagonal eigenvalue matrix. Since $\Gamma_{cc} = 2(H_{cc} + EI_{cc})$ in the closed-closed partition, we then conveniently have:

$$\begin{aligned}
\Omega_{kk} &= 2(EO_{oo}^{kk} - H_{oo}^{kk} - L_{oo}^{kk}) - \sum_{\lambda} \Gamma_{oc}(X_{k\lambda}^{-1}(2[EI - E_{\lambda\lambda}])X_{\lambda k})^{-1}\Gamma_{co} \\
&= 2(EO_{oo}^{kk} - H_{oo}^{kk} - L_{oo}^{kk}) - \sum_{\lambda} \Gamma_{oc} X_{\lambda k}[2(EI - E_{\lambda\lambda})]^{-1} X_{k\,\lambda}^{-1}\Gamma_{co} \\
&= 2(EO_{oo}^{kk} - H_{oo}^{kk} - L_{oo}^{kk}) - 2\sum_{\lambda} \frac{(EO_{oc}^{k\lambda} - H_{oc}^{k\lambda} - L_{oc}^{k\lambda})(EO_{c\,o}^{\lambda k} - H_{c\,o}^{\lambda k} - L_{c\,o}^{\lambda k})}{E - E_{\lambda}},
\end{aligned}$$

where the additional indices indicate that the matrices used above have been transformed into the representation where H_{cc} is diagonal. After solving Eq. 2.45, a generalized eigenvalue equation, we obtain N eigenvalues b_{λ} and their associated eigenvectors. The closed-channel eigenvectors are calculated using the above equations:

$$C_c = -\Gamma_{cc}^{-1}\Gamma_{co} C_o \tag{2.48}$$

$$= -\sum_{\lambda} \frac{(EO_{co}^{\lambda k} - H_{co}^{\lambda k} - L_{co}^{\lambda k})}{E - E_{\lambda}} C_o. \tag{2.49}$$

These gives the eigenvectors $Z_{\lambda\beta}$, and eigenvalues b_{β} of the R-matrix, which can then be written [10]

$$R_{ij} = -\sum_{\beta} Z_{i\beta} b_{\beta}^{-1} Z_{j\beta}. \tag{2.50}$$

The β^{th} linearly independent solution in the i^{th} channel, $F_{i\beta}(r_0)$, is equal to $Z_{i\beta}$. The channel wave functions and logarithmic derivative have now been obtained through this variational calculation. Together they provide the wave function at the reaction surface, and upon matching to the solutions outside of the R-matrix, the wave function is fully determined and reaction (K) or scattering (S) matrices can be computed. Recall that the set of channels contains both n_o open and n_c weakly closed channels, so that $N = n_c + n_o$. These both have non-zero amplitude at r_0, but the weakly closed channel functions must vanish asymptotically in the classically forbidden region, while open channel wave functions of course continue to infinity. The MQDT approach postpones setting these boundary conditions until after the K or S-matrix has been calculated. As a result these matrices, and thus properties like the quantum defects, are very nearly independent of energy. Imposition of boundary conditions as $r \to \infty$ is called closed-channel elimination, and it analytically introduces strong energy dependence reflecting channel interactions via Fano-Feshbach resonances and level perturbations. Although this will be done for the Coulomb field in chapter 5, in the following derivation we show how to calculate these properties numerically. This is done because in the investigation of negative ion photodetachment in chapter 8 the very large polarizabilities make the MQDT formulation for the polarization potential [63, 66] impractical since the channel couplings extend out very far, requiring enormous R-matrix box sizes. On the other hand, by implementing boundary conditions explicitly from the onset and numerically propagating the solutions from very far away, where they are decoupled, inwards to r_0 the matching can be done accurately. We also used this method to determine electron-atom scattering phases in section 2.3.1, although the polarization MQDT should be equally valid.

2.1.3 Calculation of asymptotic solutions and dipole matrix elements

The steps below closely follow derivations in [10, 67]. Outside of the R-matrix volume, since there are no boundary conditions yet in place for the wave function as $r \to \infty$, there are $2N$ linearly independent solutions. As $r \to \infty$, only the longest-range potentials in the Schrödinger equation remain. For the negative ion and electron-atom scattering problems focused only the centrifugal potential remains.

To set up the typical notation and concepts of the multichannel scattering formulation, let us first treat the region outside the R-matrix boundary as being free of any potentials (Chapter 5 will repeat much of this discussion for the Coulomb potential). The two linearly independent solutions in each channel are thus

$$f_i(r) = \sqrt{\frac{2}{\pi k_i}} k_i r j_{l_i}(k_i r), \; g_i(r) = -\sqrt{\frac{2}{\pi k_i}} k_i r y_{l_i}(k_i r). \tag{2.51}$$

In these energy-normalized radial functions the wavenumber is $k_i = \sqrt{-2E_i}$ and $j_n(x)$ and $y_n(x)$ are the spherical Bessel and Neumann functions, respectively. Generally, any valid solution in this region is a linear combination of these two linearly independent functions,

$$F_{i\beta}(r) = f_i(r) I_{i\beta} - g_i(r) J_{i\beta}. \tag{2.52}$$

The matrices $\underline{I}$ and $\underline{J}$ are independent of r and equal $W(g_i, F_{i\beta})/W(g_i, f_i)$ and $W(f_i, F_{i\beta})/W(g_i, f_i)$, respectively, where W is the Wronskian. Since the $F_{i\beta}$ are still linearly independent, a new solution

$$M_{ii}(r) = \sum_{\beta} F_{i\beta} I^{-1}_{\beta i} = f_i(r)\delta_{ii} - g_i(r) K_{ii} \tag{2.53}$$

can be formed, where the K-matrix is $\underline{K} = \underline{J}\underline{I}^{-1}$. This solution obeys standing wave boundary conditions, and we use this formulation so that the majority of the calculation can be performed using real arithmetic.

However, the appropriate boundary conditions to calculate the photodetachment cross section correspond to incoming and outgoing solutions f^- and f^+, rather than the standing waves f and g of the K-matrix formulation. These solutions are related by

$$f = -\frac{1}{i\sqrt{2}}(-f^+ + f^-), \;\; g = \frac{1}{\sqrt{2}}(-f^+ - f^-). \tag{2.54}$$

Insertion of these into Eq. 2.53 gives

$$M_{ii} \; = \frac{1}{i\sqrt{2}} f_i^+(r)(1 + K_{ii}\,) - \frac{1}{i\sqrt{2}} f_i^-(r)\,(1 - iK_{ii}\,)\,. \tag{2.55}$$

These solutions are once again transformed to obtain a solution obeying incoming/outgoing wave boundary conditions, giving the form of the S-matrix:

$$\begin{aligned} \sum_i M_{ii}\,(1 + iK_{i\,\gamma})^{-1} &= \frac{1}{i\sqrt{2}} f_i^+(r)\delta_{i\gamma} - \frac{1}{i\sqrt{2}} f_i^-(r)\,(1 - iK_{ii}\,)\,(1 + iK_{i\,\gamma})^{-1} \\ &= \frac{1}{i\sqrt{2}} f_i^+(r)\delta_{i\gamma} - \frac{1}{i\sqrt{2}} f_i^-(r) S^\dagger_{i\gamma}, \end{aligned} \tag{2.56}$$

where the scattering matrix is

$$\underline{S} = \frac{\underline{1} + i\underline{K}}{\underline{1} - i\underline{K}}. \tag{2.57}$$

With these definitions in mind, let us now reconsider this process in the scenario where the potential is not zero outside of the R-matrix box. The wave function for $r > r_0$ was previously defined in Eq. 2.18:

$$\psi_\mu = \sum_i \frac{1}{r} \Phi_i G_{i\mu}(r).$$

These solutions $G_{i\mu}(r)$ are given by solving the coupled-channel equations of Eq. 2.19. Unlike the solutions determined by the R-matrix calculation, $F_{i\beta}$, which have $N = n_o + n_c$ linearly independent solutions due to the boundary condition at $r = 0$, no boundary conditions can be applied to $G_{i\mu}$ except that the weakly closed channels

vanish at infinity. There must then be $2n_o+n_c$ linearly independent solutions μ, just as there was an f_i and a g_i for each channel in the potential-free case above. To start the numerical calculation of $G_{i\mu}(r)$ a radius $r_0 > r_0$ is chosen where the coupling potentials in Eq. 2.19 can be neglected. We can then use the asymptotic solutions of Eq. 2.51 at r_0: for the first n_o solutions, $1 \le \mu \le n_o$, $G_{i\mu}(r_0) = f_i(r_0)\delta_{i\mu}$; for the second n_o solutions, $n_o + 1 \le \mu \le 2n_o$, $G_{i\mu}(r_0) = g_i(r_0)\delta_{i\mu-n_0}$. Finally in the closed channels we need just one set of exponentially decaying solutions, $e^{-k_i r_0}\delta_{i\mu}$, for $2n_o+1 \le \mu \le 2n_o+n_c$. In practice r_0 is some large finite value, typically ~ 2000, and the solutions are propagated inwards to r_0 using a matrix Numerov algorithm [68].

With these solutions in hand we can reconstruct the solution outside of the box, analogous to Eq. 2.53, with the asymptotic form corresponding to K-matrix solutions. The only difference here is that we must also include the weakly closed channel solutions with their own set of coefficients.

$$\Psi_i = \sum_{\mu}^{n_o} \psi_\mu \delta_{\mu i} - \sum_{\mu=1}^{n_o} \psi_{\mu+n_o} K_{\mu i} - \sum_{\mu=n_o}^{n_o+n_c} \psi_{\mu+n_o} a_{\mu i} \,. \tag{2.58}$$

This expression is simpler after collapsing the latter two terms together, so that $a_{\mu i}$ becomes a matrix of dimension $(n_o + n_c) \times n_o$. Clearly, its uppermost $n_o \times n_o$ block is the K-matrix. Eq. 2.58 becomes

$$\Psi_i^{\text{out}} = \sum_{\mu}^{n_o} \psi_\mu \delta_{\mu i} - \sum_{\mu=1}^{n_o+n_c} \psi_{\mu+n_o} a_{\mu i} \,. \tag{2.59}$$

This wave function must now be matched to the solution inside the box. The wave functions found by solving the streamlined R-matrix equations discussed earlier are

$$\psi_\beta(r_0) = \sum_i \frac{1}{r_0} \Phi_i F_{i\beta}(r_0). \tag{2.60}$$

The most general wave function is a linear combination of these, $\Psi_i = \sum_{\beta}^{n_o+n_c} \psi_\beta b_{\beta i}$, where $b_{\beta i}$ is an unknown coefficient. Thus:

$$\Psi_i^{\rm in} = \sum_{\beta \quad i}^{n_o+n_c} \Phi_i F_{i\beta}(r_0) b_{\beta i} \, . \tag{2.61}$$

Finally, we equate $\Psi_i^{\rm in} = \Psi_i^{\rm out}$:

$$\sum_{\beta=1 \quad i}^{n_o+n_c} \Phi_i F_{i\beta}(r_0) b_{\beta i} = \sum_{\mu=1 \quad i}^{n_o} \Phi_i G_{i\mu}(r_0) \delta_{\mu i} - \sum_{\mu=1 \quad i}^{n_o+n_c} \Phi_i G_{i\mu+n_o}(r_0) a_{\mu i} \, . \tag{2.62}$$

This equality clearly holds for every i in the sum, and so we can write this set of equations, along with the set of first-derivatives at the boundary, as:

$$\sum_{\beta=1}^{n_o+n_c} F_{i\beta}(r_0) b_{\beta i} + \sum_{\mu=1}^{n_o+n_c} G_{i\mu+n_o}(r_0) a_{\mu i} = G_{ii}\,(r_0), \tag{2.63}$$

$$-b_\beta \sum_{\beta=1}^{n_o+n_c} F_{i\beta}(r_0) b_{\beta i} + \sum_{\mu=1}^{n_o+n_c} G_{i\mu+n_o}(r_0) a_{\mu i} = G_{ii}\,(r_0). \tag{2.64}$$

Solution of these $2(n_o + n_c)$ equations for the $n_o + n_c$ linearly independent solutions denoted i gives the $(n_o + n_c) \times (n_o + n_c)$ unknown coefficients in both $a_{\mu i}$ and $b_{\beta i}$. The system is therefore fully characterized. For the calculation of electron-atom scattering phase shifts in section 2.3.1 $a_{\mu i}$ is a single number since there is only one channel, and so $a_{\mu i} = \tan\delta$.

For negative ion photodetachment, the relevant observables are the partial cross sections. These are given in terms of dipole matrix elements, which connect the initial state to the states ψ_β determined by the R-matrix above,

$$d_\beta = \langle \psi_\beta || r^{(1)} || \psi_0 \rangle \, . \tag{2.65}$$

These can be calculated efficiently by first computing the transition dipole elements between all single-electron orbitals, then appropriately summing these over the initial

and final state eigenvectors. Since a linear combination of the ψ_β solutions was used above, these dipole matrix elements must also be transformed following Eq. 2.61:

$$d_\gamma = \quad b^\dagger_{\gamma\beta} d_\beta. \tag{2.66}$$

Finally, these must be transformed according to the linear transformation connecting K- and S-matrix defined in Eq. 2.56:

$$d^s_i = \sum_{\beta,\gamma} (1 + iK)^{-1\dagger}_{i\,\gamma} b^\dagger_{\gamma\beta} d_\beta. \tag{2.67}$$

In both of these equations the matrix transpose is denoted with a dagger symbol; this tranpose is needed since it is the bra part of Eq. 2.65 that is transformed at each step. With these dipole amplitudes and the K-matrix thus obtained, observables such as partial and total cross sections, alignment and orientation parameters, and scattering phase shifts can be computed. To complete this discussion, we present the formula for the partial cross section for channel i,

$$\sigma_i = \frac{4\pi\omega\alpha}{3(2J_0+1)} |d^s_i|^2, \tag{2.68}$$

where ω is the photon energy and J_0 the angular momentum of the initial state. This formula is summed over all open channels to obtain the total cross section. This formula concludes our solution of two-electron systems; we now turn to the properties of effectively one-electron Rydberg atoms.

2.2 Rydberg atoms

One key advantage taught by quantum defect theory is that Rydberg atoms are straightforward to treat theoretically: since the interaction of the Rydberg electron with the ionic core extends over only a few atomic units, the key differences

between them and the hydrogen atom are encapsulated by a few essentially energy-independent quantum defects. These can be determined experimentally or numerically. Rydberg wave functions and energy levels are thus excellently described using analytical formulae above $n \approx 10$.

The relevant quantum numbers describing a Rydberg state are the principal quantum number n, the total angular momentum $j^2 = (s_1 + l)^2$, and its projection onto the internuclear axis m_j. In case spin effects are ignored, the quantum numbers n, l, and m suffice. These quantum numbers characterize the solutions of the Rydberg Hamiltonian

$$H_0 = -\frac{1}{2}\nabla_r^2 + V(r). \tag{2.69}$$

Here $V(r)$ is, outside of a small core region where the atomic electrons can exchange energy, spin, and orbital angular momentum with the Rydberg electron, just a Coulomb potential. We focus here on the bound states, and the interested reader can consult Ref. [10] and the references therein for a complete discussion of the quantum defect theory of bound and scattering Rydberg states. The spin-independent bound states of Eq. 2.69 are infinite in number due to the Coulomb potential and have the eigenenergies and eigenfunctions:

$$H_0|n,l,m\rangle = -\frac{1}{2(n-\mu_{nl})^2}|n,l,m\rangle\ ; \tag{2.70}$$

$$r|n,l,m\rangle = \phi_{nlm}(r) = \frac{f_{nl}(r)}{r}Y_{lm}(\hat{r}) \tag{2.71}$$

$$= \frac{u_{nl}(r)}{r}Y_{lm}(\hat{r}),\ \ \mu_{nl} = 0. \tag{2.72}$$

In these expressions u_{nl} is the usual hydrogenic radial wave function, Y_{lm} are the spherical harmonics, and μ_{nl} is a quantum defect that is typically nearly independent

of n and vanishes for high l. When $\mu_{nl} = 0$ the wave functions are related to the Whittaker function [10, 69] through

$$f_{nl}(r) = \frac{W_{\nu,l+1/2}\ \frac{2r}{\nu}}{\nu^2(\Gamma(\nu+l+1)\Gamma(\nu-l)}, \quad \nu = n - \mu_{nl}. \tag{2.73}$$

The Whittaker function used here is irregular at the origin, but since the potential differs markedly from a pure Coulomb field at close range this issue is neglected by simply restricting the use of this wave function to distances greater than ~ 20 atomic units. Eq. 2.70 showed that the eigenenergies are given by the Rydberg formula, which generalizes to include the spin-orbit splitting by giving a different value for each j:

$$E_{n(s_1 l_1)jm} = -\frac{1}{2(n - \mu_{(s_1 l_1)j}(n))^2}. \tag{2.74}$$

The quantum defects are parametrized to incorporate some small n dependence to better match experiment:

$$\mu_{(s_1 l_1)j}(n) = \mu_{(s_1 l_1)j}(0) + \frac{\mu_{(s_1 l_1)j}(0)}{n - \mu_{(s_1 l_1)j}(0)\ ^2}. \tag{2.75}$$

Table 2.1 displays these parameters for ns, np, nd, and nf states of both Rb [70, 71] and Cs [72, 73], while Table 2.2 gives the same for Li, Na, and K. For higher angular momenta, the quantum defects account for core polarization through the approximate formula

$$\mu_l(n) = \frac{\alpha(X^+)[3n^2 - l(l+1)]/4}{n^2(l-1/2)l(l+1/2)(l+1)(l+3/2)}, \tag{2.76}$$

where $\alpha(X^+)$ is the polarizability of the Rydberg core of atom X. Tables 2.1 and 2.2 also give the polarizabilities of these atoms and their positive ions [74]. The hydrogenic fine structure splitting is assumed for these nonpenetrating high-l ($l > 3$) states:

$$\Delta E_{n(s_1 l_1)jm} = -\frac{\alpha^2}{2n^3} \quad \frac{1}{j+1/2} - \frac{3}{4n}, \tag{2.77}$$

where α is the fine structure constant. Since this splitting and the core polarization-induced quantum defects decrease rapidly with l, the $l > 2$ states are nearly degenerate and only slightly modify the potential curves. Finally, we give the generalization of Eq. 2.70 to include j-dependence:

$$\psi_{n(ls_1)jm_j}(r) = \sum_{m,m_1} C^{jm_j}_{lm,s_1m_1} \frac{f_{nlj}(r)}{r} Y_{lm}(\hat{r})\chi^{s_1}_{m_1}, \tag{2.78}$$

where $\chi^{s_1}_{m_1}$ is the Rydberg electron's spin wave function. $f_{nlj}(r)$ is given by Eq. 2.73 with the quantum defects by Eq. 2.75.

2.3 The Fermi pseudopotential

Since the interaction between a scattering electron and a ground state atom is quite localized in space it is amenable to techniques such as the R-matrix approach. Such calculations can obviously become very involved. If a second scattering center is introduced into the problem – for example to model a system consisting of a Rydberg ion, a neutral atom, and a Rydberg electron – the calculational effort would increase rapidly. Fortunately, most of this work is unnecessary, as Fermi showed in 1934 [57], when he introduced the now ubiquitous concepts of the scattering length and delta-function pseudopotential.

The effect of a dense background gas of neutral atoms on a Rydberg atom was first considered by Fermi in an attempt to explain the unexpected measurements of Amaldi and Segrè [82]. These two researchers studied the spectroscopy of sodium Rydberg atoms in a helium background gas and reported a change in the lineshape and line broadening. These measurements were density-dependent and, as experiments with other background gases revealed, resulted in either blue or red shifted

Rb	$\mu(0)$	$\mu\,(0)$	**Cs**	$\mu(0)$	$\mu\,(0)$
$s_{1/2}$	3.1311804	0.1784	$s_{1/2}$	4.049325	0.2462
$p_{1/2}$	2.6548849	0.2900	$p_{1/2}$	3.591556	0.3714
$p_{3/2}$	2.6416737	0.2950	$p_{3/2}$	3.559058	0.374
$d_{3/2}$	1.34809171	-0.60286	$d_{3/2}$	2.475365	0.5554
$d_{5/2}$	1.34646572	-0.59600	$d_{5/2}$	2.466210	0.067
$f_{5/2}$	0.0165192	-0.085	$f_{5/2}$	0.033392	-0.191
$f_{7/2}$	0.0165437	-0.086	$f_{7/2}$	0.033537	-0.191
	Rb	Rb^+		Cs	Cs^+
α (a.u.)	319.2	9.11	α	402.2	15.8
	Rb(ns)	Rb(5s)		Cs(ns)	Cs(6s)
A (GHz)	$18.55/(n^*)^3$	3.417	A	$3.383/(n^*)^3$	2.298

Table 2.1.
Quantum defects, polarizabilities α, and hyperfine constants A for ^{87}Rb and ^{133}Cs from [70–77]

.

lines depending on the nature of the background gas. A red-shifted line could be understood qualitatively at least by considering the energy shift from the polarizable electron clouds of the neutral atoms. As derived previously, this polarization potential is

$$V(r, R_i) = -\frac{\alpha}{2|r - R_i|^4}, \tag{2.79}$$

summed over all the positions of ground state atoms, R_i. This mean-field effect lowers the overall energy consistent with the energy shift to the red, but the blue-

Li	$\mu(0)$	μ (0)	**Na**	$\mu(0)$	μ (0)	**K**	$\mu(0)$	μ (0)
$s_{1/2}$	0.3995101	0.0290	$s_{1/2}$	1.347964	0.060673	$s_{1/2}$	2.1801985	0.13558
$p_{1/2}$	0.0471835(0.0471780)	-0.024	$p_{1/2}$	0.855380	0.11363	$p_{1/2}$	1.713892	0.233294
$p_{3/2}$	0.0471720(0.0471665)	-0.024	$p_{3/2}$	0.854565	0.114195	$p_{3/2}$	1.710848	0.235437
$d_{3/2}$	0.002129	-0.01491	$d_{3/2}$	0.015543	-0.08535	$d_{3/2}$	0.2769700	-1.024911
$d_{5/2}$	0.002129	-0.01491	$d_{5/2}$	0.015543	-0.08535	$d_{5/2}$	0.2771580	-1.025635
$f_{5/2}$	-0.000077	0.021856	$f_{5/2}$	0.0001453	0.017312	$f_{5/2}$	0.010098	-0.100224
$f_{7/2}$	-0.000077	0.021856	$f_{7/2}$	0.0001453	0.017312	$f_{7/2}$	0.010098	-0.100224
	α (a.u.)	α (a.u.) [ion]		α (a.u.)	α (a.u.) [ion]		α (a.u.)	α (a.u.) [ion]
Li	$164.9^{a,b}$	0.1923	**Na**	165.9^{a},162.7^{b}	0.9448	**K**	307.5^{a},290.6^{b}	5.3310
	^{6}Li ($i=1$)	^{7}Li		^{23}Na	^{23}Na		^{39}K	^{41}K
A (MHz)	228.2052590	803.5040866	A (MHz)	1771.6261288	1771.6261288	A (MHz)	461.719720	254.013872

Table 2.2.
Quantum defects, polarizabilities α, electron affinities, and hyperfine constants A for ^{6,7}Li, ^{23}Na, and ^{39,41}K. Hyperfine constants are from [78]. Li quantum defects are from [79] and [80].Na and K quantum defects are from [80]. The value for p_J in parentheses is for ^{7}Li. ^{a} The polarizabilities calculated in our model potential; ^{b} polarizabilities measured in [81].

.

shifted line defied interpretation. Fermi explained this phenomenon by considering the low-energy collisions between the Rydberg electron and many neutral atoms, dubbed perturbers. At low energy the elastic scattering parameters and electron wave function near the perturber may all be characterized by a single quantity, the s-wave scattering length a_s. This crucial simplification of the scattering process led Fermi to develop the Fermi pseudopotential (in atomic units)

$$V(r,R) = 2\pi a_s \delta(r-R). \tag{2.80}$$

The literature holds many derivations of this pseudopotential, extending it to arbitrary partial waves and including regularization terms important for its inclusion in direct, rather than perturbative, calculations [83–86]. Here we present instead a

more intuitive derivation of just the s-wave term, and pick up the solution derived by Omont [87] for p-wave scattering. It is not thought that any higher partial waves are relevant for Rydberg molecules.

We start with the Schrödinger equation for the Rydberg electron, which is bound to the Rydberg core by the Coulomb potential U and interacts with N perturbers through $V_i = V(r, R_i)$:

$$\nabla^2\Psi(r) + 2 \quad E - U(r) - \quad V_i \quad \Psi(r) = 0. \tag{2.81}$$

A Rydberg electron has velocity $v \propto n^{-1}$ and fills a volume $\propto n^6$. It therefore has a huge de Broglie wavelength relative to the size of the perturbers. We can consider an *averaged* Schrödinger equation in order to identify the average effect of these perturbers on the wave function:

$$\nabla^2\overline{\Psi} + 2(E - U)\overline{\Psi} - 2 \quad \overline{V_i\Psi} = 0. \tag{2.82}$$

The Wigner threshold law [88] states that the low-energy phase shifts scale as $\delta_l \propto k^{2l+1}$, justifying our assumption of s-wave scattering. The electronic wave function defined in a coordinate system $X = r - R_i$ relative to a given perturber then is:

$$\Psi(X) = \frac{u(X)}{X} Y_{00}(\hat{X}). \tag{2.83}$$

Using this form of the wave function in Eq. 2.81 we obtain a radial equation:

$$u\ (X) = 2\left(V(X)u(X) - Eu(X)\right), \tag{2.84}$$

but we can approximately set the latter term to zero since the Rydberg energy is so low. The average value of the potential's influence on the wave function is

$$\begin{aligned} 2 \quad V\Psi \mathrm{d}^3X &= 8\pi Y_{00}(\hat{X}) \int_0^{X_0} V(X)\frac{u(X)}{X}X^2\mathrm{d}X \\ &= 4\pi Y_{00} \int_0^{X_0} u\ (X)X\mathrm{d}X, \end{aligned} \tag{2.85}$$

where we have written $\frac{1}{\sqrt{4\pi}} = Y_{00}(\hat{X})$ and for $X > X_0$ we have assumed that the polarization potential is completely negligible. This assumption leads to the key result that at very low energy the radial wave function outside of the potential well is a linear function: $u(X) = C(X - a_s)$. Integrating Eq. 2.85 by parts leads to

$$\begin{aligned} 2 \quad V\Psi \mathrm{d}^3X &= 4\pi Y_{00}(\hat{X})\left(-u(X_0) + X_0 u\left(X_0\right)\right) \\ &= 4\pi Y_{00} C a_s. \end{aligned} \tag{2.86}$$

We next define an average wave function near the perturber as

$$\overline{\Psi} = \frac{1}{V} \quad Y_{00}(\hat{X})\frac{C(X - a_s)}{X}\mathrm{d}^3X. \tag{2.87}$$

Implicit in this expression is the approximation that the wave function's actual value very near the perturber, which certainly deviates from this linear form, is irrelevant when averaged over a large enough volume. Still in this large volume limit, Eq. 2.87 evaluates to $\overline{\Psi} = Y_{00}(\hat{x})C$. Thus, the average potential is related to the average wave function via

$$2 \quad V\Psi \mathrm{d}^3x = 4\pi(\overline{\Psi})a_s. \tag{2.88}$$

Still within this low-density, low-energy limit, Eq. 2.88 can be recast as an effective potential. If V is replaced with

$$V_{\mathrm{ferm}} = 2\pi a_s \delta(r - R_0), \tag{2.89}$$

Eq. 2.88 still holds. Thus this rather heuristic derivation shows that the true interaction between the electron and the perturber can be reduced to a contact delta function proportional to the scattering length, and more rigorous proofs of this relationship have the same result [85]. In spite of its simplicity, this expression accurately characterizes the true interaction and has been verified in a multitude of

experimental contexts and in comparison with other theoretical tools of increasing complexity [14, 89–96].

This effective potential generalizes to all partial waves by Fourier expansion of plane wave scattering solutions [87], giving

$$V(r,R) = 2\pi \sum_l (2l+1)\delta(r-R)A_l \; P_l\left(\frac{1}{k^2}\nabla\cdot\nabla\right), \tag{2.90}$$

where $A_l = -(\tan\delta_l)/k^{2l+1}$. Keeping just $l=0$ and $l=1$ in this expression yields

$$V_{\text{fermi}}(r,R) = 2\pi a_s[k(R)]\delta^3(r-R) + 6\pi a_p^3[k(R)]\delta^3(r-R)\overleftarrow{\nabla}_r\cdot\nabla_r. \tag{2.91}$$

This reproduces the s-wave Fermi pseudopotential and introduces the p-wave interaction involving the gradient operator, typically attributed to Omont's formulation [87]. The backwards vector implies that this gradient operator acts backwards on the bra in a matrix element; this preserves the Hermiticity of this operator. For many alkali atoms it is essential to include $l=1$ partial waves due to the presence of a shape resonance in this channel which in turn leads to a divergence in the scattering volume; as a result the p-wave interaction includes a far larger contribution than would be assumed due to the Wigner threshold law [97, 98]. The s-wave scattering length a_s and p-wave scattering volume a_p^3 depend on R through the semiclassical kinetic energy, $k(R) = \sqrt{\frac{2}{R} - \frac{1}{n_H^2}}$. Typically we take n_H to be the principal quantum number of the nearest hydrogenic manifold. These parameters depend on the energy-dependent scattering phase shifts δ_0 and δ_1 through the relationships

$$a_s[k(R)] = -\frac{\tan\left(\delta_0[k(R)]\right)}{[k(R)]},\;\; a_p^3[k(R)] = -\frac{\tan\left(\delta_1[k(R)]\right)}{[k(R)]^3}. \tag{2.92}$$

Of course, in the LS coupling scheme these phase shifts must also include spin-dependence. There are two s-wave scattering lengths corresponding to symmetries

$^1S_0$, $^3S_1$ and four p-wave scattering volumes corresponding to $^1P_1$, $^3P_{0,1,2}$ symmetries. In many early studies the singlet scattering length, which is often an order of magnitude smaller than the triplet scattering length, as well as the J-dependence of the ^3P scattering phases, was ignored. However, abundant research in recent years, including that presented in chapter 6, shows that a full theoretical model including these symmetries and splittings is necessary to obtain a correct description of experimental observations.

2.3.1 Determination of electron-atom scattering phase shifts

Clearly these low-energy atom-electron scattering phase shifts play an essential role in describing the interaction between a Rydberg atom and a neutral atom. It is therefore paramount that they be computed accurately. In our studies of Rb and Cs, phase shifts were obtained from Refs. [95,97]. Ref. [97] did not include the spin-orbit splitting of the p-wave phase shifts, so these phases were used in chapters 3 and 4 which focus on non-relativistic effects. This phase shift is equivalently obtained by an appropriately J-weighted average of the relativistic phase shifts. The phase shifts calculated by Ref. [95] do include the spin-orbit splitting of the ^3P phases, and are plotted in Fig. 2.2. The ^3P_J phase shifts for Cs were slightly shifted (by $\sim$ 1 meV) to align their resonance positions with experimental values [99, 100]. No direct experimental measurements of the Rb resonance positions yet exist, although an average value consistent with these phase shifts was extracted from observations of Rb_2 Rydberg molecules [101]. At very low energies the s-wave phase shifts for both species were smoothly connected to experimentally determined zero-energy scattering lengths [101, 102], which are approximately -16 for Rb and -22 for Cs. These experimental values are extracted from measurements of the bound

states, and typically differ from theory calculations by 10%. Ref. [103] calculated phase shifts for some of the alkaline-earth atoms: Ca, Sr, and Mg. The phase shifts for calcium, which is studied in chapter 5, are shown in Fig. 2.3.

Through these phase shifts we can forge a connection between negative ion physics, studied in Chapter 8 and calculated via the R-matrix theory described previously, and the physics of Rydberg molecules. We calculate these phase shifts, fundamental quantities in both of these processes, for the light alkali atoms, Li, Na, and K, using the non-relativistic R-matrix method. These have smaller spin-orbit splittings than Rb and Cs and are still adequately treated without including J-dependence. As an additional test of our calculations, we also calculated non-relativistic Rb phase shifts.

Scattering phase shifts for all of these atoms have been previously calculated, although at varying levels of accuracy and typically not at the ultra-low energies needed for accurate Rydberg molecule potential energy curves. Table 2.3 summarizes our results and these literature values, which are in generally good agreement. We have identified the source of some discrepancies as coming from three main areas: (a) the number of basis states or electronic configurations included in the calculation, (b) the choice of empirical parameters used to set up the calculations, and (c) the range of energies treated. As the calculations for k approaching zero are very sensitive due to the increasingly large de Broglie wavelength, it is important to address these issues properly. With regards to (a), we used 48 one-electron wave functions vanishing at $r = 0$ and $r = r_0$ along with two open wave functions which are non-zero at $r = r_0$. We included 10 partial waves and varied r_0 from 35 to 55. The lowest value was still large enough to contain the wave functions for the first several atomic bound states. We treated the long-range polarization potential by matching the scattering wave function at r_0 to numerical solutions propagated inwards from $r_0 = 2000$. Our

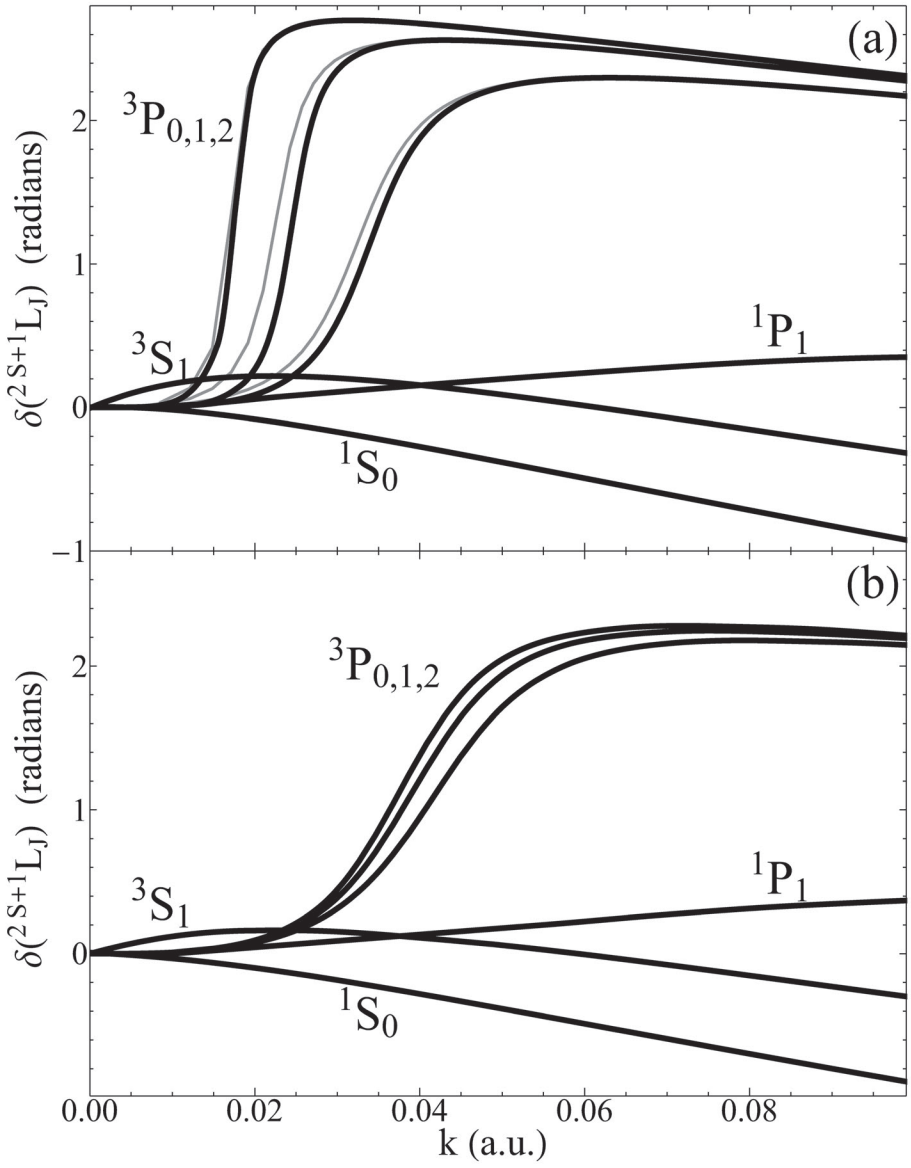

Figure 2.2. Scattering phase shifts for Cs (a) and Rb (b), extracted from Ref. [95]. In panel a the unshifted phases are shown as faint curves; the thick curves were shifted slightly to better reflect experimentally observed resonance positions. This figure is taken from Ref. [2].

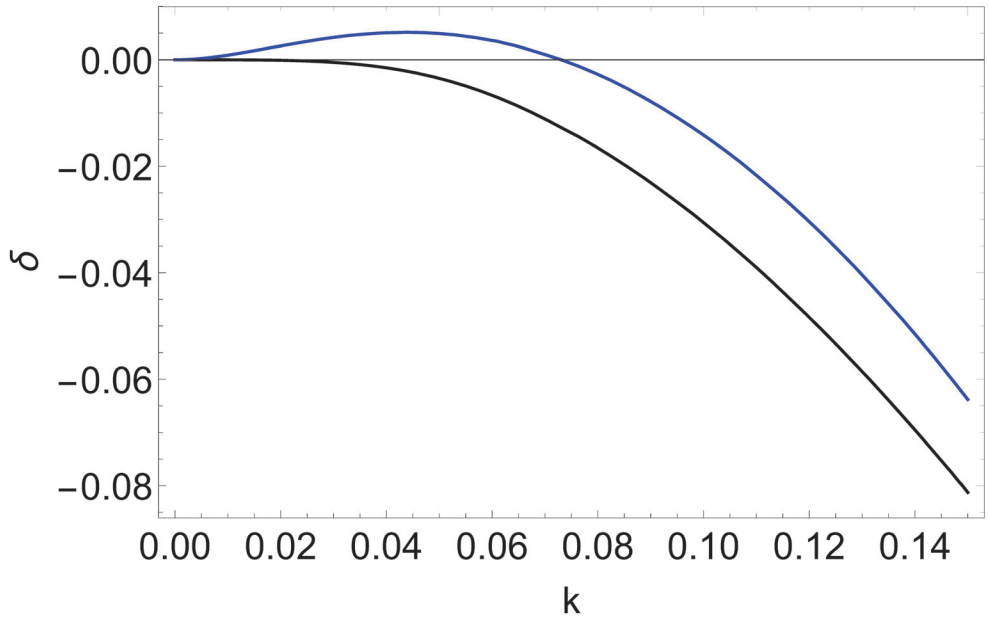

Figure 2.3. Scattering phase shifts for Ca as a function of k (in atomic units). Blue: s-wave; Black: p-wave.

results with this setup were well converged with regards to the basis size and this outer radius, but they did weakly depend on r_0 in the very low energy limit. For K, the results were most stable about $r_0 = 45$, but for Na and Li $r_0 = 35$. The larger value of r_0 needed for K likely reflects its significantly larger polarizability. We are confident in our choice of electron configurations in this basis and the value of r_0. Fig. 2.4 shows the r_0 dependence of a_s (triplet) in potassium.

Regarding item (b), we used an l-dependent model potential $V_l(r)$ for each atom. These are provided in Ref. [59], and to test the independence of our results to the specific choice of model potential we also tested the model potential given by Ref. [48]

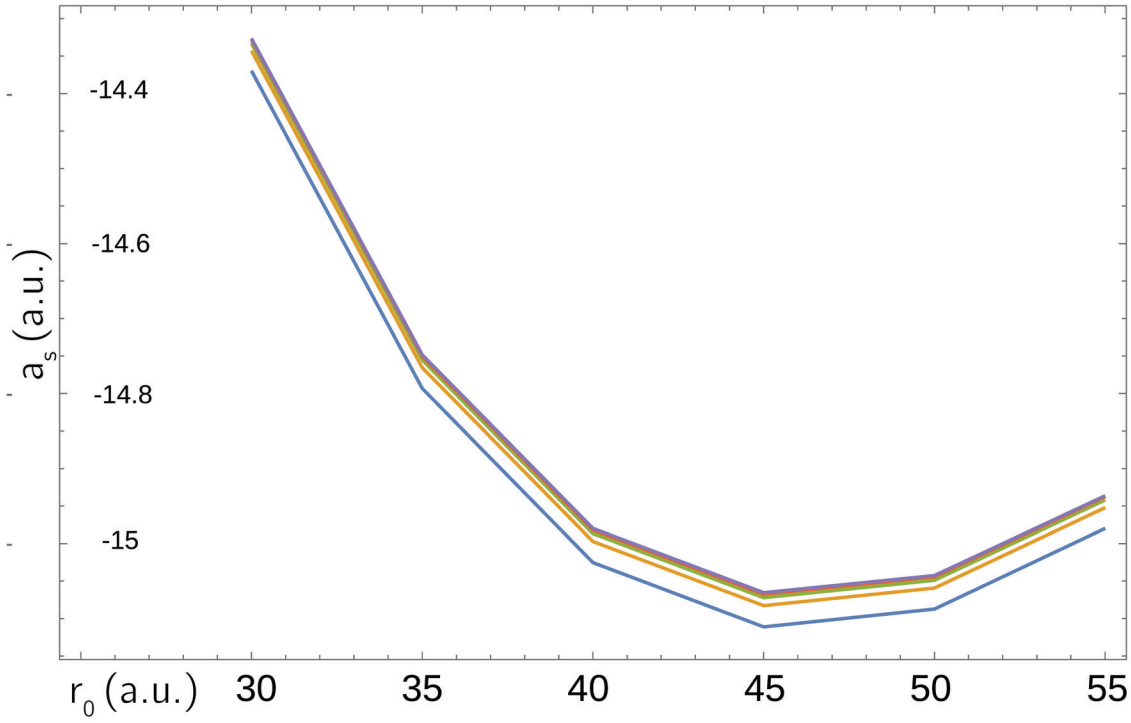

Figure 2.4. Triplet s-wave scattering lengths of potassium as a function of r_0. Separate curves indicate different fit regions used in the extrapolation $k \to 0$.

for potassium. No dependence on the choice of potential was observed. Importantly, we added a dielectronic polarizability term to the Hamiltonian of Eq. 2.1:

$$V_{pol} = -\frac{\alpha}{r_1^2 r_2^2}(1 - e^{-(r_1/r_c)^3})(1 - e^{-(r_2/r_c)^3})P_1(\hat{r}_1, \hat{r}_2). \tag{2.93}$$

This incorporates the additional effective electron-electron interaction that occurs when the core, polarized by one electron, interacts with the other electron. The form of the two cutoff functions $(1-e^{-(r/r_c)^3})$ is unimportant as long as the cutoff radius r_c is fit to match the experimental electron affinity. Without V_{pol} the Hamiltonian predicts a significantly larger electron affinity than is accurate: historically, neglecting

	$a_s^T(0)(a_0)$	$a_s^S(0)(a_0)$	$E_p^T(meV)$	$\Gamma_p^T(meV)$	EA(meV)
Li	-6.7	3.2	63.1	61.0	$617.872^i, 621.769^j$
Na	-5.7	4.2	87.9	124.8	547.539^i,563.251^j
K	-14.6	$1.3^i, 0.26^j$	$24.15^i, 11.9^j$	$19.3^i, 6.3^j$	$501.231^i, 544.872^j$
	$a_s^T(a_0)$	$a_s^S(a_0)$	$E_p^T(meV)$	$\Gamma_p^T(meV)$	$r_c(a_0)$
Li	$-7.12^b, -7.43^h$	$3.04^b, 2.99^h$	$60^d, 60.9^h$	$57^d, 67.9^h$	2.6
Na	$-5.9^a, -6.19^b$	$4.2^a, 4.03^b$	80^f,83^g	188^g	1.84
K	$-15^a, -15.4^c$	$0.55^a, 0.57^c$	$19^c, 2.4^d, 20^e$	$16^c, .6^d$	2.92

Table 2.3.

Scattering parameters for Li, Na, and K. The final column gives the electron affinities calculated with (i) and without (j) the dielectronic polarizability term. Experimental values for these EAs are: Li: 618.049 meV [104]; Na: 547.930 meV [105]; K: 501.459 meV [106].
For the other columns: the top three rows give the present results, while the bottom three columns are from: a) [107], b) [108], c) [109], d) [110], e) [111], f) [112], g) [113], h) [114]. The zero energy scattering lengths depend strongly on the polarizability. For Na, $-5.84 \rightarrow -5.7$ (triplet s), and for K ,$-15.4 \rightarrow -14.6$ (triplet s) and $0.95 \rightarrow 1.3$ (singlet s) when the polarizability of the long-range potential was changed to match the experimental value (see Table 2.2).

this term proved to be the reason why some calculations of the ^3P Cs shape resonances showed that they were in fact bound excited states [100,115]. Inclusion of this term in our calculations likewise proved to be quite important for calculating the ^1S and ^3P phase shifts. We found that some of the differences between our results and previous experimental results seem to be linked to this potential, especially in the ^1S scattering lengths and ^3P resonance parameters. One final input parameter is the atomic polarizability, which is also modified by additional core polarizability effects

not included in these model potentials [59]. Our theoretical values were within 6% of the current experimental values (Table 2.2). In the worst case, potassium, this led also to a 6% shift in the zero-energy scattering length when these two different polarizabilities were used. The final issue in calculating these phase shifts, (c), reflects

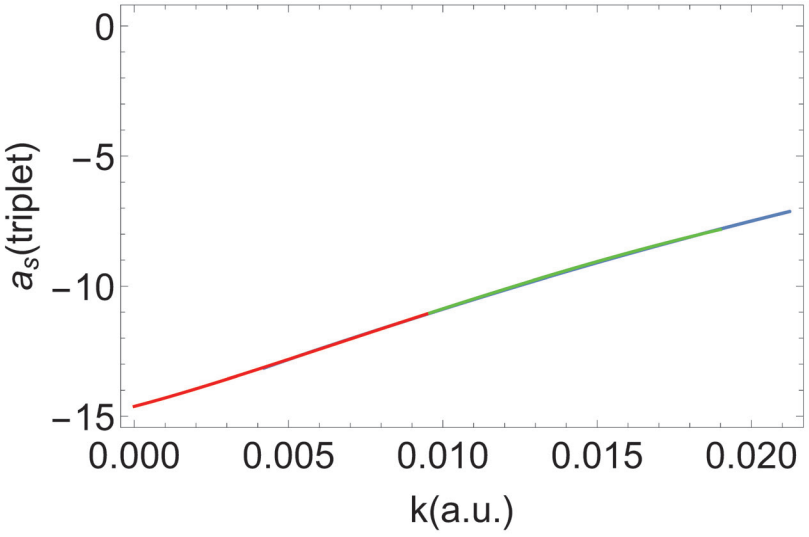

Figure 2.5. The triplet scattering length (blue) for potassium. The red curve shows the extrapolation to zero energy, while the green curve shows the extrapolation to higher energy outside of the range of the fit.

the fact that a calculation truly at zero energy is impossible, and extrapolation of some sort must be used. We trust our results to a minimum energy of 1meV. Below this, the effective range formula [116]

$$a(k) \approx a(0) + \frac{\alpha\pi}{3}k + \frac{4}{3}a(0)k^2\ln(1.23\sqrt{\alpha}k) \qquad (2.94)$$
$$+ \left(\frac{r_e}{2} + \frac{\sqrt{\alpha}\pi}{3} - \frac{\sqrt{\alpha^3}\pi}{3a(0)^2}\right)a(0)^2k^2 - \frac{\pi}{3}\alpha k^3\left(a(0)^2 + \frac{7\alpha}{117}\right).$$

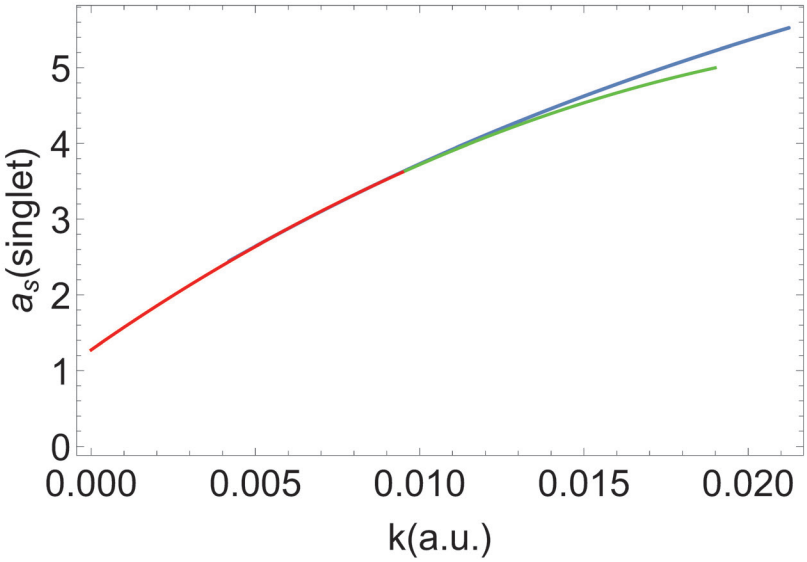

Figure 2.6. The singlet scattering length (blue) for potassium. The red curve shows the extrapolation to zero energy, while the green curve shows the extrapolation to higher energy outside of the range of the fit.

provides the scattering length. We fit this formula to our data down to 1meV to obtain the zero-energy scattering length $a(0)$ and an effective range parameter r_e. This extrapolation seemed very well behaved down to zero energy, as Figs 2.5 and 2.6 show for the triplet and singlet scattering lengths of potassium. For all these reasons – dependence on r_0, input parameters such as the atomic polarizability, and possible uncertainty in the extrapolation – we estimate that our zero-energy scattering lengths are accurate to within 10%.

Fig. 2.2 displays our calculated phase shifts. The zero-energy scattering lengths, shape resonance parameters, and comparisons with prior calculations are shown in Table. 2.3. For potassium, we have compared our energy-dependent calculations

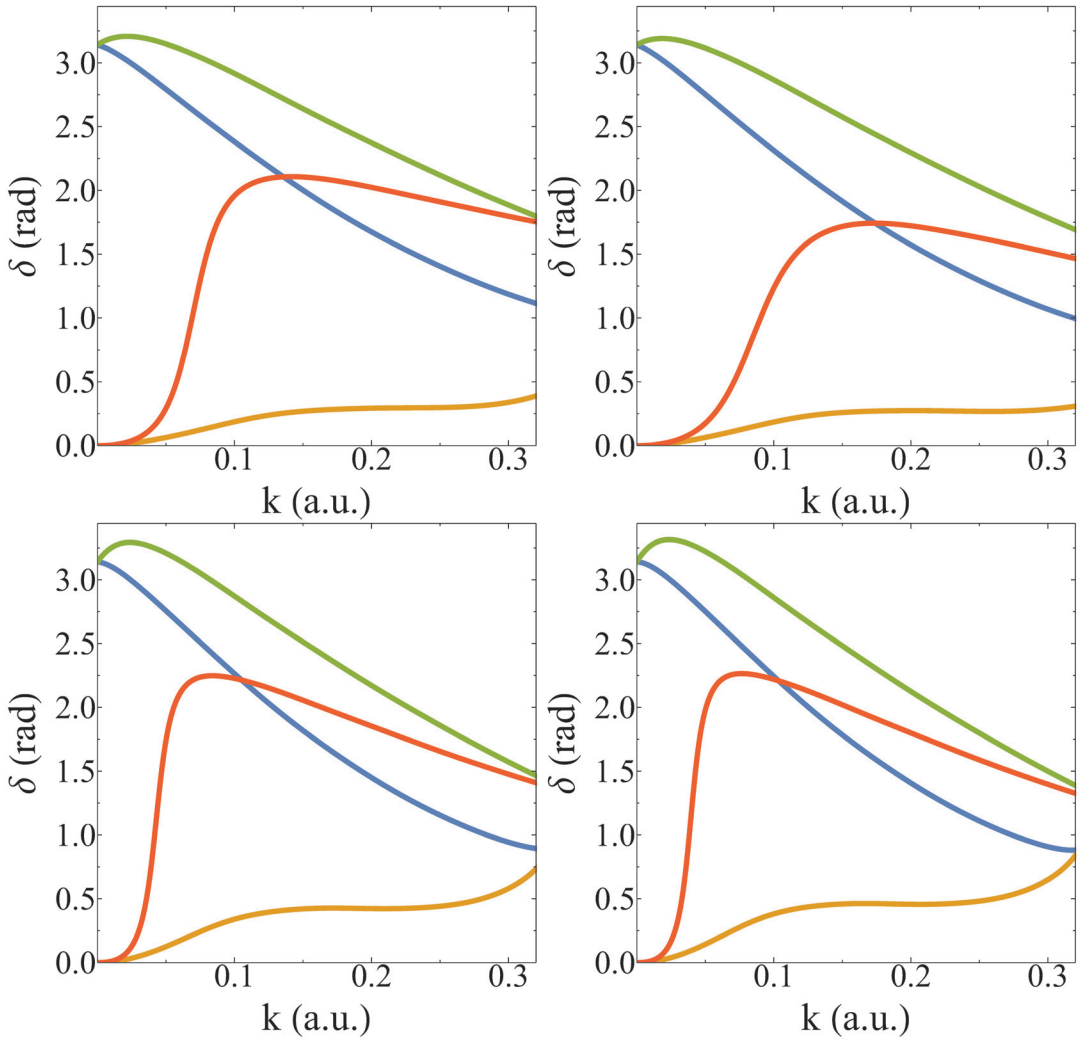

Figure 2.7. Scattering phase shifts for Li (top left), Na (top right), K (bottom left), and Rb (bottom right). Green: ^3S; blue: ^1S; red: ^3P; yellow: ^1P. π was added to the ^3S and ^1S phase shifts for a clearer plot.

with Karule [117], whose potassium phase shifts are, to the best of our knowledge, still the most detailed calculation. We have compared our extracted shape resonance positions and zero-energy scattering lengths with calculations by Fabrikant [109] and Moores [111]. Very recently, Li phase shifts were used in a proposal for Li_2 Rydberg molecules [114]. Our results and extracted parameters compare favorably. Finally, Fabrikant and coworkers [113] computed full energy-dependent scattering phases for Na.

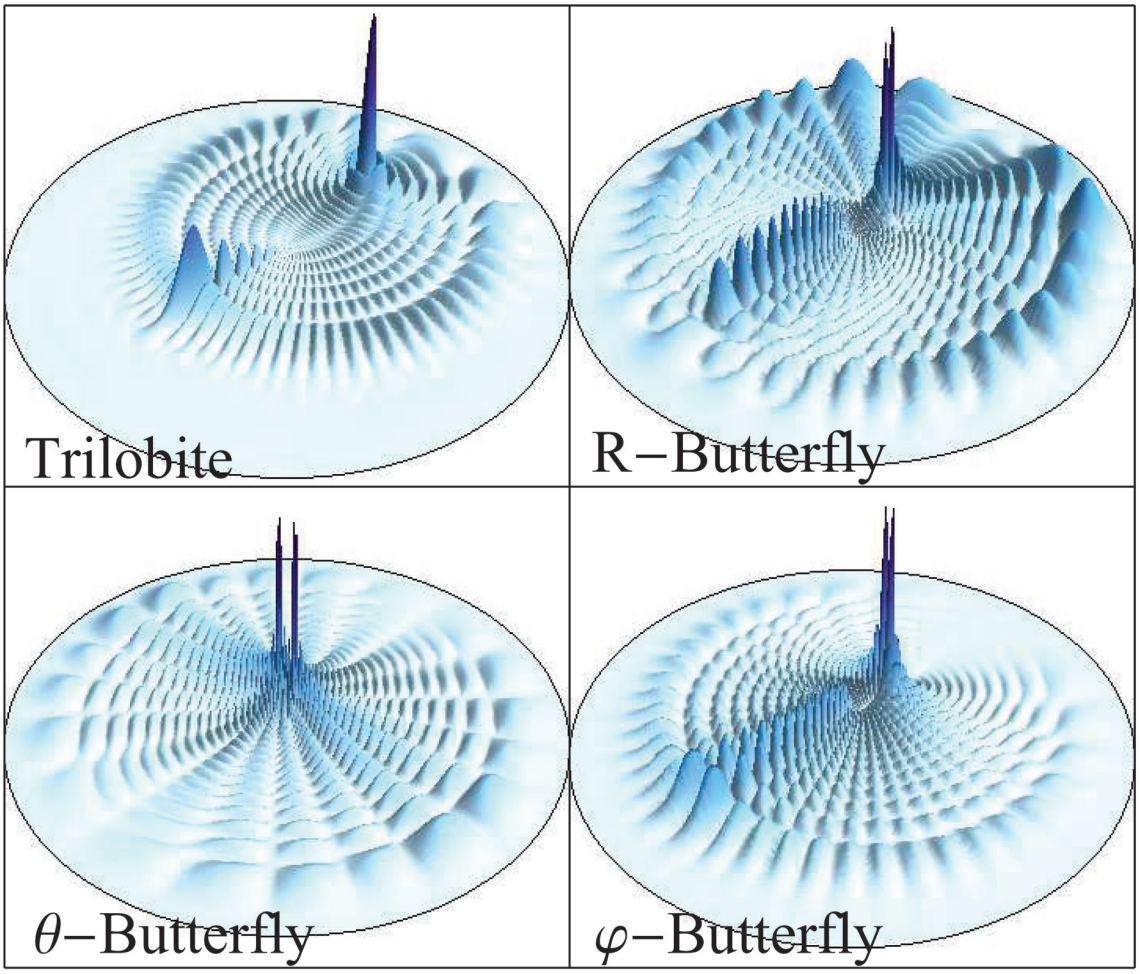

Figure 2.8. Chapter 3 introduces different types of Rydberg molecules like those shown here as planar cuts of the probability amplitudes $\sqrt{r^2\Psi(x,y,z)^2}$. These are the fundamental diatomic eigenstates. The θ-butterfly lies in the yz plane; the other three in the xy plane. $R = 840$ a.u for the trilobite and 345 a_0 for the three butterfly states. The Rydberg core is at the center of each figure and the neutral atom is underneath the most prominent spikes. This figure is taken from Ref. [4].

3. LONG-RANGE RYDBERG MOLECULES

This chapter introduces long-range Rydberg molecules, known colloquially as "trilobites" and "butterflies" due to the stunning visual similarity between these creatures and the wave functions of two classes of these Rydberg molecules. In this chapter we will review the basic properties and terminology of these molecules and situate this thesis within the existing literature. We will consider the simplest description of these molecules, focusing on alkali atoms and neglecting electronic and nuclear spin. The concepts developed at this basic level – the types of potential energy curves one expects to find, the properties of their bound states such as typical binding energies, bond lengths, rotational constants, and permanent electric multipole moments, and the nature of their wave functions – form a critical foundation for many of the following chapters.

3.1 A novel chemical bond

Although Fermi's pseudopotential had been utilized widely throughout the 1970s and 1980s to explain Rydberg line broadening, energy shifts, and charge transfer processes [109, 118–120], in 2000 Greene and coworkers [40, 89, 121] were the first to take a key conceptual leap and treat this pseudopotential seriously as the foundation for a novel chemical bond. This was in turn motivated by the remarkable breakthroughs in ultracold atomic physics culminating in the creation of Bose-Einstein condensates [31, 32]. These made it possible to study atomic clouds at ultracold

temperatures where the weak trilobite bonds would not be ripped apart, but which also had the high densities necessary to observe a non-negligible number of Rydberg molecules. Greene *et al* calculated molecular spectra and found that not only would these molecules be bound, even at such high excitations and huge internuclear distances, but they had non-trivial properties since the pseudopotential could act in a surprisingly non-perturbative way due to the high level degeneracy of Rydberg states [40]. Key among these surprising features is that the electronic wave function changes dramatically from that of an independent Rydberg electron, and the resulting eigenfunction maximizes the electronic density (for s-wave scattering) or its gradient (for p-wave scattering) at the perturber. This creates a much stronger bond as the electron is extremely localized near the perturber, and additionally the resulting charge separation creates enormous permanent dipole moments. We now derive these eigenfunctions and their associated eigenenergies.

Using the Born-Oppenheimer approximation, in which the nuclei are fixed in space and the electronic wave function and energy eigenvalues are solved at each value of the internuclear distance parametrically, we obtain separate equations for the electronic and nuclear degrees of freedom. We first solve the electronic Schrödinger equation for the energy eigenvalues $E_e(R)$ and electronic wave functions $\Psi_e(R,r)$:

$$-\frac{1}{2}\nabla_r^2 + V(r) + V_{\text{fermi}}(R,r) - E_e(R) \quad \Psi_e(R,r) = 0. \tag{3.1}$$

$V(r)$ is the predominantly Coulomb interaction with the atomic core. The entire neutral-electron interaction is contained within the Fermi pseudopotential and is readily handled perturbatively. The energy eigenvalues, $E_e(R)$, define a set of adiabatic potential energy curves (PECs) which the nuclei then traverse. The nuclear wave functions $\Psi_{N\nu}(R)$ for a molecule with reduced mass M are solutions to

$$-\frac{1}{2M}\frac{\partial^2}{\partial R^2} + E_e(R) + \frac{N(N+1)}{2MR^2} - E_{N\nu} \quad \Psi_{N\nu}(R) = 0, \tag{3.2}$$

where N is the rotational quantum number and ν is the vibrational state. To solve Eq. 3.1 explicitly, we first write the pseudopotential of Eq. 2.91 in spherical coordinates,

$$V_{\text{fermi}}(R,r) = 2\pi \quad a_s[k(R)]\delta(r-R) \tag{3.3}$$

$$+ 3a_p^3[k(R)] \quad \partial_r\delta(r-R)\partial_r + \frac{\partial_\theta\delta(r-R)\partial_\theta}{R^2} + \frac{\partial_\varphi\delta(r-R)\partial_\varphi}{R^2\sin^2\theta} \quad ,$$

or more compactly:

$$V_{\text{fermi}}(R,r) = 2\pi \sum_{\xi=1}^{4} a_\xi[k(R)]V_\xi(R,r). \tag{3.4}$$

Here $\xi = 1$ labels Fermi's s-wave pseudopotential, $V_1(R,r) = \delta(r-R)$, and $\xi = 2,3,4$ label the three gradient terms in the Omont generalization to p-wave, i.e. $V_2(R,r) = \partial_r\delta(r-R)\partial_r$, etc. $a_\xi[k(R)]$ denotes $a_s[k(R)]$ when $\xi = 1$, and $3a_p^3[k(R)]$ when $\xi = 1$. Additionally, the notation $\partial_\xi = 1, \partial_r, \frac{1}{R}\partial_\theta, \frac{1}{R\sin\theta}\partial_\phi$ for $\xi = 1,2,3,4$, respectively, will be useful later. Since every $V_\xi(R,r)$ is weak compared to H_0, the Rydberg wave functions, eigenstates of Eq. (2.70), are a very sensible orthonormal and complete basis set to expand the exact wave function into. Since we are neglecting spin in this chapter the wave function has the expansion

$$|\Psi_e \quad = \sum_{n \quad l=0}^{n-1} \sum_{m=-l}^{m=l} c_{nlm}|n,l,m \quad . \tag{3.5}$$

This approach – since many of the states $|n,l,m$ are degenerate for a given n – is called "quasi-degenerate perturbation theory." Typically this series is truncated to values of n near the Rydberg state of interest. The p-wave shape resonance can be challenging to include accurately, since it creates an unphysical divergence in the PECs. This is remedied by ensuring that the basis set includes additional hydrogenic

manifolds adjacent to the manifold of interest, which gives sensible results due to level repulsion between states of opposite symmetry [122]. The accuracy of this approach is a matter of some controversy [123], and issues related to the convergence of these delta function potentials and of this method for constraining the p-wave shape resonance are discussed in much more detail in chapter 6.

After computing the matrix elements of the Hamiltonian implied by Eq. 3.1 and diagonalizing to obtain the eigenspectrum, two distinct classes of molecular states appear which are characterized by the electron's angular momentum. As $R \to \infty$ the potential energy curves of these states are uniquely associated with asymptotic energy levels corresponding to the quantum defect-shifted energy levels of an isolated Rydberg atom. Indeed, these two classes stem from the non-zero quantum defects of $l < l_{\text{min}}$ states that separate them energetically from the hydrogenic manifold of high angular momentum $l \geq l_{\text{min}}$ states. The differences between these two classes are elucidated by considering just the limit of first order degenerate perturbation theory in the next section. This neglects couplings between states and all basis states with $n' = n$. For energies near the n manifold and away from the p-wave shape resonance this approach is quite accurate. Moreover, the form of these orbitals will be used in later theoretical approaches which retain much of this conceptual simplicity while regaining the level of accuracy given by diagonalizing into a full basis as Eq. 3.5 implies.

3.2 Molecular potential energy curves

We begin with the nondegenerate $l < l_{\text{min}}$ states. Due to their non-degeneracy, the potential energy curves for each $V_\xi(R, r)$ are given by the expectation value of the V_ξ. These PECs for $\xi = 1$ and 2 correspond to Σ states since the spherical

harmonics with $m = 0$ vanish on the internuclear axis. The PECs for $\xi = 3$ and 4 involve derivatives of these spherical harmonics and are nonzero only for $m = \pm 1$. They are therefore Π states.

$$E_{l<l_{\min},m=0}(R) = a_1[k(R)] \left(\frac{f_{nl}(R)}{R}\right)^2 |Y_{l0}(0,0)|^2 . \quad \text{(trilobite } s\text{-wave only)} \tag{3.6}$$

$$E_{l<l_{\min},m=0}(R) = E^1_{l<l_{\min},0}(R) + a_2[k(R)] \left(\frac{d}{dR}\frac{f_{nl}(R)}{R}\right)^2 |Y_{l0}(0,0)|^2 \tag{3.7}$$

$$\begin{aligned} E_{l<l_{\min},m=\pm 1}(R) = {} & a_3[k(R)] \left(\frac{f_{nl}(R)}{R^2}\right)^2 \left(\frac{d}{d\theta}Y_{lm}(\theta,0)\right)^2_{\theta=0} \\ & + a_4[k(R)] \left(\frac{f_{nl}(R)}{R^2}\right)^2 \left(\frac{mY_{lm}(\theta,0)}{\sin\theta}\right)^2_{\theta=0} . \end{aligned} \tag{3.8}$$

These PECs exhibit wells at the maxima of the radial wave function that are typically 10-100 MHz in depth for $n > 30$ and support only a few weakly bound molecular states. These molecules are best characterized by Hund's case (c) since their depths are smaller than the fine-structure coupling, but for smaller n Hund's case (a) may become the more relevant case [124].

Due to the relative ease of exciting low-l Rydberg atoms via one or two-photon excitation from the ground state, these molecules have been explored extensively in experiments. Fig. 3.1 displays a Sr30S+Sr5S potential energy curve and a few bound states like those observed in [125]. This potential curve is the simplest realistic example, as Sr lacks a p-wave shape resonance, hyperfine structure, and separate singlet/triplet scattering channels, and in its S state possesses no fine structure. This potential therefore comes closest to the potential curve obtained in first order perturbation theory, Eq. 3.6, although the calculation in Fig. 3.1 also includes the polarization potential, $-\frac{\alpha}{2R^4}$, between the ionic core and the neutral atom. Bound states can be calculated in these potentials quite easily using, for example, a three-point finite difference method.

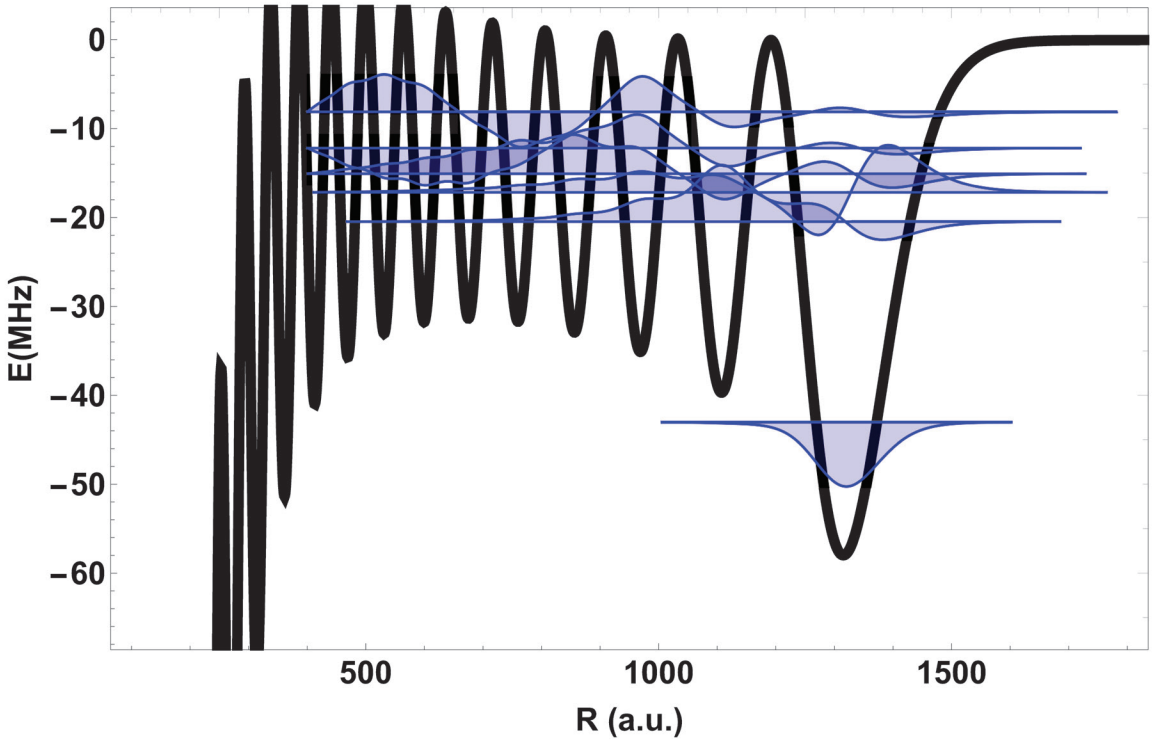

Figure 3.1. The potential energy curve for a Sr30S+Sr5S Rydberg molecule and a few bound vibrational states. The energy scale is relative to the 30S energy.

The Rb32p+Rb5s PEC is plotted in Fig. 3.2. All spin effects that are actually present in rubidium are neglected in this case, but due to the p-wave interaction Eq. 3.7 is needed. The p-wave potential leaves the outermost wells largely unchanged, but dramatically deepens wells at smaller R. For $R < 700$ the shape resonance causes these potentials to plummet down sharply.

These two examples show the main physics present in these Rydberg molecules composed of a low-l Rydberg atom and a single ground state atom. The poten-

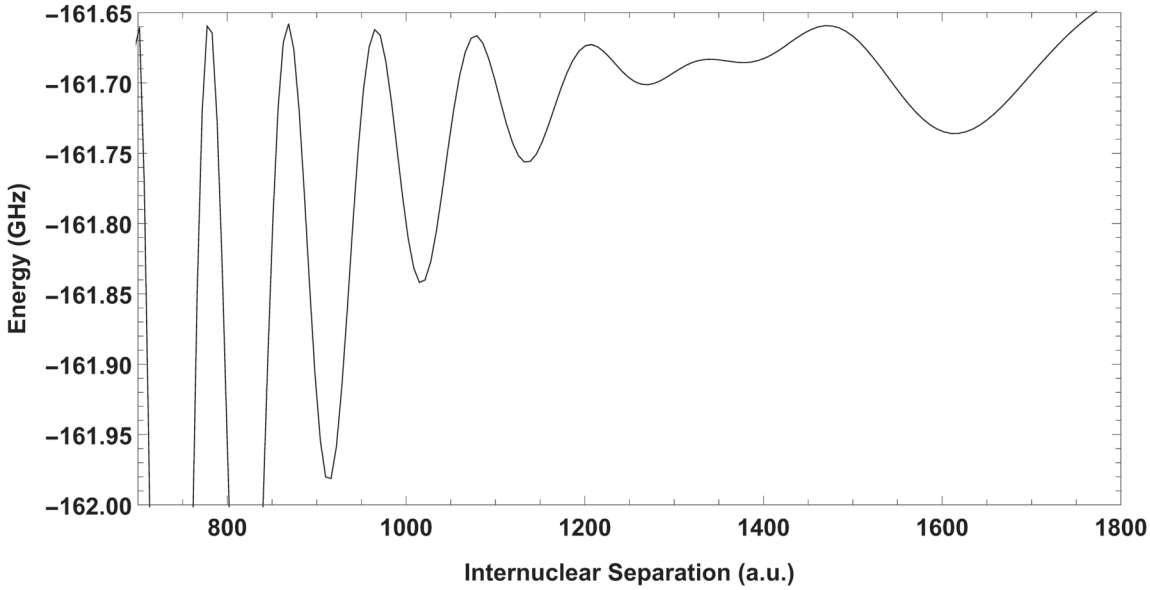

Figure 3.2. The potential energy curve for a $^3\Sigma$ Rb $32p$+Rb$5s$ Rydberg molecule state, ignoring all spin degrees of freedom. The energy scale is relative to the $n = 30$ Rydberg manifold.

tial energy curves oscillate like the Rydberg wave function, and can support a few bound states. We now turn to the four strongly perturbed eigenstates which form out of the degenerate high-l manifold. These four orbitals are the "trilobite" state for $\xi = 1$, dominated by s-wave scattering, and three "butterfly" states, called the "R-butterfly," "θ-butterfly," and "φ-butterfly, corresponding to the three directional derivatives in the p-wave interaction and enumerated by $\xi = 2, 3, 4$ respectively. These are shown in Fig. 2.8. Their PECs are nearly an order of magnitude deeper than the low-l states, and Hund's case (a) is the best characterization. Their eigen-

states and eigenenergies are obtained in degenerate perturbation theory by diagonalizing the potential matrix in the degenerate manifold, which has matrix elements

$$V_{\text{fermi},ll}(R) = \langle l| \sum_{\xi=1}^{4} a_\xi[k(R)]V_\xi(R,r)|l\rangle \quad . \tag{3.9}$$

First, we consider the $\xi = 1$ case alone. We set R parallel to $\hat{z}$ and integrate over the delta function $\delta(r-R)$ to get the matrix:

$$\frac{V^{\xi=1}_{\text{fermi},ll}}{2\pi a_s[k(R)]} = \begin{pmatrix} \phi^*_{n00}(R)\phi_{n00}(R) & \phi^*_{n00}(R)\phi_{n10}(R) & \cdots & \phi^*_{n00}(R)\phi_{nn-10}(R) \\ \phi^*_{n10}(R)\phi_{n00}(R) & \phi^*_{n10}(R)\phi_{n10}(R) & \cdots & \phi^*_{n10}(R)\phi_{nn-10}(R) \\ \vdots & \vdots & \ddots & \vdots \\ \phi^*_{nn-10}(R)\phi_{n00}(R) & \phi^*_{nn-10}(R)\phi_{n10}(R) & \cdots & \phi^*_{nn-10}(R)\phi_{nn-10}(R) \end{pmatrix}.$$

This is a rank 1 *separable matrix*, which has a single non-zero eigenvalue given by $E = \langle \phi_{nl0}(R) | \phi_{nl0}(R) \rangle$ and a corresponding eigenvector $v_E = \phi_{nl0}(R)$. When R is used in the argument of a wave function that should be evaluated at a vector position, it is to be assumed that the angular components of the wave function are to be evaluated on the z axis. For convenience, we define the following Q-functions

$$Q^{nl}_{LM_L}(R) = \delta_{m,M_L} \langle \nabla^L (\phi_{nlm}(R)) \rangle_{M_L}, \tag{3.10}$$

where

$$Q^{nl}_{00}(R) = \frac{f_{nl}(R)}{R} \overline{\frac{2l+1}{4\pi}}, \tag{3.11}$$

$$Q^{nl}_{10}(R) = \overline{\frac{2l+1}{4\pi}} \partial_R \frac{f_{nl}(R)}{R} \quad , \tag{3.12}$$

$$Q^{nl}_{1\pm1}(R) = \frac{f_{nl}(R)}{R^2} \overline{\frac{(2l+1)(l+1)l}{8\pi}}, l > 0. \tag{3.13}$$

Using these, we obtain the s-wave trilobite PEC and wave function analytically:

$$E_{\text{trilobite}}(R) = 2\pi a_s[k(R)] \sum_l \left| Q_{00}^{nl}(R) \right|^2; \tag{3.14}$$

$$\Psi_{\text{trilobite}}(R,r) = \frac{1}{\mathcal{N}} \sum_l Q_{00}^{nl}(R)\phi_{nl0}(r). \tag{3.15}$$

The summations here are assumed to range over all degenerate l values. The other interaction terms may be addressed similarly, assuming for now that the energy gaps between individual V_ξ terms is large enough that it is valid to treat each term separately. Although this is not the case near the PEC avoided crossings, we will eventually incorporate this following a re-diagonalization using these eigenstates. The R-butterfly potential curve can be calculated in exactly the same fashion, and is

$$E_{\text{R-butterfly}}(R) = 6\pi a_p^3[k(R)] \sum_l \left| Q_{10}^{nl}(R) \right|^2. \tag{3.16}$$

This has the same form as the s-wave PEC, except with radial derivatives of the hydrogenic wave functions replacing the wave functions themselves. For the remaining potential curves, which possess Π symmetry and $|m| = 1$, it can be shown that the two angular-butterfly potential operators commute and therefore their sum yields a rank 2 separable matrix with two degenerate eigenvalues [126]. The angle dependence of these PECs can be separated as $e^{im\phi}H_{lm}(\theta)$ for the θ-butterfly and $e^{im\phi}F_{lm}(\theta)$ for the φ-butterfly. These functions obey:

$$H_{l,-m}(\theta) = (-1)^{m+1}H_{lm}(\theta), \;\; F_{l,-m} = (-1)^m F_{lm}(\theta).$$

As a result, we specialize to just $m = 1$ without loss of generality:

$$F_{l1}(0)^2 = \frac{(2l+1)(l+1)l}{16\pi}; \quad H_{l1}(0)^2 = \frac{(2l+1)(l+1)l}{16\pi}.$$

The degenerate potential curves are

$$V_\theta = V_\phi = \left[6\pi a_p^3 [k(R)] \sum_l \frac{(2l+1)(l+1)l}{16\pi} \left(\frac{f_{nl}(R)}{R} \right)^2 \right] \tag{3.17}$$

$$= 6\pi a_p^3 [k(R)] \sum_l \left| \frac{Q_{11}^{nl}(R)}{\sqrt{2}} \right|^2 . \tag{3.18}$$

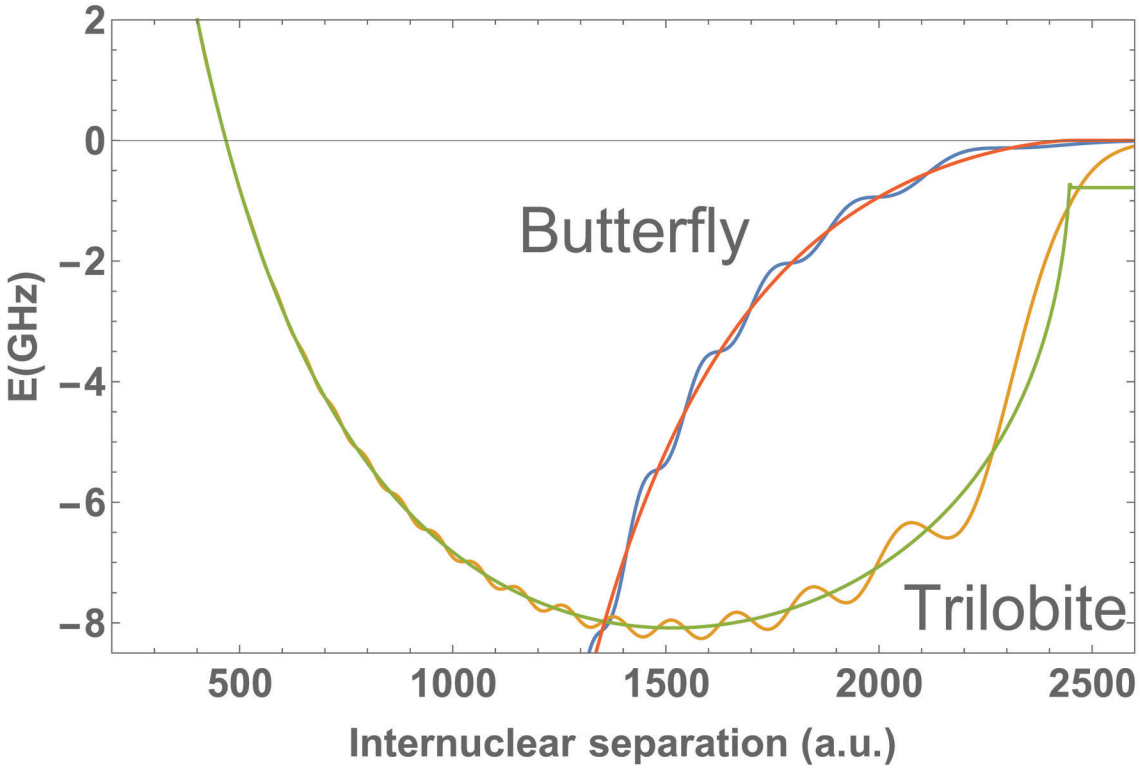

Figure 3.3. Trilobite and butterfly PECs for the $n = 35$ rubidium Rydberg molecule. Couplings between butterfly and trilobite states, their spin degrees of freedom, and all quantum defect-shifted states are ignored. The Borodin and Kazansky model gives the non-oscillatory curves.

We have obtained four PECs for the high-l states: a Σ state from the s-wave interaction, a Σ state from the radial p-wave interaction, and two degenerate Π states from the angular gradient terms of the p-wave potential. Two-dimensional cuts of the electronic wave functions corresponding to these four states are shown in Figure (2.8). The trilobite orbital was already given in Eq. 3.14, but all four can be written generally as

$$\Psi_{LM_L}(R,r) = \frac{{}_l Q^{nl}_{LM_L}(R) Y_{lM_L}(\hat{r}) r^{-1} f_{nl}(r)}{\overline{{}_l |Q^{nl}_{LM_L}(R)|^2}}. \tag{3.19}$$

In this notation we identify the Σ trilobite ($\Psi_{00}(R,r)$) and Σ, Π butterflies ($\Psi_{10}(R,r)$, $\Psi_{1\pm1}(R,r)$, respectively). Equation 3.19 is most useful in chapter 6 since it clarifies how these different eigenstates arise from the L^{th} partial wave explicitly, and it is specialized to the diatomic case where M_L is a good quantum number. However, in chapter 4 we will study polyatomics where no symmetry constraints impose restrictions on M_L, and furthermore it proves convenient to focus on which ξ term of the pseudopotential gives rise to each eigenstate. Eq. 3.19 can be written in this notation as:

$$\Psi_\xi(R,r) = \frac{1}{\mathcal{N}} \sum_{l,m} \partial_\xi \;\; \phi^*_{nlm}(R) \;\; \phi_{nlm}(r), \tag{3.20}$$

where $\mathcal{N}$ is a normalization constant. This notation will be used extensively in chapter 4, but the reader should recall that these two definitions are equivalent.

Finally, we note that the Borodin-Kazansky model [127] is an alternative, albeit less accurate, approximation for Rydberg-neutral interactions. It yields PECs that give the correct shape and magnitude of the Fermi-model PECs without the oscillatory nature due to the radial wave function modulation:

$$E_l^{BK}(R) = -\frac{1}{2n^2} + \frac{1}{2} \;\; n - \frac{\delta_l[k(R)]}{\pi} \;\; ^{-2}. \tag{3.21}$$

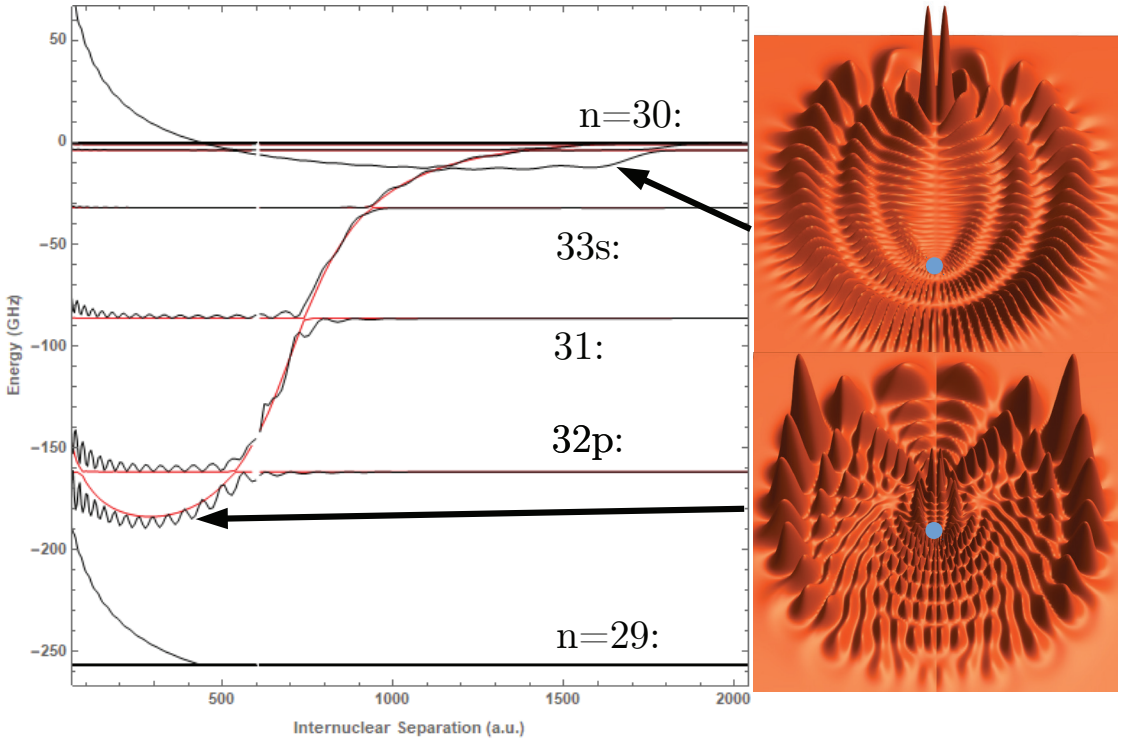

Figure 3.4. The Rb-Rb potential energy curves predicted by [40] (trilobite case only) and [122] (including the butterfly case). The wave functions giving rise to these popular names are plotted in cylindrical coordinates on the right.

We will utilize this approximation in chapter 6 to understand the challenges with convergence of the results, since these potential curves are independent of basis size and lack the divergent p-wave behavior since the resonant p-wave phase shift enters the formula as a phase shift without any divergences present in the scattering volume. Now that the trilobite and butterfly type PECs have been obtained in approximate form, let us consider the topology of the potential energy landscape including the full set of Rydberg states and couplings between all these different components.

Figure 3.4 shows the potential energy landscape for a Rydberg atom in the $n = 30$ state in the presence of a rubidium perturber. This figure shows many of the key features of this unusual class of molecules that we will revisit and expand upon throughout this thesis. Potential energy curves between $n = 30$ and $n = 29$ are plotted; the regularity of the Rydberg spectrum implies that this same picture will repeat, essentially unchanged, between every two Rydberg levels. Several mostly flat potential energy curves are seen – these correspond to the low-l quantum defect states. We are typically more interested in the trilobite and butterfly potential energy curves, marked with arrows, since these are the highly polar states with heavily modified electronic wave functions. This figure supports to some degree the assumptions of the previous discussion by showing that these potential curves are largely decoupled from one another and from the low-l states, although a series of avoided crossings between the diving p-wave potential curve and both the trilobite and the low-l states are visible, and its interaction with the $n = 29$ states is clearly critical to constrain the divergent scattering volume. The red potential energy curve shows the degenerate Π symmetry states from Eq. 3.17. Notably, it does not oscillate as a function of R: this is due to destructive interference between terms in the numerator of Eq. 4.18. An additional explanation for this from the summation formula is that high l states, with fewer radial oscillations, are weighted by a factor of order l^3, while in the trilobite curve these are weighted by just a factor of order l. Future chapters will return frequently to similar figures as Figs. 3.1-3.4, as we generalize to polyatomic potential energy surfaces (chapter 4), to multichannel atoms with more complicated Rydberg series (chapter 5), and to a far more accurate and complete picture involving all the spin degrees of freedom of the Rydberg atoms (chapter 6). The analytic expressions for the PECs and wave functions derived above will be fundamental in these studies.

3.3 Vibrational bound states and rotational spectra

With the adiabatic potential energy curves now in hand, we can solve the nuclear Schrödinger equation (Eq. 3.2) for the nuclear wave functions to obtain a complete description of the Rydberg molecule. Typically the rotational energy is neglected since the rotational constant of these molecules, inversely proportional to their bond length, is extremely small (<kHz typically). Rotational states have not been resolved in current experiments except for a few isolated cases. In the butterfly molecules, the internuclear distances are only a few hundred atomic units leading to a ∼MHz rotational constant and observable energy splittings [128]. This will be discussed in more detail in Chapter 7.

For Rydberg molecules dominated by the s-wave pseudopotential, or for deeply bound trilobite or butterfly-like states, at least the first few excited vibrational states are clearly bound in potential wells. Their wave functions decay exponentially in classically forbidden regions, even if there is significant tunneling between different wells (see Fig. 3.1). However, the sharp series of avoided crossings caused by the p-wave shape resonance and resulting butterfly potential curve add significant complications. Fig. 3.5 shows such a case for Cs, now including p-wave effects and spin degrees of freedom. In many such cases the accuracy of the adiabatic Born-Oppenheimer approximation may be in question since its applicability depends not only on the difference between nuclear and electronic masses but also on the energy separation between potential energy curves. Some works [129] have studied how these sharp avoided crossings actually lead to fascinating cold-chemistry pathways and dynamic processes like l-changing collisions due to non-adiabatic phenomena. We have not studied any of these effects here.

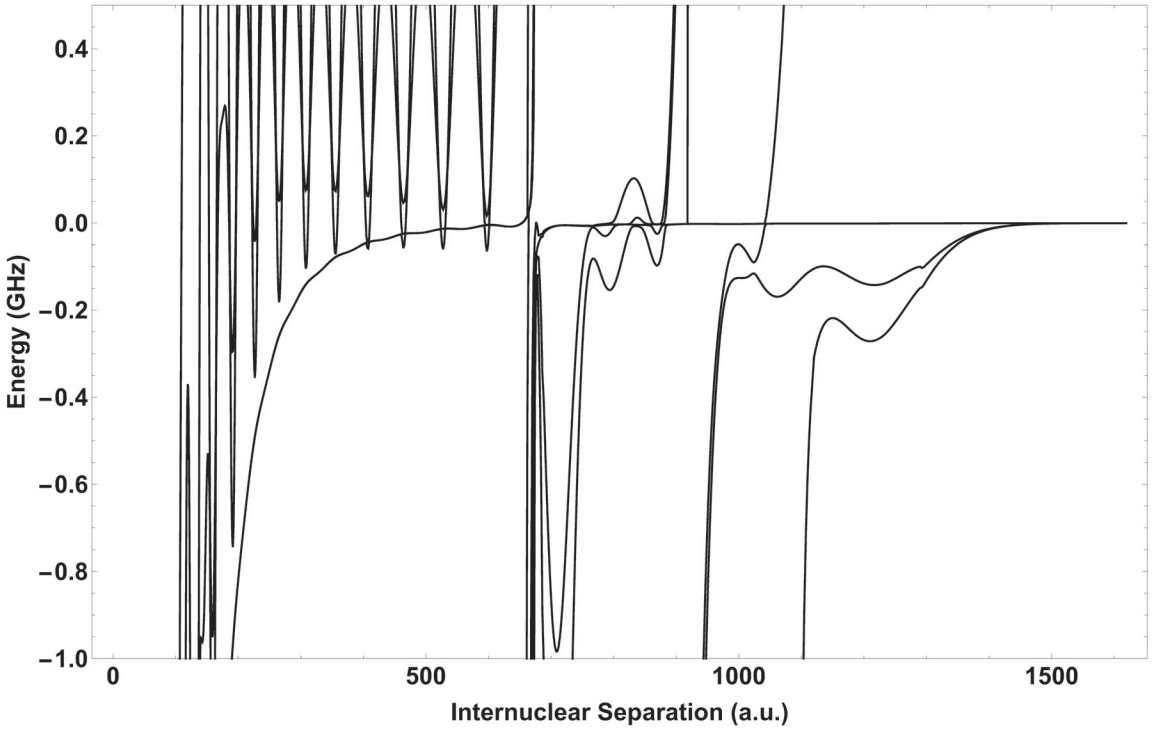

Figure 3.5. Cs $26p_{3/2}$+Cs$5s_{1/2}(F = 3)$ potential energy curves. Effects of the p-wave shape resonance dominate their structure.

However, a related and intriguing facet of these p-wave crossings is the notion that some of the excited Rydberg molecule states lying near the p-wave resonances are in fact bound by "quantum reflection." This was first observed and pointed out in Rb [101], but also should be highly relevant in Cs where the $^3P_2$ potential curve causes a very steep drop in the adiabatic potentials. Even at large internuclear distances this can affect the vibrational ground state in some cases, so it is worth briefly discussing our method for reliably calculating stable bound states in these unusual potential wells using a stabilization procedure [55, 56, 101]. This confirms

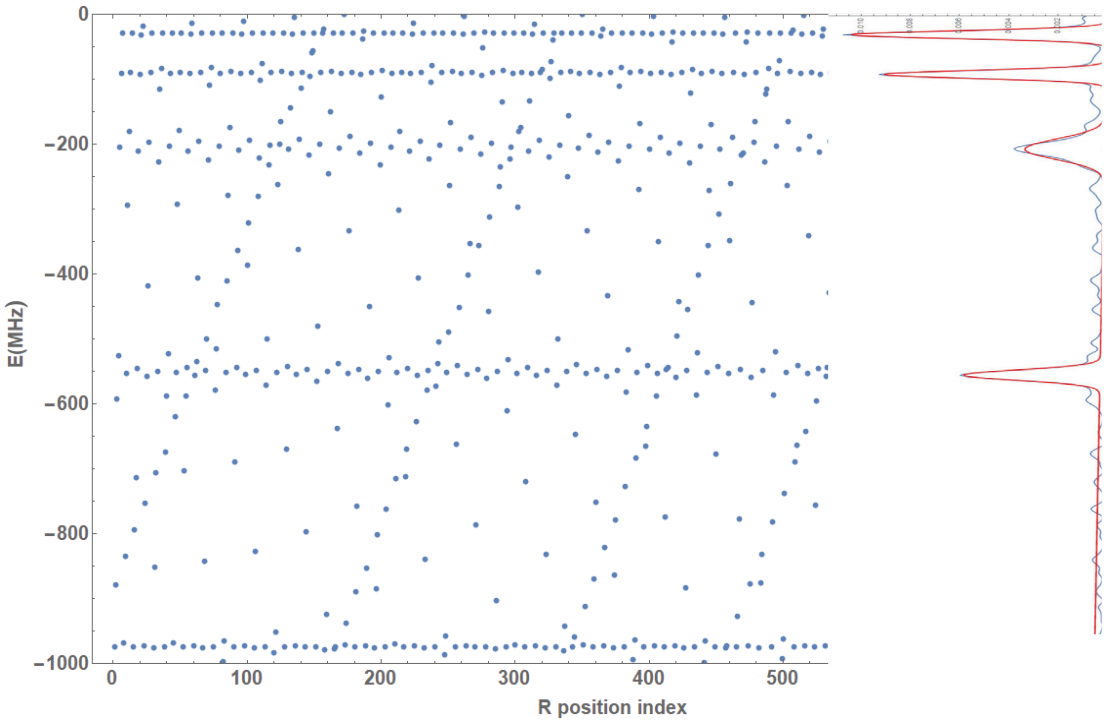

Figure 3.6. A stabilization diagram for the bound states at smaller R (purple) in Fig. 3.8. On the left are the calculated bound states as a function of box size, indexed arbitrarily, and on the right the data are binned and fit with Gaussian profiles.

that the p-wave shape resonances do not completely destabilize the molecule, and that quantized vibrational states still exist. At large internuclear distances the wave function exponentially decays into the classically forbidden region, but at smaller internuclear distances it remains classically allowed all the way to $R = 0$, well past the range of applicability of the Fermi pseudopotential. Nevertheless, by fixing an infinite barrier at some $R = R_0$ (typically in the range of 100-200 atomic units) the vibrational states are quantized, and we calculate them using a three-point finite

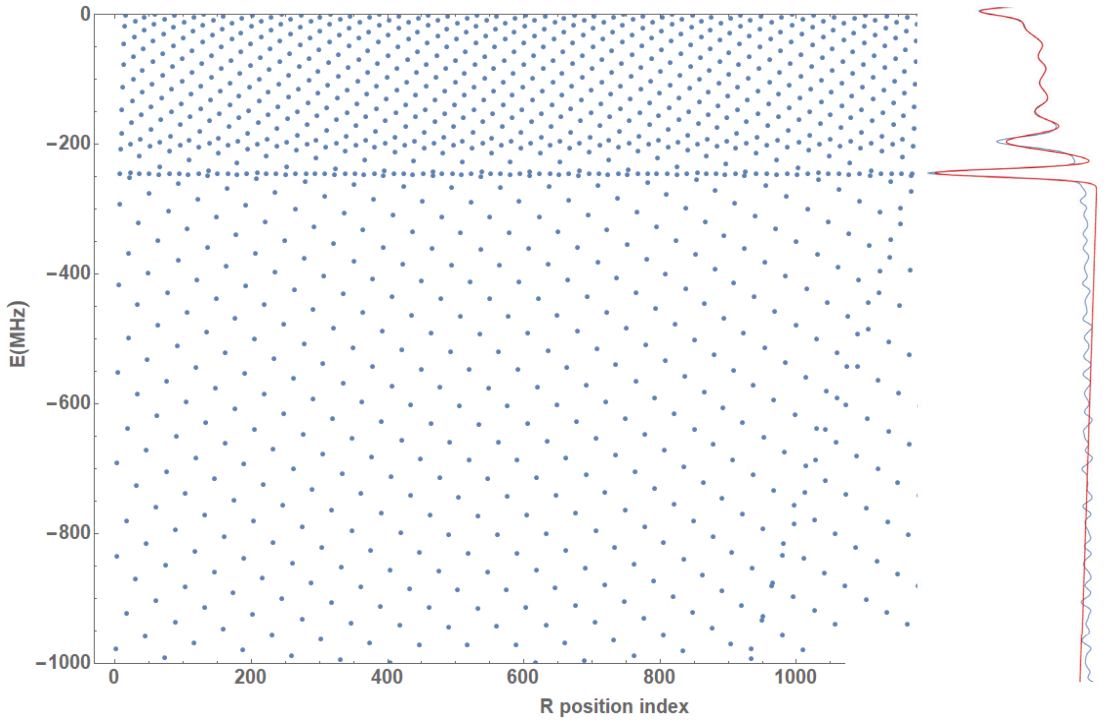

Figure 3.7. A stabilization diagram for the bound states at larger R (orange) in Fig. 3.8. On the left are the calculated bound states as a function of box size, indexed arbitrarily, and on the right the data are binned and fit with Gaussian profiles.

difference method. After repeating for many R_0 values, patterns emerge in the eigenstates as demonstrated in Figs. 3.6 and 3.7. Although the spectrum varies with R_0, on average these values cluster around specific resonance values. After binning this data and fitting to Gaussian profiles, the resonance positions can be accurately determined, and the widths of these Gaussian fits are related to the decay widths [56]. Fig. 3.8 shows some of these calculated bound states. Their localization, despite

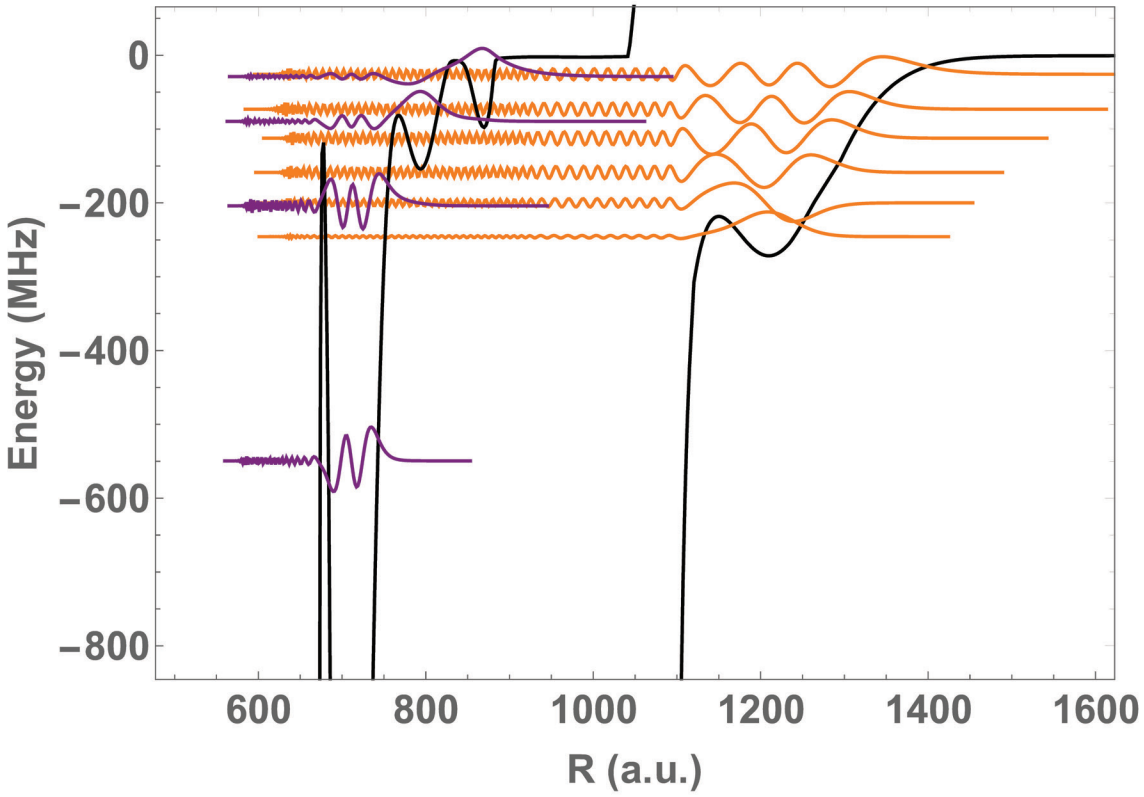

Figure 3.8. Bound states obtained using the stabilization procedure for some of the potential energy curves of Fig. 3.5. Quantum reflection stabilizes these states so that the disruption caused by the p-wave shape resonances does not destroy their ability to support bound states.

typically not being bound by a barrier to the left, can be interpreted as stemming from quantum reflection off of a steep potential drop.

In addition to these considerations, another major component of spectroscopy is the line strength associated with each vibrational state. This will not be discussed further here, but it has been explored in some detail in previous work [130] and

recently in a preprint which also includes rotational states [131]. Typically it seems that accurate predictions of the observed line shapes are still lacking, either due to an improper characterization of experimental conditions or to other subtle theoretical complications, but a couple of studies focusing more on the many-body case have calculated lineshapes which agree spectacularly with experiment [132, 133].

3.4 Multipole moments

The state mixing induced by the perturber creates large permanent electric dipole moments (PEDM) in these molecules. This even occurs in the weakly perturbed low-l states due to small admixtures of trilobite or butterfly states [134]. These PEDMs have sparked interest in the application of these molecules in dipolar gases and ultracold chemistry. The higher multipole moments are of interest for detailed calculations of inter-molecular interactions, and will be utilized in Chapter 7. The multipole moments of the i^{th} electronic configuration are $d^{k,q}_{\nu,i} = i|T^k_q|i$, where the multipole moments from classical electrostatics [135] are promoted to quantum-mechanical operators:

$$T^k_q = -r^k \sqrt{\frac{4\pi}{2k+1}} Y_{k,q}(\hat{r}). \tag{3.22}$$

Here k and q label tensor operator components; T^1_0 is the usual dipole operator. The multipole moments for the trilobite and butterfly eigenstates $\Psi_{LM}(R,r)$ of Eq. 3.19 are

$$T^k_q = \Psi_{LM}|T^k_q|\Psi_{LM} = \sum_{l,l'} \frac{Q^{nl}_{LM}(R)Q^{nl}_{LM}(R)}{\sum_{l'}|Q^{nl}_{LM}(R)|^2} \, nlM|T^k_q|nl'M \ . \tag{3.23}$$

As a reminder, l and l' are angular momenta of the Rydberg electron relative to the Rydberg core. The matrix element separates into a radial integral, $R^{nl}_{nl'}(k) =$

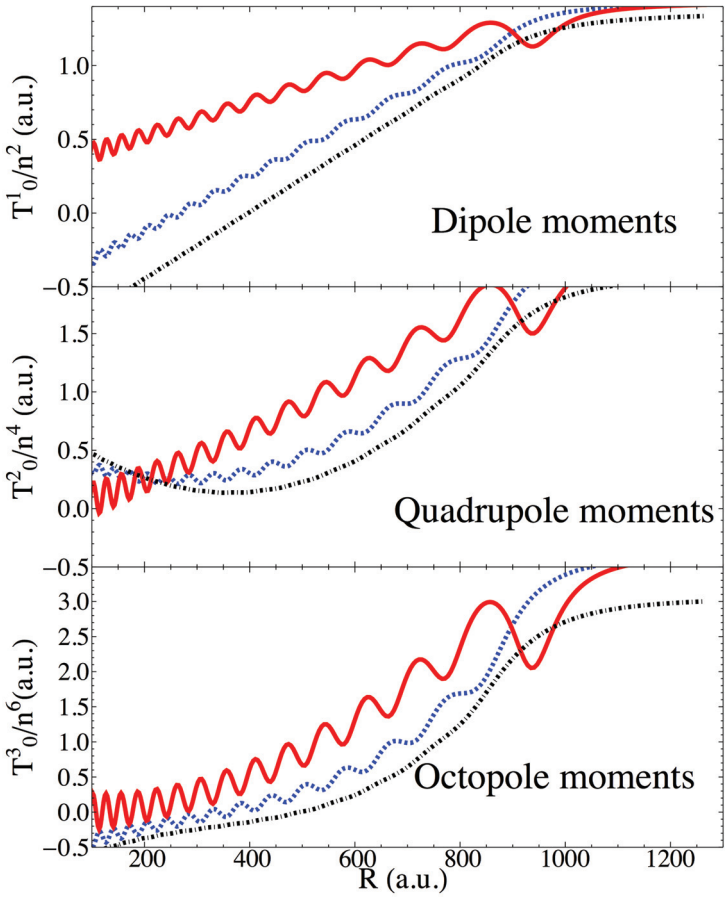

Figure 3.9. Analytic dipole, quadrupole, and octupole moments for $n = 23$ (Eq. 3.24). The trilobite (blue,dashed) and Σ butterfly state (red,solid) oscillate as a function of R, while the Π butterfly state (black,dot-dashed) is non-oscillatory; this behavior matches the potential energy curves. This figure is taken from Ref. [2].

$dr\, f_{nl}(r) r^k f_{nl}(r)$, and an angular integral. Evaluating this integral leads to the result

$$T^k_q = \sum_{l,l} \frac{Q^{nl}_{LM}(R) Q^{nl}_{LM}(R)}{\sum_l |Q^{nl}_{LM}(R)|^2} R^{nl}_{nl}(k) C^{lM}_{l\,M,kq} (-1)^{k-l} \sqrt{(2l+1)} \begin{pmatrix} l & l & k \\ 0 & 0 & 0 \end{pmatrix}. \quad (3.24)$$

The Clebsch-Gordan coefficient causes any term with $M = 0$ to vanish, reflecting the cylindrical symmetry. For the degenerate hydrogenic states considered here, $R_{nl}^{nl}(k)$ can be analytically evaluated (Eq. E.3). The dipole ($k = 1$) moments agree exactly with previous calculations [95]. These multipole moments scale in size as n^{2k}, and are displayed in Fig. 3.9 up to the octupole moments.

3.5 Overview

As this introductory chapter has demonstrated, these molecules possess many fascinating and unique properties: oscillatory potential energy curves, extremely large bond lengths and, in the trilobite and butterfly cases, highly localized wave functions with exotic nodal structure and huge permanent electric dipole moments [95, 96, 121, 134]. We have seen how these molecules are formed by the appropriate mixing of nearly degenerate high angular momentum states that maximizes the electron probability at the location of the perturber [136]. Figures 3.3 and 3.4 encapsulate the results of the first studies of these molecules. These original predictions focused on the simplest cases of ^3S [40] and ^3P [96, 122] scattering of electrons by a Rb atom. Essentially simultaneously, more sophisticated Green's function techniques were developed [96, 121, 137]; one in particular also included important spin effects such as the Rydberg fine structure, singlet and triplet scattering, and the relativistic ^3P_J splitting of the electron-atom phase shifts [95]. The behavior of Rydberg molecules when subjected to external electric [14, 121, 138, 139] and magnetic [139–141] fields has also been investigated theoretically.

Experimental investigations of these molecules have, with the exception of an early observation of satellite peaks related to minima of low-n Rydberg potential curves [137], entirely occurred in the last decade, following the first observation of

non-polar Rydberg molecules in 2009 by Tilman Pfau's group [142]. These first experiments focused primarily on penetrating Rydberg states of low orbital angular momentum, and characterized the dipole moments [134], vibrational energies and lifetimes [143], controllable orbital hybridization in the presence of weak external fields [144], and even some signatures of trimer formation [101]. Many other groups have since added other atomic species such as Cs [145] and Sr [125, 146, 147] to the mix. This experimental work led researchers to realize that a more sophisticated theoretical description was necessary to match the highly accurate spectroscopic measurements, and so additional experimental [102, 148–150] and theoretical [124, 130] studies of singlet and triplet scattering states mixing between these states caused by the hyperfine splitting of the neutral atom were performed. **Chapter 6** expands upon this wide body of literature, particularly the theoretical papers [95, 124, 130], in order to describe a fully spin-dependent approach. Very different regimes of principal quantum number were also explored, from very low-n states which could be photoassociated directly from bound Rb-Rb molecules [151, 152] to very high Rydberg states which showed resonances associated with the formation of polyatomic molecules [153]. These molecules, where multiple ground state atoms lie within the Rydberg orbit, are studied in **chapter 4**.

The first theoretical predictions were finally fully confirmed in 2015 and 2016, when trilobite molecules with kilo-Debye dipole moments were observed in Cs [154] and butterfly molecules were observed in Rb [128]. The trilobite molecules could be formed due to the nearly integer quantum defect of the Cs ns state, which admixed the $l = 0$ and high-l trilobite state together sufficiently to make it accessible via two-photon excitation. **Chapter 5** explores similar physics in multichannel atoms, where not only are favorable degeneracies like this one in Cs accessible, but in some cases due to the heavily perturbed Rydberg spectra of these complex atoms these degeneracies

are also tunable by varying n. The butterfly molecules were observed since their wells are energetically close to the nP state, so they could be photoassociated by absorption of a single photon. Their rotational spectra changed drastically when they were exposed to a weak electric field due to their large dipole moments [128]. The observation of these *pendular* states, which librate around the field axis and have an evenly spaced oscillatory level structure [155], are studied further in **chapter 7**.

This broad range of studies of Rydberg molecules reflects their surprising versatility. Beyond studying fundamental aspects of their structure, researchers have pursued many exciting research topics in past years that utilize these molecules to study or manipulate other processes in ultracold gases. In Ref. [156] Rydberg molecules were formed in an optical lattice and used as a non-destructive probe of the Mott transition, and recently a theoretical proposal to dress an ultracold gas with a Rydberg molecular state to enact an optical Feshbach resonance has been implemented [157,158]. Rydberg molecules have been proposed as miniature "colliders" to study atom-ion scattering [114] and the electron-atom scattering phase shifts more accurately [159]. They also reveal the properties of the polarization potential between the Rydberg core and surrounding neutral atoms if the Rydberg orbit is much greater than the average interatomic spacing [160]. They were observed to induce spin-flips at extremely long range [161]. Coherent control of the photoassociation process was demonstrated in [162], and it was found that signatures of vibrational bound states showed up in electromagnetically-induced transparency experiments [163]. Similarly to how the remarkable diversity of prehistoric trilobite species led to their survival over millions of years, the diversity of aspects of Rydberg molecules has led to an explosion of interest in these quantum "creatures."

To our knowledge there are three review articles discussing Rydberg molecules [159,164,165]. These articles also are good sources of information on another class of

huge, highly excited molecules called Rydberg macrodimers [41, 42, 166, 167]. These are formed by two Rydberg atoms bound weakly together with bond lengths on the order of a micron by the long-range van der Waals interaction between these highly excited atoms.

This page intentionally left blank

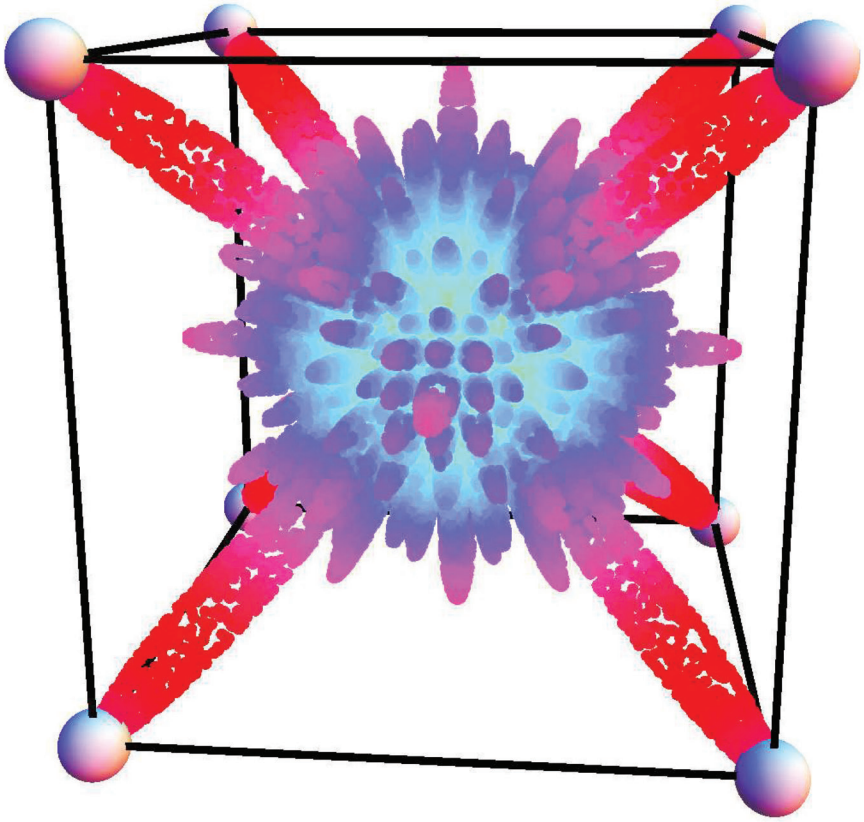

Figure 3.10. Chapter 4 discusses polyatomic molecules, like this 8-atom trilobite in an A_{1g} cube geometry. The probability $|\Psi(\theta,\phi)|^2$ at a fixed R is shown as a polar plot. This figure is modified from Ref. [4].

4. POLYATOMIC RYDBERG MOLECULES

As the principal quantum number n and atomic density ρ increase, the average number of perturbers N within a Rydberg volume grows proportionally to ρn^6. As the number of perturbers increases so does the probability that larger molecules – trimers, tetramers, and so on – can form due to electron-atom scattering as prescribed by the Fermi pseudopotential formulated in the previous chapter. Of course, in the limit of large N Fermi's original conception of this system should be recovered and the effect of all these perturbers will again be an overall mean field energy shift. Between these two extremes of $N = 1$ and $N \quad 1$ resides a range of fascinating phenomena. What kinds of polyatomic molecules will form, if they even can? Will they have any structure or symmetries? Are they less stable than dimers due to disruptions from additional perturbers, or will they instead serve to better localize the electron and thus stabilize the molecules further? What happens in this crossover regime from the few body physics of small polyatomic molecules to the mean-field many-body regime, and does the latter regime exhibit any interesting behavior beyond Fermi's original prediction? In this chapter we will explore some of these questions.

The past few years have witnessed an exciting amount of growth in this area. Experimentally, these large densities and high Rydberg states have been studied in Rb [168, 169], Cs [170], and Sr gases [133]. The Rb and Sr experiments have found evidence for both the formation of polyatomic molecules as well as rich physics associated with the affect of dozens or even hundreds of perturbers on the Rydberg atom [171]. Some of these effects could be attributed to the p-wave shape resonance

in Rb [169], while other results were interpreted in terms of the creation of Rydberg polarons and impurity physics [172, 173]. At even higher densities even the coupling between the Rydberg electron and the entire condensate [168, 174] can be studied. In Cs the focus so far has been only on trimers, but now in a configuration with non-zero Rydberg angular momentum in contrast to the other experiments of polyatomic systems, performed exclusively with isotropic ns states.

Theoretical work has focused on either the structural few-body properties of molecules, such as symmetric cuts in their potential energy surfaces [175], stretching and binding dynamics [176], three-body type forces which can lead to Borromean binding [177], survival and even enhancement in disordered environments [178] or on more general many-body physics [172, 173]. Some field effects, such as a Rydberg trimer in an electric field, have been investigated [179]. Additional theoretical work has studied a different type of polyatomic molecule formed by replacing the perturbing neutral atom with a polar dimer such as KRb [180–184].

This chapter presents our investigations of the effects of multiple perturbers on the Rydberg energy levels and the properties of polyatomic Rydberg molecular states. Sections 4.1 - 4.3 are adapted from Ref. [4] and focus primarily on trilobite and butterfly states in polyatomic molecules. The goal of these sections is to develop a generic description of polyatomic Rydberg molecules from a few-body perspective which can then be widely applied to a variety of specific cases. Special attention is paid to molecular states with high geometric symmetry in order to build intuition for the properties of polyatomic molecules. The results derived are still completely general to arbitrary configurations and environments, and thus can be employed to study everything from disordered gases to structured aggregates. Section 4.4 uses this general formulation to study the lineshape of a Rydberg hydrogen atom immersed in a dense background gas, and is based on Ref. [3]. Section 4.5 culminates this study

by generalizing some of the results of sections 4.1-4.3 to include additional effects from other Rydberg manifolds and quantum defect-shifted states, which are ignored in these prior sections. This extends the previous results, which were valid to first order in perturbation theory, to the same accuracy as the results obtained within a full basis diagonalization of the Hamiltonian. This formulation can also lead to a computationally efficient and conceptually intuitive way of including spin degrees of freedom or external field effects.

4.1 Fundamentals of polyatomic Rydberg molecules

We consider an $N > 1$ polyatomic system with N ground state atoms, located at $R_i = (R_i, \theta_i, \varphi_i)$, surrounding a central Rydberg atom. For tractability, the molecular breathing modes – where the ground state atoms share a common distance $R_i = R$ to the Rydberg core – are the primary focus of this chapter, although most formulas readily generalize and the calculations in section 4.4 will not share this restriction. We also primarily focus on the $n = 30$ states of rubidium to facilitate comparison with diatomic trilobite states, and continue to neglect spin degrees of freedom as well as singlet scattering. The p-wave scattering states are, however, included, and this physics dramatically increases the complexity of the molecular structure due to the vectorial character of the p-wave pseudopotential operator.

The first goal of this section is to generalize the diatomic results described in chapter 3 to this system with $N + 1$ constituent atoms, and thus develop a general theory capable of describing polyatomic states. The Hamiltonian generalizes readily:

we add to the dimer Hamiltonian a new pseudopotential term for each additional perturber. Thus:

$$H_N(r) = \hat{H}_0 + \sum_{i=1}^{N} V_{\text{fermi}}(r, R_i) \tag{4.1}$$
$$= \hat{H}_0 + 2\pi \sum_{i=1}^{N} \sum_{\xi=1}^{4} a_\xi[k(R_i)] V_\xi(R_i, \vec{r}).$$

For brevity we will suppress the radial dependence of a_ξ in the following expressions, writing $a_\xi[k(R_i)] = a_\xi(k)$.

We now incorporate arbitrary perturber locations into the analytic results from section 3.1 for the PECs and molecular orbitals. We saw in the previous chapter that the diatomic eigenstates and eigenenergies are superpositions of hydrogenic wave functions. Indeed, the wave functions, eigenenergies, and even the overlaps between different orbitals can be written [177] as elements of a $(4 \times 4) \otimes (N \times N)$ "trilobite overlap matrix", $\boldsymbol{\Upsilon}^{\boldsymbol{\alpha\beta}}_{\mathbf{pq}}$, where $\boldsymbol{\Upsilon}^{\boldsymbol{\alpha\beta}}_{\mathbf{pq}}{}^{*} = \boldsymbol{\Upsilon}^{\boldsymbol{\beta\alpha}}_{\mathbf{qp}}$. The lower indices p and q label the position vectors R_p and R_q of two neutral atoms; a lower index r indicates $R_r = r$. Upper indices α and β label the eigenstates: the normalized ξ^{th} eigenstate for a molecule with an internuclear axis R is therefore $\boldsymbol{\Upsilon}^{\boldsymbol{\xi 1}}_{\mathbf{Rr}} / \sqrt{\boldsymbol{\Upsilon}^{\boldsymbol{\xi\xi}}_{\mathbf{RR}}}$. This is equivalent to Eq. 3.20. The trilobite ($\xi = 1$) and three (R, θ, φ)-butterfly PECs ($\xi = 2, 3, 4$), as well as their unnormalized eigenstates, are written very concisely in terms of the trilobite overlap matrix:

$$E^{\xi}_{l>3}(R) = 2\pi a_\xi(k) \boldsymbol{\Upsilon}^{\boldsymbol{\xi\xi}}_{\mathbf{RR}}; \;\; \Psi^{\xi}(r, R) = \boldsymbol{\Upsilon}^{\boldsymbol{\xi 1}}_{\mathbf{Rr}}. \tag{4.2}$$

The trilobite overlap matrix therefore must be

$$\boldsymbol{\Upsilon}^{\boldsymbol{\alpha\beta}}_{\mathbf{pq}} = \sum_{l=l_{\min}}^{n-1} \sum_{m=-l}^{m=l} \Phi^{\alpha}_{nlm}(R_p)^{*} \Phi^{\beta}_{nlm}(R_q), \tag{4.3}$$

where the summation extends over energetically degenerate states, starting at $l_{\min} = 3$ in the atoms (except H) considered here. Φ^{α}_{nlm} is a shorthand for the wave function and components of the gradient in spherical coordinates:

$$\Phi^{\alpha}_{nlm}(r) = \begin{cases} \phi_{nlm}(r) & \alpha = 1 \\ \frac{\partial \phi_{nlm}(r)}{\partial r} & \alpha = 2 \\ \frac{1}{R}\frac{\partial \phi_{nlm}(r)}{\partial \theta} & \alpha = 3 \\ \frac{1}{R\sin\theta}\frac{\partial \phi_{nlm}(r)}{\partial \varphi} & \alpha = 4. \end{cases} \tag{4.4}$$

Two additional properties of the overlap matrix are important. $\boldsymbol{\Upsilon^{\alpha\beta}_{pq}}$ is the overlap between different diatomic orbitals α and β associated with different ground state atoms located at R_p and R_q, respectively, and the matrix element of the ξ^{th} interaction term of the Hamiltonian between an orbital α located at R_p and an orbital β located at R_q is $\boldsymbol{\Upsilon^{\xi\alpha}_{ip}\Upsilon^{\beta\xi}_{qi}}$.

Somewhat surprisingly, these sums over hydrogenic states can be analytically performed, assuming vanishing quantum defects. This was first accomplished in several papers by Chibisov and coworkers shortly following the first trilobite paper [185], but their results were not condensed into a very clear form and seem to not have been well appreciated in the literature since. Our goal is to sum

$$\sum_{l=0}^{n-1} \sum_{m=-l}^{m=l} [\Phi^{\alpha}_{nlm}(R)]^{*} \Phi^{\beta}_{nlm}(r). \tag{4.5}$$

In fact, only Eq. 4.5 with α and β set to unity need be summed; the rest can be obtained by taking appropriate derivatives. We begin with the Coulomb Green's function, which is known in closed form [185]:

$$G(r,R,E) = \frac{\Gamma(1-\nu)}{2\pi|r-R|} \quad \frac{\partial}{\partial(x/\nu)} - \frac{\partial}{\partial(y/\nu)} \quad W_{\nu,1/2}(x/\nu) M_{\nu,1/2}(y/\nu) \tag{4.6}$$

$$(x,y) = r + R \pm |r-R|$$

The Whittaker functions $M_{\nu,1/2}(\tau)$ and $W_{\nu,1/2}(\tau)$ are related by

$$\Gamma(1-\nu)M_{\nu,1/2}(\tau) = (-1)^{1+\nu}\frac{\Gamma(1-\nu)}{\Gamma(1+\nu)}W_{\nu,1/2}(\tau) + (-1)^{\nu}W_{-\nu,1/2}(-\tau). \tag{4.7}$$

For an energy E very near to a bound Rydberg state E_ν, ν approaches an integer, the principal quantum number n, and $\Gamma(1-\nu)$ diverges. The first term in Eq. 4.7 clearly dominates, and in this limit

$$\Gamma(1-\nu)|_{\nu\to n} = \frac{(-1)^n}{n^3\Gamma(n)}\frac{1}{E-E_n}, \tag{4.8}$$

where $E = -(2\nu^2)^{-1}$ and $E_n = -(2n^2)^{-1}$. To equate this description of the Green's function with Eq. 4.5, and thus evaluate the sum in Eq. 4.5, we turn to the alternative derivation of the Green function using an expansion into a complete set of orthogonal functions. In this case an appropriate choice are the hydrogenic wave functions:

$$G(r,R,E) = \sum_{nlm}\frac{\phi^*_{nlm}(r)\phi_{nlm}(R)}{E-E_n}, \tag{4.9}$$

where the sum is understood to extend into the continuum as well, with n becoming a continuous variable. Near a bound state with principal quantum number n the dominant term in this sum is $\frac{1}{E-E_n}\sum_{lm}\phi^*_{nlm}(r)\phi_{nlm}(R)$. Therefore we simply need to match this expression with the closed-form Green function asymptotically approaching a bound state energy, i.e.:

$$\frac{1}{E-E_n}\sum_{lm}\phi^*_{nlm}(r)\phi_{nlm}(R) = \frac{(-1)^n}{n^3\Gamma(n)}\frac{1}{E-E_n}\frac{1}{2\pi|r-R|}\left[\frac{\partial}{\partial(x/\nu)} - \frac{\partial}{\partial(y/\nu)}\right] \times W_{\nu,1/2}(x/\nu)\frac{(-1)^{1+\nu}}{\Gamma(1+\nu)}W_{\nu,1/2}(y/\nu)\Big|_{\nu=n}.$$

The final step is to connect the Whittaker function at an integer value of ν to the hydrogenic radial wave functions $u_{nl}(r)$:

$$W_{n,1/2}\left[\frac{2r}{n}\right] = (-1)^{n+1}n!\sqrt{n}u_{n0}(r). \tag{4.10}$$

Thus,

$$\begin{aligned}
\Upsilon^{11}_{Rr} = \sum_{lm} \phi^*_{nlm}(r)\phi_{nlm}(R) &= \frac{(-1)^n}{n^3(n-1)!}\frac{1}{2\pi|r-R|}\quad\frac{\partial}{\partial(x/n)} - \frac{\partial}{\partial(y/n)} \\
&\quad\cdot(-1)^{2n+2}n!n!nu_{n0}(x/\nu)u_{n0}(y/n)\frac{(-1)^{1+n}}{n!} \\
&= \frac{(-1)}{2\pi n^3}\frac{1}{|r-R|}\quad\frac{\partial}{\partial(x/n)} - \frac{\partial}{\partial(y/n)} \\
&\quad\cdot n^2u_{n0}(x/2)u_{n0}(y/2) \\
&= -\frac{1}{2\pi n^3|r-R|}n^3\quad\frac{\partial}{\partial x} - \frac{\partial}{\partial y}\quad u_{n0}(x/2)u_{n0}(y/2) \\
&= \frac{1}{4\pi|r-R|}\left(u_{n0}(x)u_{n0}(y) - u_{n0}(x)u_{n0}(y)\right)
\end{aligned}$$

This is the outcome we were hoping for – after a few additional definitions we obtain

$$\begin{aligned}
&\boldsymbol{\Upsilon^{11}_{Rr}} = \frac{u_{n0}(t_-)u_{n0}(t_+) - u_{n0}(t_-)u_{n0}(t_+)}{4\pi\Delta t}, \\
&\Delta t = t_+ - t_-,\ \ t_\pm = \frac{1}{2}\quad R + r \pm \quad\sqrt{R^2 + r^2 - 2Rr\cos\gamma}\quad ,
\end{aligned} \tag{4.11}$$

where γ is the angle between R and r. This expression is exact for non-relativistic hydrogen, with its vanishing quantum defects, and is an excellent approximation for the summation in equation (4.3) for energies between the high-l manifold and the low-l states with nonzero quantum defects. The three butterfly eigenstates can be found by differentiating equation (4.11) with respect to R, θ_R, and φ_R:

$$\boldsymbol{\Upsilon^{21}_{Rr}} = \frac{(r\cos\gamma - R)\mathcal{F}(t_+,t_-)}{8\pi\Delta t^3} + \frac{u_{n0}(t_+)u_{n0}(t_-) - u_{n0}(t_-)u_{n0}(t_+)}{8\pi\Delta t} \tag{4.12}$$

$$\boldsymbol{\Upsilon^{31}_{Rr}} = \cos\theta_R\cos\varphi_R\Upsilon_x + \cos\theta_R\sin\varphi_R\Upsilon_y - \sin\theta_R\Upsilon_z \tag{4.13}$$

$$\boldsymbol{\Upsilon^{41}_{Rr}} = -\sin\varphi_R\Upsilon_x + \cos\varphi_R\Upsilon_y, \tag{4.14}$$

where

$$\Upsilon_{x,y,z} = \frac{\mathcal{F}(t_+,t_-)}{8\pi(\Delta t)^3}(\sin\theta_r\cos\varphi_r, \sin\theta_r\sin\varphi_r, \cos\theta_r), \tag{4.15}$$

$$\mathcal{F}(t_+,t_-) = -2(\Delta t)u_{n0}(t_+)u_{n0}(t_-) - u_{n0}(t_-)[2u_{n0}(t_+) - (\Delta t)u_{n0}(t_+)]$$
$$+ u_{n0}(t_+)[2u_{n0}(t_-) + (\Delta t)u_{n0}(t_-)].$$

The θ, φ butterfly orbitals can be identified as vectors of magnitude $\frac{\mathcal{F}(t_+,t_-)}{8\pi(\Delta t)^3}$ parallel to the θ, φ unit vectors; the trilobite and R-butterfly orbitals are fully symmetric about the internuclear axis – the trilobite orbital acts as a scalar under a symmetry operation, and the R-butterfly behaves as a vector parallel to the internuclear axis. The diagonal elements $\boldsymbol{\Upsilon}^{\xi\xi}_{\mathbf{pp}}$ are obtained by carefully evaluating equations (4.11 - 4.14) in the limit $R_p \to R_q$ using L'Hopital's rule, and by using the radial Schrödinger equation to eliminate second or higher derivatives:

$$\boldsymbol{\Upsilon}^{\mathbf{11}}_{\mathbf{RR}} = \frac{(2n^2 - R)\left(u_{n0}(R)/n\right)^2 + Ru_{n0}(R)^2}{4\pi R} \tag{4.16}$$

$$\boldsymbol{\Upsilon}^{\mathbf{22}}_{\mathbf{RR}} = \boldsymbol{\Upsilon}^{\mathbf{33}}_{\mathbf{RR}} - \frac{u_{n0}(R)}{12\pi R^3}\left[3Ru_{n0}(R) + 2u_{n0}(R)\right] \tag{4.17}$$

$$\boldsymbol{\Upsilon}^{\mathbf{33}}_{\mathbf{RR}} = \boldsymbol{\Upsilon}^{\mathbf{44}}_{\mathbf{RR}} = \frac{4\pi R(2n^2 - R)\boldsymbol{\Upsilon}^{\mathbf{11}}_{\mathbf{RR}} - n^2u_{n0}(R)u_{n0}(R)}{12\pi n^2R^2}. \tag{4.18}$$

Recall from chapter 3 that the diatomic θ and φ butterfly – referred to together as angular butterfly – states, corresponding to potential curves $\boldsymbol{\Upsilon}^{\mathbf{33}}_{\mathbf{RR}}$ and $\boldsymbol{\Upsilon}^{\mathbf{44}}_{\mathbf{RR}}$, are degenerate $^3\Pi$ molecular states and, in contrast to the $^3\Sigma$ trilobite or R-butterfly PECs, do not oscillate as a function of R. These solutions provide useful insight into the behavior of trilobite-like wave functions and their potential energy curves. For example, section 4.4 uses Eq. 4.16 frequently to evaluate polyatomic potential energy surfaces for a many-perturber environment and to obtain convenient analytic expressions for the line shape. Additionally, these expressions provide requisite information for understanding the vectorial behavior of the p-wave terms: Eq. 4.15

reveals the geometric symmetry properties regarding rotation and reflection of the molecular orbitals.

The general idea behind the following derivations is that the trilobite overlap matrix elements correspond to the matrix elements of the Rydberg Hamiltonian, H_0, and the Fermi/Omont pseudopotential in the basis of *molecular* orbitals. Therefore, the assumption that the electronic wave function is given by a linear combination of these eigenstates [126] leads to a generalized eigenvalue equation for the molecular potential energy curves, $E(R)$, since these molecular eigenstates are non-orthogonal. As a test, for the diatomic case with $N = 1$ one finds

$$\sum_{\beta=1}^{4}\sum_{\xi=1}^{4} a_\xi(k)\boldsymbol{\Upsilon}^{\boldsymbol{\xi\alpha}}_{\mathbf{RR}}\boldsymbol{\Upsilon}^{\boldsymbol{\beta\xi}}_{\mathbf{RR}} - \frac{E}{2\pi}\boldsymbol{\Upsilon}^{\boldsymbol{\alpha\beta}}_{\mathbf{RR}} \quad \Omega_R^\beta = 0. \tag{4.19}$$

What we have done here is to approximate the problem as a four-level system involving only these molecular orbitals; in another perspective, we have constructed a highly reduced basis that nearly diagonalizes the Hamiltonian, and then used that to solve a much simpler system. Section 4.5 and Appendix B provide further details in support of this approach, which for now is taken as an *ansatz*. We now investigate the properties of polyatomic molecules using the intuition developed throughout the first part of this chapter.

First, we consider the low-l states, treating them independently from the trilobite and butterfly states for now, as in the last chapter. In a general environment, all m_l values for a given l are in principle nonzero unless there are additional imposed symmetries (for example if the molecule is restricted to a plane). Therefore $N_d = 2l + 1$ degenerate m_l states mix together. This causes $N_p = \max(4N, N_d)$ PECs to

split away from the unperturbed electronic states. For Fermi's s-wave interaction alone the PECs are the eigenvalues $E(R)$ given by the matrix equation

$$a_s(k) \quad \frac{u_{nl}(R)}{R} \quad {}^{2} \quad {}^{l} \quad {}^{N} \sum_{m=-l} \sum_{i=1} Y^*_{lm}(\theta_i, \varphi_i) Y_{lm}(\theta_i, \varphi_i) \Omega^1_m = \frac{E}{2\pi} \Omega^1_m \,. \tag{4.20}$$

The trilobite overlap matrix formalism allows us to rapidly establish the same type of equation for the high-l states, generalizing Eq. 4.19 to the polyatomic system. The trial solution used to obtain equation (4.19) is expanded to include linear combinations of trilobite and butterfly eigenstates for each diatomic Rydberg-neutral pair:

$$\Psi(r) = {}^{N} \sum_{p=1} {}^{4} \sum_{\alpha=1} \Omega^{\alpha}_p \boldsymbol{\Upsilon}^{\boldsymbol{\alpha 1}}_{\mathbf{pr}}, \tag{4.21}$$

with Ω^{α}_p a set of unknown coefficients. This formulation provides key physical insight and also greatly reduces the calculational effort to the diagonalization of at most a $4N \times 4N$ matrix, rather than the full $n^2 \times n^2$ basis size needed to diagonalize equation (4.1). The trilobite PECs may be found by operating on equation (4.21) with the Hamiltonian, after setting $\alpha = 1$, and then projecting onto the state $\boldsymbol{\Upsilon}^{\mathbf{11}}_{\mathbf{qr}}$. This yields the eigenvalue equation

$$\sum_{p}^{N} \left[2\pi \sum_{i}^{N} a_s(k_i) \boldsymbol{\Upsilon}^{\mathbf{11}}_{\mathbf{qi}} \boldsymbol{\Upsilon}^{\mathbf{11}}_{\mathbf{ip}} \right] \Omega_p = E_q(R) \sum_{p}^{N} \boldsymbol{\Upsilon}^{\mathbf{11}}_{\mathbf{qp}} \Omega_p. \tag{4.22}$$

In the special case of equal R_i emphasized here, this equation may be dramatically simplified to a regular eigenvalue equation, since $a_s(k)$ may be factored out of the sum. Defining a new vector, $v_q = \sum_{p}^{N} \boldsymbol{\Upsilon}^{\mathbf{11}}_{\mathbf{qp}} \Omega_p$, this expression becomes

$$2\pi a_s(k) \sum_{i}^{N} \boldsymbol{\Upsilon}^{\mathbf{11}}_{\mathbf{iq}} v_i = E_q(R) v_q.$$

Applying the symmetric property of $\boldsymbol{\Upsilon}^{\mathbf{11}}_{\mathbf{iq}}$, changing the dummy indices around, and returning to the Ω_q notation for the eigenvectors, we obtain

$$\sum_{q=1}^{N} a_s(k)\boldsymbol{\Upsilon}^{\mathbf{11}}_{\mathbf{pq}} - \frac{E}{2\pi}\boldsymbol{\delta}_{\mathbf{pq}} \quad \Omega^1_q = 0. \tag{4.23}$$

The p-wave interaction is included analogously to the diatomic case, yielding a generalized eigenvalue problem with a $4N \times 4N$ matrix:

$$\sum_{\beta=1}^{4}\sum_{p,q=1}^{N}\sum_{\xi=1}^{4}\sum_{i=1}^{N} a_\xi(k)\boldsymbol{\Upsilon}^{\boldsymbol{\alpha\xi}}_{\mathbf{pi}}\boldsymbol{\Upsilon}^{\boldsymbol{\xi\beta}}_{\mathbf{iq}} - \frac{E}{2\pi}\boldsymbol{\Upsilon}^{\boldsymbol{\alpha\beta}}_{\mathbf{pq}} \quad \Omega^\beta_q = 0. \tag{4.24}$$

Equations (4.20-4.24) accurately reproduce the full diagonalization results for arbitrary molecular configurations and numbers of atoms, particularly for the trilobite states. Since these results are only valid within first order degenerate perturbation theory, they are not expected to be very accurate when couplings to other hydrogenic manifolds or other angular momentum states are important. Indeed, the equations given above for low-l states should only be used qualitatively; for $n = 30$ the $l = 0$ states with three total manifolds are about 20% deeper than the first-order equations predict. In contrast, the high-l trilobite PECs of Eq. 4.24 are quite accurate. Since only one manifold is included, the deep butterfly wells caused by the p-wave shape resonance are qualitatively incorrect. For investigations in regimes, such as at energies relevant to exciting the trilobite state, where these inaccuracies are irrelevant, equation (4.24) is a valuable computational advance. This is particularly true for experiments probing high Rydberg states up to $n \sim 110$ [169, 174] due to the greatly reduced basis size. These restrictions and inaccuracies are greatly eliminated following the new extensions presented in Section 4.5.

The off-diagonal elements of $\boldsymbol{\Upsilon}^{\boldsymbol{\alpha\beta}}_{\mathbf{pq}}$, corresponding to the overlap between orbitals associated with different Rydberg-neutral pairs, determine the size of the differences

between the polyatomic states and the $N = 1$ diatomic state. In the absence of these overlaps equation (4.24) is diagonal in the lower indices and all N polyatomic PECs converge to the diatomic PEC. At large R the overlap between orbitals vanishes, and the PECs are seen to converge to the diatomic limit. Co-planar molecules typically exhibit larger splittings than three-dimensional molecules for this same reason. Additionally, as N grows the system will deviate more strongly from the $N = 1$ case; this causes the global minimum of the PECs to deepen with N. The angular dependence of the trilobite wave functions contributes considerably to the energy landscape of the system at hand, especially when two ground state atoms are close in proximity and therefore have a large overlap. More stable Rydberg molecules can thus be engineered by exploiting these features. Recent theoretical work has studied an extreme case with very large N and also much higher n values than considered here, such that hundreds of perturbers lie, configured randomly, within the Rydberg orbit. A counterintuitive scenario somewhat similar to the "birthday paradox" is seen to occur where one finds as N and n increase that two or more perturbers are *highly* likely to be found in a cluster. This gives rise to an increasingly localized trilobite state of much deeper energy and with an even larger dipole moment, since the electronic wave function can easily encompass these perturbers [178].

4.2 Symmetry adapted orbitals

To fully understand the structure of these PECs, in particular the appearance of degeneracies and level crossings in highly symmetric molecular geometries and the effects of the molecular symmetry on the coupling between trilobite and butterfly states, it is mandatory to characterize the symmetry group of the molecule. The molecular symmetry group is a subgroup of the complete nuclear permutation inver-

sion group of the molecule [52,53], which commutes with the molecular Hamiltonian in free space. Therefore, the eigenstates of such a Hamiltonian can be classified in terms of the irreducible representations (irreps) of the given molecular symmetry group, called *symmetry-adapted orbitals* (SAOs). Given a molecular symmetry group, it is possible to calculate the SAOs associated with each irrep of the group using the projection operator method, where the projection operator is [52]

$$\hat{\mathcal{P}}^j = \frac{l_j}{h} \sum_{i=1}^{h} \chi_{ji} \mathcal{R}_i. \tag{4.25}$$

The index j labels the different irreps and i denotes the group elements. These are the familiar symmetry operations: rotations, reflections, and inversions. $\mathcal{R}_i$ represents the operator associated with the i^{th} symmetry operation; l_j and χ_{ji} represent the dimension and character for the i^{th} operation, respectively. Finally, h stands for the order of the group. The traces of the projection operators, $\text{Tr}\hat{\mathcal{P}}^j = l_j$, determine the decomposition of the point group into irreps. All irreps with $l_j = 0$ are contained. SAOs associated with different irreps have different parity under the molecular symmetry group, and hence will exhibit real crossings. l_j determines the degeneracy of each irrep. The projection operator also gives the coefficients $\mathcal{A}_p^{(\alpha,j)}$ for the SAO $\mathcal{G}^{(\alpha,j)}(r)$ corresponding to the α^{th} orbital and j^{th} irrep:

$$\mathcal{G}^{(\alpha,j)}(r) = \sum_{p=1}^{N} \boldsymbol{\Upsilon}^{\mathbf{1\alpha}}_{\mathbf{rp}} \mathcal{A}_p^{(\alpha,j)}. \tag{4.26}$$

The prescription for calculating the projection operator depends on the orbital in question. The $^3\Sigma$ trilobite and R-butterfly states can be symmetry-adapted independently since they are non-degenerate. Since these orbitals are symmetric about the Rydberg-neutral internuclear axis the symmetry operations leave the orbitals unchanged except for an overall transformation of the atomic positions within the

molecule, i.e. a permutation of the basis of Rydberg-neutral pairs at different positions ψ_p: $\Psi = (\psi_A, \psi_B, ..., \psi_N)^T$. The $N \times N$ matrix representations of the symmetry operations can then be identified with a modicum of effort and the sum in equation (4.25) performed. The orthogonalized rows of $\hat{\mathcal{P}}^j$ provide the coefficients $\mathcal{A}_p^{(\alpha,j)}$ of the diatomic orbitals.

Since the θ and φ butterfly $^3\Pi$ states are degenerate, these orbitals can be mixed by symmetry operations, so these orbitals must be symmetry-adapted simultaneously. The basis size is doubled to allow mixing:

$$\Psi = (\psi_A^\theta, \psi_B^\theta, ..., \psi_N^\theta, \psi_A^\varphi, \psi_B^\varphi, ..., \psi_N^\varphi)^T. \tag{4.27}$$

The effect of a symmetry operation on the entire molecule transforms orbitals located at one Rydberg-neutral pair to another as in the trilobite/R-butterfly case: $\psi_i^\theta \rightarrow \psi_i^\theta$ and $\psi_i^\varphi \rightarrow \psi_i^\varphi$. However, the symmetry operation now modifies the orbitals themselves. The angular butterfly orbitals are vectors in Cartesian coordinates (see equations (4.13-4.14)) and the symmetry operators in the xyz coordinate basis affect them. This transforms $\psi_i^\theta \rightarrow \alpha\psi_i^\theta + \beta\psi_i^\varphi$ and $\psi_i^\varphi \rightarrow \gamma\psi_i^\theta + \delta\psi_i^\varphi$; the coefficients $\alpha, \beta, \gamma, \delta$ must then be solved to identify the matrix representation of that symmetry operation. An explicit example of this process is shown in appendix A; the final result is the full tabulation of the irreps corresponding to each orbital and the sets of coefficients $\mathcal{A}_p^{(\alpha,j)}$ providing the correct SAOs. These coefficients are listed in appendix A for the molecular symmetries exemplified in figure (4.2).

The trilobite and R-butterfly orbitals always belong to the same irreps as they have identical decompositions, while the angular butterflies have different decompositions that may still share some irreps with the trilobite. As a result each of these possible cases requires a slightly different calculation: the PECs are solutions to a generalized eigenvalue problem for a matrix of 1×1 to 3×3 dimension. These expres-

sions are listed below, starting first with the trilobite PECs to allow for comparison with previous work.

Trilobite: The trilobite PEC for the j^{th} irrep satisfies the particularly elegant expression

$$E^{(j)} = 2\pi a_s(k) \sum_{p,q=1}^{N} \mathcal{A}_p^{(1,j)} \boldsymbol{\Upsilon}^{\mathbf{11}}_{\mathbf{pq}} \mathcal{A}_q^{(1,j)}. \tag{4.28}$$

This equation exactly reproduces the results calculated more laboriously in [175]. In the following equations the explicit dependence j is dropped for brevity.

Trilobite and R-butterfly: These PECs are given by the generalized eigenvalues of the 2×2 matrix equation

$$\sum_{\beta=a}^{b} \sum_{p,q=1}^{N} \mathcal{A}_p^{\alpha} \mathcal{A}_q^{\beta} \sum_{i=1}^{N} \sum_{\xi=a}^{b} a_\xi(k) \boldsymbol{\Upsilon}^{\boldsymbol{\alpha\xi}}_{\mathbf{pi}} \boldsymbol{\Upsilon}^{\boldsymbol{\xi\beta}}_{\mathbf{iq}} - \frac{E}{2\pi} \boldsymbol{\Upsilon}^{\alpha\beta}_{\mathbf{pq}} \quad \Omega^{(\beta)} = 0; \; a = 1, b = 2. \tag{4.29}$$

Angular butterflies: The angular butterfly PEC is the solution E to equation (4.29) after setting $a = 3$, $b = 4$ and summing over α from a to b. This is needed since the θ and φ butterflies cannot (in three-dimensional geometries in particular) be considered separate orbitals, but instead form a combined $2N$ dimensional basis. In two dimensions where these orbitals are decoupled this formula still applies, since now each $2N$ length set of coefficients will have 8 vanishing coefficients for the decoupled states.

All orbitals: When all orbitals correspond to the same irrep, the PECs are eigenvalues of a 3×3 generalized eigenvalue problem

$$\sum_{\beta=1}^{3} \sum_{p,q=1}^{N} \sum_{i=1}^{N} \sum_{\xi=1}^{4} a_\xi(k) \underline{\boldsymbol{\Upsilon}^{\boldsymbol{\alpha\xi}}_{\mathbf{pi}}} \boldsymbol{\Upsilon}^{\boldsymbol{\xi\beta}}_{\mathbf{iq}} - \frac{E}{2\pi} \boldsymbol{\Psi}^{\boldsymbol{\alpha\beta}}_{\mathbf{pq}} \quad \Omega^{(\beta)} = 0, \tag{4.30}$$

where the following terms have been defined to incorporate the need for simultaneous symmetry adaptation of the θ and φ butterflies by adding the symmetry-adapted φ-butterfly ($\alpha, \beta = 4$) orbital to the symmetry-adapted θ-butterfly ($\alpha, \beta = 3$) orbital.

$$\underline{\boldsymbol{\Upsilon}^{\boldsymbol{\alpha\beta}}_{\mathbf{qp}}} = \boldsymbol{\Upsilon}^{\boldsymbol{\alpha\beta}}_{\mathbf{qp}}\mathcal{A}^{(j,\alpha)}_{q} + \delta_{\beta 3}\boldsymbol{\Upsilon}^{\boldsymbol{4\alpha}}_{\mathbf{qp}}\mathcal{A}^{(j,4)}_{q} \quad ; \tag{4.31}$$

$$\boldsymbol{\Upsilon}^{\boldsymbol{\alpha\beta}}_{\mathbf{qp}} = \boldsymbol{\Upsilon}^{\boldsymbol{\alpha\beta}}_{\mathbf{qp}}\mathcal{A}^{(j,\alpha)}_{q} + \delta_{\alpha 3}\boldsymbol{\Upsilon}^{\boldsymbol{4\beta}}_{\mathbf{qp}}\mathcal{A}^{(j,4)}_{q} \tag{4.32}$$

$$\begin{aligned}\boldsymbol{\Psi}^{\boldsymbol{\alpha\beta}}_{\mathbf{pq}} &= \mathcal{A}^{(j,\alpha)}_{p}\boldsymbol{\Upsilon}^{\boldsymbol{\alpha\beta}}_{\mathbf{pq}}\mathcal{A}^{(j,\beta)}_{q} + \delta_{\beta 3}\mathcal{A}^{(j,\alpha)}_{p}\boldsymbol{\Upsilon}^{\boldsymbol{\alpha 4}}_{\mathbf{pq}}\mathcal{A}^{(j,4)}_{q} \\ &\quad + \delta_{\alpha 3}\mathcal{A}^{(j,4)}_{p}\boldsymbol{\Upsilon}^{\boldsymbol{4\beta}}_{\mathbf{pq}}\mathcal{A}^{(j,\beta)}_{q} + \delta_{\alpha 3}\delta_{\beta 3}\mathcal{A}^{(j,4)}_{p}\boldsymbol{\Upsilon}^{\boldsymbol{44}}_{\mathbf{pq}}\mathcal{A}^{(j,4)}_{q},\end{aligned} \tag{4.33}$$

where δ_{mn} is the Kronecker delta. This expression, although somewhat complicated, seems to be the most compact way to account for the enlarged angular butterfly basis compared to the trilobite/R-butterfly sets of coefficients.

The PECs of a co-planar octagonal molecule and a body-centered cubic molecule are presented to demonstrate the accuracy of this general formulation. We begin with the octagonal configuration, which belongs to the molecular symmetry point group C_{8v}, depicted in figure (4.1(a)). The reducible representation $\Gamma_{C_{8v}}$ decomposes into seven total irreps: five for the trilobite, R-butterfly, and θ-butterfly orbitals,

$$\Gamma_{C_{8v}} = A_1 \oplus B_1 \oplus E_1 \oplus E_2 \oplus E_3, \tag{4.34}$$

and five, with two new irreps, for the for the φ-butterfly orbital,

$$\Gamma^{\varphi}_{C_{8v}} = A_2 \oplus B_2 \oplus E_1 \oplus E_2 \oplus E_3. \tag{4.35}$$

The θ-butterfly orbital is completely decoupled from the rest due to its node in the molecular plane; this is a general feature of coplanar molecules. The φ-butterfly has a different decomposition than the others because of its particular symmetry properties, as discussed in previously. In another way of looking at it, the φ-butterfly

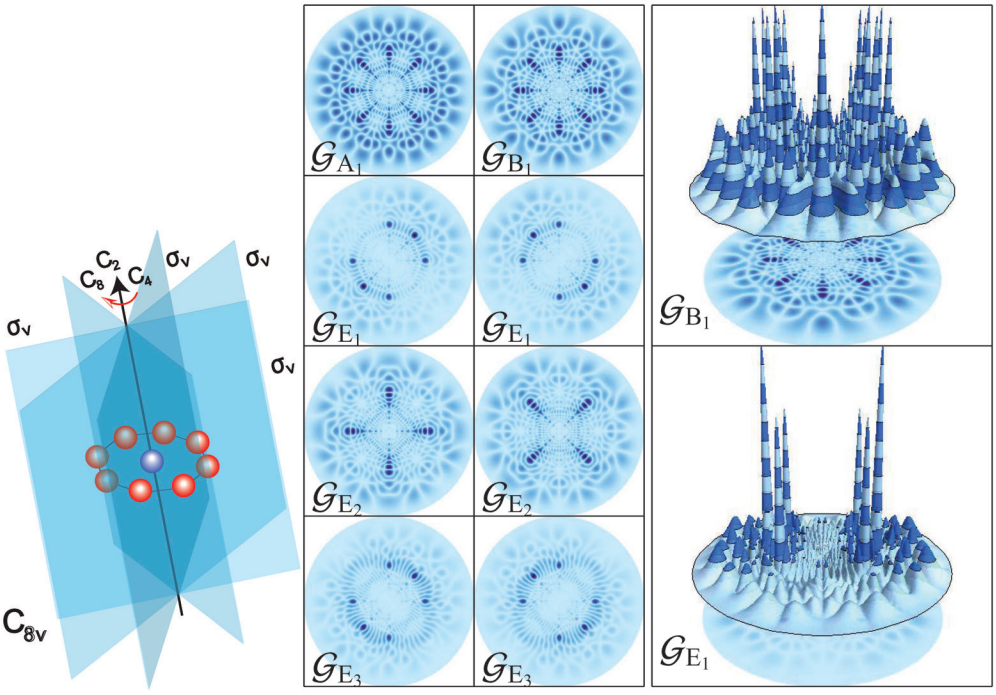

(a) (b) (c)

Figure 4.1. (a) The symmetry operations for C_{8v} symmetry. The σ_d reflection planes bisect the lines between ground state atoms and are not shown for clarity. (b) "Hoodoo" symmetry adapted orbitals for trilobite states of an octagonal molecule with internuclear distance $R = 840\ a_0$. The probability amplitude $\sqrt{r^2|\psi(x,y,0)|^2}$ is plotted in the xy plane. (c) The electron probability corresponding to the one-dimensional irrep B_1 (top) and one of the doubly-degenerate E_1 irreps (bottom) are plotted. This figure is taken from Ref. [4].

belongs to the D_{8v} group instead of C_{8v} due to its inherently three-dimensional nature. It is therefore decoupled for the one-dimensional symmetries but couples with the trilobite and R-butterfly orbitals for the doubly-degenerate symmetries, resulting in avoided crossings between these PECs.

Symmetry adapted orbitals for the trilobite PECs are displayed in figures (4.1(b)) and (4.1(c)). The internuclear distance is $R = 840\ a_0$, the location of the deepest potential well in figure (4.2(a)). These "hoodoo" states, nicknamed for their resemblance to the geological formations commonly found in the American Southwest, explicitly exhibit the allowed symmetries. The beautiful nodal patterns in these curves are the result of interference between trilobite orbitals, which is a clear signature of deviations from the $N = 1$ PEC.

The exemplary three-dimensional molecule here is a body-centered cubic, which has the highly symmetric point group O_h which decomposes into eight total irreps:

$$\Gamma_{O_h}^{\text{trilobite}} = A_{1g} \oplus A_{2u} \oplus F_{2u} \oplus F_{1g} \tag{4.36}$$

for the trilobite and R-butterfly, and

$$\Gamma_{O_h}^{\text{butterflies}} = E_1 \oplus E_2 \oplus F_{1g} \oplus F_{1u} \oplus F_{2g} \oplus F_{2u} \tag{4.37}$$

for the angular butterflies. The symmetric cubic wave function is shown at the start of the chapter in figure (3.10). The full breathing mode adiabatic potential energy curves, plotted as a function of the common ion-neutral spacing R, for both of these geometries are shown in figure (4.2). In panel (a) the neutral atoms (red spheres in the inset) are restricted to a plane and placed in an octagon; in (b) they are placed in a cube. The exact full diagonalization (black lines) and symmetry-adapted orbital calculation from equations (4.29-4.30) (colored points) are compared. The dispersion between different irreps is clearly observed, as has been previously predicted for smaller systems. [175]. Disagreements between the analytic and full diagonalization methods are apparent for energies between the f state, with its small but non-zero quantum defect, and the hydrogenic manifold; however, for larger detunings the agreement is excellent.

When the neutral atoms are displaced slightly the degeneracy imposed by the O_h group is broken, as shown in figure (4.2(c)) and similarly in figure (4.2(d)) for randomly placed atoms on a sphere. Only the trilobite state is shown for clarity. In addition to the destruction of the degeneracy and the appearance of avoided crossings, the huge splitting between orbitals of different symmetry seen at $500 \leq R \leq 1000$ is reduced.

4.3 Results and Discussion

These molecules that are not configured symmetrically can still be studied via equation (4.24), and the contrasts between these results and those of highly symmetric configurations are of substantial interest. As an example, the hybridized trilobite orbitals for a co-planar, randomly structured geometry at two Rydberg-neutral internuclear distances are displayed in figure (4.3). The orbitals at the smaller internuclear distance show substantial interference patterns. Interestingly, for each PEC the electron probability tends to be localized on a subset of the neutral atoms. This subset varies between PECs and is especially clear at the larger internuclear distance displayed in (4.3b). A possible explanation stems from semi-classical periodic orbit theory, since the trilobite state $\mathbf{\Upsilon^{11}_{Rr}}$ forms due to interference between the four semi-classical elliptical trajectories focused on the Rydberg core and intersecting at both the neutral atom and at the observation point r [136]. Since an ellipse focused on the Rydberg core can lie on at most two neutral atoms, this mechanism is a plausible explanation for why these hybridized orbitals tend to be most localized on two neutral atoms. This phenomenon is not seen in highly symmetric molecules, like the octagon of figure (4.2), since the atoms bound by the Rydberg orbit are here determined by the irrep. This could also be a signature of quantum scarring [178]. An additional

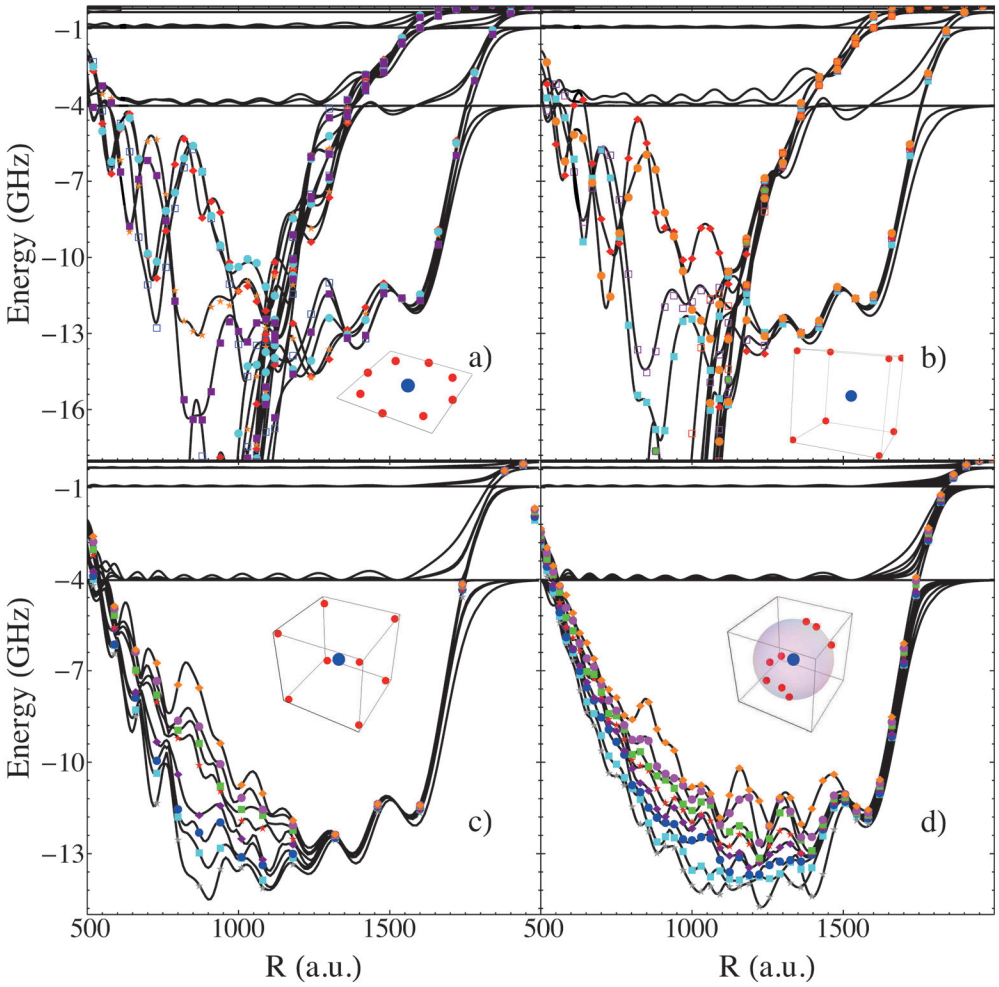

Figure 4.2. Trilobite potential energy curves for several geometries (see text for details). This figure is taken from Ref. [4].

feature of these unstructured molecules is that deepest/shallowest well partners, i.e. I and VIII, II and VII, etc. are localized on the same atoms but possess different parity with respect to reflection through the xy plane.

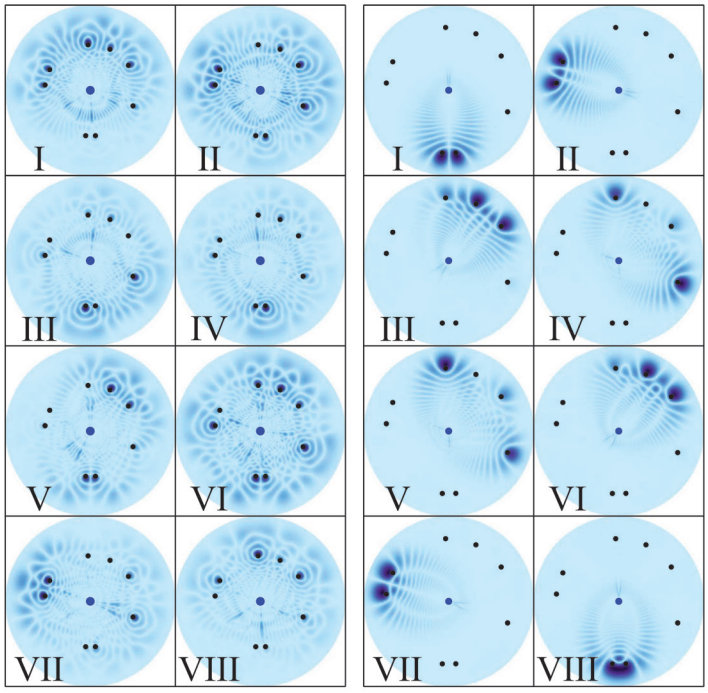

(a) (b)

Figure 4.3. (a) Hybridized trilobite orbitals for a randomly oriented molecular configuration. The Rydberg atom is located at the blue point in the middle of each panel and the neutral atoms are placed at the black points. The common distance R is 1115 a_0 at a local minimum in the lowest energy potential curve. The eigenstates depicted here correspond to potential energy curves that increase in energy from left to right, top to bottom. (b) The same as (a), but in the furthest well from the Rydberg atom at $R = 1537\ a_0$. This figure is taken from Ref. [4].

Most experimental probes of these exotic molecules thus far have focused on low-l states. It is increasingly evident [153, 169, 174] that trimers, tetramers, and even pentamers are routinely formed in these experiments, and the results studied

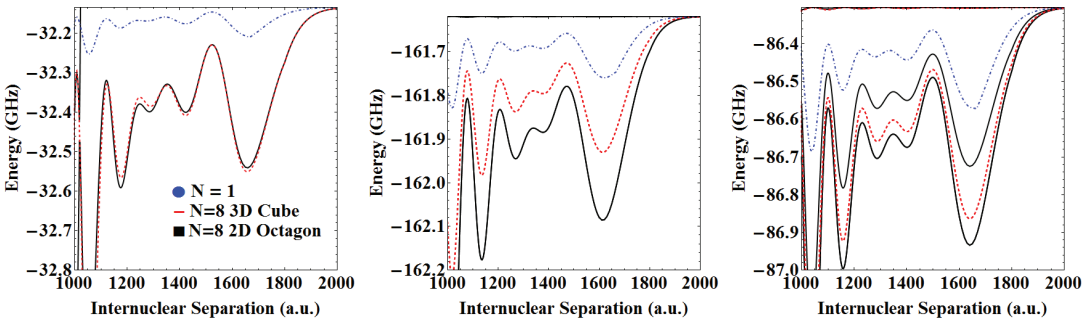

(a) (b) (c)

Figure 4.4. (a) $l = 0$, (b) $l = 1$, and (c) $l = 2$ low angular momentum potential energy curves for $N = 1$ (blue curve) and $N = 8$, arranged in both a coplanar octagonal geometry (black curves) and a cubic geometry (red curves). This figure is taken from Ref. [4].

here may be relevant in explaining the non-Lorentzian line-shapes of these spectra. Although a full application of these methods to the line-shape would require investigation of the full potential energy surfaces beyond the breathing mode cuts, some conclusions can be made. The $l = 0$ results shown in figure (4.4a) are nearly independent of geometry due to the isotropy of the unperturbed state, and their depths scale linearly with N. According to the first order theory in equation (4.20) the well depth for an N-atomic molecule is exactly N times the diatomic depth, but due to the couplings with higher-l states the depth of the largest well scales as $0.65N$ times the diatomic well depth for the $n = 30$ cases studied here. This scaling holds for arbitrary number of atoms and geometries. As such, the appearance of spectral lines at integer multiples of fundamental diatomic lines signifies the production of polyatomic molecules only for isotropic nS states [153]. In contrast, the $l = 1$ and

$l = 2$ states are more complicated as they depend strongly on N and the molecule's geometry. The spectral signatures of these polyatomic molecules will not be present as individual states, but will instead contribute to line broadening of the diatomic spectrum, and experiments with these states at high densities will need to carefully consider these effects to accurately identify spectral features. Very recent work has shown evidence for this [170]. The crossover into a density shift [153, 173] will be particularly relevant for these states.

General trends with increasing N can be identified even when the neutral ground state atoms are configured randomly. Ignoring p-wave contributions, the lowest PEC for polyatomic molecules with $N = 3$, 8, and 12 atoms placed on the surface of a sphere of radius R are studied via a Monte Carlo simulation of five hundred random geometries. The average and standard deviation of these results are presented in figure (4.5). The ground state potential curve, averaged over many configurations, deepens linearly with N, and therefore with density, and maintains nearly the same average shape as the diatomic potential curve. As described in the last section, nS Rydberg molecules deepen linearly with N as well in accordance with the typical energy shift predicted by Fermi using the pseudopotential. However, this effect is independent of the given configuration of perturbers, whereas in the high-l trilobite case only the results averaged over many configurations exhibits a consistent scaling law; the potential energy curve for a given configuration alone varies considerably with the geometry. As explained in Ref. [178], extremely deep potential curves can be found when two or more perturbers are spatially very close. An additional observation of this approach is that the averaged potential curve given by averaging all perturbed eigenstates is essentially identical to the diatomic trilobite curve; in other words, the trilobite interaction is profoundly non-additive and the presence of

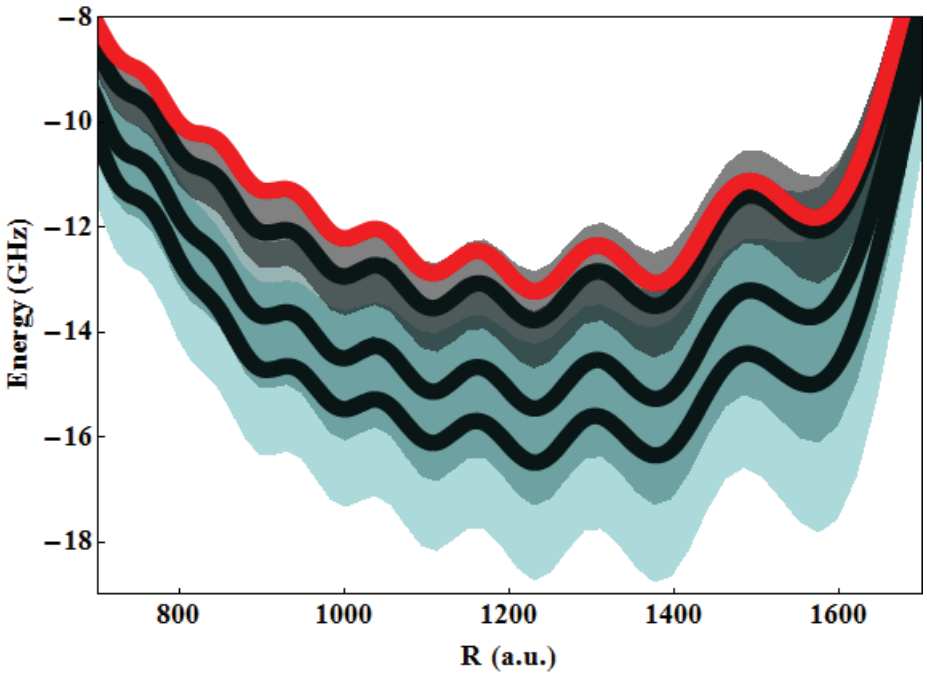

Figure 4.5. Ground state potential energy curves, averaged over five-hundred random configurations, for the diatomic $N = 1$ molecule (red) and polyatomic $N = 3, 8, 12$ molecules (thick black lines; N increases with decreasing detuning). The standard deviations are represented by overlapping color shades to indicate the range of accessible energies. The configuration-averaged shape scales linearly with N from the diatomic case. This figure is taken from Ref. [4].

additional perturbers introduces extra potential curves oscillating about the single-perturber limit.

In this section calculations elucidating the role of symmetry and geometry in the formation of polyatomic Rydberg molecules at high densities have been presented. The methodology developed in the present section applies to any geometrical configuration and to high Rydberg states. These represent a significant advance towards

understanding spectroscopic results in current experiments, and show that the spectroscopic signatures of polyatomic formation in non-isotropic Rydberg states will be challenging to interpret as the results are strongly determined by the molecular geometry and the presence of any symmetries in the atomic orientation.

These exotic molecular states could be realized by merging the current technology in optical lattices with Rydberg spectroscopy techniques. In particular, tilted optical lattices [186] can be used to generate triply occupied Mott-Insulator states; the usual techniques developed in Rydberg spectroscopy will then lead to the controlled formation of Rydberg trimers, although the position of the atoms in each lattice site will still be random. This randomness can be overcome by employing a rotational optical lattice [187], where the centrifugal force can be used to tailor a more controlled geometry. Indeed, by comparing these results with those from trimers formed in a non-rotating lattice, this method can be applied to further study the influence of the geometry. Another possibility is to use current hexagonal and triangular optical lattice technology [188] with lattice spacing on the order of 400 nm in order to have superior control over the geometry of the Rydberg molecules. To form molecules with this internuclear spacing would require higher Rydberg states on the order of $n = 70$, and thus might compromise the spectroscopy of the molecular state; optical lattices with smaller lattice spacings are therefore desirable. Finally, the possibility of optical micro traps [189, 190] has to be taken into account, since these provide opportunities to design very specific arrays of single-atom traps. These traps could be designed to avoid some of the problems caused by the line broadening, and also to emulate the same molecule under very different geometrical considerations.

4.4 Lineshape of a hydrogen Rydberg excitation

To further investigate the effects of multiple perturbers in even denser and completely disordered environments more realistic to experiments, this section explores the spectroscopic line shapes that should be observable for a hydrogen Rydberg atom immersed in a high-density hydrogen background gas. It is based on Ref. [3]. We propose a two-photon excitation scheme from the spin-polarized $1S$ ground state to either of the nS or nD Rydberg states, both of which are allowed by selection rules and energetically degenerate. Two counter-propagating, linearly-polarized beams with $\lambda \approx 181$ nm should be used to ensure that the momentum kick of the photons to the atom will be negligible. Once again we concentrate on triplet spin states because they can be readily explored in a spin-polarized BEC. The s-wave triplet scattering length has the low energy expansion coming from effective range theory [92, 116]:

$$a_s[k(R)] = a_s(0) \quad 1 - \frac{\pi\alpha_d k}{3a_s(0)} - \frac{4\alpha_d}{3}[k(R)]^2 \ln \quad \frac{\sqrt{\alpha_d}k(R)}{4} \quad ^{-1}. \tag{4.38}$$

The semiclassical momentum is $k(R)$ is defined as earlier, and the static polarizability of hydrogen is $\alpha_d = 9/2$. The triplet scattering length at zero energy is $a_s(0) = 1.7686$ a_0 [191]. As the scattering length is positive this is a different regime than studied previously: the potential energy curves are repulsive in nature. An interesting study showed that Borromean trimers can form in a triatomic configuration even with a positive scattering length [177]. This occurs because of the increased depth of the oscillations oscillations in the potential energy curves seen in previous sections. This type of level repulsion leads to repulsive gerade/ungerade-type potential surfaces which nevertheless produce wells, blue-detuned from the atomic line, which could support metastable states prevented from escape into the continuum by a large enough potential barrier. In principle these types of states could occur also in hy-

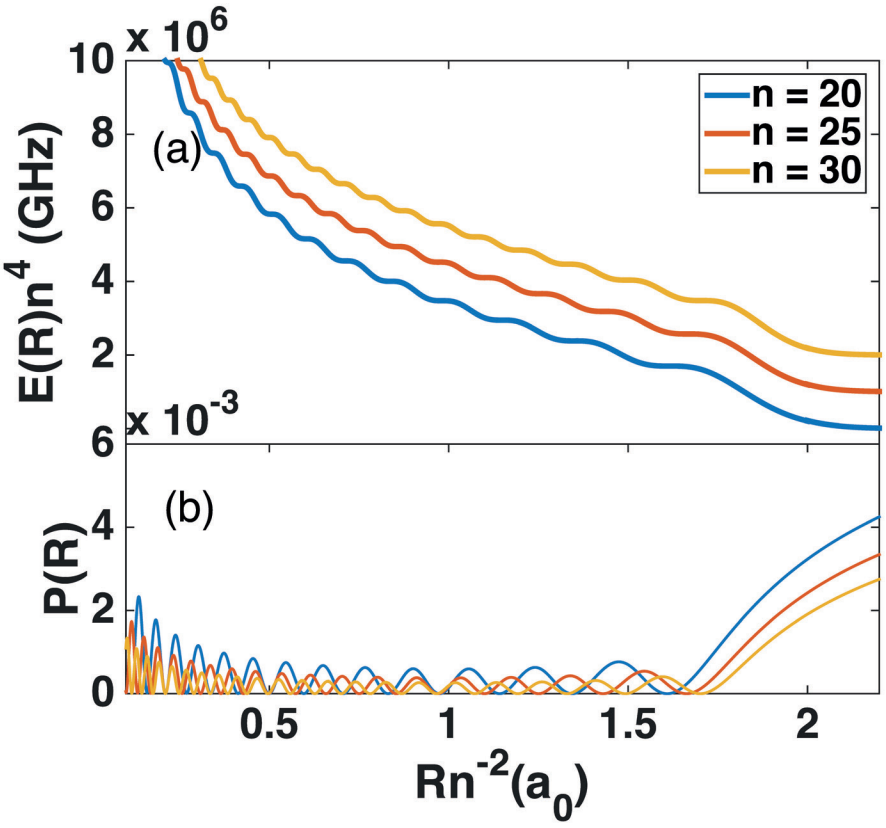

Figure 4.6. Panel (a): diatomic potential energy curves $E(R)$ in GHz for different triplet Rydberg states of hydrogen, $H(n)+H(1s)$, plotted in scaled coordinates and spaced vertically by 10^6 in these scaled units for clarity. The step-like structure of these potentials similarly arises in calculations of singlet $H(n)+H(1s)$ potential energy curves [92]. Panel (b): probability of two-photon excitation $\mathcal{P}(R) = |\langle nD|\Psi_T\rangle P_D^n + \langle nS|\Psi_T\rangle P_S^n|^2$, integrated over angular degrees of freedom as a function of the distance (see text for details) for the same Rydberg states of panel (a). This figure is taken from Ref. [3].

drogen, although the much lighter mass and added complexity in the higher-density regime we study here make this unlikely.

As seen earlier, the energy shift can be obtained in standard degenerate perturbation theory, although this becomes calculationally cumbersome since the number of states scales as n^2. We therefore switch to the trilobite orbital basis again, reducing the dimensionality to at most N, and solve the generalized eigenvalue equation of Eq. 4.22. Each of the N nonzero eigenvalues of this expression defines a $3N$-dimensional potential energy surface; the k^{th}- eigenenergy corresponds to the eigenstate

$$\Psi_k(\{R_i\},\vec{r}) = \frac{1}{\mathcal{N}} \sum_i a_{ik} \boldsymbol{\Upsilon}^{\mathbf{11}}_{\mathbf{ir}}; \tag{4.39}$$

$$\mathcal{N}^2 = \sum_{i,j} a_{ik} a_{jk} \boldsymbol{\Upsilon}^{\mathbf{11}}_{\mathbf{ij}}.$$

For the single-perturber case the sole non-zero eigenenergy is given in closed form by

$$E(R) = 2\pi a_s [k(R)][u_{n0}(R) Y_{00}(\hat{R})]^2 \quad [k(R)]^2 + [Q(R)]^2 \quad , \tag{4.40}$$

where $Q(R) = u_{n0}(R)/u_{n0}(R)$. This is just Eq. 4.16 in a more convenient notation for the current problem. The potential energy curves for a single perturber within the Rydberg orbit are shown in Fig. 4.6a, which shows the oscillatory structure of the potentials. Some of the oscillations exhibit very shallow local minima in $E(R)$ due to the energy dependent nature of the phase-shift, although these are far too weak to support any metastable states.

Potential energy surfaces in hand, we can calculate the excitation lineshape provided the transition amplitude from the ground state is known. As mentioned above, since we have a two-photon excitation scheme in mind the different final states correspond to different routes to the trilobite configuration. These two different transition amplitudes, denoted as P^n_S and P^n_D, respectively, have been calculated using a Sturmian basis set leading to accurate results (within $\sim 10\%$) in comparison with other approaches [192, 193]. We have calculated $P^{20}_S = -0.11$, $P^{20}_D = 0.48$; the ratio of

these values changes by less than 10% for $n = \infty$. We have therefore assumed these values for all n [194]. The trilobite state can be excited via its nS or nD character, depending on the nature of the Rydberg state. When a single perturber is present the probability of excitation, allowing for both pathways and averaged over the relative angle between the internuclear axis and the quantization axis, is:

$$\begin{aligned}\mathcal{P}(R) &= (4\pi)^{-1} \int \mathrm{d}\Omega \, |\langle nD|\Psi_T\rangle P_D^n + \langle nS|\Psi_T\rangle P_S^n|^2 \\ &= \frac{(P_S^n)^2 + \left(\frac{u_{n2}(R)}{u_{n0}(R)} P_D^n\right)^2}{[R^2([k(R)]^2 + [Q(R)]^2)]}. \end{aligned} \tag{4.41}$$

The apparent interference term between nD and nS states, implied by the first line of Eq. 4.41, vanishes when averaged over all space. The probability of excitation as a function of the distance for different Rydberg states are shown in Fig. 4.6b. These show an oscillatory behavior related to the nD and nS hydrogenic wave functions, but tend towards a constant for large perturber-Rydberg distance. For multiple perturbers, the probability to excite the k^{th} eigenstate is given by

$$\begin{aligned}\mathcal{P}^k(\{R_i\}) &= \sum_i \left| a_{ik} \left(P_S^n \langle nS|\Psi(R_i, \vec{r})\rangle + P_D^n \langle nD|\Psi(R_i, \vec{r})\rangle \right) \right|^2 \\ &= \frac{\left| \sum_i a_{ik} \left(P_D^n \psi_{n20}(R_i)) + P_S^n \psi_{n00}(r_i) \right) \right|^2}{\sum_{i,j} a_{ik} a_{jk} \Psi(R_i, R_j)}. \end{aligned} \tag{4.42}$$

The spectroscopy of a single Rydberg hydrogen atom in an ultracold background gas of hydrogen is modeled assuming the quasistatic theory of line broadening [195–198]. In this theory, the absorber (the ground state atom which will become the Rydberg atom) is assumed to be at rest and absorbs photons at $\omega_0 + \Delta\omega$, where ω_0 is the frequency between the two states of the Rydberg atom and $\Delta\omega$ accounts for the shift of the involved levels by the perturbing potential of the neighboring atoms. An additional assumption is that only the perturbers located in a given interacting

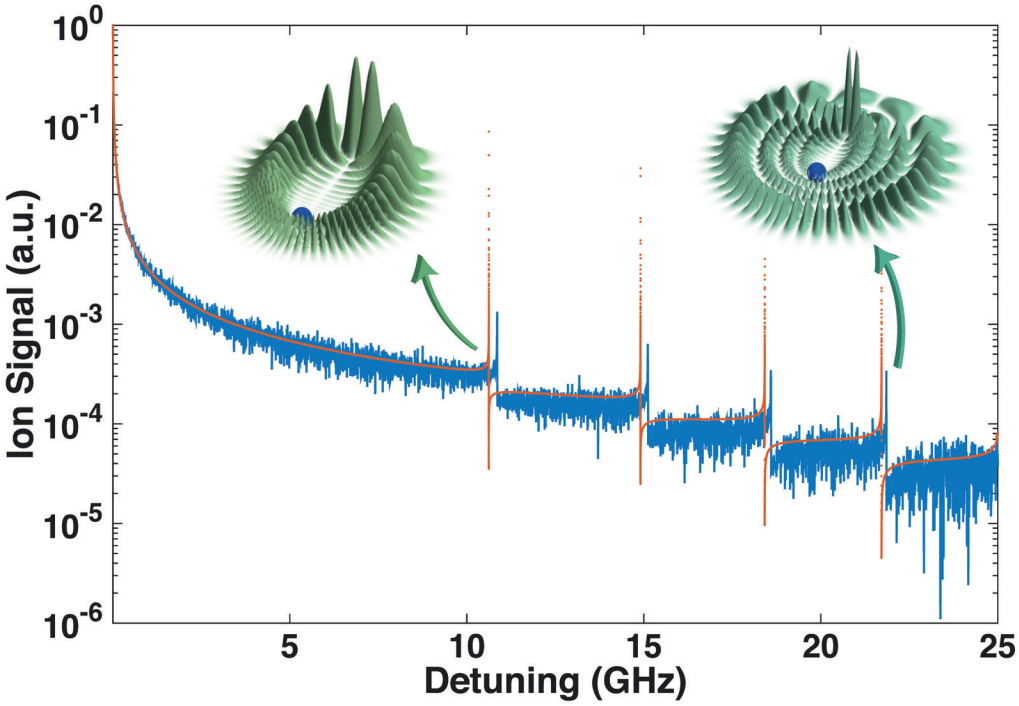

Figure 4.7. Normalized spectra of a single hydrogen Rydberg atom with $n = 20$ in a high density background gas of hydrogen at $\rho = 10^{15}$ cm^{-3}. Only detunings higher than 25 MHz, where the quasistatic approximation is accurate, are shown. The Monte Carlo results for the line shape is depicted by the blue line, whereas the red line represents the line shape assuming a two-body model (Eq. 4.47). Each of the peaks of the spectra correlates with the existence of local extrema in the Rydberg-perturber interaction potential. 5×10^6 Monte Carlo events have been employed in this simulation. This figure is taken from Ref. [3].

region, which in the present case is the volume of the Rydberg atom, V_{Ryd}, will contribute to the line broadening.

The quasistatic picture for the line broadening breaks down when the collision time is close to or less than the inverse detuning, $\tau_c \sim 1/\Delta\omega$ [198,199]. In this regime the Rydberg-perturber collisions give the major contribution to the line broadening. The collision time can be estimated as $\tau_c = b/\ v$, where the impact parameter b is assumed to be of the same order of magnitude as the Rydberg orbit size, *i.e.*, $b \sim 2n^2$. Considering a thermal cloud of hydrogen, in Rydberg levels $20 \lesssim n \lesssim 50$ and at $T \sim 50$ μK, $\tau_c \sim$ 20 - 200 ns. Thus, for a thermal cloud of hydrogen the line shapes in the range $\Delta\omega \gtrsim 25$ MHz can be approximated by by the quasistatic approach.

The simulations of the line profile are performed following the method of Ref. [169]. In a homogeneous gas of density ρ, the probability of finding a certain number of atoms in the volume of the Rydberg atom defines a Poisson distribution with a mean number $N = \rho V_{Ryd}$, where N denotes the average number of perturbers in the Rydberg volume. This Poissonian distribution is employed to sample uniformly the N atoms within the Rydberg volume. For the i^{th} sample of the number of perturbers in the Rydberg orbit, the target Rydberg state experiences an energy shift E_j; each of these energies are then weighted by the probability of the excitation of the given configuration. Finally the line shape is given by the $\mathcal{P}$-weighted distribution of calculated energies in each of the samples, $S(E)$. In the present work the reported spectra are presented in terms of the ion signal since an ionization detection technique is assumed, as is commonly utilized in the field. The spectra are normalized to unity with respect to the highest signal at small detunings.

The spectrum of a single hydrogen Rydberg atom with $n = 20$ in a dense and ultracold gas is shown in Fig.4.7, which prominently displays the existence of certain sharp spectral features following a quasi-periodic pattern in terms of the detuning of the excitation field. This pattern is intimately related with the underlying PEC; in

particular, each of the peaks reflects the existence of a plateau in the potential energy landscape (see Fig.4.6). In each of these regions the Rydberg electron is repeatedly elastically scattered by, primarily, just one of the perturbing atoms, leading to a trilobite-like wave function for the Rydberg-perturber system [40]. At each plateau, as the detuning increases, an angular node is exchanged for an additional radial node such that the total number of nodes remains $n-1$. This reflects the fact that the electronic wave function at each of these plateaus is predominantly characterized by a single elliptical eigenstate [136]. Therefore, the line shape of the Rydberg spectrum directly maps the Rydberg-perturber PEC, leading to a very robust spectroscopic method for observation of this system.

A simple model for the lineshape, assuming that only a single perturber lies in the Rydberg orbit, conveys significant physical intuition about the system's lineshapes and spectral features. This has been shown in the case of long-range forces by Kuhn [196, 197]. This assumption is clearly more accurate for dilute gases or low Rydberg excitations, but is also a valuable limiting case for the many-perturber scenario and qualitatively displays some of the same features. For a given density ρ the probability to find a single perturber between distances R, $R+dR$ from the ion is given by the nearest neighbor distribution,

$$P(R) = \frac{3}{\Delta}\left(\frac{R}{\Delta}\right)^2 e^{-(R/\Delta)^3}, \quad \Delta = (4\pi\rho/3)^{-1/3}. \tag{4.43}$$

This distribution must be additionally modified to include the radial dependence of the radial probability of exciting the trilobite state. Thus the probability distribution is that of Eq. 4.43 multipled by Eq. 4.41:

$$P(R) = \frac{3e^{-(R/\Delta)^3\left[(P_S^n)^2+\left(P_D^n \frac{u_{n2}(R)}{u_{n0}(R)}\right)^2\right]}}{\Delta^3([k(R)]^2+[Q(R)]^2)}. \tag{4.44}$$

The line shape is then given by converting this into a probability distribution with respect to the energy via the relationship $|P[R(E)]\mathrm{d}R| = |P(E)\mathrm{d}E|$. This introduces the derivative of the potential energy, which can be calculated analytically:

$$\begin{aligned}\frac{dE}{dR} &= \frac{dV(R)}{dR} \\ &= -a_s[k(R)] \left[\frac{u_{n0}(R)}{R}\right]^2 + \frac{\frac{da_s[k(R)]}{dR}[u_{n0}(R)]^2}{2} \left[[k(R)]^2 + [Q(R)]^2\right] + \frac{2\alpha_d}{R^5}. \quad (4.45)\end{aligned}$$

Upon inverting the PEC to obtain R as a function of the detuning, denoted $R_E = R(E)$, the line shape for the situation of a single perturbing atom within the Rydberg orbit is given by

$$P(E) = \frac{3e^{-(R_E/\Delta)^3\left[(P_S^n)^2+\left(P_D^n\frac{u_{n2}(R_E)}{u_{n0}(R_E)}\right)^2\right]}}{\Delta^3([k(R_E)]^2 + [Q(R_E)]^2)} \left|\frac{dE}{dR_E}\right|^{-1}. \quad (4.46)$$

This expression compactly separates into two factors. The first, a broad background, is given by the first factor of Eq. 4.47. The second contains the peak structure and is unity for nearly all detunings except at the detunings of the series of sharp doublet peaks, and is given by the second factor of Eq. (4.47):

$$\begin{aligned}P(E) = &\frac{3}{2}\frac{R_E^2 e^{-(R_E/\Delta)^3}}{\Delta^3 E} \quad (4.47)\\ &\times \left(\frac{(P_S^n)^2 + \left|P_D^n\frac{u_{n2}(R_E)}{u_{n0}(R_E)}\right|^2}{1 - \frac{1}{a_s[k(R_E)][u_{n0}(R_E)]^2}\frac{a_s[k(R_E)]}{a_s[k(R_E)]}R_E^2 E + \frac{2\alpha_d}{R_E^3}}\right).\end{aligned}$$

The smooth background given by the first factor can also be obtained by considering the approximate PEC derived by Borodin and Kazansky [127]. The asymptotic limits for small and large detunings of the functional form in Eq. (4.47) establishes the power-law scaling of the lineshapes, previously introduced by Kuhn for the case of van der Waals forces [196, 197]. For small detunings, corresponding to large R, the

potential is very insensitive to R and so the inverse function R_E is nearly constant. The first factor in Eq. 4.47 is therefore proportional to E^{-1}, and the second is unity in this limit. A power law fit to the simulated lineshapes over an energy range from zero to the location of the first peaks gives $E^{-0.86\pm0.01}$, quite independently of density and the Rydberg state. This change in the power law, along with the small constant shift in the location of the doublet peak structure in Fig. 4.7, indicate the expected deviation beyond the single-perturber model.

At large E, corresponding to fairly low R, the radial wave function $[u_{n0}(R)]^2$ increases roughly proportional to $R^{1/2}$; the modulating factor $k^2 + Q^2$ introduces a factor R^{-1} making the leading order dependence of the potential curve for small R (but not so small as for the polarization potential to dominate yet) $E \sim R^{-1/2}$. Inverting then gives $R \sim E^{-2}$, so that $P(E) \sim E^{-5}$. This is a good estimate for the power law behavior in this regime, which numerical fits typically match well with $P(E) \sim E^{-4} - E^{-5}$, for detunings greater than ~ 10 GHz for $n = 30$. This power law behavior is of course only satisfied when the second factor is unity; near the peak regions this term dominates.

An analysis of the components of equation (4.46) explains the locations and shape of these sharp peaks in the spectra. For clarity throughout this discussion, we ignore the energy dependence of the scattering length and the polarization potential, so that $|dE/dR_E|^{-1} = |a_s(0)(u_{n0}(R)/R)^2|^{-1}$. This clearly demonstrates that the peaks in the spectrum stem from the plateaus of the potential energy curve. These are located at the nodes of the s-wave radial wave function. The first factor of Eq. (4.46) also depends on R_E in a complicated fashion, but near the nodes of $u_{n0}(R_E)$ it behaves as $[P_S^n u_{n0}(R_E)]^2 + [P_D^n u_{n2}(R_E)]^2$. If only the S component was excited, the $u_{n0}(R_E)$ factors would cancel and the spectrum would no longer exhibit peaks. However, the nD component is proportional to the ratio $u_{n2}(R_E)/u_{n0}(R_E)$ and thus

vanishes at the node of the d-wave radial wave function very near the peak due to the node of the s-wave radial wave function, leading to the asymmetric profile seen in Figs. (4.7) and (4.8) where a sharp peak is immediately followed by a step-like drop in the line shape. Inclusion of the energy dependence of the scattering length in fact allows the nS character to exhibit peaks since it slightly offsets the location of the inflection points of the potential curve from the location of the s-wave radial nodes, but this effect is mostly overwhelmed by the dominant nD character.

The dependence of the lineshape on density is another fascinating feature of this system. The spectrum of a single Rydberg hydrogen atom with $n = 30$ immersed in a perturbing gas as a function of its density is displayed in Fig.4.8a. $10^6 - 5 \times 10^5$ Monte Carlo events were simulated, with the number of events decreasing as the density increases. The horizontal axis has been scaled by n^4 as in Fig. 4.7 to emphasize the regular spacing of the peaks and the increased number of peaks per unit detuning as n increases. 5×10^6 events were simulated for $n = 20$ and 8×10^5 for $n = 25, 30$. The line shape is found to be independent of the density of the perturbing gas. These results seem to contradict the established line broadening theory which predicts a linear dependence of the line broadening with respect to the density of the perturbing gas [198], since higher numbers of perturbers lead to larger shifts of the excited levels involved in the absorption process. However, the special nature of this system shows that the effect of different perturbers is clearly non-additive, as the last sections demonstrated. In particular, for N perturbers, N eigenenergies split about the single-perturber eigenenergy, and so on average the contributions from higher-energy potential energy curves will be counteracted by contributions from lower-lying curves; as a result the line shape should be independent of the number of perturbing atoms and only depend on the Rydberg state. Indeed, this is numerically corroborated in Fig.4.8b, where the spectrum for a given density and

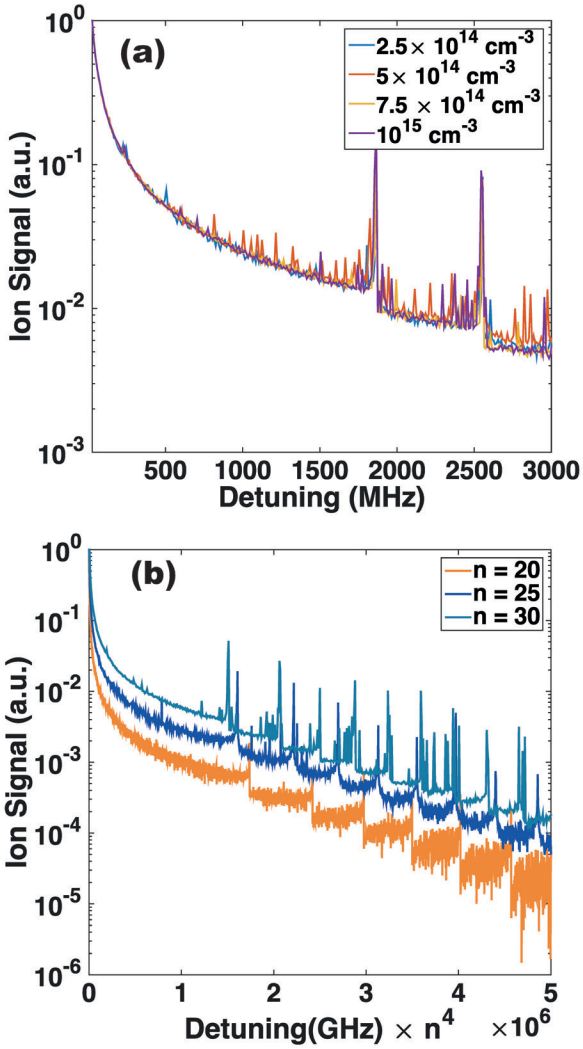

Figure 4.8. Normalized spectra of a single hydrogen Rydberg atom in a thermal gas at ultracold temperatures. The Rydberg spectra for $n = 30$ and different densities is shown in panel (a). The spectrum for $\rho = 10^{15}$ cm^{-3} for different Rydberg states is shown in panel (b). See text for further details. This figure is taken from Ref. [3].

different Rydberg states is shown. These results will no longer apply when the probability of finding at least one perturber within the Rydberg orbit is substantially smaller than one, or else so high that the number of perturbing atoms exceeds the number of states available to construct the trilobite state, n^2. These two limits set the range of applicable densities at $N\rangle\sim\ 0.1 \leq \frac{32\pi n^6}{3}\rho \leq n^2$. Within these limits, this system would be the first, to our knowledge, to exhibit a lineshape independent of the density.

The dependence on n has also been explored: the Rydberg spectrum of a single Rydberg excitation in a dense background gas as a function of the Rydberg state has been calculated within the quasistatic approach of the line broadening and the results are shown in Fig. 4.8b for three Rydberg states at the same density. These lineshapes possess the expected regular series of peaks, and show the same overall behavior as expected based on the potential energy curves, especially in that they exhibit the same regular scaling, n^4, as the potential energy curves.

In this section a generalization of the quasistatic line broadening theory has been applied for the Rydberg excitation spectra of a single Rydberg hydrogen atom immersed in a high-density background hydrogen gas. The simulations not only account for the position and energy shift due to the perturbers, but also the probability of excitation of different atomic configurations by means of the S and D character of the target state. As a result, Rydberg hydrogen atoms immersed in a dense background gas of hydrogen will show a quasi-periodic series of peaks in the line shape correlating with the fundamental nature of the underlying Rydberg-neutral interaction. In particular, the positions of these peaks relate closely to the locations of the plateaus in the potential curves, which depend sensitively on the calculated energy dependent electron-hydrogen scattering lengths. Thus, our findings clearly indicate

the possibility to use direct line shape data to explore the Rydberg-perturber energy landscape.

The calculated spectra clearly show a positive detuning in relation with the repulsive nature of the Rydberg-perturber interaction, as well as a density independent line shape, in stark contrast with the conventional line broadening theory, which predicts a linear density dependence of the line shift and line broadening. These findings have been explained by appealing to the unusual and intriguing properties of the polyatomic trilobite-like states, suggesting a consistent and convincing explanation of the spectra.

Rydberg states are also present in astrophysical spectra, where even $n = 1000$ and higher have been observed [13, 200]. Although these Rydberg states form in very dilute interstellar clouds where the interatomic spacings are very large, trilobite states could form for very high n. The theory developed here could be applied to explain some aspects of the recombination lineshape due to the effect of a nearby neutral atom.

4.5 Generalized trilobite molecular orbital theory

To conclude this chapter we show some recent results demonstrating how the theory described above can be developed further. A major limitation of our approach, in which the trilobite and butterfly-type orbitals hybridize together to form polyatomic molecular orbitals, is that it completely neglected couplings to low-l states as well as to other hydrogenic manifolds. As a result it was most applicable to trilobite states and could only describe the butterfly curves near the trilobite states, and not the much deeper potential wells where butterfly molecules are actually bound. Additionally it could not predict any of the non-perturbative effects on the low-l states caused

by interactions with trilobite-like states. Both of these problems hinder the broad applicability of this approach, although of course the full diagonalization could still be performed. This is computationally expensive even in this simplest possible case as the number of Rydberg states in an arbitrary geometry scales as n^2; if spin degrees of freedom are included in the future this problem becomes even more pronounced.

To remedy these issues, this section shows that in fact this molecular orbital concept generalizes to include these inter-manifold couplings and the effects of quantum defect-shifted states. We show that, by using only this reduced basis set consisting of trilobite and butterfly orbitals associated with each Rydberg-atom pair and as many low-l states as is desired, the calculation remains exact unless additional operators which substantially break the degeneracy of high-l states are added also. Even in these cases, such as when electric or magnetic fields are applied to the system, this approach works surprisingly well.

Our Hamiltonian is still given by Eq. 4.1. Instead of choosing the full basis of Rydberg states, $\{|nlm|\rangle\}$, we select just the trilobite orbitals from several different n manifolds along with the low-l states (up to an arbitrary cutoff l_{min} determined by the quantum defects): $\Upsilon^{\alpha 1}_{pr,n}$, $\phi_{n(l<l_{min}m}(r)$.

Using this basis to diagonalize and solve the generalized eigenvalue equation $\underline{H}\Gamma = E\underline{O}\Gamma$ is just a matter of setting up the overlap elements between different basis states, the matrix elements of the potential V_N, and the matrix elements of H_0. These are readily obtained using the properties of the trilobite overlap matrix.

$$\begin{aligned}
\Upsilon^{\alpha 1}_{pr,n}|H_0|\Upsilon^{\beta 1}_{qr,n} &= \sum_{l,l} \phi^{\alpha}_{nlm}(R_p) \quad \phi^{1}_{nlm}(r)^* \quad -\frac{1}{2n^2} \quad \phi^{1}_{n\,l\,m}(r)\phi^{\beta}_{n\,l\,m}(R_q)^* \mathrm{d}^3 r \\
&= -\frac{1}{2n^2}\delta_{nn} \sum_{l,l} \delta_{ll}\,\delta_{mm}\,\phi^{\beta}_{n\,l\,m}(R_q)^*\phi^{\alpha}_{nlm}(R_p) \\
&= -\frac{1}{2n^2}\Upsilon^{\alpha\beta}_{pq,n}\delta_{nn}\,, \qquad (4.48)
\end{aligned}$$

and

$$\begin{aligned}
\Upsilon^{\alpha 1}_{pr,n}|V_N|\Upsilon^{\beta 1}_{qr,n} &= \sum_{l,l} \phi^{\alpha}_{nlm}(R_p) \quad \phi^{1}_{nlm}(r)^* \\
&\times \quad 2\pi \sum_{i,\xi} a_\xi \nabla^\xi \delta^3(r-R_i)\nabla^\xi \quad \phi^1_{n\ l\ m}(r)\phi^\beta_{n\ l\ m}(R_q)^* \mathrm{d}^3 r \\
&= 2\pi \sum_{i,\xi} a_\xi \sum_{l,l} \phi^{\alpha}_{nlm}(R_p)\phi^{\xi}_{nlm}(R_i)^*\phi^{\xi}_{n\ l\ m}(R_i)\phi^{\beta}_{n\ l\ m}(R_q)^* \\
&= 2\pi \sum_{i,\xi} a_\xi \Upsilon^{\alpha\xi}_{pi,n}\Upsilon^{\xi\beta}_{iq,n}\,. \qquad (4.49)
\end{aligned}$$

The overlap matrix between trilobite states is given by $\Upsilon^{\alpha\beta}_{pq,n}\delta_{nn}$. The matrix elements of the low-l subspace are just those calculated for the full diagonalization:

$$\phi_{nlm}(r)|H_0+V|\phi_{n\ l\ m}(r) = -\frac{1}{2(n-\mu_l)^2}\delta_{nn}\,\delta_{ll} + 2\pi \sum_{\xi,N} a_\xi \phi^{\xi}_{nlm}(R_i)^*\phi^{\xi}_{n\ l\ m}(R_i).$$

Since these states are orthogonal their overlap is $\delta_{nn}\,\delta_{ll}$.

The last matrix elements to compute are those describing coupling between the trilobite/butterfly states and the low-l states:

$$\begin{aligned}
&\Upsilon^{\alpha 1}_{pr,n}|H_0+V_N|\phi^1_{n\ l\ m}(r) \\
&= \sum_{l} \phi^{\alpha}_{nlm}(R_p) \quad \phi^{1}_{nlm}(r)^* \quad -\frac{1}{2n^{\,2}} + 2\pi \sum_{i,\xi} a_\xi \nabla^\xi \delta^3(r-R_i)\nabla^\xi \quad \phi^1_{n\ l\ m}(r)\mathrm{d}^3 r \\
&= 2\pi \sum_{i,\xi} \Upsilon^{\alpha\xi}_{pi,n}\phi_{n\ l\ m}(R_i). \qquad (4.50)
\end{aligned}$$

These states are orthogonal since the trilobite states by definition have no low-l components.

Numerical diagonalization of this matrix yields potential curves that are identical to those calculated via a full expansion into the entire hydrogenic basis. Figs. 4.9 and 4.10 demonstrate this for the cubic molecule example studied earlier, where the

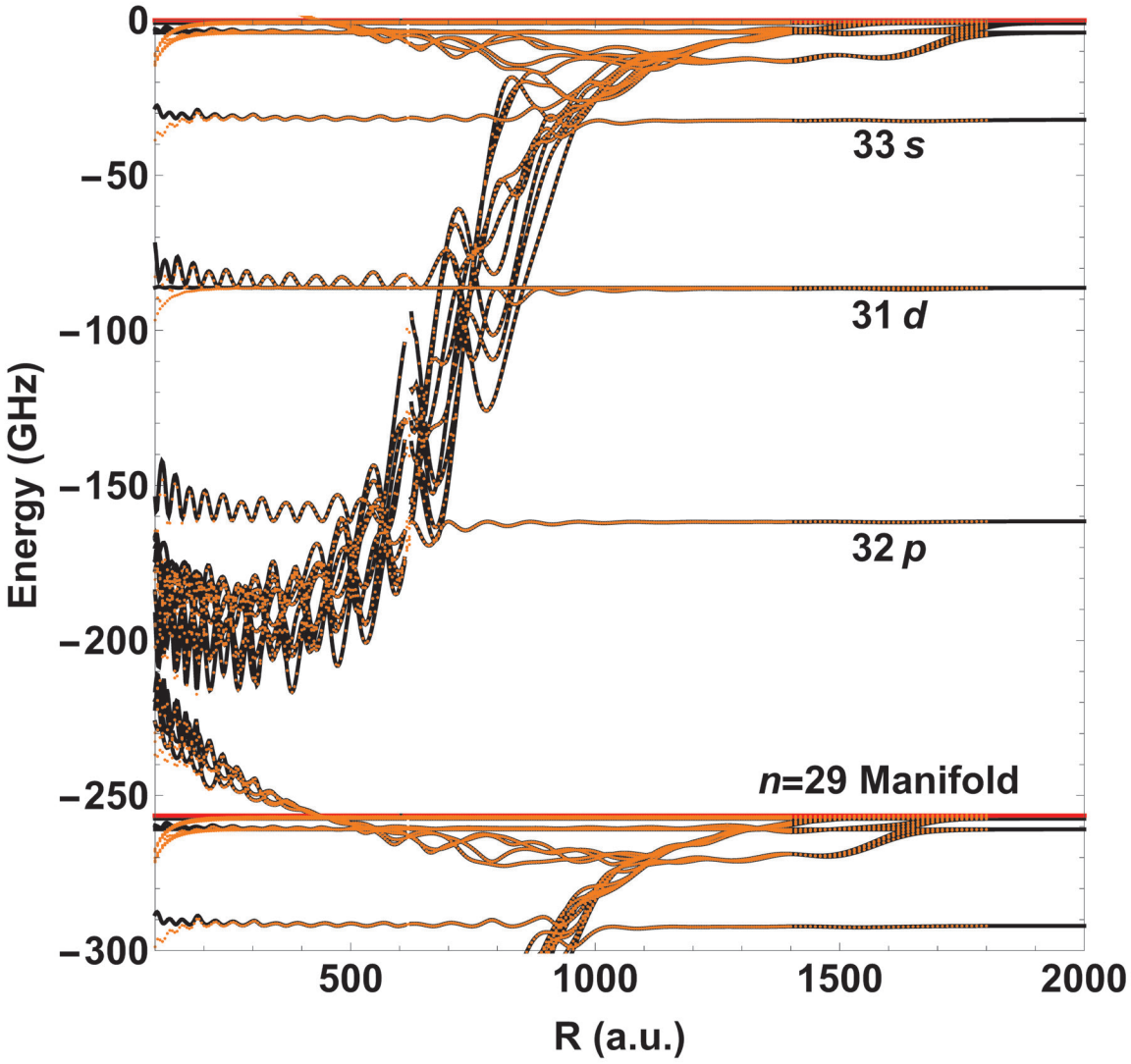

Figure 4.9. The full potential energy landscape of the breathing modes of a cubic molecule with $n = 30$. The black curves shown are the results of a full diagonalization, and the orange dots are the results of this reduced basis calculation.

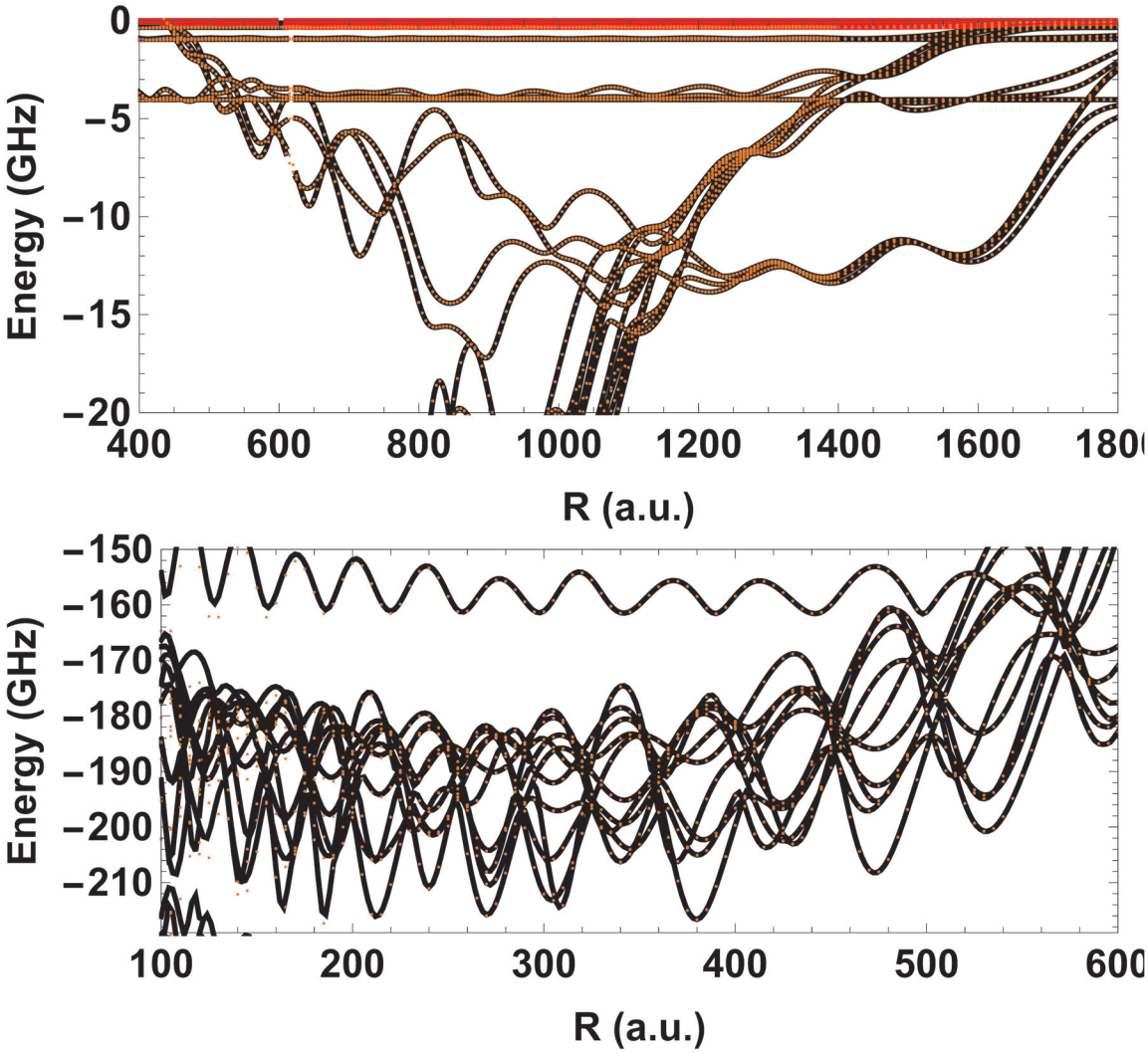

Figure 4.10. The trilobite (top) and butterfly (bottom) potential energy curves of a cubic molecule with $n = 30$. The black curves shown are the results of a full diagonalization, and the orange dots are the results of this reduced basis calculation.

Rydberg state of interest had $n = 30$ and the surrounding manifolds $n = 29$ and 31 were included for convergence. The results agree exactly. For this comparison

$l_{min} = 5$ to include even the f and g states which have very small quantum defects; typically $l_{min} = 3$ is more than sufficient. The total size of the reduced basis was $M \times (4N + (l_{min} + 1)^2) = 204$, where M is the number of manifolds. This is over an order of magnitude smaller than the full basis size, 2702. This approach is clearly less useful for polyatomic molecules with very large N but small n, but in the opposite limit becomes even more useful; for example, for $n = 70$ the basis size for full diagonalization is greater than 10^4, while the reduced matrix size remains unchanged. The utility of using this basis state also increases if spin degrees of freedom are also included, as the dimension increases much more slowly than if every single l state is multiplied by additional spin states. The reasoning behind why this approach works *approximately* relies heavily on the degenerate, effectively rank-4 subspace of the trilobite and butterfly orbitals in each Rydberg manifold, but the reason it is truly an *exact* calculation is still rather nebulous. Appendix B outlines a derivation of the structure of the matrix elements defined here to prove this.

This same logic can also be extended to the influence of electric and magnetic fields on these Rydberg molecule states, which even in the diatomic case requires n^2 matrix elements if the field and internuclear axes are not aligned. Unlike for the field-free case this approach will clearly break down for high field strengths since the high-l eigenstates no longer remain degenerate. We begin with the magnetic field for the trilobite state, choosing the z axis to point in the direction of the magnetic field and neglecting the diamagnetic term, which is proportional to B^2 and has only

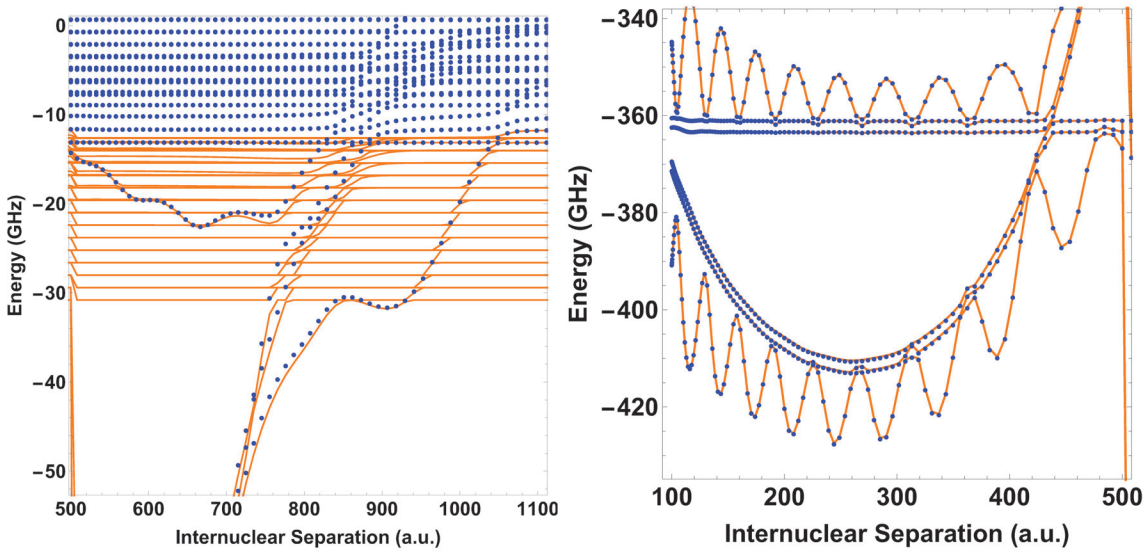

Figure 4.11. A diatomic molecule with $n = 23$ in a large 1000G magnetic field. Left: trilobite region, right: butterfly region. The solid orange lines are calculated using the approximate orbital approach, while the blue dots were obtained in a full diagonalization.

minimal effect on the potentials for typical field strengths. We therefore need to construct matrix elements:

$$\begin{aligned}
\frac{B}{2}\langle \Upsilon^{\alpha 1}_{pr,n}|L_z|\Upsilon^{\beta 1}_{qr,n'}\rangle &= \frac{B}{2}\delta_{nn'}\sum_{lm} m\phi^{\alpha}_{nlm}(R_p)\phi^{\beta}_{nlm}(R_q) \\
\frac{B}{2}\langle \Upsilon^{\alpha 1}_{pr,n}|L_z|\phi_{n'lm}(r)\rangle &= \frac{B}{2}\delta_{nn'}\phi^{\alpha}_{nlm}(R_p)m \\
\frac{B}{2}\langle \phi_{nlm}|L_z|\phi_{n'l'm'}\rangle &= \frac{B}{2}\delta_{nn'}\delta_{ll'}\delta_{mm'}m.
\end{aligned}$$

The approach is very similar for an external electric field F. We put the electric field in the $\hat{z}$ direction, and then calculate the matrix elements:

$$\begin{aligned} \boldsymbol{\Upsilon}^{\boldsymbol{\alpha 1}}_{\mathbf{pr,n}} | Fr\cos\theta | \boldsymbol{\Upsilon}^{\boldsymbol{\beta 1}}_{\mathbf{qr,n}} &= F \sum_{lm \;\; l\,m} \phi^{\beta}_{n\;l\;m}(R_q)^{\;*}\, \phi^{\alpha}_{nlm}(R_p) \\ &\times \int \mathrm{d}^3 r\, r\cos\theta \;\; \phi^{1}_{nlm}(r)^{\;*}\, \phi^{1}_{n\;l\;m}(r). \end{aligned} \tag{4.51}$$

The integral can be evaluated:

$$\begin{aligned} \alpha p, n | Fr\cos\theta | \beta q, n &= F \sum_{lm \;\; n\,l\,m} \phi^{\beta}_{n\;l\;m}(R_q)^{\;*}\, \phi^{\alpha}_{nlm}(R_p) \delta_{mm}\, \delta_{ll\;\pm 1} \\ &\times \sqrt{\frac{(l_< - m + 1)(l_< + m + 1)}{(2l_< + 1)(2l_< + 3)}} R^{n\,l}_{nl}(k=1), \end{aligned} \tag{4.52}$$

where $l_< = \min(l, l\,')$ and $R^{n\,l}_{nl}(k=1) = \int r u_{nl}(r) u_{n\;l}(r) \mathrm{d}r$ (Eq. E.3). The selection rules implied by the delta functions reduces the number of terms in this sum from n^4 to a number of order $3n^2$, so that these sums evaluate quickly using the analytic result for $R^{n\,l}_{nl}(k)$. As expected for these polar states, this term is proportional to nF and gives a linear Stark shift. Finally,

$$\begin{aligned} \boldsymbol{\Upsilon}^{\boldsymbol{\alpha 1}}_{\mathbf{pr,n}} | Fr\cos\theta | \phi_{n\;l\;m}(r) &= F \int \mathrm{d}^3 r \sum_{lm} \phi^{\alpha}_{nlm}(R_p) \;\; \phi^{1}_{nlm}(r)^{\;*}\, \phi^{1}_{n\;l\;m}(r) z \\ &= F \sum_{lm \;\; l\,m} \phi^{\beta}_{nl\;m}(R_q)^{\;*}\, \phi^{\alpha}_{lm}(R_p) \\ &\times \sqrt{\frac{(l_< - m + 1)(l_< + m + 1)}{(2l_< + 1)(2l_< + 3)}} R^{n\,l}_{nl}(k=1). \end{aligned} \tag{4.53}$$

The accuracy of this approach is demonstrated here only for the B-field diatomic case, for the specific configuration where the molecule points in the direction $\theta = 2.55, \phi = 0.4$ relative to the B-field, parallel to the z axis. Fig. 4.11 shows both the trilobite and butterfly regions. In both cases the agreement is excellent, particularly for the butterfly state. The Zeeman splitting of the many high-l states disrupt the

trilobite PECs somewhat, but the agreement is still excellent, particularly since a high $l_{min} = 5$ was chosen. The high magnetic field used for this comparison is also an extreme case, and for weaker fields the agreement improves as well. Numerical calculations for the electric field case have been performed as well in order to compare with the results of Refs. [138, 179], and agree similarly. Future work should consider the effects of combined fields and the impact on polyatomic states as well.

This page intentionally left blank

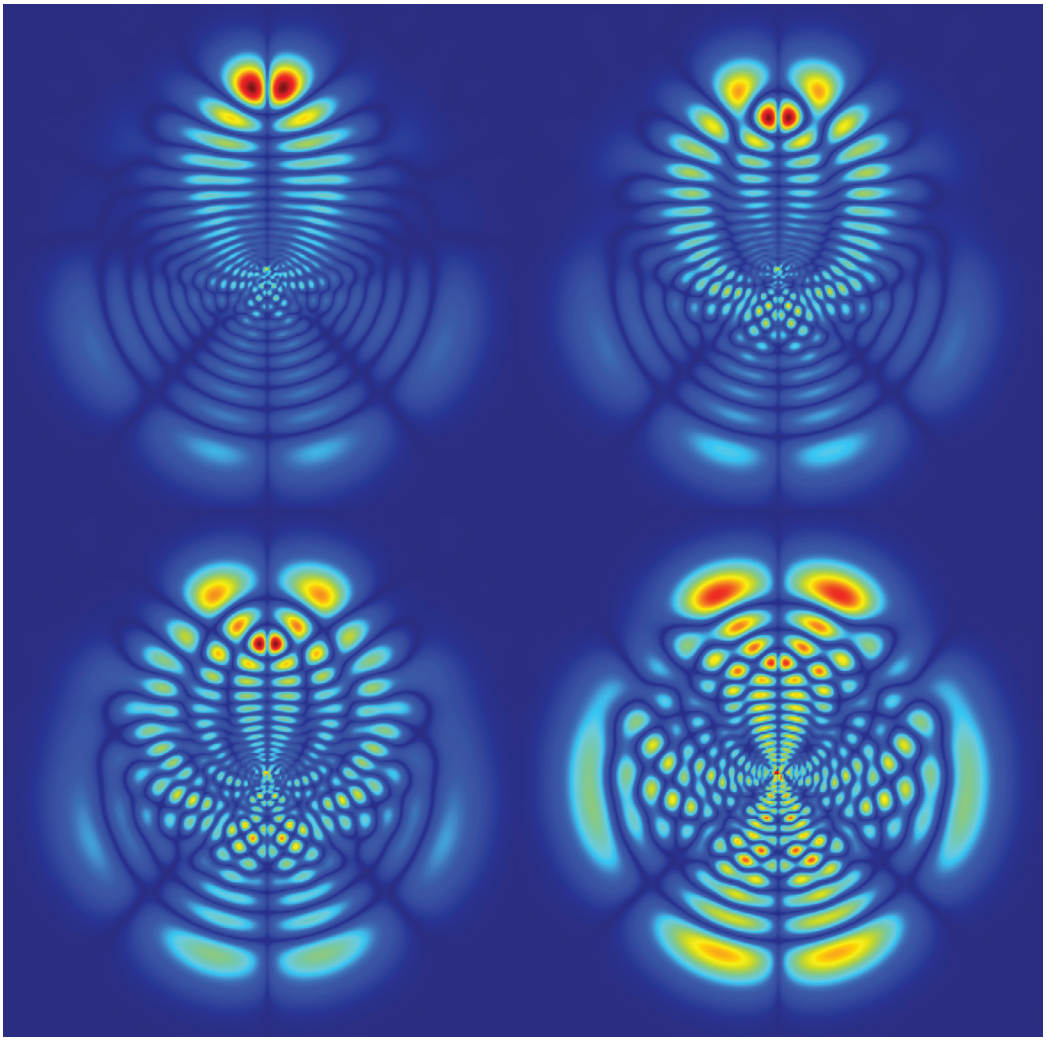

Figure 4.12. Chapter 5 describes Rydberg molecules in non-alkali atoms, such as these calcium trilobites shown as density plots

5. RYDBERG MOLECULES FORMED FROM MULTICHANNEL ATOMS

Thus far this thesis, along with the overwhelming majority of other experimental and theoretical efforts, has focused on alkali atoms. With their regular Rydberg spectra and nearly energy-independent quantum defects, alkali atoms provide a simple and easily-controlled system for the excitation of novel molecular states. However, Rydberg atoms throughout the rest of the periodic table are far richer and more complex, as they consist primarily of perturbed, multichannel Rydberg spectra [10, 12, 15, 16]. This chapter demonstrates some of the opportunities provided by this richer class of multichannel Rydberg atoms. The existence of doubly-excited perturbers, which are states with two excited electrons that couple to and shift the usual Rydberg series of a single excited electron, could be used in the alkaline earth atoms to directly excite long-range trilobite molecules. Another possibility raised by the existence of doubly-excited perturbers is that energy eigenfunctions exist whose multichannel character exhibits two very different length scales. The content of this chapter is primarily based on Ref. [5].

5.1 Calcium: level perturbations due to doubly excited interlopers

The first multichannel states to be considered are the 4snd $^1D_2$ levels in calcium, where perturbations from the doubly excited states 3d4d and 3d5s $^1D_2$ cause the 4snd singlet quantum defect to vary rapidly in the vicinity of these perturbing levels

[17]. Fig. (5.1) depicts the strong n-dependence of the nd quantum defects. We have chosen to study calcium because the d-wave quantum defects fortuitously pass through unity as the principal quantum number n increases between $n \sim 20 \pm 2$; the nd state is therefore highly degenerate with high angular momentum states in the $n-1$ manifold. This accidental degeneracy strongly couples these states together, allowing for direct two-photon excitation of trilobite molecules, circumventing the usual challenges of exciting high angular momentum states [40]. This is similar to the coincidental degeneracy allowing for coupling to the trilobite state in Cs through its ns character [154]

Two characteristics of the phase shifts differentiate this interaction in calcium from those previously studied in the alkalis. Since calcium does not possess a p-wave shape resonance [97, 103], the potential wells due to the interaction given by Eq. (2.91) at all but very small internuclear distances are determined almost entirely by s-wave electron-atom scattering properties. The second contrast is that the p-wave phase shift is negative except at very low energies, so the scattering volume is positive over nearly the entire range of internuclear distances. These two differences eliminate the strongly attractive p-wave interactions leading to "butterfly" type bound states in Rb and Cs [122], and instead the p-wave interaction produces a weakly repulsive potential. A similar effect has recently been studied in Sr Rydberg molecules [125], and it has been seen that this results in more stable long-range molecules [146]. Adiabatic potential energy curves for $18 \leq n \leq 21$ are presented in Fig. (5.2a). As n increases the $(n+1)d$ state sweeps downwards through the n manifold, and for $n = 19, 20$ in particular it is strongly mixed into the trilobite state. This systematic change of quantum defects with energy, caused by familiar level perturbations in multichannel spectroscopy [10], is ubiquitous in the heavier alkaline earth metal atoms and in most other atoms in the periodic table. The states shown here in Ca

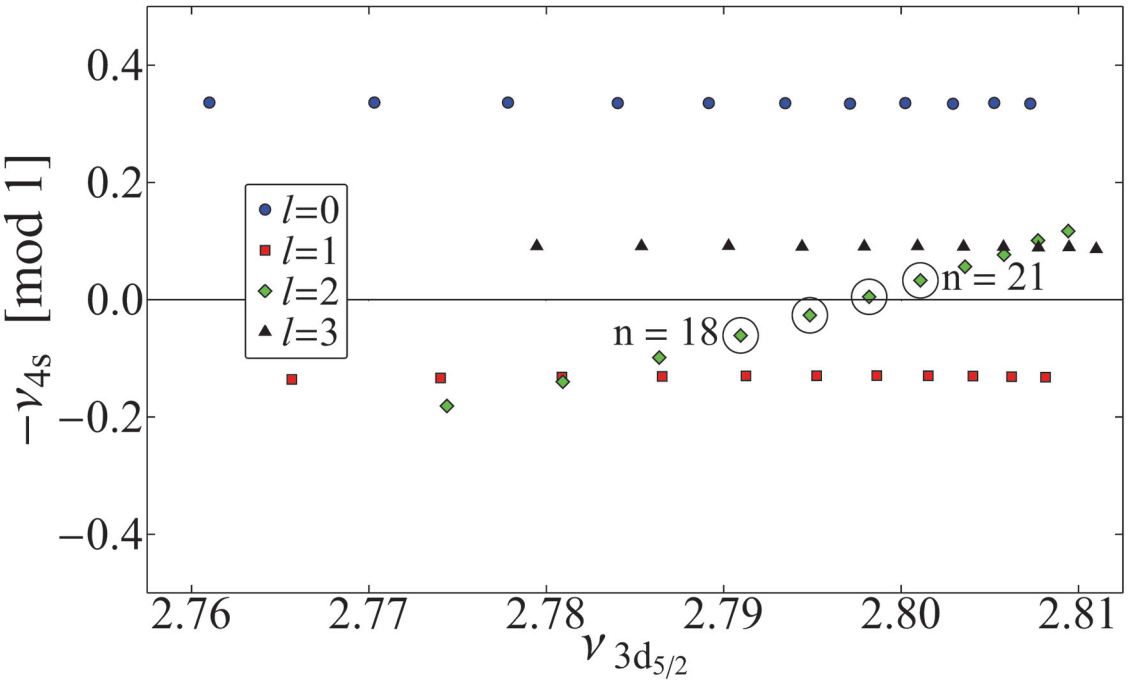

Figure 5.1. A Lu-Fano plot [201] highlighting the effects of level perturbers on the quantum defects of the nd states of Ca [202], in contrast to the energy-independent behavior of the quantum defects for s, p, and f states. The quantum number n rises from 15 to 24 from left to right. This letter investigates the circled states. This figure is taken from Ref. [5].

have a level of mixing intermediate between these low and high l regimes discussed in section 3.1. The expansion coefficients are plotted below the potential energy curves, and show the locations of the trilobite states (large mixing of high angular momentum states) and the amount of $(n+1)d$ mixing in the trilobite state. Fig. (5.2b,c) displays the electronic wave functions, demonstrating the change in character from primarily g and "trilobite" states in $n = 18$, 19 to primarily d and trilobite character in $n = 20$, and a mix of these three major contributions in $n = 21$.

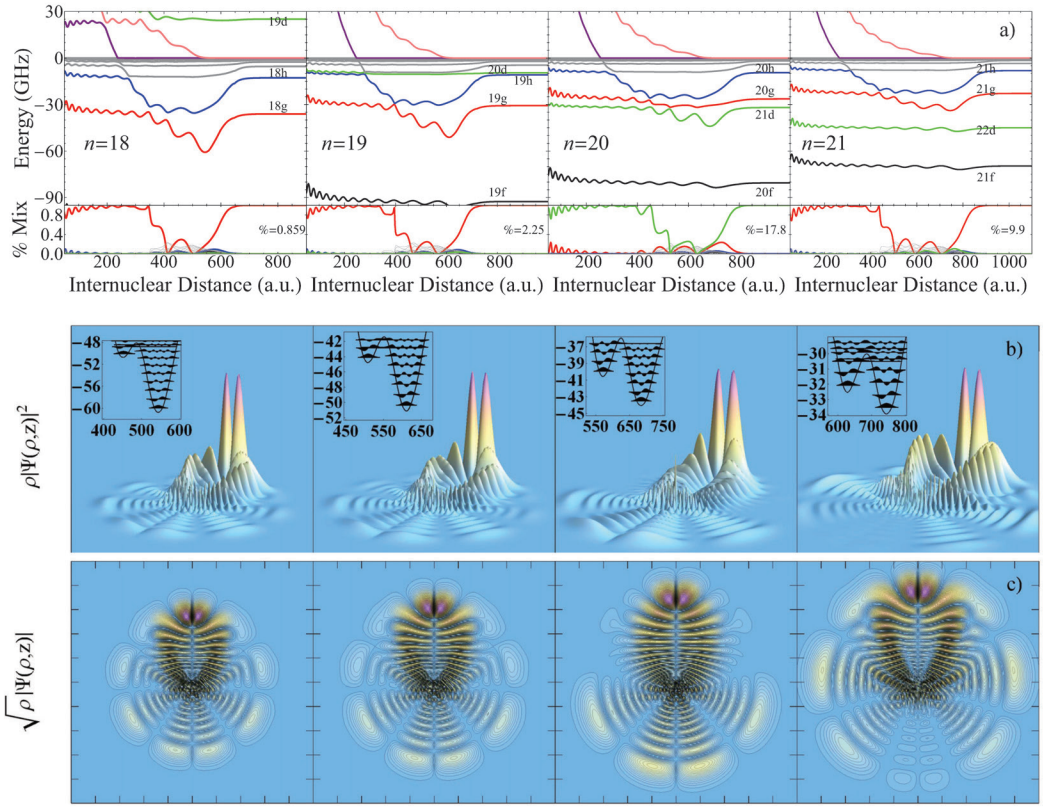

Figure 5.2. a) Potential energy curves for $\Omega = 0$ states, with n increasing from 18-21 from left to right. The energy scale is relative to $-\frac{1}{2n^2}$. The $(n+1)d$ state descends through the degenerate manifold with increasing n. The expansion coefficients are plotted with the same color scheme, and the percentage label gives the percent contribution of the d state in the trilobites plotted in panels b) and c).
b) Electron probability densities $\rho|\Psi(\rho,z)|^2$ in cylindrical coordinates over a region in the $(\rho, z, 0)$ plane spanning $(-1000, 1000)$. These characteristic trilobite-shaped wave functions are in the deepest minimum of the potential wells, shown in the inset along with the lowest vibrational states (in GHz, as a function of internuclear distance).
c) Contour plots of the probability amplitudes. In all panels the abscissa is ρ and runs in steps of 200 a_0 from -1000 to 1000; the ordinant is z and runs over the same range. This figure is taken from Ref. [5].

The molecular vibrational levels seen in the potential well inset are approximately spaced at 1 GHz. Many vibrational bound states are supported in these wells, which range from 30 to 60 GHz deep. These molecules should therefore be somewhat more tightly bound than those predicted for rubidium [40, 95]. The permanent electric dipole moments associated with these molecules are many hundreds of Debye, allowing for the possibility of delicate manipulation of these molecules with electric and magnetic fields [138, 140]. The stability of these states is limited by black body radiation [12], with an estimated lifetime of a few μs. [203]

Other atomic species could exhibit related behavior to that predicted here in calcium. The nS Rydberg molecules studied in Sr have corroborated the behavior of the p-wave phase shifts seen in Ca, but the nS quantum defects in Sr are very regular; so far the multichannel character of strontium has not been studied in these experiments. As in calcium, the Sr nD levels exhibit significant level perturbations. Despite this promising similarity, Sr does not also exhibit the fortuitous energy degeneracies of Ca, limiting the utility of these states for the type of beneficial degeneracy described here. In the past two decades, rare earth metals such as dysprosium, erbium, and ytterbium have become vogue in ultracold atom experiments g [204–206]. Their popularity stems from their often enormous magnetic moments which lead to rich dipolar interactions. They are also marked by immensely complicated internal structure, typically having anisotropic ground state configurations with non-zero angular momentum and myriad hyperfine thresholds. Robicheaux *et al* have recently described the theory of Rydberg states of these atoms through an MQDT approach [207]. One promising state of holmium observed experimentally showed that the Rydberg states near $n = 50$ with S character clearly reveal the influence of a doubly excited perturber, which also causes the quantum defect to pass through zero [208]. Provided the electron-atom scattering length is negative,

this could be a new opportunity to study highly polar Rydberg molecules in a new atomic species. The electron-atom scattering phase shifts for all the atomic species discussed in the present paragraph have yet to be calculated.

5.2 Silicon: a multichannel system with two thresholds

A second example of the rich physics provided by two-electron systems is given by exploiting the complex channel interactions due to the fine-structure splitting to create long-range molecules that display two distinct length scales. In silicon the $3p\ ^2P^o_{1/2}$ and $3p\ ^2P^o_{3/2}$ ionization thresholds are separated by $\Delta E = 287.84\,\mathrm{cm}^{-1}$. Nonperturbative interactions between Rydberg series in different channels converging to these two thresholds require the framework of multichannel quantum defect theory (MQDT) to describe the bound states of the atom [9, 10, 209, 210]. Silicon has been studied in this framework both from a semi-empirical standpoint [211–213] and through nearly *ab initio* R-matrix calculations [10, 214, 215].

Although the full R-matrix methods outlined in Chapter 2 could be directly applied to silicon, in this chapter we elect to use the semi-empirical standpoint, closely following [10]. We treat the elements of a diagonal short-range reaction matrix in LS coupling, $K^{(LS)}_{ii} = \delta_{ii} \tan \pi\mu_i$ as fit parameters. We will fit these by matching experimental quantum defects μ_i with MQDT predictions. The advantage of this MQDT formulation is that these elements have slow energy dependence in the short-range region near the core since asymptotic boundary conditions have not yet been enforced. Thus, we know that a few quantum defect parameters determined from empirical data, perhaps with small linear energy dependence added in, should suffice to describe the whole high-energy spectrum of Si. This same idea has been employed recently in a MQDT study of Sr [216].

The following discussion overlaps significantly with chapter 2, but whereas there the electron-neutral interaction motivated many of the specific details here the emphasis is on Rydberg states bound in the long-range Coulomb potential. The reaction matrix $\underline{K}$ is related to the scattering matrix,

$$LS|\hat{S}|L\ S \quad = \underline{S} = e^{2i\underline{\delta}}, \tag{5.1}$$

where $\underline{\delta}$ is a diagonal phase-shift matrix, through the relationships

$$\underline{K} = \frac{i(\underline{I} - \underline{S})}{\underline{I} + \underline{S}}; \quad \underline{S} = \frac{(\underline{I} + i\underline{K})}{\underline{I} - i\underline{K}}. \tag{5.2}$$

Some simple algebra reveals that in LS coupling $\underline{S} = e^{2i\underline{\delta}}$ and $\underline{K} = \tan \pi\underline{\mu}$. Although both matrices can be used, we choose the K matrix formalism for simplicity since it is explicitly real. An analogous derivation for $\underline{S}$ is found in appendix C. $\underline{K}$ defines the linearly-independent solutions at each E in this LS-coupled representation, also known as the "eigenchannel" representation, where the i $^{\text{th}}$ linearly independent wave function outside of the short-range scattering region is

$$\Psi_i \ = \mathcal{A} \sum_i \Phi_i(\omega) \ \ f_i(r)\delta_{ii} \ - g_i(r)K_{ii}^{(LS)} \ \ , \tag{5.3}$$

where i labels different channels, $\Phi_i(\omega)$ contains the wave functions of the atomic core and all spin and orbital angular momentum degrees of freedom of the Rydberg electron, and (f, g) are the regular/irregular solutions to the Schrödinger equation with a Coulomb potential outside of the atomic core [9]. An antisymmetrization operator is denoted here as $\mathcal{A}$, although since the Rydberg electron overlaps the core electrons to such a vanishing degree exchange terms can be neglected and this antisymmetrization is irrelevant. The atomic core and Rydberg electron orbital angular momenta are referred to, respectively, as l_c and l_e. LS coupling, which couples the orbital and spin angular momenta separately and is described by the ket, $|[(l_c l_e)L(\frac{1}{2}\frac{1}{2})S]JM_J\ \ $ is

accurate for low-lying states where the electron is near the core and exchange effects dominate [9].

Once again, as emphasized in Chapter 2, we encounter another example of the idea underlying so many of our theoretical methods: different physics is important in different regions of space, and an appropriate partitioning of this configuration space can lead to very straightforward approximations that are extremely accurate. When the Rydberg electron is near the core, this tiny fine structure splitting of a few hundred wave numbers is absolutely overwhelmed by the energy scales of the electrostatic interactions, and therefore it can be ignored and LS coupling holds. This coupling scheme breaks down as the electron moves out far away from the core and accumulates radial phase at rates strongly depending on its energy. By energy conservation, this of course depends on the energy of the inner electron, so at these large distances the small energy splitting between the two fine structure thresholds begins to have crucial, non-perturbative effects. Here a "geometric" orthogonal frame transformation matrix U_{ij}, given by standard angular momentum algebra, is used to transform into the more appropriate jj-coupling scheme represented by the ket $|[(l_c\frac{1}{2})J_c(l_e\frac{1}{2})J_e]JM_J\rangle$ [217]. The jj-coupled K matrix is $K^{(jj)}_{ii} = \sum_{jj} U_{ij}K^{(LS)}_{jj}U^T_{j\,i}$. The matrix U_{ij} is:

$$U_{ij} = \sqrt{(2j_c+1)(2j_e+1)(2L+1)(2S+1)} \begin{Bmatrix} l_e & s_e & j_e \\ l_c & s_c & j_c \\ L & S & J \end{Bmatrix}.$$

We seek a determinantal equation providing the quantum defects and the channel mixing coefficients. We start with the set of linearly independent wave functions corresponding to each channel i: these solutions, written F_{ii}, exactly solve the Schrödinger equation near the core. At some distance $r > r_0$ away where only the

Coulomb potential remains, we write these solutions as linear combinations of the f and g solutions to the Coulomb Schrödinger equation:

$$F_{ii}\,(r) = f_i(r)I_{ii}\ - g_i(r)J_{ii}\,. \tag{5.4}$$

A more useful set of linear combinations is given by the matrix $\underline{M}(r) = \underline{F}(r)(\underline{I})^{-1}$:

$$\begin{aligned} M_{ii}\,(r) &= f_i(r)I_{i\beta}I^{-1}_{\beta i} - g_i(r)J_{i\beta}I^{-1}_{\beta i} \\ &= f_i(r)\delta_{ii}\ - g_i(r)K_{ii}\,(r), \end{aligned}$$

where $\underline{K} = \underline{J}(\underline{I})^{-1}$. This is our fundamental starting point for working with the reaction matrix, and so far has mirrored the discussion in Chapter 2. Now, however, MQDT is used to match the wave functions and close off divergent behavior in the closed channels rather than the numerical approach employed there. We partition these matrices into open/closed submatrices depending on the channel energies relative to a given threshold:

$$\begin{bmatrix} M_{oo} & M_{oc} \\ M_{co} & M_{cc} \end{bmatrix} = \underline{f} - \underline{g} \begin{bmatrix} K_{oo} & K_{oc} \\ K_{co} & K_{cc} \end{bmatrix},$$

where $\underline{f}$ and $\underline{g}$ are now diagonal matrices of these regular/irregular functions. This is further simplified by writing $\underline{M}^{-} = \underline{M} \begin{bmatrix} B_o \\ B_c \end{bmatrix}$, so that:

$$\begin{bmatrix} M_{oo} \\ M_{co} \end{bmatrix} = \underline{f} \begin{bmatrix} B_o \\ B_c \end{bmatrix} - \underline{g} \begin{bmatrix} K_{oo}B_o & K_{oc}B_c \\ K_{co}B_o & K_{cc}B_c \end{bmatrix}$$

$$\begin{aligned} \implies M_{co} &= f_cB_c - g_c(K_{co}B_o + K_{cc}B_c) \\ &= -g_cK_{co}B_o + (f_c - g_cK_{cc})B_c. \end{aligned}$$

To match boundary conditions at long range, we need the long-range asymptotic behavior of f and g. In energetically open channels they oscillate sinusoidally with a

$\pi/2$ phase difference; in closed channels they may be analytically continued, giving linear combinations of exponentially increasing/decreasing terms. The exponentially increasing terms in closed channels survive at infinity and give $g_c \to -\cos\pi\beta$ and $f_c \to \sin\pi\beta$, with additional (equal) coefficients that are neglected here. The set of open matrix elements within closed channels then correspond to:

$$M_{co} \to \cos\pi\beta K_{co} B_o + (\sin\pi\beta + \cos\pi\beta K_{cc}) B_c. \tag{5.5}$$

This linear combination must vanish in order to satisfy correct boundary conditions and remove the exponential behavior at infinity:

$$B_c = -(\sin\pi\beta + \cos\pi\beta K_{cc})^{-1} \cos\pi\beta K_{co} B_o. \tag{5.6}$$

This is the transcendental equation that must be solved in order to obtain the closed-channel energies. However, in energy regimes where all channels are closed $B_o = 0$ and the determinantal equation simplifes to

$$(\sin\pi\beta + \cos\pi\beta K_{cc}) B_c = 0 \implies \det(\tan\pi\beta + K_{cc}) = 0. \tag{5.7}$$

This is the bound state condition that is solved numerically for $\beta = \pi(\nu - l)$. The same expression sets $K_{cc} = -\tan\pi\beta$ and therefore

$$M_{co} = (f_c - g_c(-\tan\pi\beta)) B_c = (-\cos\pi\beta f - \sin\pi\beta g) \frac{(-B_c)}{\cos\pi\beta}. \tag{5.8}$$

We now connect this with the final asymptotic wave functions, given by solving the single-channel radial equation for the Coulomb problem where each channel is weighted by a coefficient Z_i:

$$\Psi = \sum_i \frac{1}{r} \Phi_i(\omega) W_i(r, \nu_i, l_i) Z_i. \tag{5.9}$$

W_i is an energy normalized rescaled Whittaker function solution ([10] Eq. 2.53): :

$$W(r,\nu,l) = \nu^{3/2}[\nu^2\Gamma(\nu+l+1)\Gamma(\nu-1)]^{-1/2} \times W_{\nu,l+1/2} \quad \frac{2r}{\nu} \tag{5.10}$$

This rescaled Whittaker function is explicitly connected to out/ingoing wave solutions by

$$W(r,\nu_i,l_i) = \frac{i}{\sqrt{2}}e^{-i\beta_i}f^+ - \frac{i}{\sqrt{2}}e^{i\beta_i}f^-; \tag{5.11}$$

these out/ingoing waves are related to the regular/irregular functions (f,g) through

$$-if = \frac{1}{\sqrt{2}}(-f^+ + f^-), \;\; g = \frac{1}{\sqrt{2}}(-f^+ - f^-).$$

These are then inverted:

$$g - if = \frac{2}{\sqrt{2}}(-f^+) \implies f^+ = \frac{1}{\sqrt{2}}(if - g)$$
$$g + if = -\frac{2}{\sqrt{2}}f^- \implies f^- = -\frac{1}{\sqrt{2}}(g + if).$$

The Whittaker functions can now be connected:

$$W = \frac{i}{\sqrt{2}} \quad \frac{e^{-i\beta}}{\sqrt{2}}(if-g) + \frac{e^{i\beta}}{\sqrt{2}}(g+if) \quad = \frac{i}{2} \;\; if(e^{i\beta}+e^{-i\beta}) + g(e^{i\beta}-e^{-i\beta})$$
$$= -f\cos\beta - g\sin\beta,$$

which matches the form of M_{co} given in equation (5.8). Thus:

$$\Psi = \sum_i \frac{1}{r}\Phi_i(\omega)W_i(r,\nu_i,l_i)\frac{-B_i}{\cos\pi\beta} \tag{5.12}$$

To summarize: imposition of boundary conditions at long-range requires that

$$\delta_{ii}\ \sin\beta_i + \cos\beta_i K_{ii}^{(jj)} \quad B_i \ = 0;\ \beta_i = \pi(\nu_i - l_i). \tag{5.13}$$

Ensuring a vanishing determinant constrains the allowed values of $n - \mu_i = \nu_i$ to take on discrete values, and the eigenvector B_i can be matched at long-range to an

expansion in re-normalized Whittaker functions $W(r, \nu_i, l_i)$ that exponentially decay at long-range: this is the contents of equation (5.12). The critical parameters in this expression are the mixing coefficients $B_i/\cos(\pi\beta_i)$, which determine the weighting of each channel eigenfunction in the energy eigenstate; these coefficients as well as the bound state energies are given by solutions to equation (5.13). The quantum defects in LS coupling, μ_i, were taken as fit parameters. To obtain additional accuracy, the reaction matrix can further be modified by multiplying by a set of orthogonal rotation matrices [217], i.e. $\underline{K} \rightarrow \underline{\mathcal{R}_1}^\dagger \ldots \underline{\mathcal{R}_M}^\dagger \underline{K} \underline{\mathcal{R}_1} \ldots \underline{\mathcal{R}_M}$, where the M is the number of rotation matrices of of dimension N for an N-channel K matrix. For 2 and 3 channels,

$$\mathcal{R} = \begin{pmatrix} \cos\theta & \sin\theta \\ -\sin\theta & \cos\theta \end{pmatrix} \quad \mathcal{R}_x = \begin{pmatrix} 1 & 0 & 0 \\ 0 & \cos\theta_x & \sin\theta_x \\ 0 & -\sin\theta_x & \cos\theta_x \end{pmatrix}$$

$$\mathcal{R}_y = \begin{pmatrix} \cos\theta_y & 0 & -\sin\theta_y \\ 0 & 1 & 0 \\ \sin\theta_y & 0 & \cos\theta_y \end{pmatrix} \mathcal{R}_z = \begin{pmatrix} \cos\theta_z & -\sin\theta_z & 0 \\ \sin\theta_z & \cos\theta_z & 0 \\ 0 & 0 & 1 \end{pmatrix},$$

and analogous generalizations exist for 4 channels (with 6 rotation angles) etc. This approach introduces additional channel coupling through these rotation angles, which are also fit by matching to experimental levels.

Spectroscopic data for $l_e = 0, 2$ odd parity and $l_e = 1$ even parity states with $J = 0 - 3$ were fitted this way, with results (Fig. 5.3) that compare favorably with Lu-Fano plots derived via R-matrix methods [214,215]. Most high-lying experimental energies were fitted to within 0.5cm^{-1}, but the results for $l_e = 1$ are very uncertain due to a dearth of experimental values available for fitting. The model's accuracy

can be seen by comparing the larger points on Fig. (5.3) with the theoretical points.

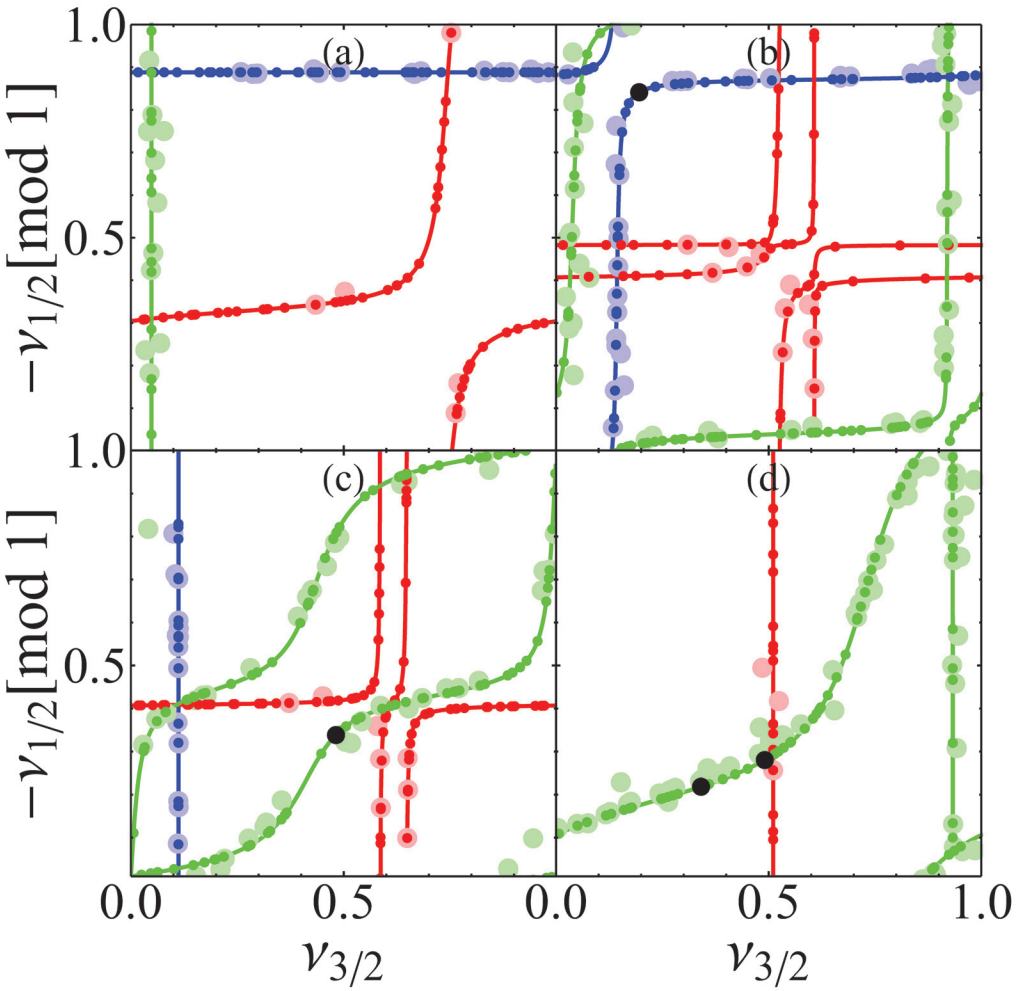

Figure 5.3. Lu-Fano plots for a) $J = 0$, b) $J = 1$, c) $J = 2$, and d) $J = 3$ symmetries. Blue points are $l_e \approx 0$ odd parity; red are $l_e \approx 1$ even parity, and green are $l_e \approx 2$ odd parity. Larger points represent experimental levels; smaller points theoretically predicted. Black points mark the states in Fig (5.4). This figure is taken from Ref. [5].

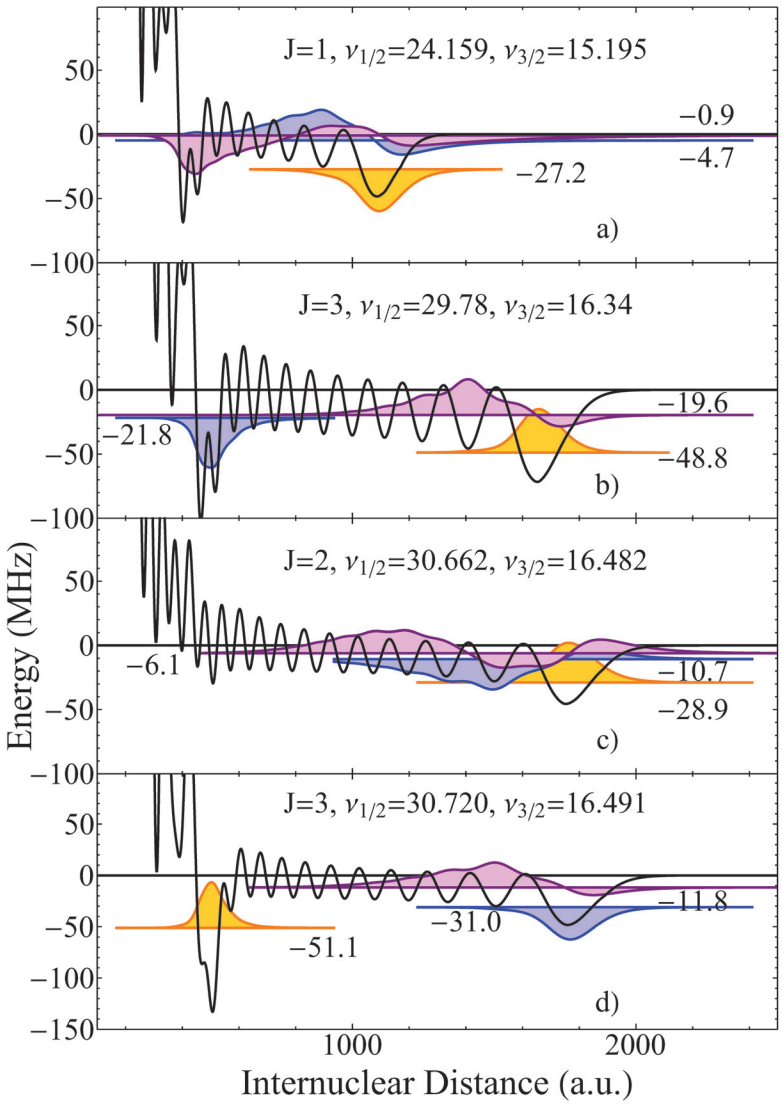

Figure 5.4. Adiabatic potential energy curves, bound state energies, and molecular vibrational wave functions (in color) for various low-J levels of the $M_J = 0$ Si*-Ca Rydberg molecule. This figure is taken from Ref. [5].

After the spectrum of a Rydberg Si atom is calculated, its interaction via the Fermi pseudopotential with a Ca ground state atom is studied. This heteronuclear dimer was chosen in contrast to the homonuclear Si*-Si dimer because silicon's scattering information is poorly known. A very dilute Si gas within a much denser Ca gas is envisioned. Fig. (5.4) displays potential curves and vibrational spectra for low angular momentum states, similar to class (a) from [40]. The binding energies (in MHz) labeling each bound state are listed relative to the asymptotic atomic energy, which can be obtained from $E = E_1 - 1/2\nu_{1/2}^2 = E_2 - 1/2\nu_{3/2}^2$. We estimate an uncertainty of 0.5 MHz in these values.

Those states exhibiting the multi-scale binding behavior predicted here must lie on rapidly varying portions of the Lu-Fano plot; hence, the $J = 3$, $l_e \approx 2$ states most consistently display deep separated wells. Panels b) and d) of Fig. (5.4) show two typical potential curves for this symmetry, while a) shows one of the few $J = 1$, $l_e \approx 0$ states to display two well separated deep wells. Panel c) demonstrates that a locally non-linear Lu-Fano plot is a necessary but not sufficient condition for multi-scale binding, as the angular momentum components $\Phi_i(\Omega)$ in Eq. (5.12) also contribute to the amount of mixing between channels. Specifically, the angular momentum state must have a substantial $m_{l_e} = 0$ component, since this is the only non-zero contribution for $M_J = 0$. The increasing well separation is due to the spatial scaling of each single-channel wave functions with ν_i^2. The potential curves are typically separated from neighboring curves by several hundred MHz or more. The ability of these potentials to support bound states is enhanced by the relatively high molecular reduced mass and the absence of a p-wave resonance in Ca.

5.3 Conclusion

To summarize, we have presented two scenarios to illustrate the rich effects of the physics of long-range multichannel molecules formed by divalent atoms. Interactions with doubly excited states in Ca allow for direct excitation of trilobite molecules through low-l channels, providing a new method for experimental realization of these molecules through direct excitation. We expect that the alkaline atoms will be fertile fields of progress in ultralong-range molecular studies. In the Si*-Ca molecules predicted here, the multichannel description of the Rydberg structure predicts far richer low angular momentum potential energy curves than those studied in the alkalis. Although calcium, and certainly silicon, are unlikely candidates for imminent experiments, we hope that these proposals will influence near-term experiments in more available atomic species. As we have seen, rare-earth atoms are a budding area in ultracold physics, although their spectroscopy is relatively unexplored, and could potentially possess states similar to both of those described here. Likewise, multichannel atoms with hyperfine splittings have many different ionization thresholds relatively close in spacing like the fine-structure split threshold of Si. One example is fermionic Sr, which can be tackled very similarly to our approach for Si here [207, 218–220], and which is of recent interest in Tom Killian's group at Rice Univeristy. Its spectrum will also have mixed Rydberg states, except at higher n because the hyperfine splitting is much smaller even than the fine structure splitting of silicon.

This page intentionally left blank

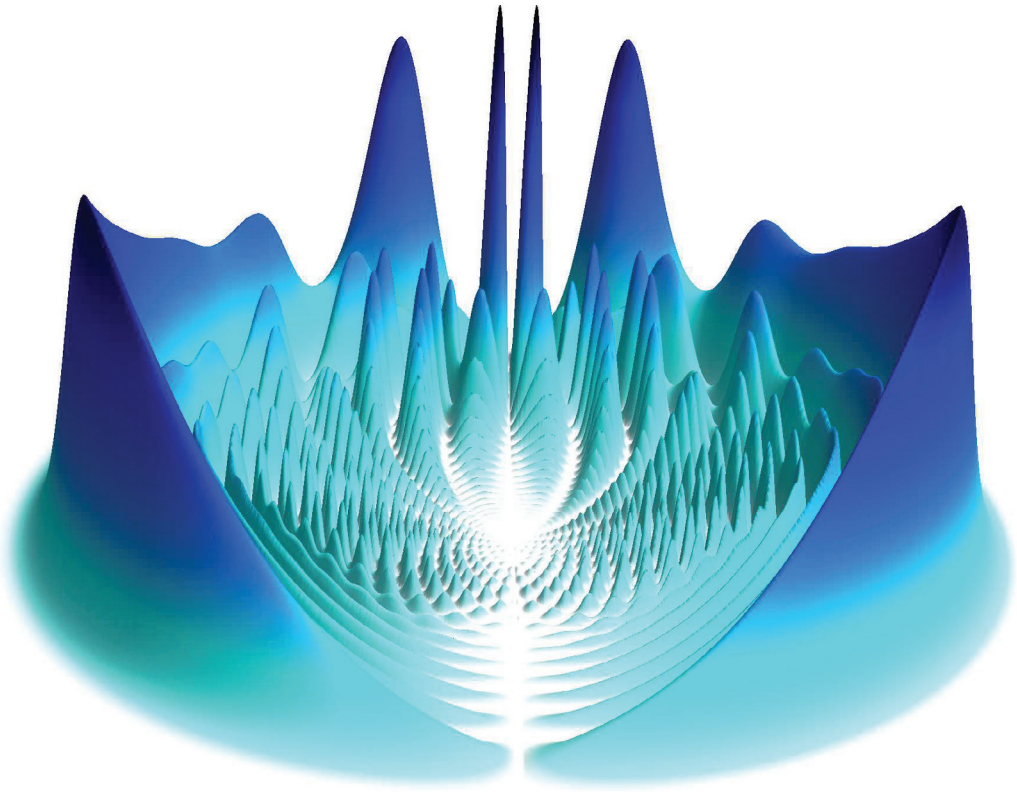

Figure 5.5. Spin degrees of freedom play an important role in Rydberg molecules, like this cesium trilobite discussed in Chapter 6.

6. SPIN EFFECTS IN LONG-RANGE RYDBERG MOLECULES

In this chapter, adapted from Ref. [2], we study the properties of long-range Rydberg molecules of the heavy alkali atoms, Rb and Cs, in much greater detail than chapter 3. Here we include all relevant internal interactions of the two individual atoms: the fine structure of the Rydberg atom and the hyperfine level of the perturber. We also include the spin-dependence of the electron-atom scattering interaction by using phase shifts which depend on the singlet / triplet state of the electron-perturber complex. This unifies past theoretical approaches into a complete model for the first time. A major new component of this theory is the inclusion of ^3P_J splittings within the pseudopotential model, which is important for quantitative calculations. We obtain highly accurate potential energy curves and relevant observables such as dipole moments. These are modified surprisingly strongly by the ^3P_J splitting, as shown by the much better agreement between the predicted dipole moments obtained using our full theory and those observed in butterfly molecules. This study is important to reach an improved understanding of scattering properties and control possibilities of these molecules, and provides a strong foundation for studies of many-body and mean-field effects in polyatomic systems, an area of current interest that demands accurate two-body information [4, 153, 169, 171, 173, 176]. Additionally, the modified ^3P_J-wave pseudopotential could find applications in other ultracold systems or in parallel systems in nuclear physics [86, 87, 221, 222]. Note that the present treatment, which aims to replace the Green's function technique by a phase shift-dependent op-

erator that can be numerically diagonalized, connects with the spirit and motivations of effective field theory [223].

6.1 Construction of the Hamiltonian matrix

The Hamiltonian we consider includes all relevant relativistic effects:

$$\hat{H}(r;R) = \hat{H}_{Ryd}(r) + \hat{V}_{\text{fermi}}(R,r) + \hat{H}_{HF} - \frac{\alpha}{2R^4}. \tag{6.1}$$

As discussed in section 2.2, the Hamiltonian of the Rydberg atom, $\hat{H}_{Ryd}(r)$, includes the effects of core electrons and the Rydberg spin-orbit splitting, parameterized by measured quantum defects from atomic spectroscopy. $\hat{V}_{\text{fermi}}(R,r)$ is the electron-perturber pseudopotential generalized to include all electron-scattering channels up to P-wave: ${}^1S_0$,${}^3S_1$,${}^1P_1$, and ${}^3P_{0,1,2}$. $\hat{H}_{HF}$ is the hyperfine interaction between the perturber's nuclear and electronic spins, and $-\frac{\alpha}{2R^4}$ is the polarization potential between the Rydberg core ion and the perturber. These terms will be described in more detail below as their matrix elements are constructed.

Fig. 6.1 schematizes these different interactions and illustrates the two centers inherent to this system, which are crucial when dealing with the ${}^3P_J$ scattering states. The first center, the Rydberg ion, determines the good quantum numbers of the Rydberg electron's wave function in the absence of a perturbing atom, $|n(ls_1)jm_j\rangle$. These quantum numbers are the same as defined in section 2.2, and a sensible choice of basis to represent the Hamiltonian includes these unperturbed eigenfunctions along with the uncoupled nuclear and electronic spin states of the perturber, $|s_2m_2;im_i\rangle$. Diagonalization of $\hat{H}_{Ryd}(r)$, which would otherwise involve the numerical solution of the electron's dynamics in some model potential describing the alkali atom, is trivial

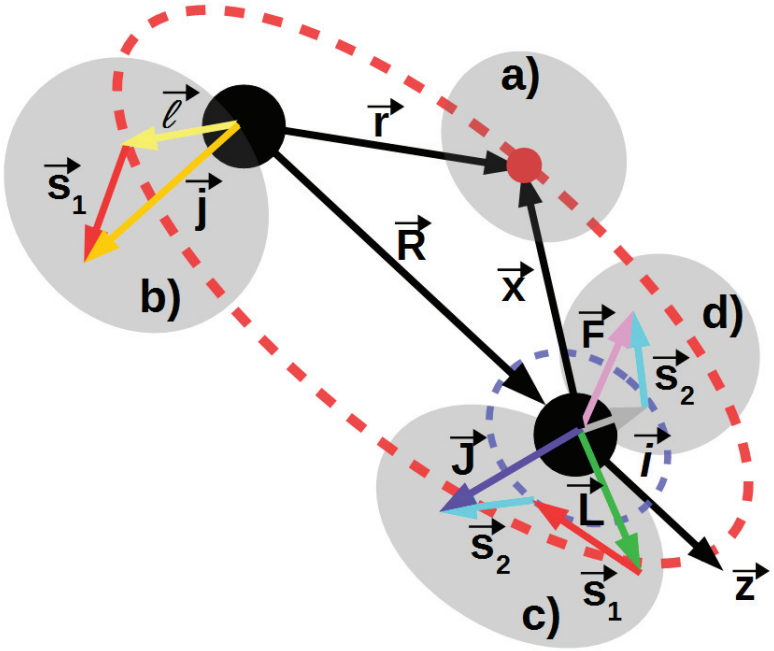

Figure 6.1. The molecular system and relevant angular momenta. The internuclear axis lies parallel to the body-frame z axis passing through the ionic core (left) and the ground state atom (right). The red (blue) dashed oval represents the Rydberg (ground state) electron's orbit. a) The Rydberg electron is located at r relative to the core and at $X = r - R$ relative to the perturber. b) The spin of the Rydberg electron, s_1 (red), couples to its orbital angular momentum relative to the core, l (yellow), to give a total angular momentum j (orange) with projection $m_j = m_l + m_1$. c) The interaction between the Rydberg electron and neutral atom depends on the total electronic spin, $S = s_1$ (red) $+s_2$ (cyan), coupled to the orbital angular momentum L (green) relative to the perturber to form total angular momentum J (purple), with projection $M_J = m_l + m_1 + m_2$. d) The spin of the perturber's outer electron, s_2 (cyan) interacts with the perturber's nuclear spin, i (gray) to form F (pink) and its projection $M_F = m_2 + m_i$. The only good quantum number of the combined system is $\Omega = m_j + m_2 + m_i$. This figure is taken from Ref. [2].

in this basis. Eq. 2.74 and Eq. 2.78 provide the relevant eigenenergies and spin-orbit coupled wave functions.

The hyperfine Hamiltonian is $\hat{H}_{HF} = AI \cdot S_2$. Table 2.1 gives the constant A; for the Rydberg atom this decreases as n^{-3} and is irrelevant at the level of accuracy considered here [75–77]. The matrix elements of $\hat{H}_{HF}$ in the uncoupled basis are

$$\begin{aligned} \alpha i m_i, s_2 m_2 | AI \cdot S_2 | \alpha\, i\, m_i, s_2 m_2 \; &= \frac{A}{2} \delta_{\alpha\alpha} \sum_{FM_F} C^{FM_F}_{s_2 m_2, i m_i} C^{FM_F}_{s_2 m_2, i m_i} \\ &\times \left[(F(F+1) - i(i+1) - s_2(s_2+1) \right], \end{aligned} \tag{6.2}$$

where $\alpha = \{n, l, s_1, j, m_j\}$ and the nuclear spin $i = 3/2(7/2)$ for ^{87}Rb(^{133}Cs). $C^{j_3 m_3}_{j_1 m_1, j_2 m_2}$ is a Clebsch-Gordan coefficient.

As described in section 3.5, Khuskivadze *et al.* [95] were the first to include spin-orbit effects in the P-wave scattering potential via a Green's function treatment and a finite range potential for the electron-atom interaction. Here we develop an alternative procedure that is much more convenient for the diagonalization treatments with zero-range interactions that are typically implemented. The small coupling between $^1P_1$ and $^3P_1$ symmetries is neglected so that the Fermi pseudopotential remains diagonal in spin. We consider two complementary approaches to emphasize different aspects of this derivation and provide alternative physical pictures. The first involves a recoupling of the tensorial operators involved in the Fermi pseudopotential so that J-dependent phase shifts can be incorporated, while the second reformulates the pseudopotential so that it is diagonal in the $|(LS)J\Omega$ basis with matrix elements proportional to the J-dependent scattering volumes, and then considers an expansion of the electronic wave function near the perturber. The first approach begins with a single term of the Fermi pseudopotential (see Eq. 2.91) generalized to

include singlet/triplet states using a projection operator $(\chi^S_{M_S})^\dagger$ for the total spin of the electron-perturber system:

$$\hat{V}_{\text{fermi},LS} = \mathcal{A}(SL,k) \sum_{M_S} \chi^S_{M_S}(\chi^S_{M_S})^\dagger \nabla^L \delta(X) \cdot \nabla^L. \tag{6.3}$$

Here $X = r - R$, and $\mathcal{A}(SL,k) = (2L+1)2\pi a(SL,k)$, where $a(SL,k)$ is the energy dependent scattering length(volume) for $L = 0(1)$ and for $S = 0$ or 1. ∇ and $\chi^S_{M_S}$ represent conjugate operators acting to the left. Eq. 6.3 is expressed using zero-rank tensor operators composed of the tensorial sets $\chi^{(S)}_{M_S}$ and $\nabla^{(L)}_{M_L}$ via standard angular momentum theory:

$$\begin{aligned}\hat{V}_{\text{fermi},LS} = \mathcal{A}(SL,k)\delta(X) \quad & \overline{(2L+1)(2S+1)}(-1)^{-L-S} \\ \times \quad & \left\{ \nabla^{(L)} \times \nabla^{(L)} \right\}^{(0)} \times \left\{ \chi^{(S)} \times (\chi^{(S)})^\dagger \right\}^{(0)}_{0}.\end{aligned} \tag{6.4}$$

The J-dependence is included by recoupling these operators in the usual spirit of Wigner-Racah algebra [224–226]. The recoupling coefficient is calculated using properties of Wigner 9J symbols, and $\mathcal{A}(SLJ,k)$ may now be brought inside the final scalar product and allowed to become J-dependent:

$$\begin{aligned}\hat{V}_{\text{fermi},LS} = \delta(X) \sum_{J} & \mathcal{A}(SLJ,k)\sqrt{2J+1}(-1)^{-L-S} \\ \times \quad & \left\{ \nabla^{(L)} \times \chi^{(S)} \right\}^{(J)} \times \left\{ \nabla^{(L)} \times (\chi^{(S)})^\dagger \right\}^{(J)}_{0}.\end{aligned} \tag{6.5}$$

After decoupling and also summing over the different S and L states, this scalar operator is

$$\begin{aligned}\hat{V}_{\text{fermi},J} = \sum_{L,S} \hat{V}_{\text{fermi},LS} = \delta(X) \sum_{(L,S),J} & \sum_{\Omega} \sum_{M_L,M_L} \mathcal{A}(SLJ,k) C^{J\Omega}_{LM_L,S\Omega-M_L} \\ & \times C^{J\Omega}_{LM_L,S\Omega-M_L} \nabla^{(L)}_{M_L}(\chi^{(S)}_{\Omega-M_L})^\dagger \nabla^{(L)}_{M_L} \chi^{(S)}_{\Omega-M_L}.\end{aligned} \tag{6.6}$$

To further manipulate this expression into a useful form for the basis we have chosen, the angular momenta must be recoupled a second time: the Rydberg electron's spin and orbital angular momenta must be uncoupled so that the electronic spins s_1 and s_2 can be coupled together. These steps will be shown more explicitly below in the second derivation. This allows us to construct matrix elements of $\hat{V}$ using the $Q^{nl}_{LM_L}$ terms defined in Eq. 3.10 by promoting them to include the j-dependence of the radial term, i.e. $Q^{nl}_{LM_L} \rightarrow Q^{nlj}_{LM_L}$ and $f_{nl}(r) \rightarrow f_{nlj}(r)$. The resulting pseudopotential matrix $\underline{V}$ is given in Eq. (6.21), which we now derive directly following the alternative second approach. This starts from a reformulation of the Fermi pseudopotential in which all the angular dependence has been projected out, thus explicitly incorporating J-dependent scattering phase shifts by projecting into states with good quantum numbers $\beta = \{(LS)J\Omega\}$ describing the electron-atom interaction. To reformulate in this fashion, we start with Eq. 6.3, which we want to manipulate so that it immediately shows how to project onto wave functions of total J, $V_{\text{fermi}} \propto \quad {}_J|(LS)J\Omega\ A_{LSJ}\ (LS)J\Omega|$. This is accomplished by taking Eq. 6.3, switching $L \rightarrow L\ $, and then summing over $L\ $ and S to obtain the full operator:

$$V_{\text{ferm}} = \underset{L\ ,S}{\mathcal{A}(SL\ ,k)} \underset{M_S}{\chi^S_{M_S}(\chi^S_{M_S})^\dagger \nabla^L\ \delta(X)\cdot\nabla^L} \tag{6.7}$$

We next apply the projection operator $\quad {}_{LM\ L}|LM_L\ \ LM_L|$ to the left and to the right of the Fermi pseudopotential operator:

$$\begin{aligned} V_{\text{fermi}} = & \underset{LM_L}{|LM_L\ \ LM_L|} \\ & \times \underset{L\ ,S}{\mathcal{A}(SL\ ,k)} \underset{M_S}{\chi^S_{M_S}(\chi^S_{M_S})^\dagger \nabla^L\ \delta(X)\cdot\nabla^L} \underset{L\ M_L}{|L\ M_L\ \ L\ M_L|} \end{aligned}$$

Performing the integrations implied by the Dirac braket notation shows that we must integrate over all the angular parts. Down the road, when we form matrix elements

of this operator in the basis we use for diagonalization, only an integration over the radial part will remain.

$$V_{\text{fermi}} = 2\pi \sum_{\substack{LM_L\ S,M_S\ \ L \\ L\ M_L}} (2L\ \ +1)a(SL\ \ ,k)|LM_L, SM_S\rangle\langle L\ M_L, SM_S| \times \quad Y^*_{LM_L}(\hat{X})\nabla^L\ \ \cdot \delta^3(X)\nabla^L\ Y_{L\ M_L}(\hat{X})d\hat{X}\ \ . \tag{6.8}$$

This expression is diagonal in S. Eventually, as made explicit in Eq. 6.17, we will want to write our basis states as a power series in $X^L, L \leq 1$. This implies that this operator is diagonal in $L, L:$ if the exponent on the gradient operator does not match the exponent of X, these terms vanish. We have also switched notation for the spin state, substituting $\chi^S_{M_S} \rightarrow \langle\ SM_S|$. This leaves:

$$V_{\text{fermi}} = 2\pi \sum_{LM_L, M_L\ S,M_S} (2L+1)a(SL,k)|LM_L, SM_S\rangle\langle LM_L, SM_S| \times \quad Y^*_{LM_L}(\hat{X})\nabla^L \cdot \delta^3(X)\nabla^L Y_{L\ M_L}(\hat{X})d\hat{X}\ \ . \tag{6.9}$$

The integration over $\hat{X}$ can now be performed. Explicitly, for $L = 0$:

$$Y^*_{00}(\hat{X})\delta^3(X)Y_{00}(\hat{X})d\hat{X} = \frac{\delta(X)}{X^2}Y_{00}(0,0)Y_{00}(0,0). \tag{6.10}$$

And, for $L = 1$:

$$Y^*_{1M_L}(\hat{X})\nabla \cdot \delta^3(X)\nabla Y_{1M_L}(\hat{X})d\hat{X} = \frac{\delta(X)}{X^2} \quad \partial_X\partial_X Y_{1M_L}(0,0)Y_{1M_L}(0,0) + \frac{1}{X^2}\frac{(2L+1)(L+1)L}{8\pi}\delta_{M_L,M_L}\delta_{|M_L|,1} \quad . \tag{6.11}$$

Here $\partial_X\partial_X$ is the radially-dependent term of the dot product of the two gradient operators, where ∂_X acts to the left. Since our current analysis only considers func-

tions linear in X for $L = 1$, the derivative term can be effectively replaced by a X^{-2} factor to give the following compact form for the full pseudopotential:

$$V_{\text{fermi}} = 2\pi \sum_{LM_L,M_L\, SM_S} |LM_L, SM_S\ \frac{(2L+1)^2}{4\pi} a(SL,k)\frac{\delta(X)}{X^{2(L+1)}}\delta_{M_L,M_L}\ LM_L, SM_S|. \tag{6.11}$$

The angular momenta may now be coupled and summed over M_L:

$$V_{\text{fermi}} = 2\pi \sum_{LM_L\ SM_S\ J\Omega,J\ \Omega} |(LS)J\Omega\ C^{J\Omega}_{LM_L,SM_S}\frac{(2L+1)^2}{4\pi} a(SLJ,k)\frac{\delta(X)}{X^{2(L+1)}}C^{J\ \Omega}_{LM_L,SM_S}\ (LS)J\ \Omega\ | \tag{6.12}$$

Summation over M_L and M_S replaces the product of Clebsch-Gordan coefficients with $\delta_{JJ}\,\delta_{\Omega\Omega}$, along with the triangularity condition relating the possible values of L and S to the allowed values of J. Finally,

$$V_{\text{fermi}} = 2\pi \sum_{(L,S)J\Omega} |(LS)J\Omega\ \frac{(2L+1)^2}{4\pi} a(SLJ,k)\frac{\delta(X)}{X^{2(L+1)}}\ (LS)J\Omega|, L \leq 1 \tag{6.13}$$

This pseudopotential form, with the angular dependence situated in the projectors, is the desired form to incorporate the J-dependent scattering parameters correctly.

$$\hat{V}_{\text{fermi}} = \sum_{\beta} |\beta\ \frac{(2L+1)^2}{2} a(SLJ,k)\frac{\delta(X)}{X^{2(L+1)}}\ \beta|. \tag{6.14}$$

Here,

$$\hat{X}|\beta\ = \sum_{M_L,M_S} C^{JM_J}_{LM_L,SM_S} Y_{LM_L}(\hat{X})\chi^S_{M_S}. \tag{6.15}$$

Notice that the result of the preceding derivation shows that moving into this projection operator form introduces a factor of $(2L+1)/4\pi$; the $1/4\pi$ might be expected since effectively the three-dimensional delta function has been modified into just a

radial delta function, but the nontrivial $(2L+1)$ factor reveals the vectorial form of the p-wave operator.

Since the good quantum numbers β are incompatible with those characterizing the eigenstates of the Rydberg electron, the Rydberg wave function of Eq. (2.78) is expanded to first order about the position of the perturber:

$$\psi_{n(ls_1)jm_j}(r) = \sum_{m,m_1} C^{jm_j}_{lm,s_1m_1}\chi^{s_1}_{m_1} \left[\phi_{nljm}(R) + \nabla \left[\phi_{nljm}(R) \right] \cdot X \right], \tag{6.16}$$

where $\phi_{nljm}(R) = \frac{f_{nlj}(R)}{R} Y_{lm}(\hat{R})$. After using the spherical tensor representation of $\nabla\phi_{nljm}(R)$ given by the Q functions and expressing X in terms of spherical harmonics $Y_{LM}(\hat{X})$ centered at the perturber, it becomes clear that this expansion mediates the transformation from spherical harmonics relative to the Rydberg atom, $Y_{lm}(\hat{r})$, to S and P partial waves relative to the perturber, $Y_{LM}(\hat{X})$:

$$\psi_{n(ls_1)jm_j}(r) = \sum_{m_1=-s_1}^{m_1=s_1} \sum_{L=0}^{1} \sum_{M_L=-L}^{M_L=L} X^L f_L C^{jm_j}_{lM_L,s_1m_1} Q^{nlj}_{LM_L}(R) Y_{LM_L}(\hat{X}) \chi^{s_1}_{m_1}, \tag{6.17}$$

where $f_L = \sqrt{\frac{4\pi}{(2L+1)}}$. Coupling $\psi_{n(ls_1)jm_j}(r)$ from Eq. (6.17) to the perturber's spin introduces $S = 0, 1$ states:

$$\psi_{n(ls_1)jm_j}(r)\chi^{S_2}_{m_2} = \sum_{m_1=-s_1}^{m_1=s_1} \sum_{\substack{L=0,S=0 \\ M_L,M_S}}^{\substack{L=1,S=1 \\ M_L,M_S}} X^L \chi^S_{M_S} C^{jm_j}_{lM_L,s_1m_1} C^{SM_S}_{s_1m_1,s_2m_2} Q^{nlj}_{LM_L}(R) f_L Y_{LM_L}(\hat{X}). \tag{6.18}$$

The matrix elements of this operator are obtained from Eq. 6.18 after a trivial integration over X and introducing the Clebsch-Gordan coefficients $C^{J\Omega}_{LM_L,SM_S} = (LS)J\Omega|LM_L, SM_S\rangle$. These matrix elements are compactly expressed by first con-

structing the matrix representation of Eq. (6.14) in the basis of quantum numbers centered at the perturber, $|\beta\ = |(LS)J\Omega$:

$$U_{\beta,\beta\ } = \delta_{\beta,\beta} \frac{(2L+1)^2}{2} a(SLJ,k). \tag{6.19}$$

The transformation of this diagonal matrix into one in the $|\alpha s_2 m_2\ $ basis, where $\alpha = \{n,l,s_1,j,m_j\}$, is mediated by a "frame-transformation" matrix $\mathcal{A}$. In this context this is physically equivalent to a change of coordinates and good quantum numbers between the two geometrical centers of this system, analogous to what is done in multiple scattering theory [227]. This matrix is readily deduced from the prior steps of the derivation:

$$\mathcal{A}_{\alpha s_2 m_2,\beta} = \sum_{M_L=-L}^{M_L=L} f_L C^{jm_j}_{lM_L,s_1 m_j - M_L} Q^{nlj}_{LM_L}(R) C^{Sm_j - M_L + m_2}_{s_1 m_j - M_L, s_2 m_2} C^{Jm_j+m_2}_{LM_L,Sm_j - M_L + m_2}. \tag{6.20}$$

The final scattering matrix is diagonal in m_i and for every n and l consists of a block matrix:

$$\underline{V} = \underline{\mathcal{A}} \times \underline{U} \times \underline{\mathcal{A}^\dagger}. \tag{6.21}$$

These matrix elements can be equivalently obtained from Eq. 6.6 after the same recoupling of the basis states, but without the need for an expansion of the wave function. The mixing of M_L, M_L implied by Eqs. 6.6 and 6.21 is critical for an accurate physical description of this splitting, since the total spin vector S and total orbital L precess during each P-wave electron-perturber collision. This was first recognized and incorporated in the Green's function calculation of Ref. [95]. However, all subsequent work has neglected this detail. We expect that the much simpler description developed here using zero-range potentials will correct this oversight. This mixing of M_L projections invalidates the use of Σ and Π symmetry labels to categorize the ^3P_J potential curves. Incidentally, the Clebsch-Gordan coefficients

vanish for $M_L = 0$ for the $^3P_1$ state, so that it remains a Π state in the absence of the hyperfine interaction.

To highlight the impact of the ^3P_J splitting effect, it is isolated by ignoring the fine structure of the Rydberg atom and the hyperfine structure of the ground state atom. In this case the matrix elements of the Fermi/Omont pseudopotential are given in the total spin basis, $|nlmSM_S$, where $|nlm$ is the wave function of the Rydberg electron. For definiteness, only the $L = 1, S = 1, \Omega = 0$ matrix elements are considered:

$$\begin{aligned} & nlmSM_S|\hat{V}|n\,l\,m\,S\,M_S \qquad (6.22) \\ = & \sum_J 6\pi a(11J,k)\delta_{m,-M_S}\delta_{m\,,-M_S}C^{J0}_{1m,1-m}C^{J0}_{1m\,,1-m}\,Q^{nl}_{1m}(R)Q^{n\,l}_{1m}\,(R)\delta_{S,S}\,. \end{aligned}$$

To check the basic validity of this expression, we can neglect the scattering volume's J-dependence. Summation over J eliminates the two remaining Clebsch-Gordan coefficients, yielding a diagonal matrix in m, m , as expected. Eq. (11) of [130] is the same as 6.22 but multipled by $\delta_{mm}\,\delta_{M_S M_S}$. Fig. 6.2a displays the matrix elements of the ^3P_J scattering potential within a restricted Hilbert space, with fixed $n, n\,, l, l\,$. Since $\Omega = 0$, only states with opposite m, M_S are nonzero. The size of the non-diagonal elements reflects the mixing of m values. As Fig. 6.2b illustrates, these off-diagonal elements are truly essential in capturing the physics of this process, as they are needed to obtain three distinct eigenvalues out of different linear combinations of states of different m. If only the diagonal elements are included, the eigenvalues labeled 2 and 3 are degenerate, and only two butterfly potential wells develop.

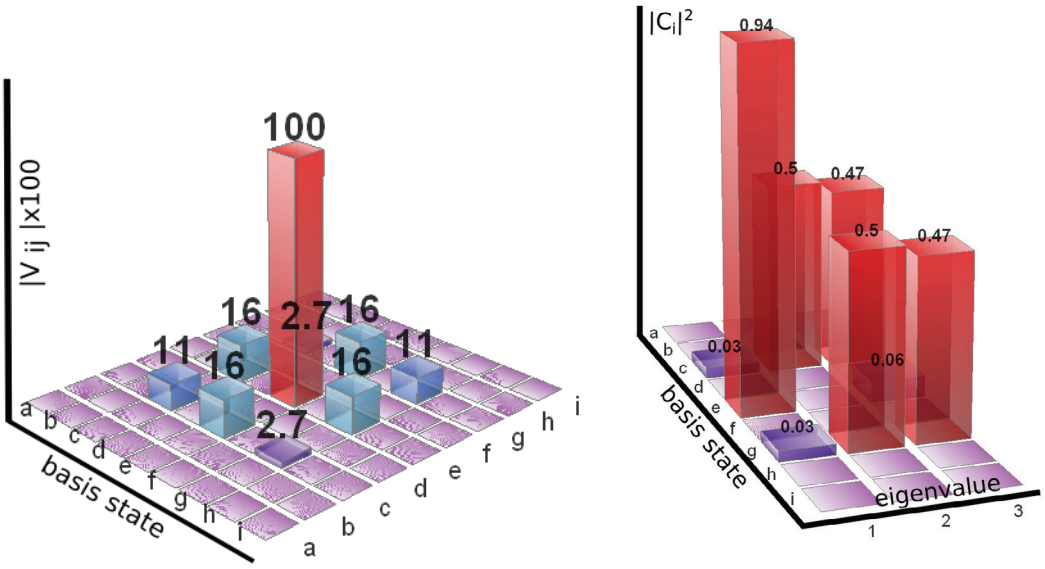

Figure 6.2. a) Absolute (normalized so that the largest is 100) values of the elements of the scattering matrix $V_{ij} = \langle nlS, mM_S|\hat{V}|nlS, m\, M_S\rangle$ at $R = 700$ and with $n = 30$,$l = 10$, and $S = 1$, for Cs. The basis states are labeled by $|mM_S\rangle$; labels $a, b, ...i$ correspond to $|11\rangle$, $|01\rangle$, $|-11\rangle$, $|10\rangle$, $|00\rangle$, $|-10\rangle$, $|1-1\rangle$, $|0-1\rangle$, $|-1-1\rangle$, respectively. Ref. [130] gives only the diagonal elements. b) Absolute squares of the normalized eigenvector components, $|c_i|^2$, for the three non-zero eigenvalues. m, m are mixed for $^3P_0$ and $^3P_2$, while the $^3P_1$ scattering state has no $m = 0$ component. This figure is taken from Ref. [2].

6.2 Details of the calculation

The energy-dependent scattering lengths and volumes are calculated identically as in earlier chapters, and the Hamiltonian matrix $\underline{H}$ is diagonalized at every value of the internuclear distance, R. The dimension of this matrix is finite in the spin quantum numbers, while the infinite number of states of different n must be truncated. Typically four total manifolds $\{n_H - 2, n_H - 1, n_H, n_H + 1\}$ are employed in

the results presented here, which are set so that zero energy is fixed at the $n_H = 30$ level. The only good quantum number of this system is the total spin projection, $\Omega = m_j + m_2 + m_i$. At long-range, where the perturber-electron interaction vanishes, the potential curves can be identified asymptotically via the electronic angular momenta l and j, and the perturber's total nuclear spin F. Since only $L \leq 1$ partial waves are included in the electron-perturber scattering, only states with $|m_j| \leq 3/2$ will be shifted, and so $\underline{H}$ is block diagonal in Ω, $|\Omega| < \frac{7}{2}$ $\frac{11}{2}$ for Rb(Cs). For states around $n_H = 30$ the basis size ranges from approximately 2200(2000) for Cs(Rb) with $|\Omega| = 1/2$, down to 275 for the maximal Ω. The accuracy and convergence of these PECs is a controversial issue. A number of adjacent manifolds must be included in the basis so that level repulsion constrains the divergences in the scattering volumes caused by the ^3P_J shape resonances [122]. However, a study of the ns potential wells has shown that the inclusion of additional manifolds deepens these long-range wells uncontrollably due to the highly singular delta function potential [123]; numerical tests also show that the deepest butterfly potential wells are sensitive to the basis size (see the discussion of Fig. 6.7). Two independent benchmarks are employed here to find the most satisfactory values for the potential curves, given their formal non-convergence. The Borodin and Kazansky model [127] (BK hereafter) was given in Eq. 3.21. It determines the smooth structure of the trilobite and butterfly PECs through the phase shifts. This serves as a crude convergence benchmark, since the true PECs should not differ dramatically from these results. The second convergence check is the comparison between the potential curves from the present model with those calculated in Ref. [95]. Good agreement with these two benchmarks was found after including one more manifold below the level of interest than above; specifically, the set $\{n_H - 2 ... n_H + 1\}$ is used. The n^{-3} scaling of the Rydberg level spacing lends some physical justification to this heuristic approach, since the manifolds above the

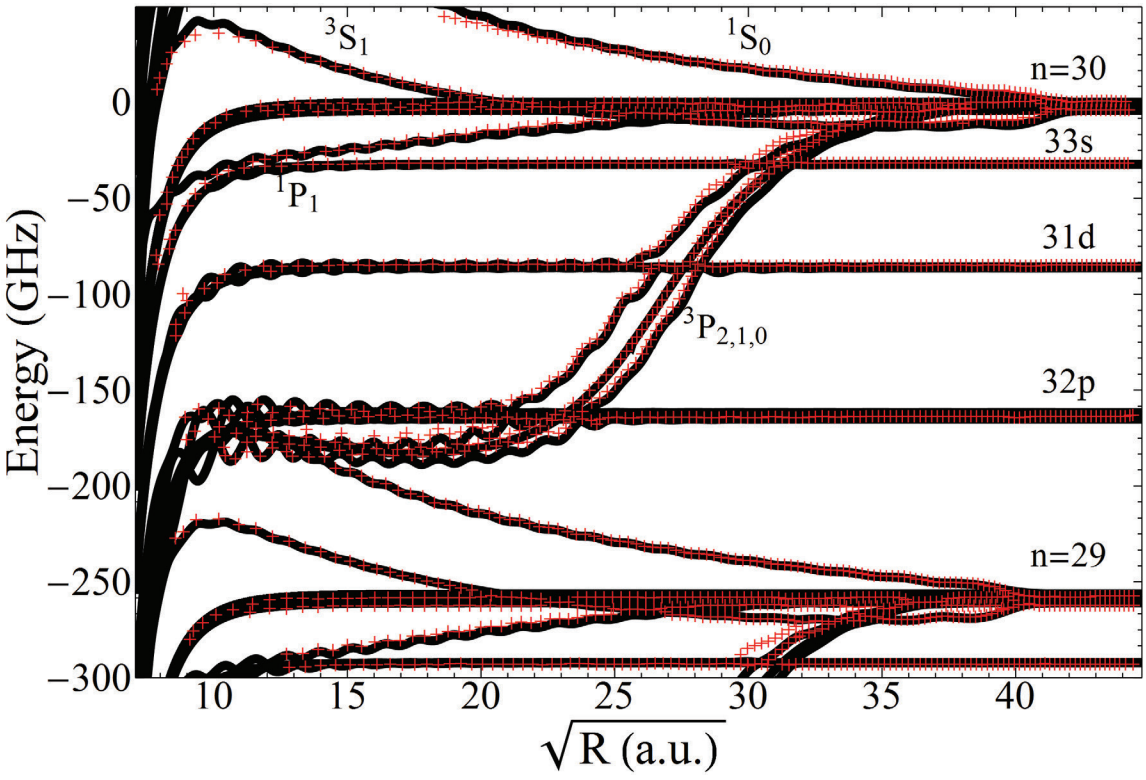

Figure 6.3. Potential energy curves of Rb_2, $\Omega = 0$ (black) without the hyperfine splitting. The results of Ref. [95] (red crosses) is also plotted. The abscissa is the square root of R, which more uniformly spaces the potential wells. This figure is taken from Ref. [2].

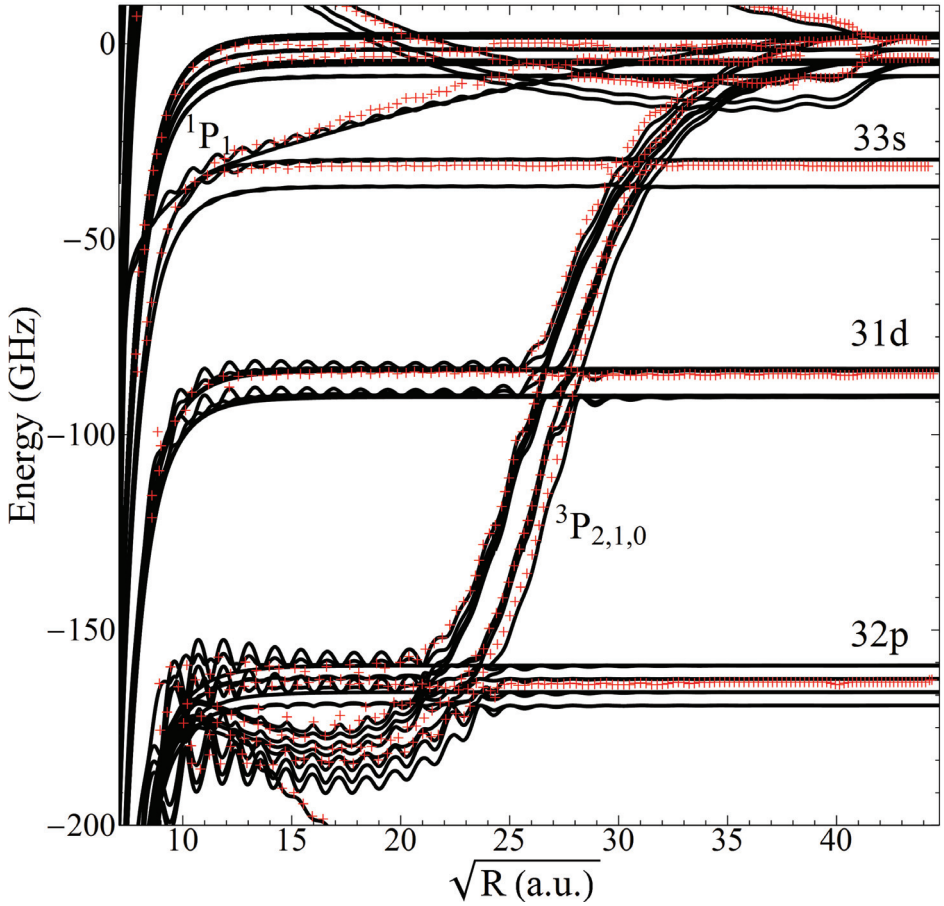

Figure 6.4. Potential energy curves of Rb_2, $\Omega = 1/2$, with the hyperfine splitting of the ground state atom (black). The results of Ref. [95] (red crosses) is plotted, although these ignore hyperfine and fine structure splittings. The inclusion of the additional fine and hyperfine structure creates a multitude of additional ^3P_J-scattered states and splits the trilobite potential energy curves into separate hyperfine states. The labelling is the same as Fig. 6.3. This figure is taken from Ref. [2].

level of interest contribute more weight to the level repulsion due to their relative closeness in energy; the additional manifolds below "balance" this repulsion. For

clarity, only comparisons with Ref. [95] and not the BK comparisons are included in the figures. Some further nuances and convergence tests will be discussed in later sections.

6.3 Adiabatic potential energy curves

As a straightforward confirmation of the validity of this full theory, the PECs for Rydberg energies around $n_H = 30$ are compared with the calculations of Ref. [95]. Figs. 6.3-6.6 show these comparisons and reveal a wealth of information. In Fig. 6.3, the hyperfine structure is neglected for clarity. The main features of Ref. [95] are reproduced excellently, validating this basis set truncation and the accuracy of our ^3P_J pseudopotentials. Low-l molecules can be adequately described without the ^3P_J splitting, since the butterfly potentials cross the low-l states with comparable slopes and distances, although quantitative results still require this level of accuracy. The J-dependence become qualitatively crucial in the depths of the butterfly states and in their PEDMs (see Figs. 6.8,6.11).

Inclusion of the hyperfine structure adds significant complexity: it increases the multiplicity of butterfly states, further mixes these states, introduces many avoided crossings, and splits the low-l states by several GHz. Fig. 6.4 shows results for Rb_2 with $n_H \sim 30$ and $\Omega = 1/2$, highlighting the importance of these additional splittings in shifting the long-range asymptotes and creating a tangle of avoided crossings in the butterfly potential wells. Fig. 6.5 shows the PECs for larger values of Ω. As Ω increases the allowed J values also increase, eliminating some PECs until for the highest nontrivial Ω value only a $^3P_2$ potential curve of Π symmetry remains.

Fig. 6.6 is the same as Fig. 6.4, but for Cs_2. Again, the major features of the potential curves from Ref. [95] are reproduced excellently, but several discrepancies

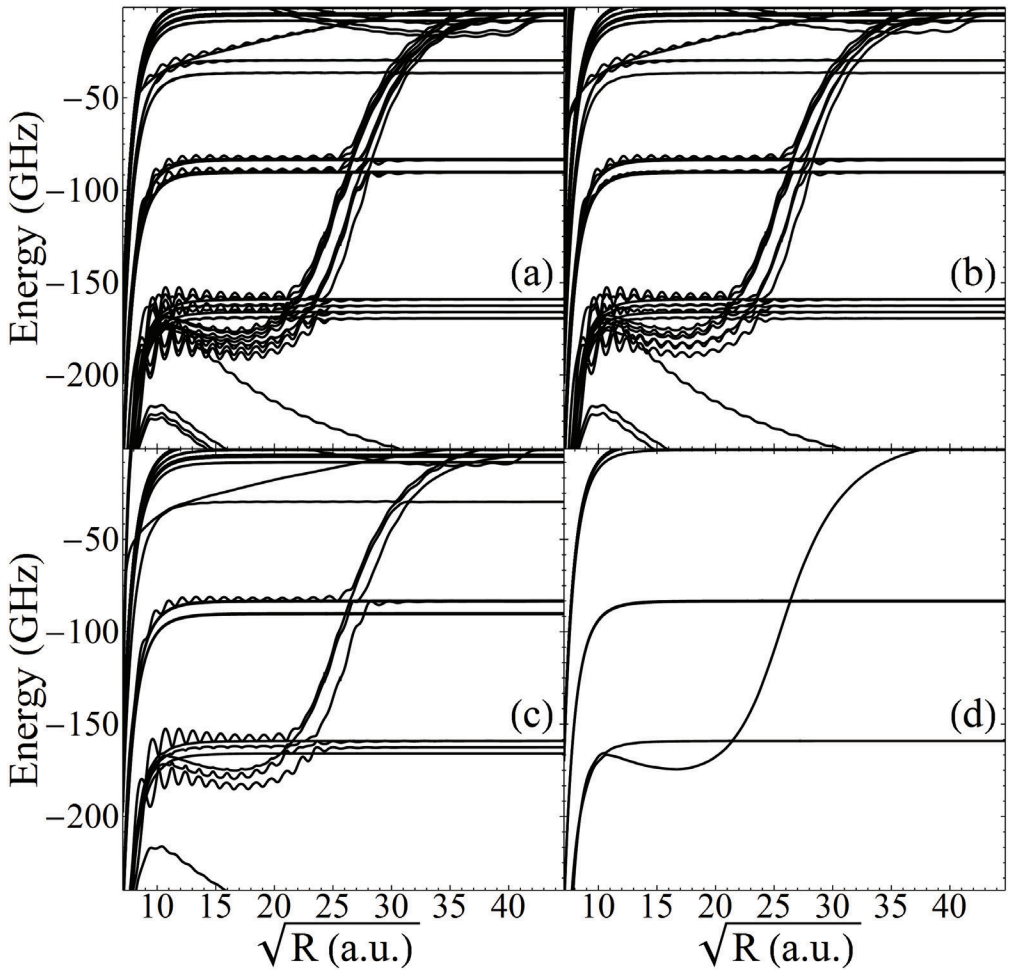

Figure 6.5. Potential energy curves of Rb_2, for a) $\Omega = 1/2$; b) $\Omega = 3/2$; c) $\Omega = 5/2$; d) $\Omega = 7/2$. This figure is taken from Ref. [2].

necessitate discussion. The larger hyperfine and fine-structure splittings of Cs create significant differences in the low-l asymptotes and crossings with the ^3P_J butterfly states. The main differences in the ^3P_J states are due to the modified phase shifts, since those employed here were modified to reflect direct experimental input. Differences remain, particularly in the ultra-long-range $^3P_0$ state, even when identical

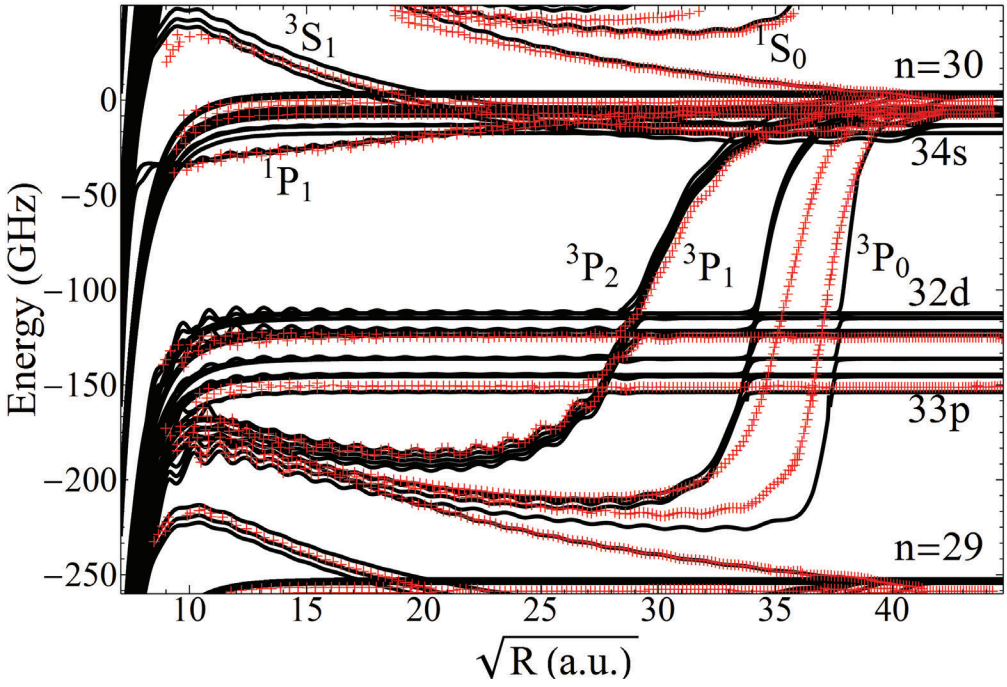

Figure 6.6. Potential energy curves of Cs_2, including the hyperfine splitting of the ground state atom, for the projection $\Omega = 1/2$ are plotted in black. The results of Ref. [95] are shown as red crosses. This figure is taken from Ref. [2].

phase shifts are used. These discrepancies, appearing particularly at long-range and low scattering energy, are also visible in in the long-range "trilobite" region at the order of a few GHz. The alternative Green's function approach utilizing zero-range potentials of [122] agrees closely with the diagonalization results presented here, suggesting that these differences stem from the finite range potential formalism of Ref. [95].

As a numerical test of the convergence of these results, three different basis sets ($\{n_H - q, ..., n_H, n_H + 1\}$, with $q = 3, 2, 1$) were used to calculate the PECs of Cs_2 in

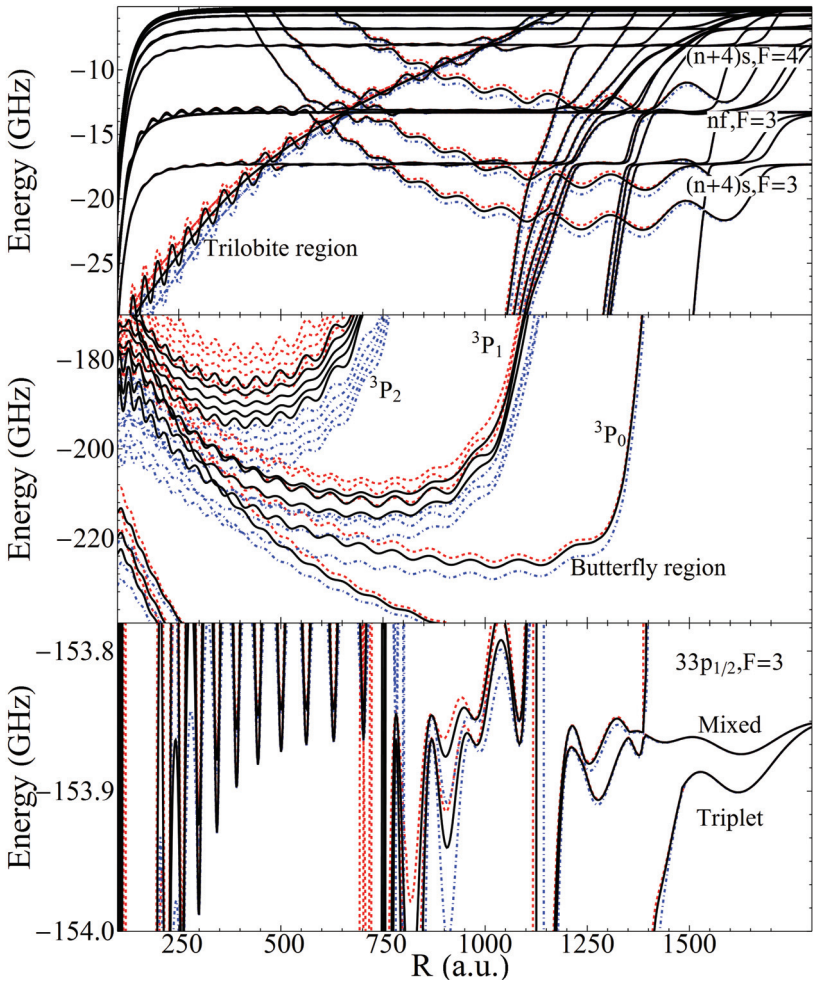

Figure 6.7. Potential energy curves of Cs_2, $\Omega = 1/2$. The results using the $\{29, 30, 31\}$ basis (dot-dashed, blue), the $\{28, 29, 30, 31\}$ basis (solid, black) and the $\{27, 28, 29, 30, 31\}$ basis (dashed,red) are plotted. Each panel displays a different regime, showing that at long-range the calculation is quite well converged with either basis, but the short-range butterfly curves in particular vary severely with the basis size. This figure is taken from Ref. [2].

three of the most interesting regimes. These comparisons are shown in Fig. 6.7. At long range the inclusion of additional manifolds *below* the level of interest does not contribute to the non-convergent increase in well depth seen by [123], but at short range these additional manifolds have a strong effect on the potential wells, repulsing them upwards. Setting $q = 2$ agrees well with Ref. [95] and BK. An expanded convergence test was additionally performed for basis sets $\{n_H - q, ..., n_H + p\}$. with $q = 1, 2, ...6$ and $p = 1, 2$, giving an estimated uncertainty of 3GHz for the butterfly states and 5MHz for the long-range states. This uncertainty in the butterfly states applies to their absolute depths since issues with the basis size is manifested primarily as a global shift. The shape and relative depth of the individual wells is less sensitive, and the uncertainty on the relative energies of observed states is estimated to be about 0.5 GHz, comparable to the vibrational spacing of these states.

As a final comparison, the observed butterfly states of Rb are considered in Fig. 6.8. Overlayed onto the PECs are the observed bound states (red points), whose bond lengths, extracted from rotational spectra, fix them as points in the two-dimensional energy/position plane. Additionally, the full spectrum is overlayed as horizontal lines, showing the range of energies and change in density of states as higher excited states are observed. Qualitative agreement is observed for both these comparisons, although at shorter internuclear distances the observed states are further detuned than our PECs allow. This could be due several factors: the potential wells here are very sensitive to the ^3P_J phase shifts; this could reflect further problems with the convergence of these PECs; or, this might signify the presence of D-wave scattering. Future work is required to determine if the simple delta function potentials truly cannot be accurately converged, and if either a Green's function method or a more suitable set of basis configurations are necessary [123]. Some likely improvements include: a varying number of basis states as a function of R, an R-matrix treatment

along the lines of the recent study by [92], or the renormalization method of [90]. Additionally, some of these problems might stem from the use of the semiclassical electron momentum; $k(R)$ could be modified self-consistently until a converged result is attained.

6.4 Discussion

The elements investigated in a photoassociation process determine many key properties of the Rydberg molecules. The prominent differences between the two alkali atoms considered here are their quantum defects and ${}^3P_J$ scattering properties. The top panel of Fig. 6.7 shows the PECs in the Cs_2 "trilobite" region near the $n_H = 30$ manifold. The near-degeneracy between the $(n+4)s$ states and this manifold allows two-photon excitation of the trilobite molecule [145,154]; this is not reasonable in Rb since the trilobite state admixes almost exclusively high-l states. Figure 6.9 shows two examples of such trilobite states. The trilobite, with one set of nodes (a) and three sets of nodes (b) is superimposed over a faint nS state admixture by which the trilobite-state can be accessed.

Likewise, the positions of the ${}^3P_J$ shape resonances and their energy dependences strongly change the butterfly potential wells. The ${}^3P_0$ resonance in cesium occurs at such a low electronic energy that the associated PECs cross the low-l states at very large internuclear distances, destabilizing the longest-range states to a greater degree than in Rb (Fig. (6.8) displays rubidium's np and butterfly PECs). The butterfly states of Rb possess significant p-character, making a single-photon excitation through this admixture possible; the butterfly states of Cs are much further detuned from the np asymptotes (e.g. see Fig. 6.6), and possess less p character. Additionally, the much larger ${}^3P_J$ splittings in Cs greatly spread the butterfly wells,

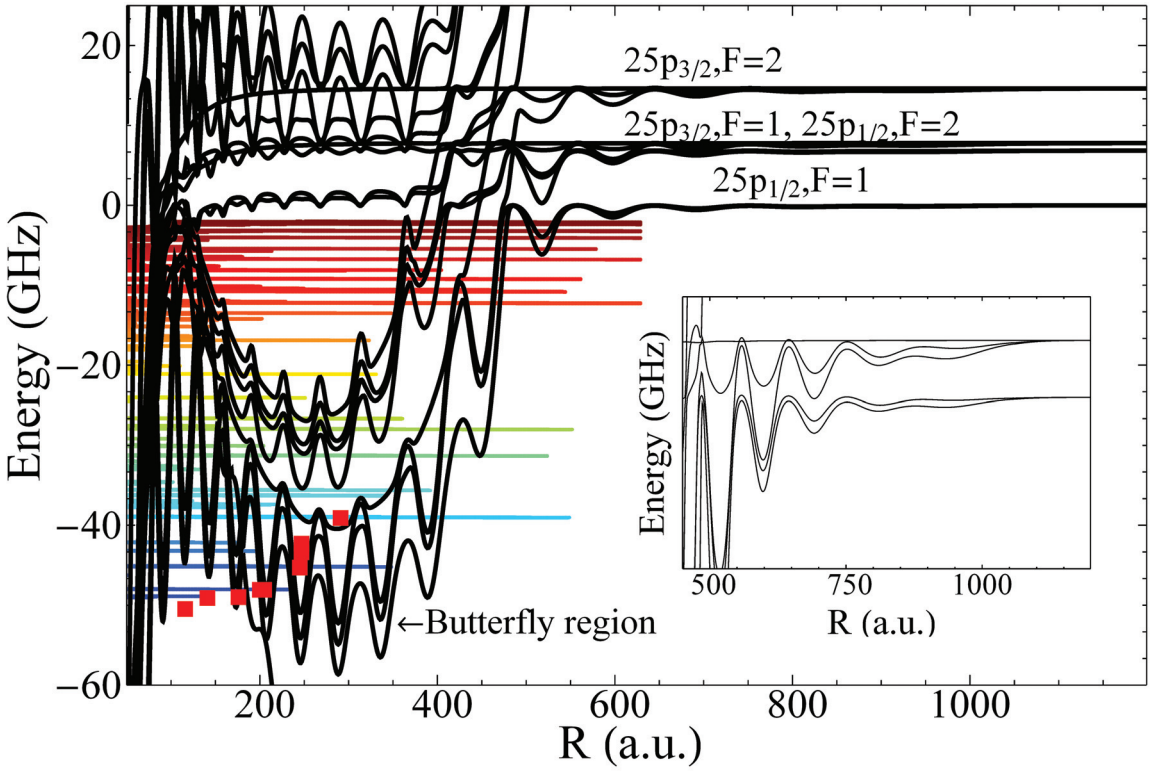

Figure 6.8. $\Omega = 1/2$ Rb_2 potential energy curves (black/solid) near the $25p$ Rydberg states. Zero energy is set to the $25p_{1/2}, F = 1$ asymptote. The bound states whose permanent electric dipole moments were measured in Ref. [128] are plotted as red squares, while the observed spectrum of that experiment is overlayed. The color scheme matches that of Ref. [128], and has no meaning but to guide the eye. The $25p_{3/2}, F = 1$ and $25p_{1/2}, F = 2$ potential wells are highlighted in the inset, since for this Rydberg level the interplay between the fine and hyperfine states makes these states nearly degenerate. This figure is taken from Ref. [2].

limiting the number of avoided crossings. Some of these butterfly states are shown in figure 6.10. In a) an unusual butterfly is plotted which is situated in the deepest

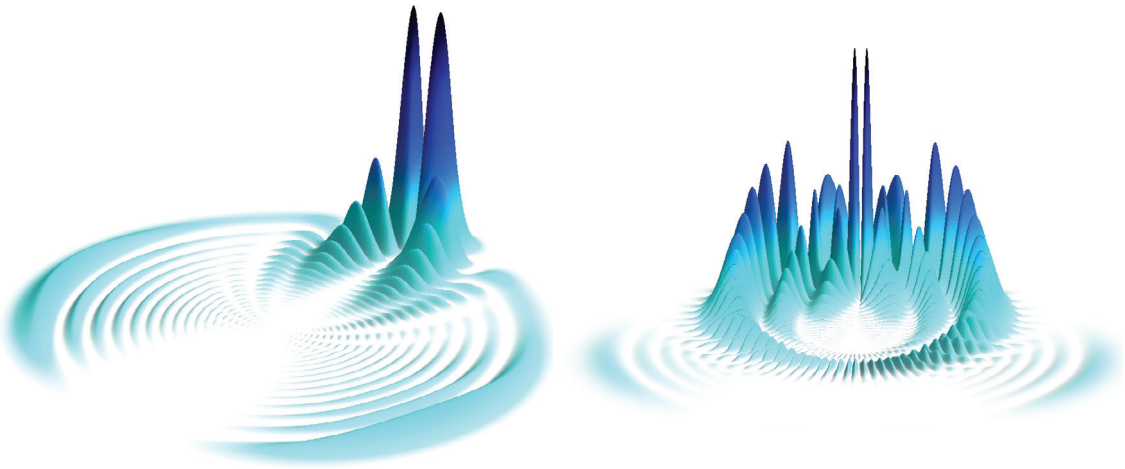

Figure 6.9. Trilobite-like wave functions for Cs.

$^3P_0$ well with a trilobite-like internuclear distance of over 1250 bohr. In size and overall shape this state resembles a trilobite molecule due to the similar bond length, but the specifics of its nodal character reveal that it is in fact a butterfly type state. Panels b-c show three butterflies with varying admixtures of Π and Σ symmetry. Fig. 6.10b shows a primarily Π-state butterfly, while *c* shows one that is primarily Σ and most resembles the first butterfly prediction in Rb [122]. Most butterfly states, due to the Π/Σ mixing caused by the J-dependent phase shifts, are some admixture of these two cases, as Fig. 6.10d shows.

The interplay between different fine and hyperfine splittings can also be used to engineer Rydberg molecules with specific spin characters, and notably can be tuned via the principal quantum number to induce spin flips in the perturbing atom or to strongly entangle the nuclear spin of the perturber with the electronic spin of the

Rydberg atom [161]. The PECs for these states are highlighted in Fig. (6.8). In particular, the near-degeneracy of $25p_{3/2}, F = 1$ and $25p_{1/2}, F = 2$ states strongly mixes their spin character; this degeneracy can be varied over a range of quantum numbers from 24-29. Similar degeneracies are found in the np states of Cs, for $n = 31-35$ [130], or also in the Cs nd states for $n = 21-25$. The myriad differences between these two alkali species provide a wide range of parameters influencing the properties of the Rydberg molecules, and future work could investigate how the impact of different properties of other alkali atoms such as Li, Na [108], K, or Fr [228] in their respective long-range Rydberg molecules. Other interesting opportunities involve studies of heteronuclear Rydberg molecules: for example, an excited Cs atom bound to a ground state Rb atom would take advantage of the favorable near-degeneracy between the $(n+4)s$ and $n, l > 3$ energies without the added complications of the large ${}^3P_J$ splitting of the e-Cs scattering resonances. Chapter 9 presents some exploratory results along these lines, while chapter 5 showed how non-alkali atoms possess many attractive features. These results together reveal a surprising depth to these Rydberg molecules due to the wide range of interchangeable ingredients of this system.

6.5 Multipole moments

For a final test of the spin-dependent nature of these molecules, we generalize the results of subsection 3.4 to include spin dependence within the full model derived above. We replace the hydrogenic eigenstates with the numerically calculated eigenstates, $|s\rangle = \sum_k a_{sk}|k\rangle$, where $|s\rangle$ is an electronic eigenstate, k is a composite

quantum number $k = \{n(ls_1)jm_jm_2m_i\}$, and a_{sk} is the eigenvector corresponding to the s^{th} eigenstate. The multipole moments are then

$$\begin{aligned} s|T^k_q|s &= \sum_{k,k} a_{sk}a_{sk}\,\delta_{m_2,m_2}\delta_{m_i,m_i}\delta_{m_j,m_j}R^{n\,l\,j}_{nlj}(k)(-1)^{s_1+j+l-l} \\ &\times \sqrt{(2j+1)(2l+1)(2l+1)}C^{jm_j}_{j\,m_j,kq}\begin{pmatrix} l & l & k \\ 0 & 0 & 0 \end{pmatrix}\begin{Bmatrix} l & s_1 & j \\ j & k & l \end{Bmatrix}. \end{aligned} \tag{6.23}$$

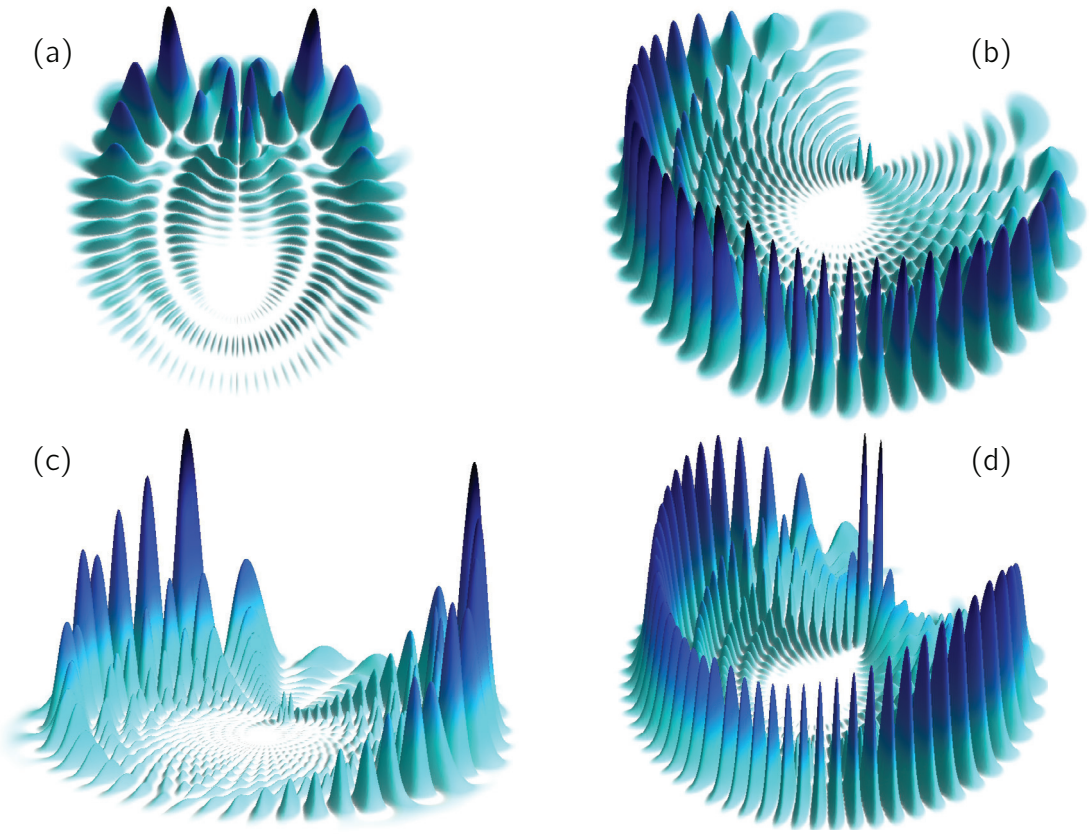

Figure 6.10. Butterfly-like wave functions for Cs.

Several PEDMs are plotted in Fig. 6.11: those corresponding to $^3P_0$ and $^3P_1$ states, the analytic curves for Σ and Π symmetries of Eq. 3.24, the butterfly curve neglecting ^3P_J splitting used in Ref. [128], and the experimentally observed values.

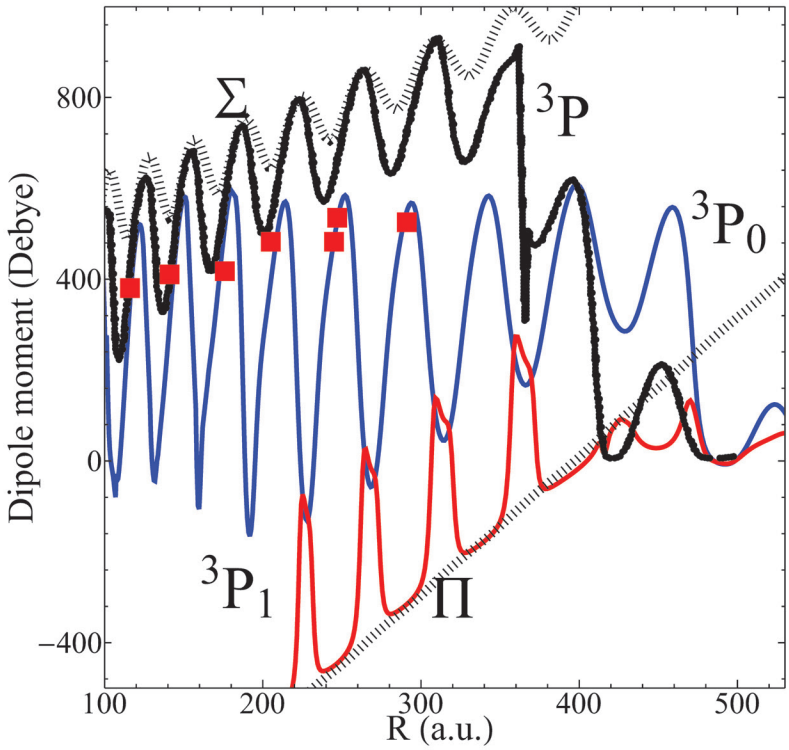

Figure 6.11. Analytic permanent electric dipole moments (black, dashed), permanent electric dipole moments ignoring the ^3P_J splitting (black, solid, labeled ^3P), and permanent electric dipole moments from the full spin model for electronic states dominated by $^3P_0$ scattering (blue,solid), and $^3P_1$ scattering (red,solid), are plotted. The red squares are placed at the observed bond lengths and permanent electric dipole moments [128]. The $^3P_0$ and $^3P_1$ permanent electric dipole moments correspond to states of mixed M_L, although the mixing is quite weak for $^3P_1$ scattering and the analytic and exact results agree more closely. The $^3P_2$ case is not shown, for simplicity. This figure is taken from Ref. [2].

The observable PEDMs are obtained from the theoretical curves by averaging over the vibrational wave functions of the relevant states. The $^3P_0$ PEDM is noticeably smaller and oscillates more dramatically than the Σ and ^3P curves. The maxima in this curve are correlated with the positions of bound states in the relevant potential wells. At large $R > 400$ these PECs connect adiabatically with the np states, which explains the rapid decrease in the PEDMs as R increases.

The reduced strength of the $^3P_0$ PEDM relative to the results neglecting J-dependence (the ^3P curve) stems from the M_L-mixing caused by the SO splitting of the electron-perturber interaction. The PEDMs extracted from pendular state measurements are systematically smaller (by $\sim$25%) than predicted by the ^3P curve (solid black), which follows the approximate Σ curve quite closely [128]. The full theory explains this systematic difference: the $M_L = 0$ states focus the electronic wave function near the perturber, while $|M_L| = 1$ states maximize the wave function closer to the Rydberg core ion; their mixing places the mean value of the electron's position closer to the positively-charged core and reduces the PEDM. Fig. 6.10 shows some exemplary butterfly molecules revealing this mixing. Examination of Fig. 3.9a reveals that any mixture of M_L in this region of internuclear distances mixes negative and positive PEDMs, reducing the total strength. Quantitative agreement is seen between the experimental PEDMs and the theoretical curves they lie directly on at the bond lengths extracted from the experiment, which also agree with the potential minima predicted by the theory. The ^3P prediction does not even overlap most experimental points. This is evidence that even though the relatively small e-Rb ^3P_J scattering splittings do not dramatically shift the PECs, these splittings do have significant impact on observables such as the PEDMs. For Cs, this effect will be even greater. Further insight into this spin mixing is given by considering the $^3P_1$ curve, which is predominantly a Π symmetry state except for hyperfine-induced mixing,

which occurs near avoided crossings of the potential curves. Fig. 6.11 shows that this PEDM lies on the straight line predicted by the approximate Π curve, except for deviations located at avoided crossings in the relevant potential curves.

This chapter has presented a full theoretical model which accurately includes all relevant relativistic effects. This serves as a foundation for future experimental efforts requiring the most complete theoretical picture, and provides a basis for future theoretical work studying new systems or novel applications of these exotic molecules. The results presented here help to better understand the character of these molecules, as well as their binding energies and PEDMs. The prospects of forming these butterfly molecules in Cs will perhaps be more challenging since the p character of the butterfly state is much smaller, but the huge separation between ^3P_J potential curves greatly enlarges the range of internuclear distances and PEDMs accessible in these molecules. The improved description of the nearly-degenerate high-l manifold with the very close $(n+4)s$ state given here lends a more complete theoretical description of this state that should encourage further exploration of the trilobite state in Cs.

This page intentionally left blank

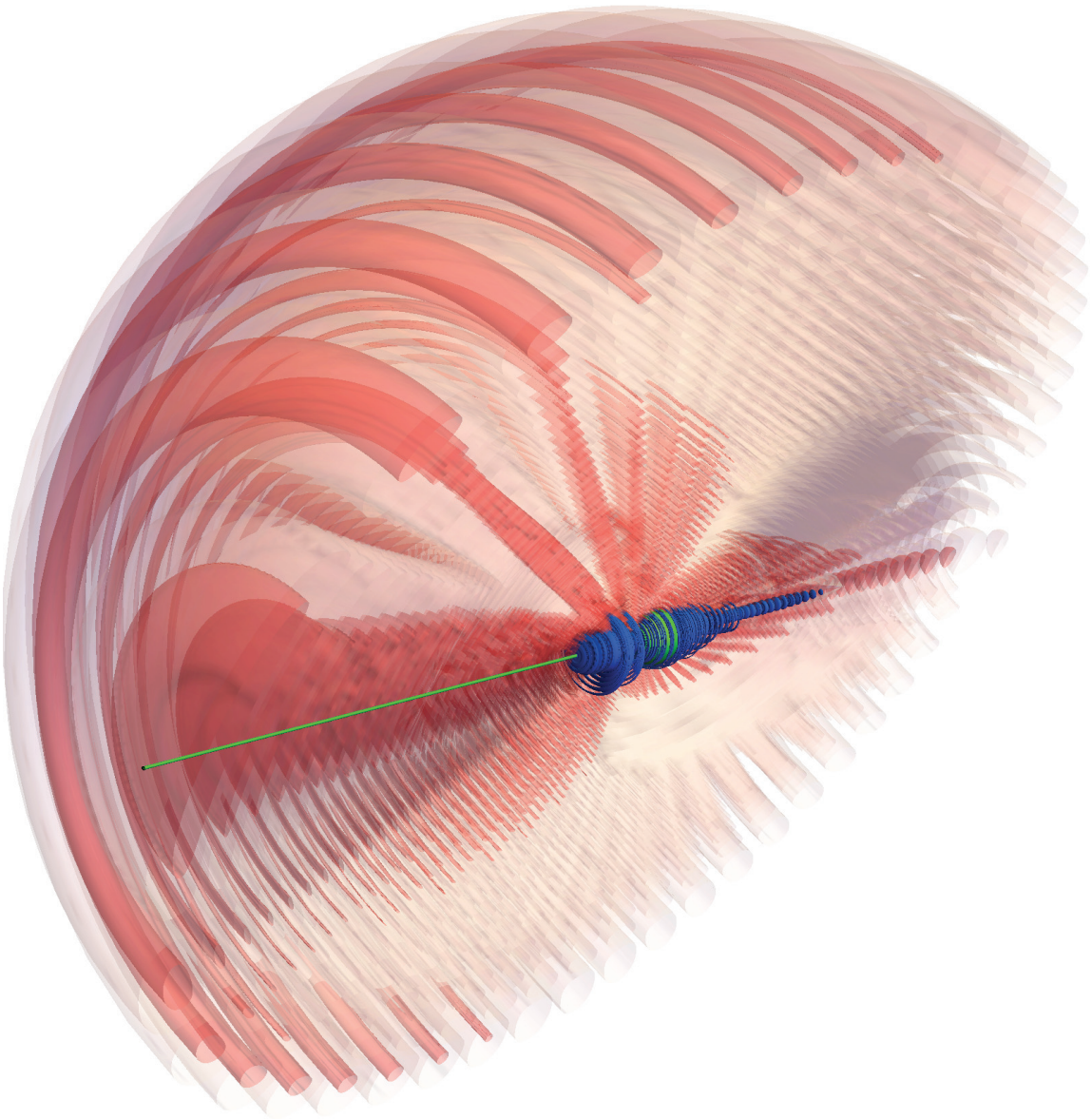

Figure 6.12. Butterfly molecules, like this $n = 70$ molecule displayed using several isosurfaces of probability density, are the subject of Chapter 7. This figure is adapted from Chapter 9.

7. MOLECULAR CONTROL: PENDULAR BUTTERFLY STATES AND RYDBERG BLOCKADE

As previous chapters have shown, one particularly interesting aspect of trilobite and butterfly Rydberg molecules is their enormous permanent electric dipole moments. This chapter, based on Ref. [1], explores the dipolar physics of and interactions between butterfly molecules. The general field of ultracold dipolar gases is of great recent interest because dipolar systems provide an ideal environment for the study of novel ultracold chemical reactions or quantum chaos in non-linear dynamical systems [132,229–232], the design of robust quantum information protocols [27,233,234], and investigations of universality in few- and many-body physics [235–246]. These promising applications hinge on the premise that regimes exist where the dipole-dipole interaction (DDI) is the dominant force in the system. Prior to the study presented here, three main experimental implementations of DDI have been studied: ultracold polar molecules [247–250], ultracold lanthanide atoms with large magnetic moments [132, 232, 251–254], and Rydberg atoms in external fields [23, 255, 256]. These are challenging experiments: large external fields ($\sim 10^4$V/cm) are required to align polar dimers [257], and their production in their rovibrational and hyperfine ground state is a titanic experimental effort [247]. On the other hand, the small atomic magnetic moments require the reduction of the atom-atom interaction using Feshbach resonances [258, 259]. The properties of polar dimers and magnetic atoms are rarely tunable. Rydberg atoms suffer from comparatively short lifetimes, and only interact through the purely isotropic van der Waals interaction unless dipole

moments are induced via an external field [260] or a Förster resonance [28]. These techniques require detailed knowledge of the Stark-induced avoided crossings and delicate control of applied electric fields.

As this chapter shows, Rydberg molecules such as the butterfly provide a competitive hybrid system combining the promising properties of these alternative systems: they have the exaggerated characteristics of Rydberg atoms and the internal structure and polar attributes of molecules, and while lacking the simplicity and stability of magnetic atoms, their interactions are strongly dominated by dipole-dipole forces. We explore the dipolar physics of butterfly molecules in a one-dimensional array of molecules aligned by a weak (< 1V/cm) external electric field applied at an angle θ relative to the longitudinal trap axis (Fig. 7.1c shows the basic setup). Although these calculations are specific to the physical parameters of butterfly molecules, the general concept applies to all Rydberg molecules, which are discussed briefly later in the chapter.

A generalized Rydberg blockade, wherein intermolecular forces prevent the resonant excitation of two molecules within the butterfly blockade radius $R_b(\theta)$, occurs in this system. The blockade radius is the limit where the anisotropic intermolecular potential, $V(R_b, \theta)$, exceeds the laser bandwidth, Γ (~ 0.5 MHz), and $R_b(\theta)$ can be tuned by the applied field. At the "magic angle" satisfying $P_2(\cos\theta_M) = 0$ (P_L is the Legendre polynomial of order L) the DDI vanishes and higher-order terms in the molecular interaction, namely the quadrupole-quadrupole/dipole-octupole and van der Waals, dominate. Thus, the molecular density reveals these interactions via its dependence on θ. The high tunability and exaggerated scales of this proposal has implications in studies of the polaron problem, angulon interactions, tunable interactions, and crystalline phases.

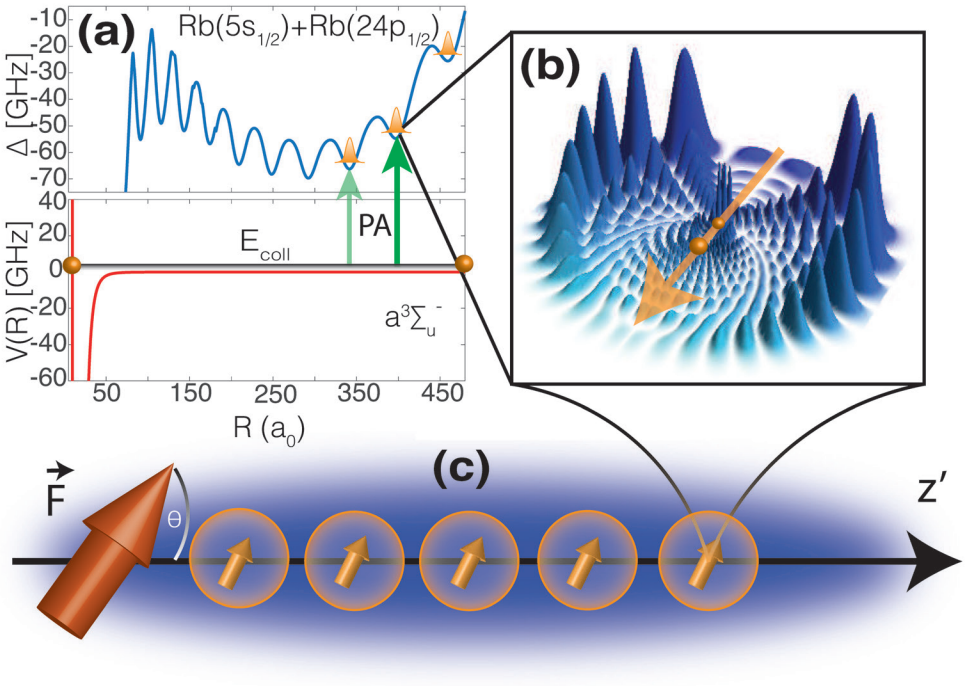

Figure 7.1. a) The proposed single photon photoassociation scheme. The target bound state is selected by the laser frequency. b) The electronic probability density $\rho|\Psi(\rho,z)|^2$ in cylindrical coordinates. The two atoms (sphere) and electric dipole (arrow) are shown. c) The experiment: aligned pendular butterfly molecules in a quasi-one-dimensional cloud. The blockade radius prevents simultaneous excitation of two close molecules. This figure is taken from Ref. [1].

The organization of this chapter follows the hierarchy of energy scales in this system. First, in section 7.1 the properties of butterfly molecules, which are bound by several GHz and have electronic/vibrational spacings of a few GHz are discussed. Next, the pendular states are calculated within the rigid-rotor approximation; their energy splittings are a few tens of MHz. Section 7.2 describes further attributes of

the pendular states within the harmonic oscillator approximation, and details the perturbative calculation of the intermolecular interactions; their maximum strength for our considerations is restricted by Γ ($\sim$ 500kHz). Once this interaction is calculated the density of molecules is readily obtained as a function of θ, and these results are given in section 7.3 along with a discussion of possible future directions.

7.1 Pendular states of long-range butterfly molecules

A typical butterfly molecule potential curve and vibrational states are plotted in Fig. 7.1a, and the electronic state associated with this potential is shown in Fig. 7.1b. Fig. 7.2 displays various molecular parameters of the ground state as a function of n. The reduced multipole moment, calculated in chapter 6, of molecule X averaged over the vibrational molecular wave function is $q(L_X) = Q_0^{L_X}/n^{2L_X}$. Greater tunability is possible if different molecular states are excited; the dipole moment varies over a factor of ~ 3 for different vibrational states.

In the absence of external fields, polar molecules rotate freely with random orientations. Application of a field shifts the molecular energy through the dipole-field coupling $-d \cdot F$, where F is the electric field and d is the molecular PEDM. Setting the quantization axis parallel to the electric field, the molecular Hamiltonian is $H_{\rm mol} = B_e \hat{N}^2 - dF\cos\theta$, with rotational constant B_e and rotational angular momentum operator $\hat{N}$ [1]. When the dimensionless parameter $\omega = \frac{dF}{B_e}$ is large ($\omega \sim 10^2 - 10^3$ for field strengths $\sim$ 1 V/cm, four orders of magnitude lower than needed for typical heteronuclear molecules [128, 247]), the rotational states become trapped in a nearly harmonic potential and are called pendular states in analogy with the harmonic oscillator [155, 261]. These states are found by diagonalizing $H_{\rm mol}$ in the basis of spherical harmonics $Y_{NM_N}(\theta, \phi)$; in the large ω limit two-dimensional harmonic

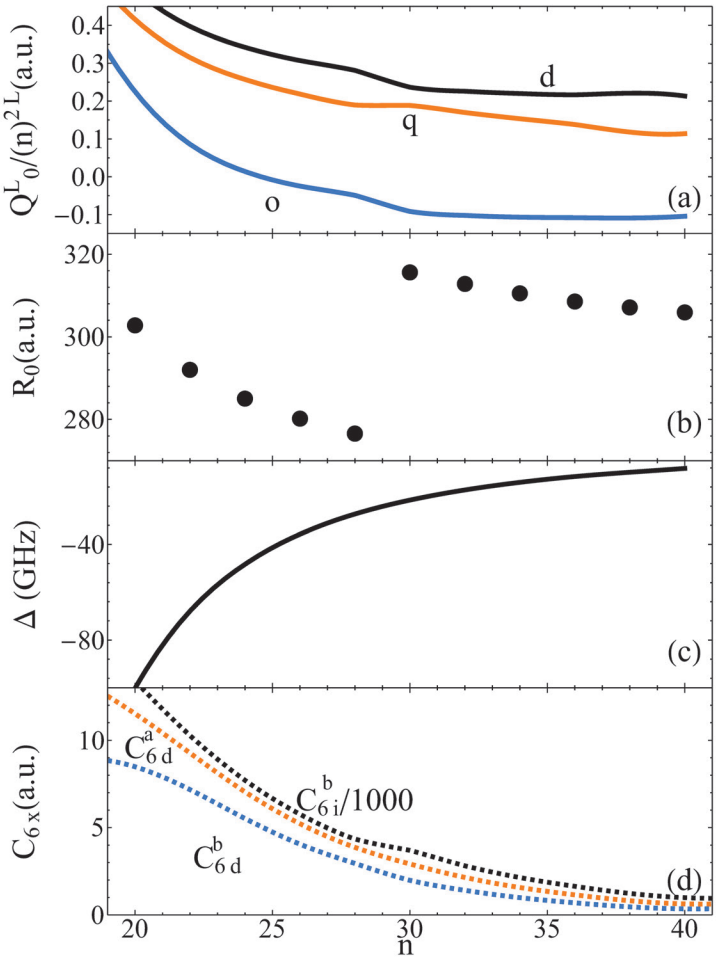

Figure 7.2. Properties of the deepest pendular state as a function of n: a) multipole moments, labeled $d = Q_0^1/n^2$, $q = Q_0^2/n^4$, and $o = Q_0^3/n^6$; b) bond lengths; c) binding energies; d) Relevant van der Waals coefficients at $F = 1\text{V/cm}$. (Eq. 7.5). This figure is taken from Ref. [1].

oscillator eigenfunctions are excellent approximations (red points in Fig. 7.3a are calculated using this approximation, which will be described further in Sec. 7.2).

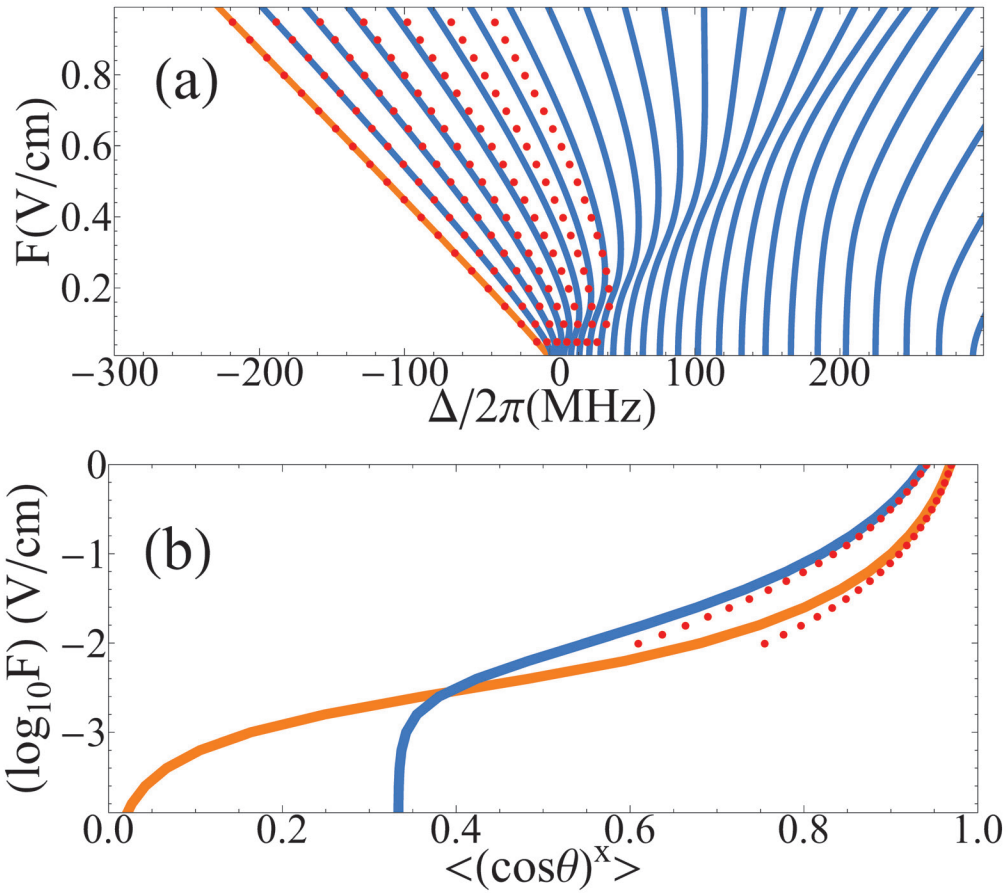

Figure 7.3. (a) Stark spectrum of the $n = 24$ pendular states, showing the energy shift Δ as a function of the applied electric field for $M_N = 0$. The red points correspond to the two-dimensional harmonic oscillator approximation. (b) Orientation ($x = 1$) (orange) and alignment ($x = 2$) (blue) of the lowest pendular state [orange line in (a)]. This figure is taken from Ref. [1].

The pendular states $|\tilde{N}M_N\rangle$ are characterized by their librational state, $\tilde{N}$, and the good quantum number M_N. The ground state, $|00\rangle$, is the most aligned pendular

state. Fig. 7.3a shows the resulting Stark spectrum for the $n = 24$ case. Fig. 7.3b shows $\cos\theta$ and $\cos^2\theta$.

7.2 Calculation of the intermolecular interaction

Fig. 7.1c depicts a sketch of the geometry of our proposal. The electric field points in the lab frame's z axis; a strongly confining potential in the x and y dimension creates a Q1D chain of Rb atoms in the z direction [262], where $\cos\theta = \hat{z}\cdot\hat{z}$. The laser is tuned to excite the $|00$ pendular butterfly state, although greater parameter ranges can be explored via the internal structure associated with other rotational states. Two molecules are separated by a distance R that depends on the atomic density and the long-range intermolecular interaction.

To calculate the potential surface $V(R,\theta)$, the pendular states of a single molecule in the presence of an electric field are calculated, and then these states are used to calculate the interaction potential perturbatively. An accurate method for calculating pendular state eigenfunctions expands the rigid rotor Hamiltonian, $H_{\rm mol}$, into the rotational basis of spherical harmonics $Y_{NM_N}(\theta,\phi)$, where M_N is a good quantum number since the quantization axis is set parallel to the electric field. The pendular states, $\Psi_{\tilde{N}M_N}(\theta,\phi) =$ $_N C^{M_N}_{\tilde{N},N} Y_{NM_N}(\theta,\phi)$, are characterized by their librational state, $\tilde{N}$. It proves convenient to define $W = E/B_e$ and $\omega = dF/B_e, \omega$ 1. Diagonalization of this matrix using values up to $N = 25-30$ gives a converged spectrum for the first ~ 10 excited states. The energy spacings in this spectrum are typically an order of magnitude smaller than the vibrational or electronic spacings.

The intermolecular interaction, given by the two-center multipolar expansion of the Coulomb force [263–268], is valid for $R > 2(\sqrt{\langle r_A^2 \rangle} + \sqrt{\langle r_B^2 \rangle})$ [269], which is satisfied for all distances studied here.

$$\hat{V} = \sum_{L_A,L_B} q(L_A)q(L_B)\frac{f^n_{L_A,L_B}}{R^{L+1}} \sum_{m_A,m_B,m} \begin{pmatrix} L_A & L_B & L \\ m_A & m_B & m \end{pmatrix} \times D^{L_A}_{m_A 0}(\theta_A,\phi_A)^* D^{L_B}_{m_B 0}(\theta_B,\phi_B)^* D^{L}_{m 0}(\theta,0)^*, \tag{7.1}$$

where $L = L_A + L_B$ and $D^{L_X}_{m_X 0}(\theta_X,\phi_X)^*$ is a Wigner D-Matrix rotating the multipole operator between the lab and molecule frame. n is the principal quantum number and $q(L)$ is the L^{th} reduced multipole moment. $D^L_{m0}(\theta,0)$ describes the geometry of the trap axis relative to the electric field axis, and

$$f^n_{L_A,L_B} = (-1)^{L_A} n^{2L} \left[\frac{(2L+1)!}{(2L_A)!(2L_B)!}\right]^{1/2}. \tag{7.2}$$

Using Eq. 7.1 is the standard approach for calculating the interaction potentials between Rydberg atoms. The additional molecular rovibrational stucture in the current problem adds a separate level of complication. Typically Eq. 7.1 is expanded into a large basis of Rydberg atomic states and diagonalized to obtain the most accurate potential energy curves [41, 42, 159, 166, 167]. Our expanded basis, including molecular states, is prohibitively large to perform a full diagonalization, so we use perturbation theory instead. To first order we include terms in Eq. 7.1 up to $L = 4$, which includes quadrupole-quadrupole and dipole-octupole terms. We also neglect retardation effects, falling off as $1/R^7$. It is calculated to order R^{-6}, requiring second order perturbation theory. We thus neglect contributions from other electronic or vibrational levels in the second-order sum over intermediate states, which should introduce errors in the $1/R^6$ potentials of 10% or less due to the larger energy separations. The overall n-scaling of the dipole moments in the second-order terms factors

out, along with an additional n^3 for the second-order terms from their energy denominators: the van der Waals term is thus proportional to $D = n^{11}d^4/R^6$. Additionally, it splits naturally into induction (C_{6i}) and dispersion (C_{6d}) terms [268]. These are calculated independently, since the summation in the induction term is just over the quantum numbers $\tilde{N}_B$ and M_B of one molecule, while the dispersion term is summed over the virtual states of both molecules.

$$V_{ind}(R,\theta) = D \quad \frac{|\langle \tilde{N}_A M_A \tilde{N}_B M_B|\hat{V}|\tilde{N}_A M_A \tilde{N}_B M_B\rangle|^2}{E_0 - E_{N_B,M_B}} \tag{7.3}$$

$$V_{dis}(R,\theta) = D \quad \frac{|\langle \tilde{N}_A M_A \tilde{N}_B M_B|\hat{V}|\tilde{N}_A M_A \tilde{N}_B M_B\rangle|^2}{2E_0 - E_{N_B,M_B} - E_{N_A,M_A}}. \tag{7.4}$$

E_0 is the unperturbed energy of a single molecular state.

Performing this full calculation gives an intermolecular potential of the form

$$\begin{aligned} V(R,\theta) = &-\frac{2C_3 d^2 n^4}{R^3}P_2(x) - \frac{8n^8}{R^5}P_4(x) \quad C_{5a}do - C_{5b}q^2 \\ &- 2\frac{4d^4n^{11}}{R^6} \quad C^a_{6i}[P_2(x)]^2 + C^b_{6i}\frac{(xy)^2}{4} \\ &- \frac{4d^4n^{11}}{R^6} \quad C^a_{6d}[P_2(x)]^2 + \frac{C^c_{6d}}{4}y^4 + C^b_{6d}\frac{(xy)^2}{4} \quad , \end{aligned} \tag{7.5}$$

where $x = \cos\theta, y = \sin\theta$, and where all coefficients C are positive. We obtain $C_3 \sim 0.95$, $C_{5a} \sim 0.83$, and $C_{5b} \sim 0.63$ for the first-order coefficients, independent of n within 2% over the range $n = 20 - 40$. Eq. 7.5 presents the first calculation of the interaction between two Rydberg molecules, and reveals the wide range of adjustable parameters and anisotropy present here, in marked contrast to Rydberg atoms. This stems from the molecular nature, since all of the coefficients and multipole moments depend on the internal structure and are not fixed properties of the atomic species. The van der Waals coefficients depend also on the field strength, and vary slowly with n as seen in Fig. 7.2d. Insight into the relative strengths and angular dependencies

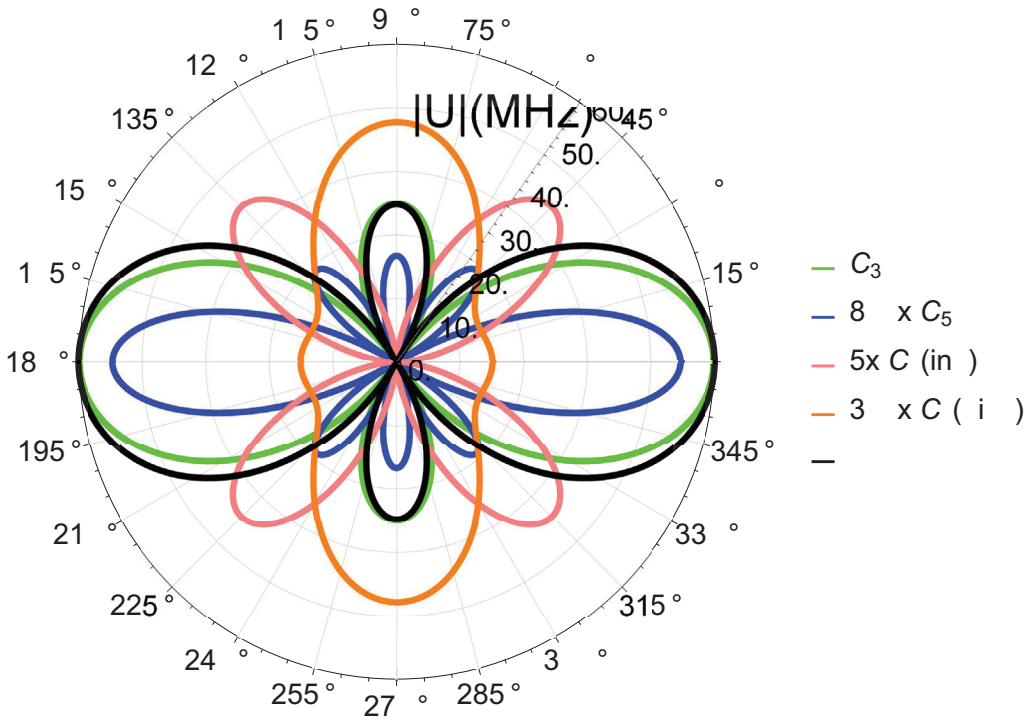

Figure 7.4. Anisotropy of the different terms of the potential, Eq. 7.5, labeled by their coefficients: C_3 is the dipole-dipole term, C_5 is the sum of the dipole-octupole and quadrupole-quadrupole term, and the two C_6 terms are split into induction and dispersion terms. The different components are plotted with weight factors to compensate for their different scales. R is fixed at $1\mu m$. As R increases the C_3 and total curves become totally indistinguishable since the other terms all fall off much faster than R^{-3}.

are seen in the polar plot of Fig. 7.4, where $V(R,\theta)$ is plotted at $R = 1\mu m$. Several unexpected properties of the coefficients of these different terms emerged numerically: the independence of the first-order coefficients on n, the numerical relationship $\frac{C^a_{6i}}{2} = \frac{C^c_{6d}}{9} = C^a_{6d}$, and the large relative size of C^b_{6i} (~ 1000 times larger than the others).

Greater insight into the character of these pendular states and the origin of these unusual coefficient relationships is given by considering the limit $\omega \to \infty$, since to lowest order in $1/\omega$ the Schrödinger equation can be written as a two-dimensional harmonic oscillator. Using the explicit form for $\hat{N}^2$ in spherical coordinates, the Schrödinger equation is

$$\frac{\partial^2}{\partial\theta^2} + \cot\theta\frac{\partial}{\partial\theta} + \frac{1}{\sin^2\theta}\frac{\partial^2}{\partial\phi^2} + \omega\cos\theta + W \quad \Psi(\theta,\phi) = 0. \tag{7.6}$$

This equation maps onto the 2D harmonic oscillator by setting $\xi = 2\alpha\tan(\theta/2)$, where $\alpha = \quad \overline{\omega/2}$. A separable solution in ξ and ϕ is then obtained, where $\Psi(\xi,\phi) = U(\xi)\frac{1}{\sqrt{2\pi}}e^{im\phi}$, $m = |M|$. $U(\xi)$ is then given by:

$$0 = \quad 1 + \frac{\xi^2}{4\alpha}^{\quad 2} \quad \frac{d^2}{d\xi^2} + \frac{1}{\xi}\frac{d}{d\xi} - \frac{m^2}{\xi^2} \quad U(\xi) + \frac{WU(\xi)}{\alpha} + \frac{\omega}{\alpha}\frac{4-\xi^2/\alpha}{4+\xi^2/\alpha}U(\xi). \tag{7.7}$$

Since in the pendular regime $\alpha \quad 1$, we discard all terms of order $1/\alpha$ to obtain the standard harmonic oscillator Schrödinger equation

$$\frac{d^2}{d\xi^2} + \frac{1}{\xi}\frac{d}{d\xi} - \frac{m^2}{\xi^2} \quad + \beta - \xi^2 \quad U(\xi) = 0, \tag{7.8}$$

where $\alpha\cdot\beta = W + \omega$. The energies of the pendular states are then given by

$$E = B_e(\sqrt{2\omega}(2\tilde{N} + |M| + 1) - \omega), \tag{7.9}$$

and the pendular states are

$$\Psi_{\tilde{N},M}(\xi) = (-1)^M \quad \overline{\frac{2\tilde{N}!}{\Gamma(\tilde{N}+M+1)}}e^{-\frac{\xi^2}{2}}\xi^M L_{\tilde{N}}^M(\xi^2), \tag{7.10}$$

where $L_N^M(x)$ is a Laguerre polynomial. The accuracy of the large ω approximation is demonstrated in Fig. 7.3. Using Eq. 7.1, the matrix element connecting different two-molecule states is

$$\begin{aligned}
&\tilde{N}_A M_A \tilde{N}_B M_B|\hat{V}|\tilde{N}_A M_A \tilde{N}_B M_B \qquad (7.11)\\
&= \sum_{L_A,L_B} \frac{q(L_A)q(L_B)(4\pi)^{3/2} f^n_{L_A,L_B}}{R^{L+1}\sqrt{(2L+1)(2L_A+1)(2L_B+1)}}\\
&\times \sum_{m_A,m_B,m} \begin{pmatrix} L_A & L_B & L \\ m_A & m_B & m \end{pmatrix} Y_{L,m}(\theta,0) K^{\tilde{N}_A M_A}_{\tilde{N}_A M_A, L_A M_A} K^{\tilde{N}_B M_B}_{\tilde{N}_B M_B, L_B M_B},
\end{aligned}$$

using $K^{\tilde{N}_A M_A}_{\tilde{N}_A M_A, L_A M_A} = \tilde{N}_A M_A|Y_{L_A,m_A}(\xi,\phi)|\tilde{N}_A M_A$. The first-order shift for the ground state simplifies to

$$\begin{aligned}
00,00|\hat{V}|00,00 \;&= -2\frac{d^2 n^4}{R^3} P_2(x) \quad \frac{4\pi}{3} \quad K^{00}_{00,10}{}^2 \qquad (7.12)\\
&\quad - \frac{8n^8}{R^5} P_4(x) \quad \frac{4\pi}{\sqrt{21}} K^{00}_{00,10} K^{00}_{00,30} do - \frac{3\pi}{5} \quad K^{00}_{00,20}{}^2 \quad .
\end{aligned}$$

These three matrix elements can be found analytically in the harmonic oscillator approximation, and have relatively simple asymptotic forms for $\omega \gg 1$:

$$\frac{4\pi}{3} \quad K^{00}_{00,10}{}^2 \quad \to 1 + \frac{3}{2\omega} - \quad \frac{\overline{2}}{\omega} \qquad (7.13)$$

$$\frac{3\pi}{5} \quad K^{00}_{00,20}{}^2 \to \frac{3}{8\omega}(21 - 6\sqrt{2\omega} + 2\omega) \qquad (7.14)$$

$$\frac{4\pi}{\sqrt{21}} K^{00}_{00,10} K^{00}_{00,30} \to 1 + \frac{14}{\omega} - \frac{7}{\sqrt{2\omega}}. \qquad (7.15)$$

These saturate for large ω, which is why the coefficients C_3, C_{5a}, and C_{5b} can be taken as constant over the range of values studied here. For the second order dispersion terms, at the level of truncation discussed above, are

$$V_d(R,\theta) = \frac{128\pi^3 d^4 n^8}{3R^6} \sum_{\substack{\tilde{N}_A,\tilde{N}_B \\ |M_A|\leq 1 \\ |M_B|\leq 1}} \frac{\left[\begin{pmatrix} 1 & 1 & 2 \\ -M_A & -M_B & M \end{pmatrix} K^{\tilde{N}_A M_A}_{00,1-M_A} K^{\tilde{N}_B M_B}_{00,1-M_B} \right]^2}{2E_0 - E_{\tilde{N}_A,M_A} - E_{\tilde{N}_B,M_B}}, \quad (7.16)$$

where $\tilde{N}_A = M_A = 0$ and $\tilde{N}_B = M_B = 0$ terms are excluded from the sum, and $M = M_A + M_B$. Before evaluating this expression to arbitrarily large $\tilde{N}_A$, $\tilde{N}_B$, we present the asymptotic forms of the relevant matrix elements ($a = \sqrt{\frac{3}{8\pi}}$):

$$K^{00}_{00,10} \to a \quad \sqrt{2} - \frac{1}{\sqrt{\omega}} \quad (7.17)$$

$$K^{10}_{00,10} \to a \quad -\frac{\sqrt{2}}{\omega} + \frac{1}{\sqrt{\omega}} \quad (7.18)$$

$$K^{01}_{00,1-1} \to a \quad \frac{1}{(2\omega^3)^{1/4}} - \left(\frac{2}{\omega} \right)^{1/4} \quad (7.19)$$

$$K^{11}_{00,1-1} \to a \quad \frac{1}{(2\omega)^{3/4}} - \frac{3}{(2\omega)^{5/4}} \quad (7.20)$$

$$K^{20}_{00,10} \to a \quad \frac{1}{\sqrt{2}\omega} - \frac{9}{4\omega^{3/2}} \quad (7.21)$$

$$K^{21}_{00,1-1} \to a\frac{\sqrt{3}}{2} \quad \frac{1}{2^{3/4}\omega^{5/4}} - \frac{3}{2^{1/4}\omega^{7/4}} \quad . \quad (7.22)$$

These asymptotic forms suggest that the sum should converge rapidly, as all terms with final state in the $\tilde{N} = 2$ level are suppressed by additional factors of order $1/\sqrt{\omega}$. This is confirmed numerically; to better than 1% accuracy the sum can be truncated to include only $\tilde{N}_A = \tilde{N}_B = 1$. After collecting into terms with the same

angular dependence, this gives the first-order potential of Eq. 7.5, and gives explicit formulas for the coefficients:

$$C_{6d}^{a} = \frac{8\pi^2}{9} \quad \frac{\left|K_{00,1-1}^{01}\right|^4}{2E_0 - 2E_{0,1}} + \frac{2\ \left|K_{00,10}^{10}\right|^4}{2E_0 - 2E_{1,0}} + \frac{2\ \left|K_{00,1-1}^{01}\right|^2\ \left|K_{00,1-1}^{11}\right|^2}{2E_0 - E_{0,1} - E_{1,1}} + \frac{\left|K_{00,1-1}^{11}\right|^4}{2E_0 - 2E_{1,1}} \tag{7.23}$$

$$C_{6d}^{b} = 32\pi^2 \quad \frac{\left|K_{00,10}^{10}\right|^2\ \left|K_{00,1-1}^{01}\right|^2}{2E_0 - E_{0,1} - E_{1,0}} + \frac{\left|K_{00,10}^{10}\right|^2\ \left|K_{00,1-1}^{11}\right|^2}{2E_0 - E_{1,0} - E_{1,1}} \tag{7.24}$$

$$C_{6d}^{c} = 8\pi^2 \quad \frac{\left|K_{00,1-1}^{01}\right|^4}{2E_0 - 2E_{0,1}} + \frac{2\ \left|K_{00,1-1}^{01}\right|^2\ \left|K_{00,1-1}^{11}\right|^2}{2E_0 - E_{0,1} - E_{1,1}} + \frac{\left|K_{00,1-1}^{11}\right|^4}{2E_0 - 2E_{1,1}} \quad . \tag{7.25}$$

In this large ω regime, the only term making $C_{6d}^{c} = 9C_{6d}^{a}$ not an exact relationship is $2\ \left|K_{00,10}^{10}\right|^4/(2E_0 - 2E_{1,0})$ in C_{6d}^{a}. This term declines rapidly with increasing ω: rigorously computing the ratio C_{6d}^{c}/C_{6d}^{a} for $\omega \quad 1$ limit shows the explicit ω dependence:

$$C_{6d}^{c}/C_{6d}^{a} \to 9 + 9 \quad \overline{2/\omega^3} - 9/(2\omega) \tag{7.26}$$

We now calculate the induction term,

$$V_i(R,\theta) = \frac{128\pi^3 d^4 n^8}{3R^6} \sum_{\tilde{N}_B\ \ M_B|\leq 1} \frac{\left[\begin{pmatrix} 1 & 1 & 2 \\ 0 & -M_B & M_B \end{pmatrix} K_{00,10}^{00} K_{00,1-M_B}^{\tilde{N}_B M_B}\right]^2}{E_0 - E_{\tilde{N}_B, M_B}}, \tag{7.27}$$

including only terms with $\tilde{N}_B \leq 1$ for the same reasons given above. Once again, after collecting terms with the same angle-dependence Eq. 7.5 is found and the coefficients are defined

$$C_{6i}^{a} = \frac{16\pi^2}{9} \frac{\left|K_{00,10}^{00}\right|^2\ \left|K_{00,10}^{10}\right|^2}{E_0 - E_{1,0}} \tag{7.28}$$

$$C_{6i}^{b} = 16\pi^2\ \left|K_{00,10}^{00}\right|^2 \quad \frac{\left|K_{00,1-1}^{01}\right|^2}{E_0 - E_{0,1}} + \frac{\left|K_{00,1-1}^{11}\right|^2}{E_0 - E_{1,1}} \quad . \tag{7.29}$$

Comparing C^a_{6i} with C^a_{6d}, the ratio $16/8 = 2$ is indicative of the relationship $C^a_{6i} = 2C^a_{6d}$, although it is not transparent how the different terms within the parentheses are equivalent. Once again, evaluating this ratio in the large ω limit reveals:

$$C^a_{6i}/C^a_{6d} = 2 - 2 \quad \overline{2/\omega}. \tag{7.30}$$

Finally, computing the ratios C^b_{6i}/C, where C is any of the other coefficients, in the large ω limit shows that all of these ratios increase, at worst, as $\sqrt{\omega}$, explaining the large size of this coefficient compared to the rest. We have now gained a more satisfactory understanding of the behavior of these coefficients, otherwise determined purely numerically in the perturbation theory calculation in the exact pendular state basis set. We can now study the potential surface itself, displayed for $n = 24$ in Fig. 7.5. Two different plots are given: in panel a three cuts of the potential surface at $\theta = 0^o, \theta_{M,24}$, and 90^o are plotted, while panel b displays a density plot of the potential. Lines of force are superimposed, and the inner(outer) white contours represent the blockade radius for 0.5(0.1)MHz. At this scale this potential is largely determined by the dipole-dipole interaction, as hinted at by Fig. 7.4, with higher order effects playing a dominant role near $\theta_{M,n}$. This is seen in panel a, where the red dashed curves only include the DDI term, revealing that near the magic angle the higher order terms cause a repulsive barrier to form rather than the purely repulsive potential expected from the DDI alone.

7.3 Results and discussion

Fig. 7.6 displays the key result of this article: the predicted density of butterfly molecules for a laser bandwidth $\Gamma = 0.5$MHz for several n values. The n-dependent magic angle $\theta_{M,n}$ ranges from $56.7^{\rm o} - 57.3^{\rm o}$ (0.99-1.0 radians) [2] and differs slightly

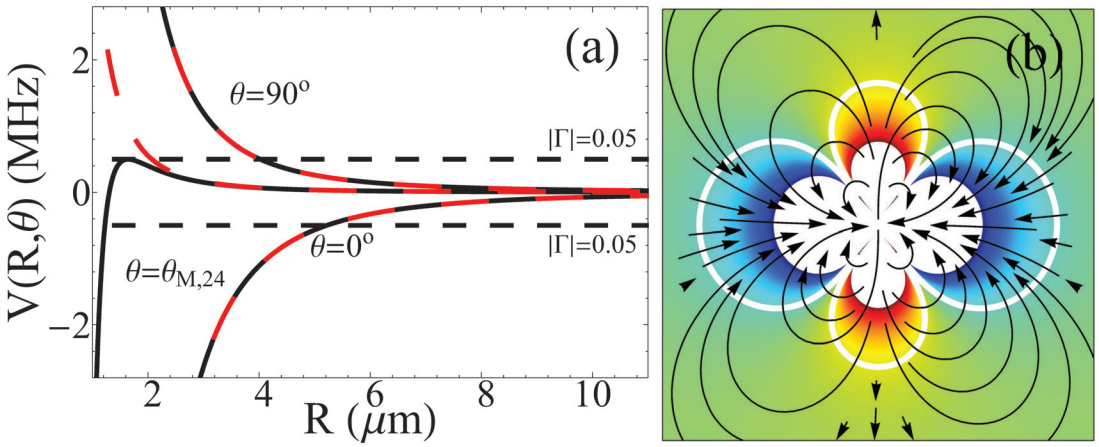

Figure 7.5. (a) The interaction potential $V(R,\theta)$ for $n = 24$ is plotted for three exemplary θ values. The pure dipole-dipole attraction is shown as in the dashed red curves, showing the importance of higher order terms near the magic angle. (b) The same potential is shown in cartesian coordinates, where blue(red) regions are attractive(repulsive). The inner white region (outer white contour) is the blockade radius satisfying $|V(R_B)| \geq \Gamma$, where $\Gamma = 0.5(0.1)$MHz. Lines of force are overlayed. The length of a side of the figure is 2×10^5 a.u. This figure is taken from Ref. [1].

from the DDI magic angle $\theta_M = 54.7^\circ$ due to the higher-order n-dependent terms in $V(R,\theta)$. Decreasing with n due to the stronger interactions at higher n, the density is ~ 4 times greater at $\theta_{M,n}$ than at $\theta = 0$ and corresponds to a maximum blockade radius of $\sim 1\mu$m. The inset highlights the region near the $\theta_{M,n}$ to exaggerate the striking behavior here, in particular the discontinuity for θ barely greater than $\theta_{M,n}$. At this point the density drops discontinously. This stems from the interplay between the attractive van der Waals interactions and the DDI, as revealed in Fig. 7.5a. When the latter interaction is repulsive, a potential barrier is created for R

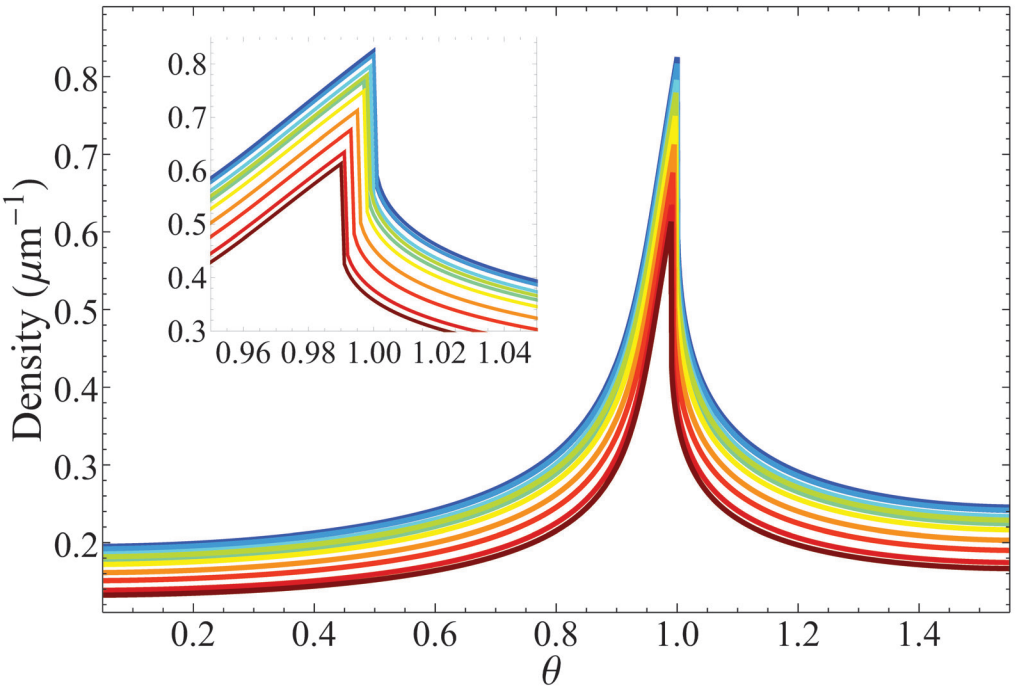

Figure 7.6. Simulated density as a function of the angle between the field and trap axes. As n increases from 20-40 the color changes from blue to red. The inset shows the density discontinuity for $\theta > \theta_{M_n}$. This figure is taken from Ref. [1].

greater than the inner crossing point where $V(R, \theta) = -\Gamma$. As the DDI increases relative to the van der Waals terms this repulsive barrier increases until it reaches $+\Gamma$, shifting the blockade radius suddenly. Fig. 7.7 displayed a type of experimental signature one might obtain via an atomic-imaging tool, such as that demonstrated in [260].

To perform this experiment large atomic densities are required: a density of $2 \times 10^{15}\text{cm}^{-3}$ gives two butterfly molecules per blockade volume. More favorable conditions are granted at higher Rydberg levels, where the interaction strengths are

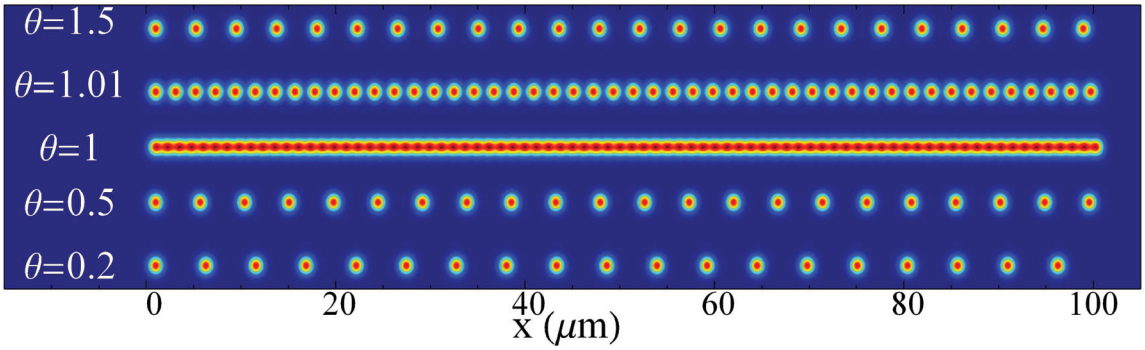

Figure 7.7. Simulated measurements of the molecular yield in a one-dimensional arrangement. Near the magic angle the density increases dramatically, yielding an obvious experimental signature.

greater and the formation probability is enhanced due to the larger internuclear distance. A narrower bandwidth laser extends the effective range of the intermolecular interactions. Finally, an alternative setup could use a Q1D optical lattice in a doubly-occupied Mott insulator state [156]. Other experimental schemes involving different classes of Rydberg molecules could also be studied: for example, trilobite molecules, through two-photon excitation of either Cs_2 [145,154] or Ca_2 as presented in Chapter 5. The larger bond lengths and dipole moments of these molecules allow for more favorable density conditions. However, their lifetimes are shorter and the two-photon excitation is more difficult. Even low-l molecules exhibit weakly polar behavior from their small admixture of trilobite-sized dipole moments [134,270].

The dipolar length, which characterizes the length scale of the DDI, is $a_{dd} = \frac{d^2 m}{12\pi\epsilon_0\hbar^2}$ (in SI units), where m is the mass of the particles. For the butterfly molecules, $a_{dd} \sim 10^7 - 10^8 a_0$ (0.05 - 0.5 cm), whereas for the typical heteronuclear molecule KRb, $a_{dd} \sim 1\mu m$. This overwhelming difference translates into huge dipolar interactions

relative to ultracold collision interactions, characterized by the scattering length a. We assume that the butterfly-butterfly scattering length is the geometric size of the molecule, i.e., $a = 4n^2$ a$_0$. The key ratio $\varepsilon_{dd} = a_{dd}/a$, which is $\sim 10^4 - 10^5$ for butterfly molecules and 20 for KRb, characterizes the importance of dipolar physics. For magnetic atoms such as Cr or Dy a_{dd} ranges from 16 to 130 a_0, giving $\varepsilon_{dd} \sim 1$ depending on the value of a. Following the work of Kalia and Vashishta [271], the present proposal leads to a crystal phase for butterfly molecules for the assumed $\sim \mu$K temperature. Indeed, the predicted one-dimensional array of molecules should resemble a linear crystal structure due to the fact that butterfly molecules are in the strongly interacting regime at ultracold temperatures. Moreover, the Tomonaga Luttinger liquid parameter [237], given by $K = \rho a_{dd}$ in the strongly interacting regime [272, 273], is $\sim 10^3$ which clearly indicates the absence of density fluctuations and the prevalence of phase fluctuations.

An obvious generalization of this study is the extension to two or three dimensional systems. These should exhibit some form of large-scale structure or long-range correlations. As a proof of principle, we simulated the excitation of Rydberg molecules in a 2D gas. For simplify, only the dipole-dipole term of the was included:

$$V(R,\theta) \approx -\frac{2C_3 d^2 n^4}{R^3} P_2(\cos\theta). \tag{7.31}$$

A stochastic treatment of the molecular association process was employed to determine realistic experimental behavior through the following process. First, atoms were randomly seeded throughout a large 2D region. Of these, a list of molecular "candidates" were found which had the right orientation with respect to the electric field and the correct bond length. Once the excitation laser is turned on these candidates can be excited to a butterfly molecule upon absorbing a photon. However, this cannot occur if the total intermolecular interaction, $|\quad_i V_i|$, between this candidate

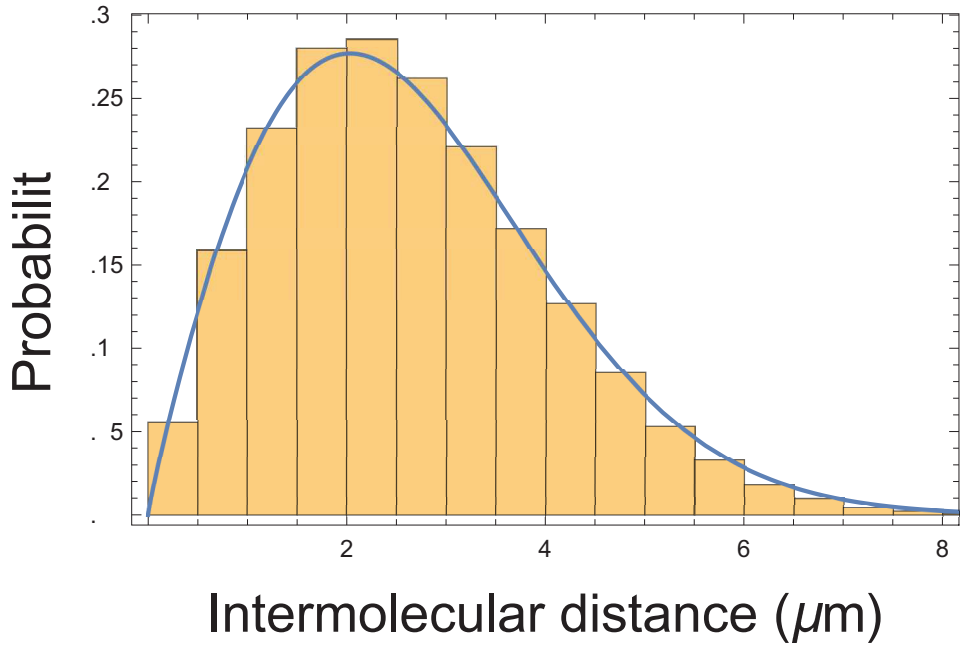

Figure 7.8. Nearest neighbor distribution of simulated butterfly molecules. The blue line is the fit function $(1.243 \times 10^{-5}) r^{0.9} e^{-0.1234 r^{1.9}}$; the nearest-neighbor distribution in two dimensions has the form re^{-br^2}.

molecule and all pre-formed molecules exceeds the laser bandwidth. We therefore check if this criterion is matched before adding each candidate molecule, and discard it otherwise. In this way the position and number of molecules created in the system grows stochastically.

For this proof of concept calculation, an 2D area of size πR^2, where $R = 3 \times 10^7$ a_0, was chosen to host a large number, 2.8×10^5, of candidate molecules at a density of $1 \times 10^{-10} a_0^{-2}$. The nearest-neighbor distribution of these candidate molecules fits the expected distribution, are^{-br^2}, very well, and shows a mean nearest-neighbor distribution of about 2 μm (see Fig, 7.8). Of these candidate particles, 10^5 were

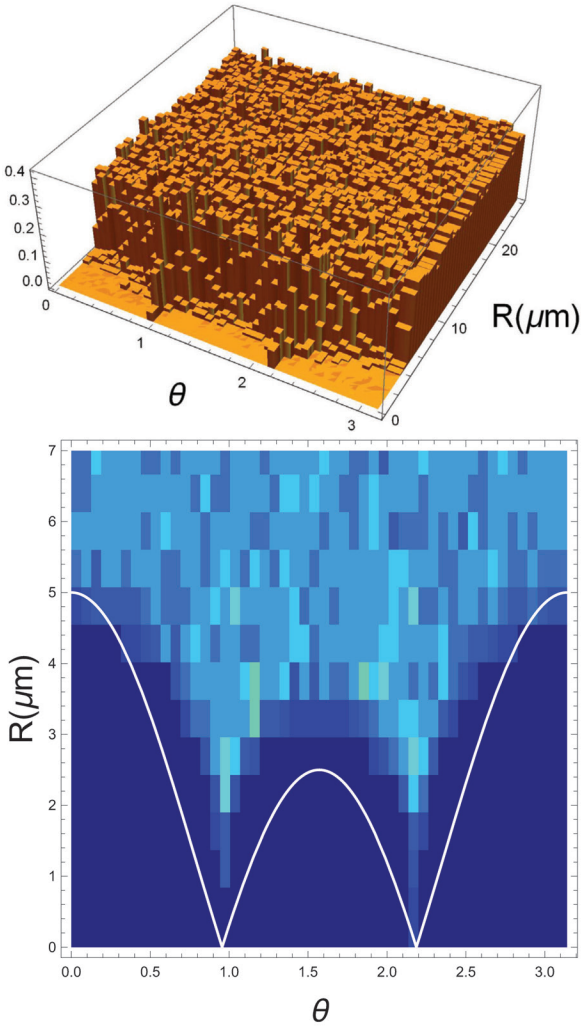

Figure 7.9. Histograms of relative intermolecular distances and angles, as described in the text. Top panel: 3D histogram; bottom panel: density plot of the histogram with the angular-distribution of the dipole-dipole interaction overlayed.

selected at random to absorb a photon, and of these about 50000 were not prevented by the intermolecular blockade. This relatively high number relative to the number of

candidates is due to the large interparticle separation In a less dilute gas the blockade effect should have a much stronger impact, but might be obscured by many-body effects.

Of these molecules, the relative separations and angles with respect to the aligning field were found, and from by histogramming these distances and angles a two-body correlation function can be found. This is shown in Fig. 7.9, the main result of this exploration. As expected, this correlation function exhibits the angular distribution signifying the dipole-dipole interaction at close interparticle separations, showing essentially no counts for molecules within a blockade radius except near the magic angle and even tracing out the general angular shape (lower panel). At large R the correlation function becomes isotropic as the interactions drop off rapidly. This sort of calculation would be an interesting, and more easily experimentally attainable, approach to explore dipolar physics in Rydberg molecules. The extension to three-dimensions would likewise be trivial here. Finally, along the lines of a much more involved recent study of dipole-dipole interactions between Rydberg atoms [274], these classical calculations could be incorporated into a more sophisticated quantum-mechanical calculation.

7.4 Conclusions

This chapter presented an effective method to control the density of pendular butterfly molecules in a one-dimensional trap as a means of exploring the dipole-dipole interactions present in this system, and to explore the unique and exaggerated properties of this scheme contrasted with Rydberg atomic systems, polar molecules, or magnetic atoms. Future effort could explore the consequences of the inherently mixed nature of this system, consisting of dipolar impurities immersed

in a sea of bosons, and thus could study polaron-polaron interactions in ultracold gases. The tunability of the polaron interaction provides information about the role of the internal structure of the impurities in the dynamics of the quasiparticles, which would elucidate the validity of the Fröhlich Hamiltonian [275] in the weak interaction regime and the study of the role of many-body correlations in the strong interaction regime, going beyond the single polaron physics very recently observed in ultracold gases [276,277]. The newly developed theory of angulon and pendulon quasiparticles could be generalized to include impurity interactions, and could be realized in the present system [278, 279]. In two or three dimensions it could become possible to study the quantum phase transition between the superfluid and supersolid phases, or between supersolid and crystal phases [237]. Decay mechanisms are also interesting and largely unstudied. These decay mechanisms, such as Penning ionization, can be investigated using the anistropic interactions, since these can either be attractive, leading to collapse, or repulsive due to a potential barrier, stabilizing the condensate. It is possible that this long-range interaction could lead to the formation of tetramers, consisting of two Rydberg molecules bound together; this would be a fascinating combination of long-range Rydberg-neutral molecules and Rydberg-Rydberg macrodimers.

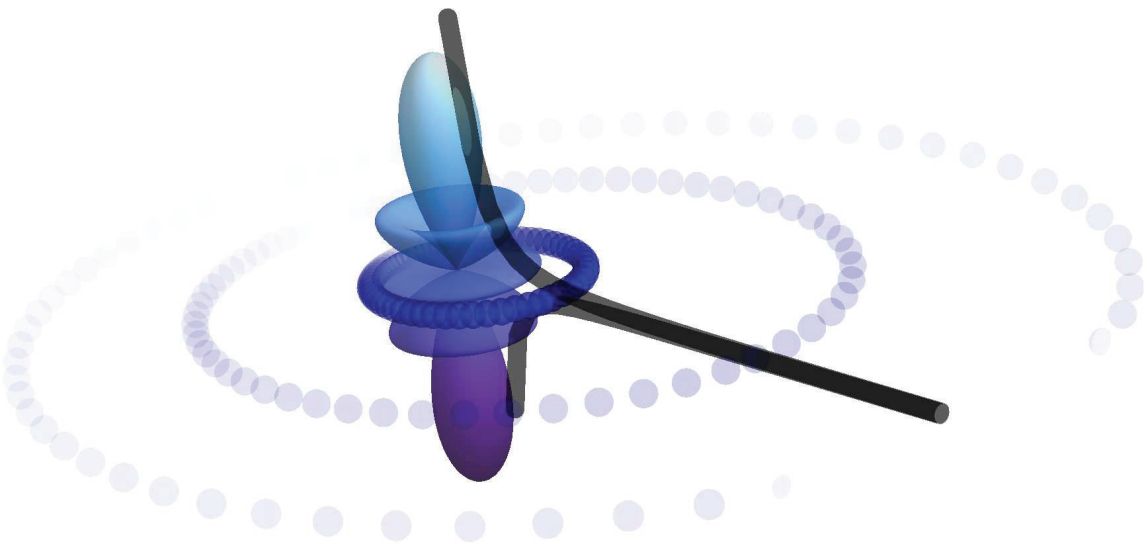

Figure 7.10. Chapter 8 describes negative ion photodetachment for highly excited states with large angular momenta, depicted here. The ejected electron escapes to infinity while feeling the effects of very strong long-range potentials, which can be either repulsive or attractive, as depicted here.

8. PHOTODETACHMENT OF EXCITED NEGATIVE IONS

This chapter presents our study of photodetachment of alkali negative ions. We are primarily interested in photodetachment into the excited 5f and 5g states of potassium, but we also make some predictions about the 6f, 6g, and 6h partial cross sections in order to help elucidate the behavior of the 5f and 5g states. A similar regime in sodium is studied as well to help unravel the fundamental physics. We find that near-degeneracies in the energy spectrum, due to the high angular excitation of the neutral atom and the photodetached electron, play a critical role in determining threshold properties and the behavior of partial and total photodetachment cross sections. This study examines recent cross section measurements and interprets them in terms of the relevant dipole-field parameters, assuming exact degeneracy of the residual high-l atomic states, rather than in terms of the atomic polarizabilities more commonly used.

8.1 Background

Negative ions of light alkali atoms such as lithium, sodium, and potassium are fertile sources of information, both theoretical and experimental, about the behavior of correlated electrons, shape and Fano-Feshbach resonances, and Wigner threshold laws for dissociation processes. These anions support only one bound state of ${}^1S^e$ symmetry, typically with an electron affinity on the order of half of an eV. Absorption

of an energetic photon ejects an electron and excites the residual atom, creating many fascinating resonance and threshold structures in the total and partial cross sections [11].

This process is very similar to photoionization in neutral atoms with two active electrons. Photoionization is typified by an infinite series of Fano-Feshbach resonances in the autoionization continuum [280]. Here the interactions are dominated by the strong Coulomb attraction between the ionized electron and the positively-charged core, and subtle electron-electron correlation is often masked. In negative ion photodetachment the residual core is neutral, so correlation is revealed by the much weaker forces between the electron and the atom. For example, in hydrogen, the high degeneracy of excited states and the correlation between electrons leads to a linear Stark shift and a dipole $\frac{-\alpha_d^2-1/4}{2r^2}$ potential [281]. This potential has the remarkable property that for real α_d it supports an infinite number of resonances states (within the non-relativistic limit; relativistic effects that break the degeneracy truncate this infinite series) [282]. This has been extensively studied theoretically, and verified in an impressive series of experiments at Los Alamos [43–46, 67].

In the alkali negative ions, the breaking of degeneracy by the complex core yields instead a polarization potential, $-\frac{\alpha}{2r^4}$, which only supports a finite number of bound states. Various theoretical efforts dedicated to accounting for this polarizability have been developed [63, 66, 283]. In scenarios where the residual atom remains in a high angular momentum state of a highly excited state, $l_{max} = n-1$, these polarizabilities rapidly reach values on the order of $10^4 - 10^6$ atomic units, since $\alpha \sim n^7$. At sufficiently high l_{max} a nonintuitive quantum phenonemon arises: the polarizability can become negative, leading to an entirely repulsive potential. Table 8.1 shows our calculated channel polarizabilities for these states. Experimental investigations of negative ion photodetachment in channels possessing these huge polarizabilities were pub-

l	n	$\alpha(nl, \varepsilon l_-)$	$\alpha(nl, \varepsilon l_+)$	l	n	$\alpha(nl, \varepsilon l_-)$	$\alpha(nl, \varepsilon l_+)$
s	4	-	307.5	p	4	619.5	720.8
	5	-	4996.1		5	7204	8237
	6	-	32867		6	44170	49583
	7	-	139013		7	180730	199873
	8	-	449308		8	571507	624121
d	3	1865	1931	f	4	-24045	-24564
	4	43268	44354		5	5.008(6)	5.053(6)
	5	230154	235456		6	2.652(7)	2.676(7)
	6	837825	855971		7	9.205(7)	9.288(7)
	7	2.450(6)	2.500(6)		8	2.565 (8)	2.588(8)
g	5	-5.151(6)	-5.178(6)	h	6	-7.165(7)	-7.191(7)
	6	4.461(7)	4.474(7)		7	2.615(8)	2.618(8)
	7	2.305(8)	2.313(8)		8	1.366(9)	1.368(9)

Table 8.1.
Channel-dependent dipole polarizabilities, in atomic units, for potassium. $l_- = l - 1$, $l_+ = l + 1$, and (A) represents $\times 10^A$.

lished recently for potassium, sodium, and cesium [47, 49, 284, 285]. Partial and total photodetachment cross sections of the $^1P^o$ symmetry were recorded, and fascinating deviations from the standard Wigner threshold law, $\sigma = (E_{h\nu} - E_{th})^{l+1/2} = E_e^{l+1/2}$, in sodium and potassium were interpreted as resulting from these huge, negative polarizabilities [88, 286, 287].

We calculated partial and total cross sections for both Na and K over a range of photon energies 4.5 - 5.5 eV. Even though the final state symmetry following single-photon detachment is $^1P^o$, the two electrons may be both excited into states of very high angular momentum. The most interesting regions for us are just above the nearly degenerate $5f$ and $5g$ thresholds of both atoms. In potassium, Ref. [47] reported that the partial cross sections observed in these two channels differed wildly: a steplike onset just above the channel opening is seen in the $5f$ channel, while the cross section rises very slowly in the $5g$ channel, modulated by a broad resonance. The authors reported that these two effects were differentiated by the effect of the polarization potential, which is either strongly repulsive or attractive depending on the channel. A similar measurement in Na^- photodetachment, which exhibits the same behavior without the observed resonance, was performed to test this explanation [49]. These measurements are displayed in Fig. 8.1.

8.2 Two competing models

In this section we present two competing models to explain the behavior of these partial cross sections. The first, a semiclassical model emphasizing the role of the huge polarizabilities, comes from Ref. [47]. The second, which instead emphasizes the role of the quasi-degeneracy of these states in creating a dipole-type potential, stems from our analysis of the adiabatic potential energy curves determined by our full eigenchannel R-matrix calculation. The details of this full calculation are given in the next section.

Semiclassical model: The step-like onset in the $5f$ channel is caused by the hugely attractive polarization potential, which greatly reduces the centrifugal barrier. Assuming that the dominant ejection channel is $5f\epsilon d$, a check of the total potential,

$-\frac{\alpha}{2r^4} + \frac{l(l+1)}{2r^2}$, gives a barrier height around 30 μeV. The partial cross section in this channel should therefore saturate rapidly just above threshold.

To explain photodetachment into the $5g$ channel, the semiclassical model of Ref. [47] begins with the radial Schrödinger equation including the polarization potential:

$$\frac{d^2u_{nl}(r)}{dr^2} = -\frac{\alpha}{r^4} + \frac{l(l+1)}{r^2} - 2E \quad u_{nl}(r) = [p(r)]^2 u_{nl}(r).$$

Making the approximation that these potentials hold even to small r, this totally repulsive potential (for the negative α of interest) defines a classically forbidden region where $r < r_0$, where $r_0 = \left(\frac{|\alpha|}{2E}\right)^{1/4}$ is the classical turning point. The centrifugal repulsion is neglected in defining r_0 since α is so large. In this region the final state wave function for the free electron is given by the Wentzel-Kramers-Brillioun (WKB) expression

$$\psi_k(r) = \frac{C(E_e)}{r\sqrt{p(r)}} \exp\left(-\int_r^{r_0} p(x)\mathrm{d}x\right), r < r_0. \tag{8.1}$$

Here the wavenumber is $k = \sqrt{2E_e}$, the momentum is $p(r)$, and $C(E_e) \approx E_e^{-1/4}$ is a normalization constant ensuring continuum normalization in momentum space. Upon evaluating the integral in the exponential, keeping only first-order terms in r/r_0, and then using that approximate wave function to compute the scattering amplitude between initial and final states, Ref. [47] claims that the cross section above threshold follows an exponential threshold law:

$$\sigma_{th} \propto \exp[DE_e^{1/4}]. \tag{8.2}$$

They applied this to the 5g partial cross sections of both potassium and sodium, and found that it fit the partial cross sections reasonably well. A possible resonance feature in the potassium measurements complicated the analysis somewhat [47]. Within their model, the fit parameter D is related to the polarizability by $D = 2850|\alpha|^{1/4}$, so

they could extract polarizabilities that were indeed large but still nearly two orders of magnitude smaller than obtained theoretically, casting doubt on the reliability of this model, but not denying its qualitative agreement.

Our alternative approach is based on the assumption that, over the energy range measured, the two thresholds are essentially exactly degenerate, and therefore an improved analysis of the relevant physics involves the dipole potentials. To model this, we included only the two most relevant photodetachment channels: $\mathrm{K}(5f) + e^-(\epsilon d)$ and $\mathrm{K}(5g) + e^-(\epsilon f)$. The development of this model closely follows [10, 63]. The coupled channel equations for the radial wave functions $M_j(r)$, discussed in section 2.1, are in this case

$$-\frac{1}{2}\frac{d^2}{dr^2} + \frac{1}{2}\frac{l_j(l_j+1)}{r^2} - (E - \ _j) \quad M_j(r) + \quad \underset{i}{} V_{ij}(r)M_i(r) = 0, \tag{8.3}$$

where $V_{ij} = \ i|\frac{1}{r^2}r_c\cos\theta_c|j$ and $\ _j$ is the threshold energy of channel j. Using hydrogenic wave functions to approximate the exact wave functions of these highly excited states we obtain a radial matrix element of $-45/2$ and an angular matrix element equal to $-2\sqrt{3}/7$. Including the splitting between these two channels, Δ -317 GHz, the coupled channel equations of equation (8.3) simplify to:

$$-\frac{1}{2}\frac{d^2}{dr^2}\underline{1}M(r) + \begin{pmatrix} \frac{6}{2r^2} - (E - \ _{5f}) & \frac{90\sqrt{3}}{14r^2} \\ \frac{90\sqrt{3}}{14r^2} & \frac{12}{2r^2} - (E - \ _{5g}) \end{pmatrix} M(r) = 0, \tag{8.4}$$

where $\underline{1}$ is the identity matrix. We proceed, closely following Watanabe and Greene [63], by solving this equation adiabatically. The adiabatic transformation of Eq. 8.4 gives

$$-\frac{1}{2} \quad \underline{1}\frac{d}{dr} + \underline{P}(r) \quad ^2 - [(E\underline{1} - \_) - \underline{u}(r)] \quad F(r) = 0, \tag{8.5}$$

where $F(r) = \underline{W}(r)M(r)$, $\underline{u}(r)$ is a diagonal matrix of the eigenvalues of the coupling matrix in equation (8.4), $\underline{W}(r)$ is the orthogonal matrix of their eigenvectors, and the

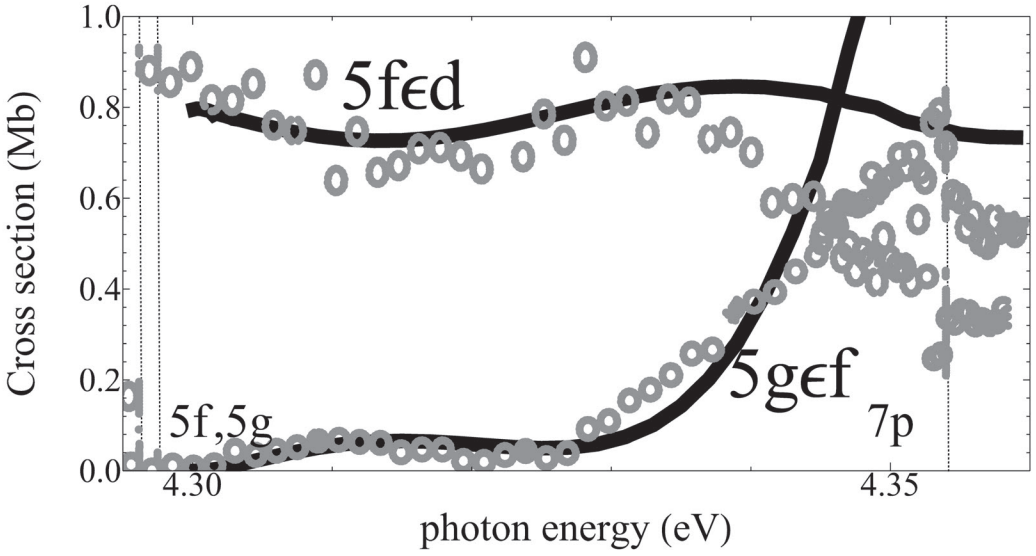

Figure 8.1. The $5g\epsilon f$ and $5f\epsilon d$ partial cross sections over the energy range between the 5f,5g thresholds and 7p threshold. Qualitatively, the behavior of the experimental measurement (dots) matches the simple two-channel model presented in the text (black lines) [47].

P-matrix is $\underline{P} = \underline{W}(r)\frac{d}{dr}\underline{W}^T(r)$. This matrix contains all interchannel coupling now in the adiabatic representation. This coupled set of equations is solved for $\vec{M}(r)$, and the scattering phase shifts are obtained by comparison with the asymptotic Bessel function solutions. As in section 2.1.3, this process gives the smooth dipole matrix elements in each channel, $d_i^S = \sum_\beta \left[(\underline{I} + i\underline{J})^{-1}\right]_{i\beta} d_\beta$, where d_β are the reduced dipole elements connecting the intial and final states and the matrices $\underline{I}$ and $\underline{J}$ are given by Wronskians of the long-range Bessel functions and numerical solutions to the coupled channel equation derived above. The partial cross sections are, finally, proportional to the squared smooth dipole matrix elements. Since this two-channel model did not consider any of the two-electron physics taking place in this region of the potassium

atom, the reduced dipole elements and the initial condition of the escaping electron are unknown. We therefore vary these parameters to obtain partial cross sections that match the experiment to test the validity of this model. Fig. 8.1 shows the experimental measurements and the results of this simple model, showing that they are in relatively good agreement, and that our model even gives the small peak that is identified by [48, 284] as a resonance.

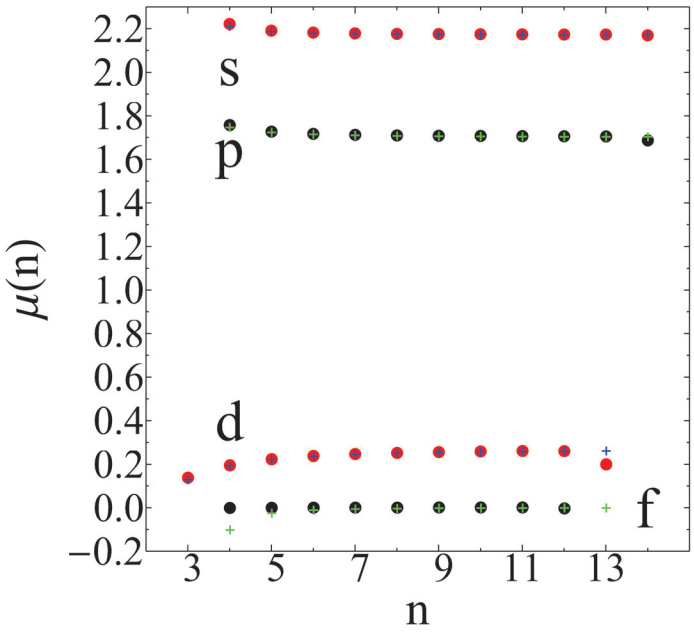

Figure 8.2. Quantum defects of potassium. The solid points give the lowest one-electron energies obtained in our calculation, and the + symbols give the fitted quantum defects given by Table 2.1.

8.3 Eigenchannel R-matrix calculation

We have supplemented this approximate two-channel model with a full R-matrix calculation along the lines of section 2.1. We used 15 partial waves with 98 closed and 2 open functions for each. A large R-matrix box size of 350 atomic units is used to ensure that only one electron leaves the box for all excited states under consideration. This requires a maximum box size $\sim 2n_{max}^2 < 150$. Having such a large R-matrix box also helps to include more of the long-range physics stemming from these highly polarizable atomic states in the full two-electron calculation. Even so, the polarization potentials still strongly couple different channels outside of the R-matrix box, and so it is critical to match to numerical wave functions at the R-matrix radius. These were matched to spherical Bessel solutions at a distance of 2000 atomic units. For our potassium calculation we have used the model potential of Liu [48] to facilitate comparison with his results, whereas for sodium we used the potential found in [59]. In either case these model potentials give highly accurate energies for the excited states of the neutral atom, and are identical to at least four significant digits with appropriately fine-structure-averaged experimental energies. Figure 8.2 shows the calculated quantum defects of the target atomic states using this approach. Discrepancies at the lowest n occur because the fitted quantum defects of Table 2.1 are not accurate for the ground state; the solid points agree exactly with experimental spin-weighted energies. At high n the deviations signal the onset of one-electron states that no longer fit within the R-matrix box and are thus used to describe continuum states rather than realistic atomic states. In the final state calculation 18352 basis states were included based on these parameters; these improvements allowed us to push the limits of this calculation past what was reported in Refs.

[48,288], where the R-matrix approach was similarly used to study these same alkali anions.

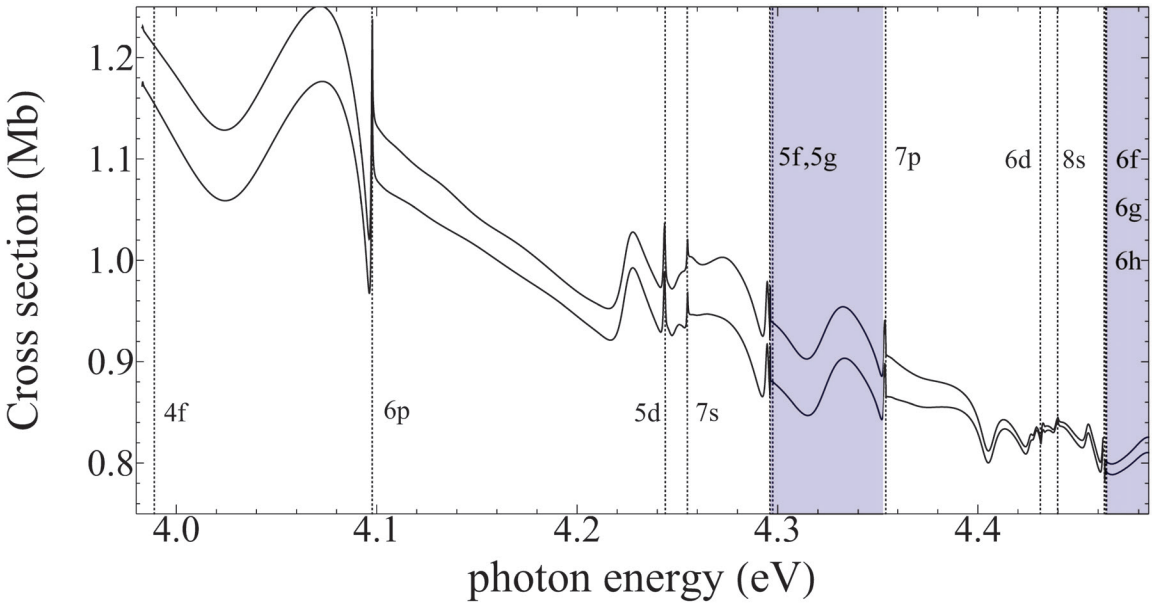

Figure 8.3. The total photodetachment cross section for potassium. Results in both length and velocity gauges are presented. The quality of these results is comparable to calculations peformed by Liu [48]. The two regions of interest are highlighted.

Figure 8.3 shows the total cross section for K^- photodetachment into the $^1P^o$ final state calculated over a wide range of photon energies. Our results are in good agreement with the calculation of [48] over the same energy ranges, although we have calculated 200 meV higher than reported there, extending up to the next hydrogenic manifold (the 6f,6g, and 6h channel openings). The agreement between length and velocity results signify that our results are adequately converged, but fu-

ture experimentation with the R-matrix box radius should be done to try to improve the agreement between these two measures. Since our interest lies in the partial cross sections, which show excellent agreement between length and velocity gauges, this is not a crucial point at this stage.

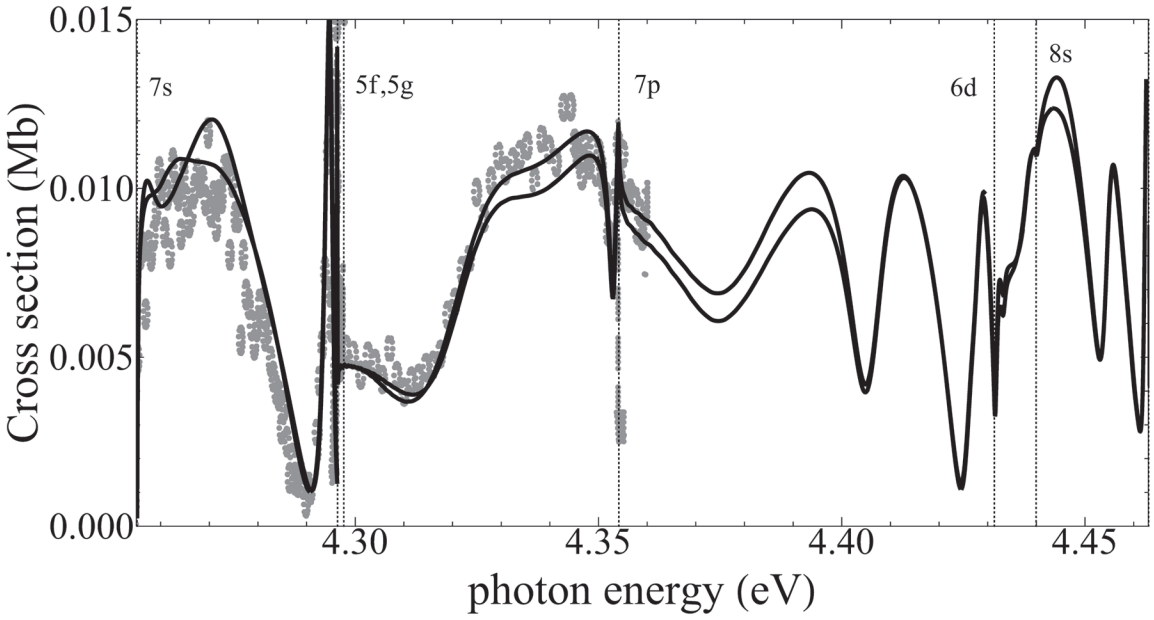

Figure 8.4. Observed (dots) and calculated (solid lines, length and velocity) 7s partial cross sections for potassium.

The 7s partial cross section is reported in Fig. 8.4. Here the polarization potential is an order of magnitude weaker than in the higher partial waves, and so the excellent agreement between the theory and experiment is not surprising as most of the critical physics is handled within the large R-matrix box. This is further confirmation that the R-matrix theory as implemented here will provide very accurate results, especially when the resonances and threshold cusps in this partial cross sec-

tion are considered. Above 4.35 eV the theory curve is a prediction, as data has not been reported above the 7p threshold. The $5f$ partial cross section is reported

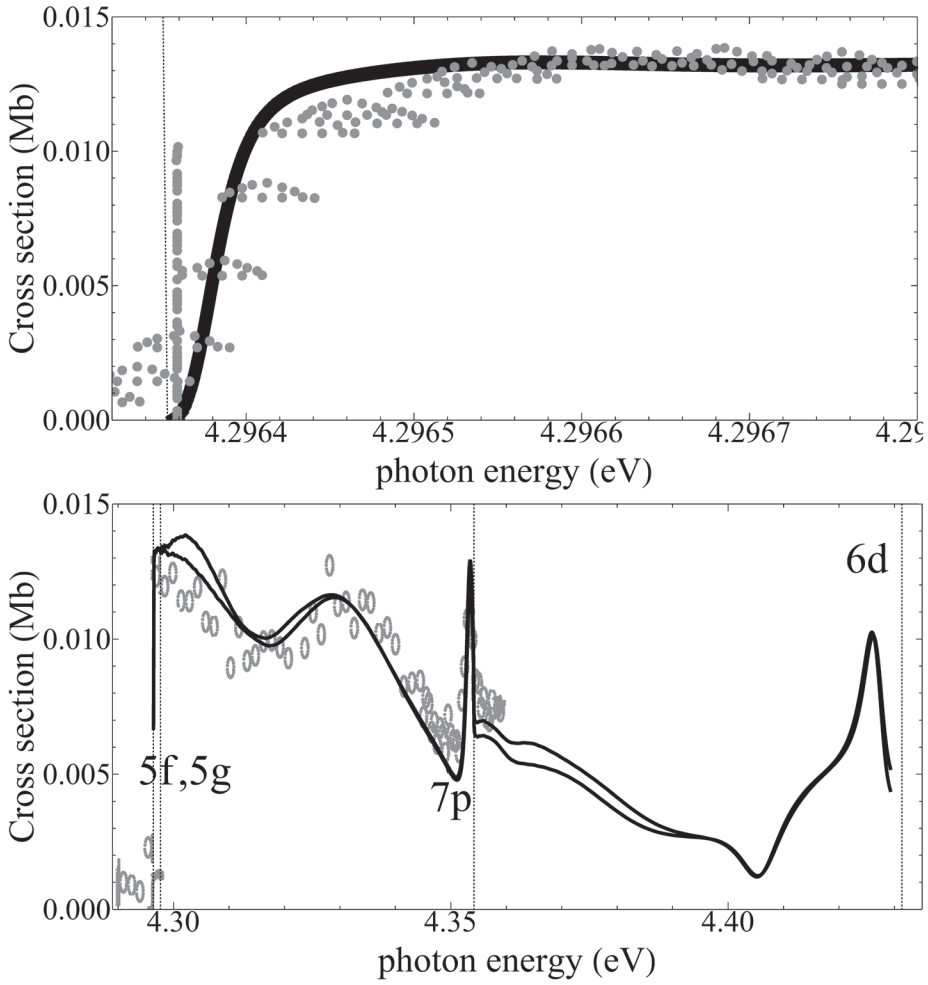

Figure 8.5. Observed (dots) and calculated (solid lines, length and velocity) $5f$ partial cross sections for potassium over the region between thresholds (top), and above both thresholds (bottom).

and compared with experiment in Fig. 8.5. In the first panel, we show just the tiny

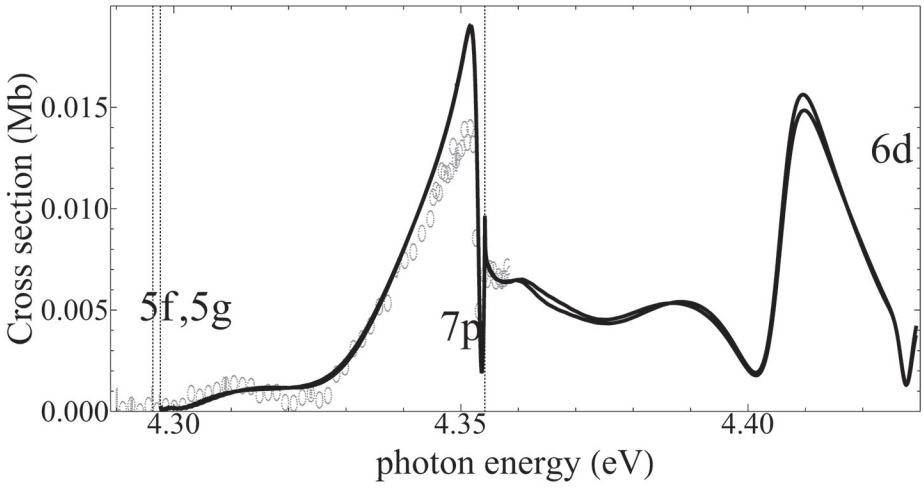

Figure 8.6. Observed (dots) and calculated (solid lines, length and velocity) $5g$ partial cross sections.

region in between the $5f$ and $5g$ thresholds, showing that we can resolve the rapid onset of the 5f partial cross section in good agreement with experiment. Above both thresholds, our calculation agrees very well with the gently modulated behavior of the cross section as reported by [47].

Fig. 8.6 shows the $5g$ partial cross sections over this same energy range. Our calculations are generally in good agreement with the observed values, but some discrepancies that are much stronger in this partial cross section than in the $5f$ and $7s$ partials reported previously could signify the appearance of additional physics. We first considered the possibility that the alignment of the fragments left behind by photodetachment – which, of course, have significant angular momenta and are thus very anisotropic –could be detected in this observation.

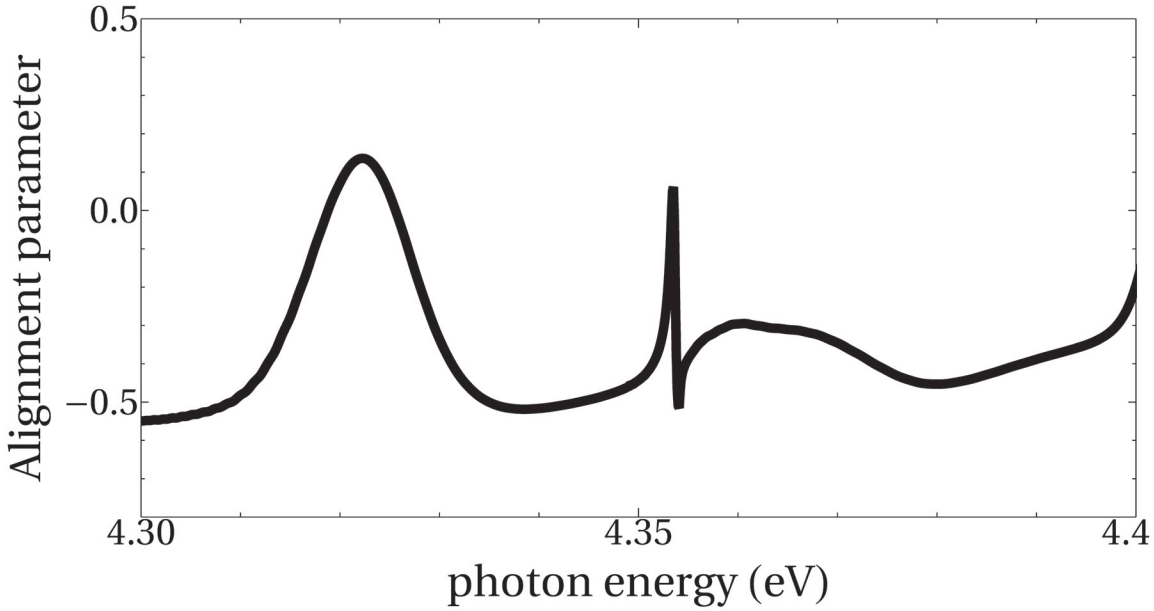

Figure 8.7. The alignment parameter for photodetachment into the $5g\epsilon f$ and $5g\epsilon h$ channels of potassium, plotted for the same energy range as Fig. 8.6. The peaks are correlated with the regions of interest in Fig. 8.6.

Quantitatively, the amount of aligment is given by the alignment parameter defined in Eq. 45 of [226]:

$$\mathcal{A}_0(l_c) = \frac{\sigma_{nl_c,l_c-1}\left(-\frac{2l_c+3}{5l_c}\right) - \sigma_{nl_c,l_c+1}\left(\frac{-(2l_c-1)}{5(l_c+1)}\right)}{\sigma_{nl_c,l_c-1} + \sigma_{nl_c,l_c+1}}, \tag{8.6}$$

where l_c is the angular momentum of the residual atomic core ($l_c = 4$ in the present case). The cross sections in Eq. 8.6 are the separate partial cross sections $5g\epsilon f$ and $5g\epsilon h$. Qualitatively, negative values of this alignment parameter are associated with large contributions from small M_L components, while small or positive values correspond to large M_L values. In the experiment, the excited residual atoms are detected by exciting them to a higher Rydberg state, which is then field ionized and

counted [284]. For the $5g$ partial cross section the upper Rydberg state is $23f$, so all states with maximal $|M_L| = 4$ are lost due to angular momentum selection rules during this process. This argument only holds if the polarizers of both laser photons are linear and parallel. This would imply that, if very high M_L values are heavily populated in the residual atomic state at certain energies, the measured cross section would be reduced since these cannot be detected. To model this, the cross section can be multiplied by the intensity for the excitation process from a state with total angular momentum J_i to one with $J_i - 1$, as is done in the experiment [226]

$$I = \frac{I_0}{3} \quad 1 + h^{(2)}_{J_i,J_f} \mathcal{A}_0(J_i) \quad , \; h^{(2)}_{J_i,J_i-1} = -\frac{J_i + 1}{2J_i - 1}. \tag{8.7}$$

In Fig. 8.7 the alignment parameter for the $5g$ state is shown over this same range of energies. Intriguingly, we see that in these regions where the full theory calculation disagrees most severely with the experimental points the alignment is most positive. This suggests that it is possible that these high M_L states are not being fully detected. Fig. 8.8 shows the partial cross section, multiplied by the energy-dependent intensity factor from Eq. 8.7, which a modest improvement over the calculation ignoring this possible alignment. Further work is necessary to fully justify this argument, but it looks promising that the anisotropy of these highly excited angular momentum states could be an interesting observable, and possibly has already been detected.

These results have shown that we can calculate and make predictions about this photodetachment process, but thus far they have not helped to explain the role of near-degeneracy in the photodetachment process. In particular, since the dipole approximation (where we assume that the $5f$ and $5g$ thresholds are degenerate) and the semiclassical model based on the large negative polarizability of the $5g$ state are both consistent with the observed partial cross sections and with the results of the full R-matrix theory, little can be claimed about the importance of this degeneracy

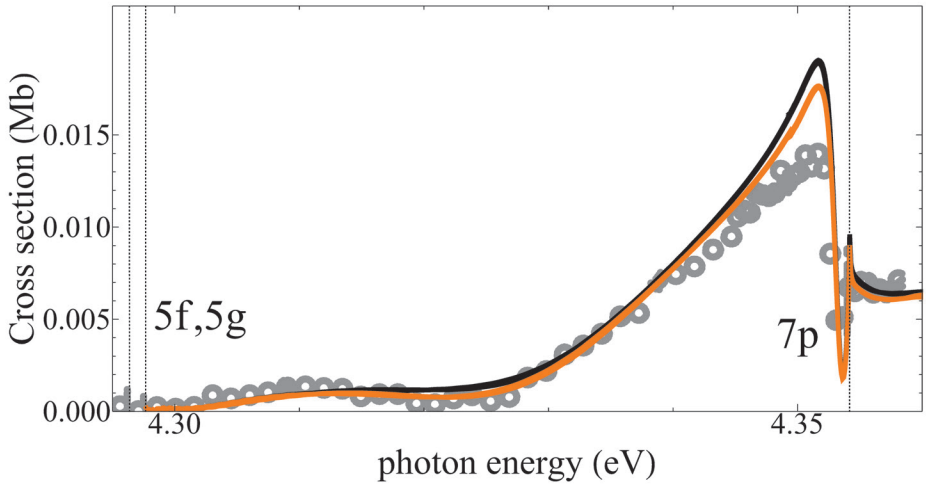

Figure 8.8. Observed (dots) and calculated (solid lines, length and velocity) $5g$ partial cross sections. The orange curve is modulated by the intensity, eq. 8.7.

thus far. To gain more information about this system and the relevant long-range physics, we will rely on three more lines of argumentation. First, we will consider the adiabatic potential energy curves, given by the two-electron calculation that is the basis of the R-matrix method, and see what these curves say about the long-range physics. Second, we will investigate these same partial cross sections in sodium. The resonance feature seen in the potassium results is missing in sodium, clarifying that the behavior of the $5g$ cross section is not caused by the resonance observed in potassium. Third, based on the information contained in the adiabatic potential energy curves, we will consider the next set of nearly degenerate states in potassium, the $6f$, $6g$, and $6h$ partial cross sections.

8.4 Analysis and conclusions

We first plot the adiabatic potential energy curves, i.e. the eigenvalues of the matrix $\delta_{ij}\quad{}_{1i}+\frac{l_{2i}(l_{2i}+1)}{2r^2}\quad+\quad\sum_{\lambda=1}^{3}\frac{d_{ij}^{\lambda}}{r^{\lambda+1}}$ at fixed values of r. Examination of these curves, shown in Figs. 8.9, 8.11, and 8.12, is a straightforward way to gain more intuition about this system and better understand the form of the long-range physics. These figures show potential energy curves in the energy ranges near potassium $(5f, 5g)$, sodium $(5d, 5f, 5g)$, and potassium $(6f, 6g, 6h)$, respectively. By comparing these adiabatic potential curves with the polarization potentials, shown in magenta, one can see that that it is only at very large distances that the polarization potentials begin to accurately describe the long-range potentials. Indeed, as demonstrated by the red curves, over much of the energy range of interest the potentials are much better described by r^{-2} potentials than the polarization potentials. These potentials even can be traced diabatically upwards through the avoided crossings between the adiabatic potentials. The simple two-channel model, extended to include the four and six channel degenerate subspaces, respectively, for the 5f,5g and 6f,6g,6h cases, gives the dipole parameters needed to compute these potentials. In the four-channel case we diagonalize the 4×4 matrix:

$$\begin{pmatrix} 6 & 0 & \frac{90\sqrt{3}}{7} & 0 \\ 0 & 20 & -\frac{5}{7} & 10\sqrt{5} \\ \frac{90\sqrt{3}}{7} & -\frac{5}{7} & 20 & 0 \\ 0 & 10\sqrt{5} & 0 & 30 \end{pmatrix}, \tag{8.8}$$

which has eigenvalues 47.9, 31.5, -13.5, and 2.1. In the six channel case for $6f$, $6g$, and $6h$ the eigenvalues of the coupling matrix are 80, 61.6, 34, 15, -21.9, and -38.6. In sodium, the $5d$, $5f$, and $5g$ thresholds are all nearly degenerate, and the coupling matrix has the eigenvalues 57.6, 43, 23.3, 8.3, -18.8, and -31.4.

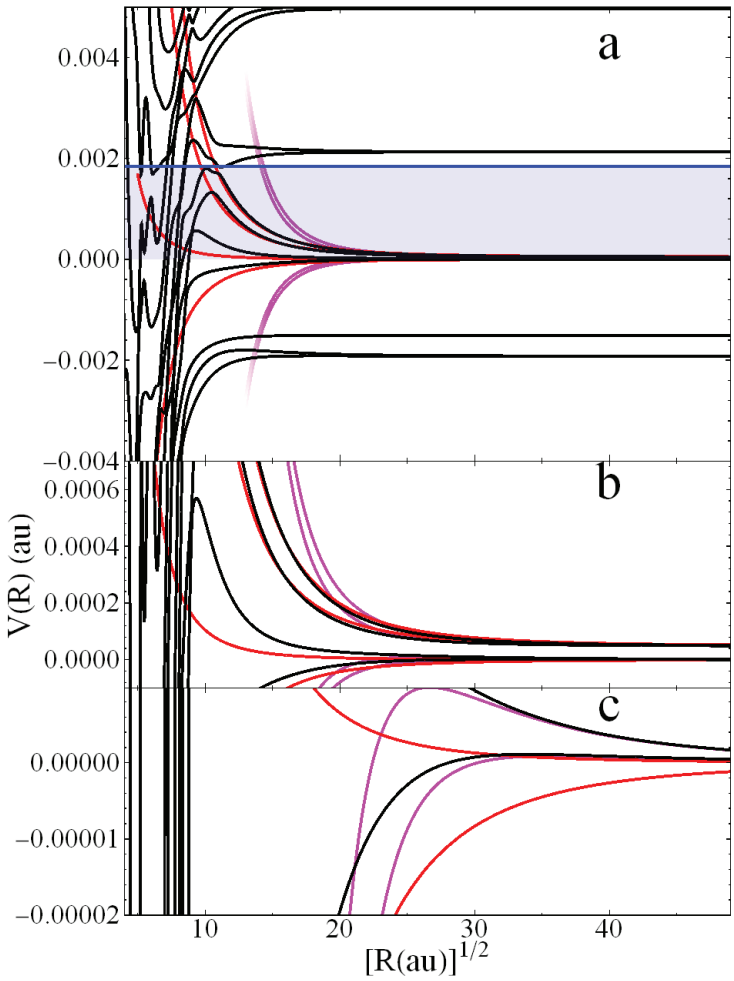

Figure 8.9. Long-range potential energy curves (black) for potassium, relative to the $5f$ level. In a), the region surveyed in the experiment is shown in blue. The red curves are the $a/2r^2$ potentials derived in the Gailitis-Damburg model, while the magenta curves are the $\alpha/2r^4$ potentials appropriate for the polarization potential. b) and c) show zooms of the $5f$ and $5g$ potentials.

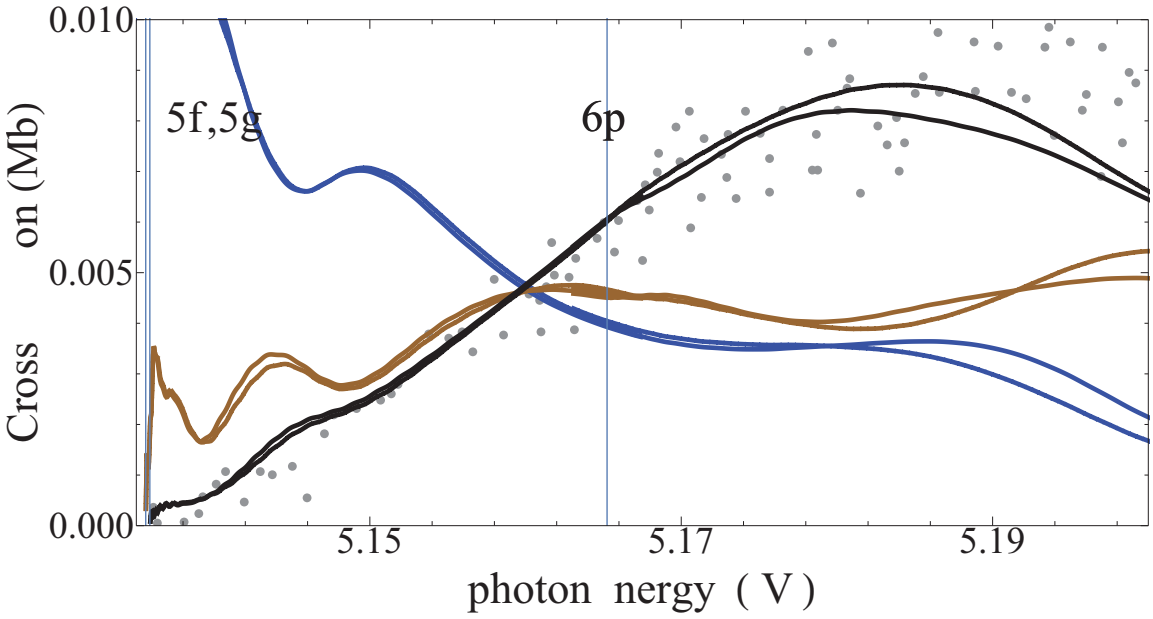

Figure 8.10. Observed (dots) and calculated (solid lines, length and velocity) partial cross sections. The blue curve is the 5d partial cross section, the brown curve is the 5f partial cross section, and the black curve is the 5g partial cross section, which was the only reported cross section measured over this energy range citeHanstorpNa.

As Fig. 8.9 shows, the potential energy curves are qualitatively similar for the $5f$ and $5g$ channels for both the polarizability and dipole approximations, even though the dipole approximation is a much better on a quantitative level. We thus turn to sodium to try to find a clear observable distinction between the properties of these long-range potentials. Fig. 8.10 shows our calculated $5d$, $5f$, and $5g$ partial cross sections along with the measured $5g$ cross section [49]. Again, the agreement is excellent. The 5g and 5d partial cross sections behave as the semiclassical polarizability model predicts, rising slowly above threshold due to a strongly repulsive potential, or sharply saturating then slowly oscillating well above threshold due to a very short

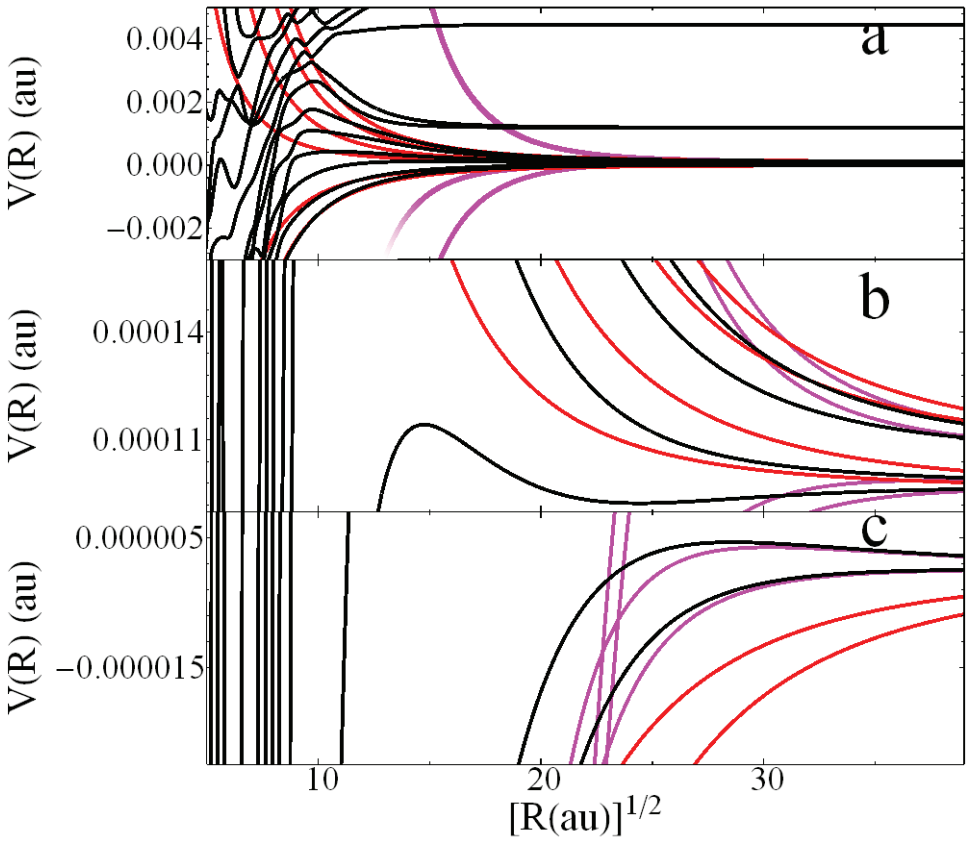

Figure 8.11. Long-range potential energy curves (black) for sodium, relative to the $5d$ state. The red curves are the $a/2r^2$ potentials derived in the Gailitis-Damburg model, while the magenta curves are the $\alpha/2r^4$ potentials appropriate for the polarization potential. b) and c) show zooms of the $5f, 5g$ and $5d$ potentials, respectively.

potential energy barrier. The dipole potentials also predict this same behavior, as can be seen by the qualitative agreement in Fig. 8.11. The $5f$ partial cross section is not explained particularly clearly by either of these interpretations, however, and it is clear from Fig. 8.11 that the actual potential curves are modified by level repulsion

from other potential curves and are not particularly well described by either simple long-range model. The polarization potential for this state is attractive, whereas the dipole potential is actually repulsive; the actual potential curve exhibits a potential well at about 400 atomic units before rising into a small potential barrier well within the R-matrix box. The comparison of dipole and polarizability potentials in this case is unfortunately again somewhat ambiguous.

Thus, we finally turn to a particularly interesting range of energy in potassium, lying 0.07 atomic units above the $5f, 5g$ states. Here, at the $n = 6$ threshold, there are now six approximately degenerate channels, and the Gailitis-Damburg model is expected to be even more accurate due to the closer degeneracy of these channels. More importantly, as inspection of Fig. 8.12 reveals, here the polarization potentials and dipole potentials behave qualitatively differently: there are a total of four out of six attractive polarization potentials since only one polarizability is negative, but there are a total of four repulsive dipole potentials and only two attractive ones. Unlike in sodium, where the degeneracy was much more approximate, the dipole potentials here are in excellent agreement with the adiabatic potential curves, suggesting that in this energy range we can unambiguously associate the observed behavior of the partial cross sections with the dipole, not polarization, physics. Figure 8.13 presents our prediction for the partial cross sections above this threshold. Of these, two partial cross sections behave similarly to the 5g partial cross section: they slowly rise above threshold, undergoing some modulations that could in actuality be resonances, until rising with an almost exponential increase far above threshold. Only one partial cross section behaves like the 5f partial cross section, rising suddenly just above threshold. We emphasize that this behavior is in agreement with what was observed in the experiment and associated with repulsive or attractive potentials, and only the dipole potentials have the correct behavior in this case. These

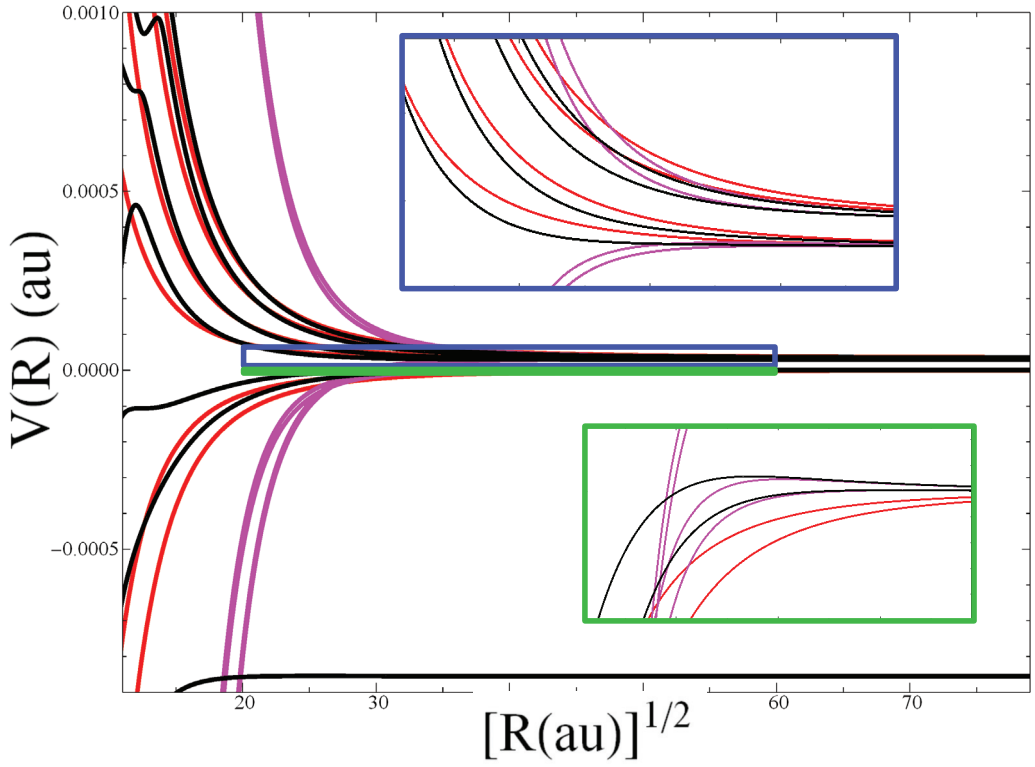

Figure 8.12. Long-range potential energy curves (black) for potassium, relative to the $6f$ state. The red curves are the $-a/2r^2$ potentials derived in the Gailitis-Damburg model, while the magenta curves are the $-\alpha/2r^4$ potentials appropriate for the polarization potential. The blue and green regions, showing the potential curves extending to the 6g, 6h and 6f states, respectively, are enlarged in the insets.

predicted partial cross sections are thus in disagreement with the interpretation in terms of polarization potentials, and unambiguously demonstrate the importance of the near-degeneracy of these high l atomic states on the long-range physics.

In summary, the results presented here show that our eigenchannel R-matrix method can very accurately reproduce tiny partial cross sections for negative ion

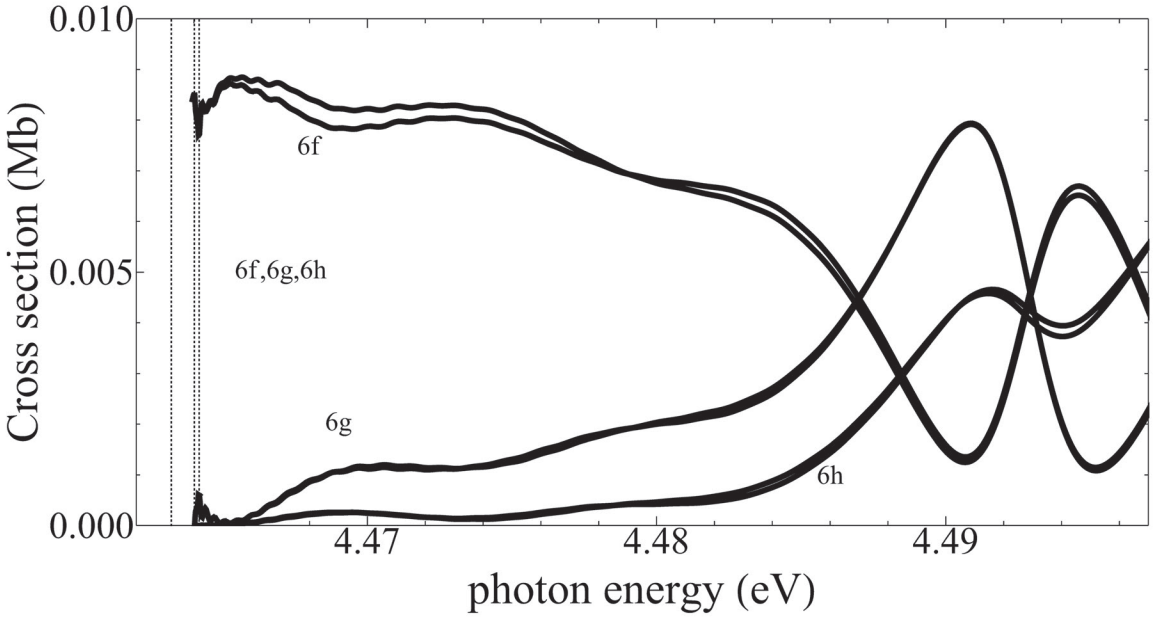

Figure 8.13. Partial cross sections for the $6f$, $6g$, and $6h$ states of potassium.

photodetachment into highly excited residual states of both potassium and sodium. We have emphasized the role of atomic near-degeneracies in influencing observables such as total and partial cross sections. One major goal of this was to re-interpret the experimental findings [47] and to show that the unexpected near-threshold cross section behavior and rapid deviations from the Wigner threshold law are more properly attributed to the dipole potential at long-range, rather than the polarization potential. Moreover, we have predicted that this same unusual behavior will be observable in higher excited states, namely the $6g$ and $6h$ partial cross sections, and in this case we expect to see a clear confirmation of our suspicion since only one, rather than the requisite two, polarization potentials are repulsive. These partial cross sections should be resolvable with the current state of experiment.

Further theoretical work is also needed in order to fully understand these partial cross sections, in particular their resonant features. One initial step will be to calculate time delay matrices and eigenphases for both of these photodetachment processes, and compare them. A preliminary eigenphase analysis in potassium does not show clear evidence for the resonance-like feature observed above the $5g$ threshold in potassium, although Ref. [48] did predict a broad resonance within the experimental error bar. Since this feature is missing in sodium a comparison of these quantities between atoms, which otherwise behave quite similarly in this region, will be helpful. Further work studying the oscillations above the $6g$ threshold, which are qualitatively similar to the modulation identified as the resonance above the $5g$ threshold, is still necessary also. One intriguing possibility is that these oscillations are representative of Stueckelberg oscillations revealing the passage of outgoing flux passes between adiabatic channel potentials.

This page intentionally left blank

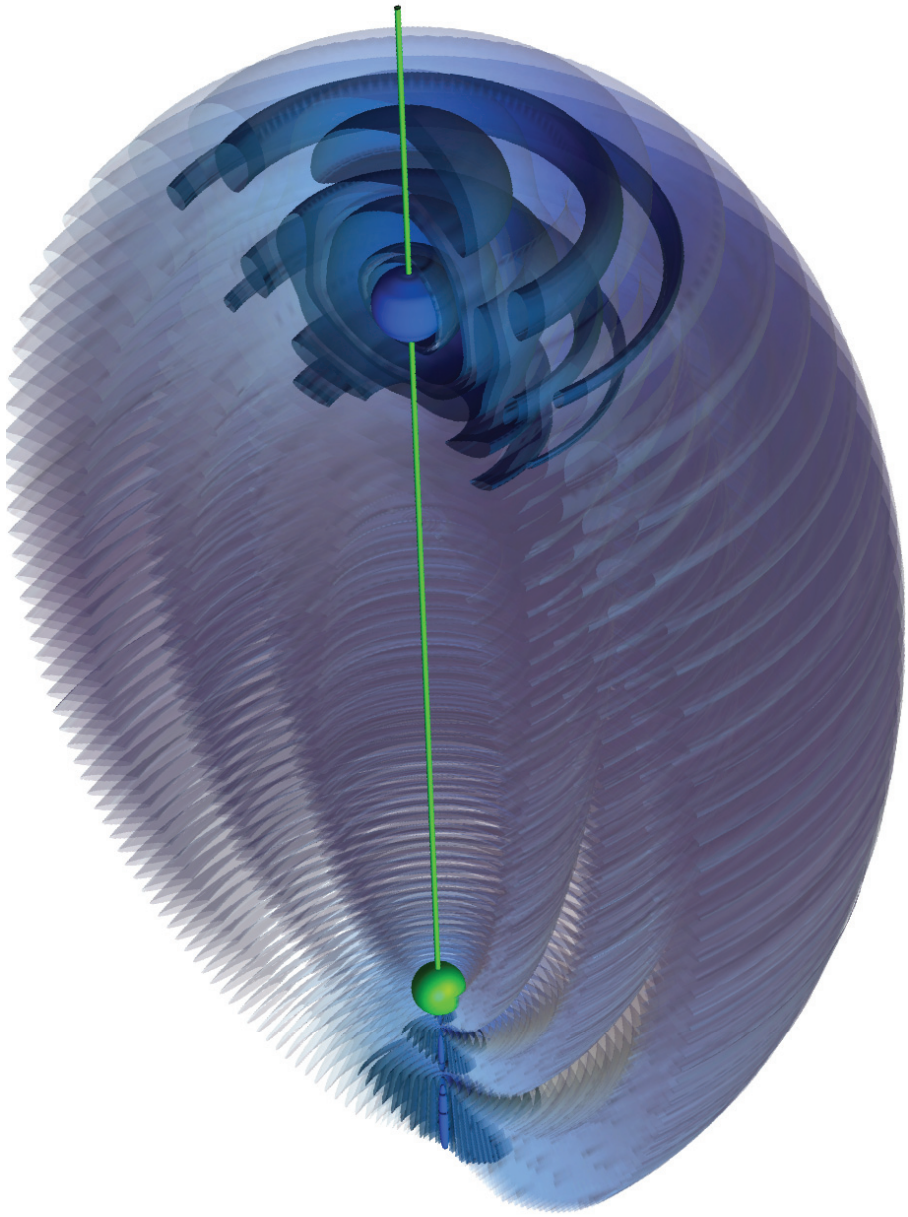

Figure 8.14. A “ghost” trilobite, studied in Chapter 9.

9. FUTURE EXPLORATIONS

This chapter describes some generalizations of the concepts discussed in this thesis, some of which we have already explored in great detail, and others which are still germinating. As previous chapters have shown, the Rydberg molecule concept is quite versatile and encompasses a wide variety of new phenomena introduced by including more interactions or using different atomic species. This chapter explores two such ideas. First, we replace the perturber atom with a "ghost" atom. What we mean by this is that we can create a trilobite or butterfly orbital which extends from the Rydberg atom to an empty point in space by applying electric and magnetic field pulses, which cause the wave function to evolve into the same superposition of atomic states that would be created by a real perturber. Following this, we replace either the Rydberg atom or the perturber with lighter alkali atoms. Although the basic principles followed by Rb-Rb or Cs-Cs Rydberg molecules are the same here, the wide range of quantum defects, fine and hyperfine splittings, and phase shift behavior create a surprising number of new features, particularly in the greatly enlarged parameter space allowed by considering *hetero*nuclear Rydberg molecules.

9.1 Ghost trilobites

We have seen how trilobite and butterfly molecules are formed when degenerate high angular momentum orbitals hybridize to maximize either the electron probability (trilobite) or the probability gradient (butterfly) near a ground state

atom [128, 150, 154]. The unique properties of these chemical bonds rely on the high level degeneracy of non-penetrating high-l Rydberg states. For a bond length R_b this superposition of degenerate l states (in hydrogen) leads to a wave function (see section 4.8)

$$\Psi(R_b, \vec{r}) = \mathcal{N} \sum_{l=l_0}^{n-1} c^b_{nl,x} \phi_{nl}(r), \tag{9.1}$$

where $\mathcal{N}$ is a normalization constant, l_0 restricts the summation to degenerate states ($l_0 \approx 3$ in alkali atoms) and $\phi_{nl}(r) = \frac{u_{nl}(r)}{r} Y_{l0}(\theta, \phi)$ are standard hydrogenic Rydberg wave functions. The label x can refer to either a trilobite or a butterfly. Due to cylindrical symmetry and the functional form of the pseudopotential $m_l = 0$. The coefficients $c^b_{nl,x}$ are determined by diagonalizing the Fermi pseudopotential in the basis of degenerate hydrogenic states. For example, $c^b_{nl,\text{trilobite}} = \phi_{nl}(R_b)$. For a general target state these coefficients can be compactly expressed as a vector, c_T.

The degeneracy needed to form these exotic states is exact for all l in nonrelativistic hydrogen. Since the hydrogen-electron scattering length is positive, the repulsive trilobite potential curves cannot support vibrational bound states. Nevertheless, theoretical evidence suggests that the Rydberg electron-atom interaction still evinces resonant behavior related to the stationary points of the potential curves [3, 92]. These are located at R_b satisfying $u_{n0}(R_b) = 0$ [289]. The index b thus labels a series of trilobite states with specific bond lengths and nodal structure; at these R_b also the wave function is dominated by just a few eigenfunctions of the Schrödinger equation in elliptical coordinates [136].

Here we show that it is possible to create these chemical bonding orbitals with the ground state atom absent, and for this reason we refer to the electronic wave function (Eq. 9.1) as a *ghost chemical bond*. By employing a carefully engineered sequence of alternating magnetic and electric fields, we evolve the wave function from an isotropic

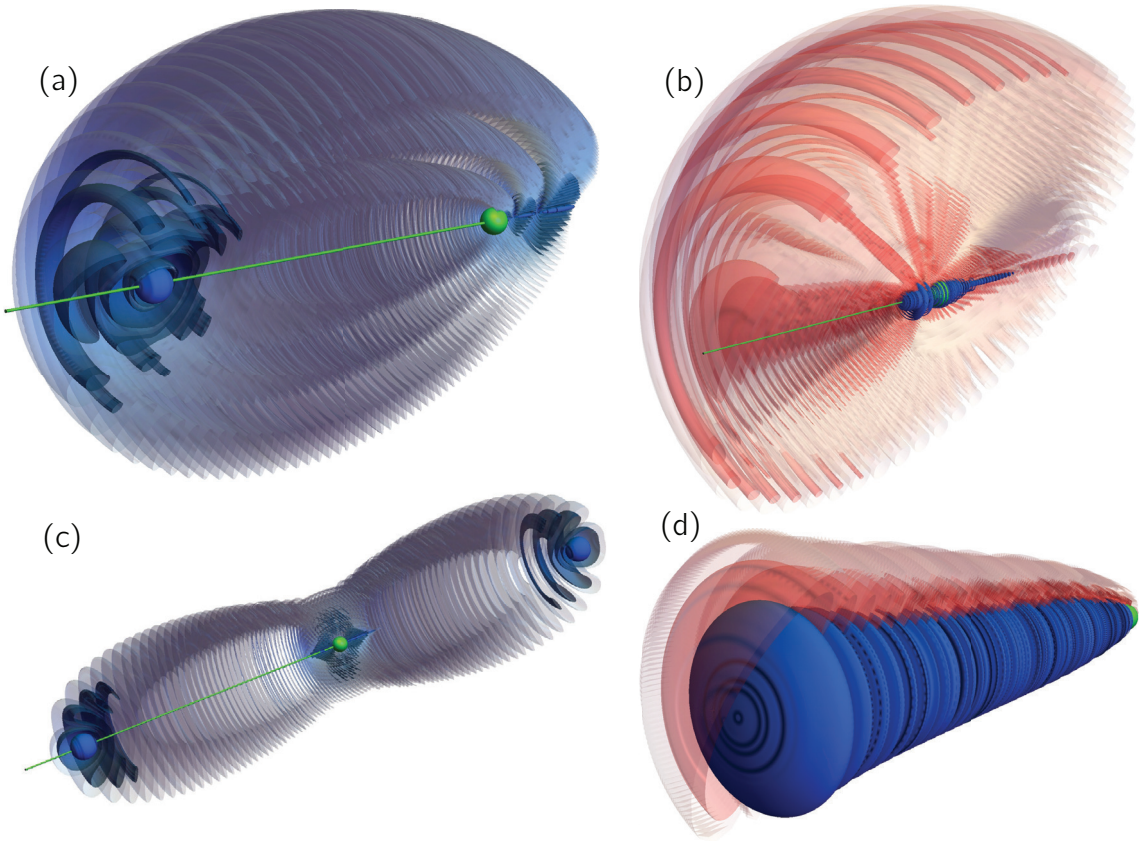

Figure 9.1. A gallery of $n = 70$ ghost molecular bonds, depicted as isosurfaces, defined where $|\Psi(x, y, z)|^2$ is $C\%$ of Max $(|\Psi_{\text{trilobite}}(R_{b=1}; x, y, z)|^2)$. They are cut away to reveal the inner structure. The Rydberg ion, not to scale, is the green sphere and the green line ($1.1\times10^4 a_0$ long) provides a scale. (a) A $b = 3$ trilobite; (c) an even-parity collinear $b = 1$ trilobite trimer. The color scheme is bright blue when $C = 15.4$, darker blue when $C = 1.54$, and transparent blue when $C = 0.308$. (b) a butterfly with $R_0 = 653$; (d) the deepest Stark state. The color scheme is bright blue when $C = 1.54$, red when $C = 0.154$, and translucent pink when $C = 1.54 \times 10^{-2}$.

ns state into precisely the same orbital that would form a chemical bond if a ground state atom were located at R_b. The time evolution is described via unitary operators in degenerate perturbation theory. A gradient ascent algorithm derived from optimal control theory optimizes the field sequence to ensure excellent overlap with the target trilobite state. Several possible detection mechanisms are proposed as ways to image and study this chemical bond. Fig. 9.1 displays several ghost chemical bonds for $n = 70$, revealing their key properties. Perhaps the most distinctive characteristic of trilobite bonds is their nodal structure: as b increments by one, a new lobe in the direction perpendicular to the intermolecular axis appears (a $b = 3$ trilobite is shown in Fig. 9.1a). Moreover, they are remarkably localized, maximally so in the $b = 1$ trilobite shown in Fig. 9.2f, where 20% of the electron density occupies a region around the ghost atom smaller than 0.1% of the total classically allowed volume. The butterfly molecule chemical bond (Fig. 9.1b) has a bond length an order of magnitude smaller than the trilobite, and the wave function, fanning out into a winglike structure, fills much more of the classically allowed volume. In addition to these ghost orbitals, we can also form polyatomic Rydberg molecules such as those discussed in chapter 4 (Fig. 9.1c). Equation 9.6 gives $c^b_{nl,x}$ for these Rydberg chemical bonds [4,95,289]. The Stark state (Fig. 9.1d) as well as the Zeeman state (Fig. 9.2b) highlight the fact that even highly localized electron wave functions in static fields are entirely different from Rydberg molecule wave functions.

Fig 9.2 depicts the experimental implementation of this concept. First, a hydrogen atom is excited to an ns Rydberg state. Next, a magnetic field ramps on to a final amplitude B. Immediately following the end of the ramp, a sequence of N electric field pulses of amplitude F are applied. After the N^{th} pulse the magnetic field ramps off. For the $n = 70$ Rydberg state considered here, the ramp times are typically tens of μs, while the electric field durations and separations are sev-

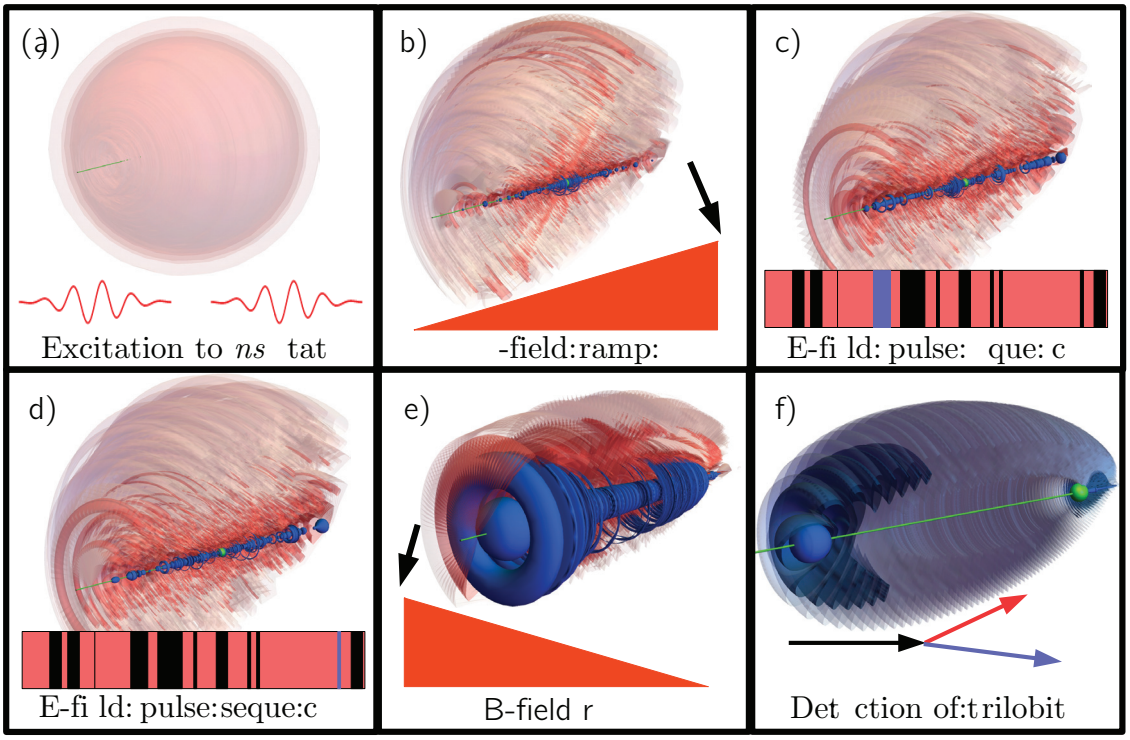

Figure 9.2. The proposed scheme, illustrated with the $n = 70, b = 1$ trilobite and the same color scheme as in Fig. 1. a) An nS Rydberg state is created. b) The magnetic field ramps on, creating a quadratic Zeeman state. c,d) Many short electric field pulses are applied over the constant magnetic field background, creating complicated superpositions of the degenerate states. At different points in the sequence, marked blue in the field sequence sketch, the wave function is strongly mixed. e) At the end of the sequence of electric field pulses, a proto-trilobite is created. The magnetic field ramps off and this state evolves into the trilobite state, f), which is detected.

eral nanoseconds each, lasting in total several tens of μs as well. This whole process thus occurs within the natural radiative and blackbody lifetime of the Rydberg state. The trilobite molecule is particularly long-lived, more so than the butterfly molecule, since it is an admixture of predominantly high$-l$ states and is therefore mostly affected by blackbody radiation. We set a conservative lower lifetime bound at 200μs; this time increases approximately linearly with decreasing ambient temperature, extending to several milliseconds at 10K [12, 290–293]. As lower l states "bleed" away, the dominant components of the trilobite molecule persist, leading to the remarkable scenario where the Rydberg electron remains localized in a small point several hundreds of nanometers away from the proton for many dozens of microseconds. Interesting effects arise if a small electric field is pulsed on in this final state. The ghost chemical bond will revive every $\tau = \frac{2\pi}{3Fn}$, which is about 37 ns for a 0.1V/cm electric field. Furthermore, the decay mode of the ghost molecule will change as the Stark-shifted trilobite state is no longer degenerate. It will decay as one quantum state, as expected from Fermi's golden rule, following a rate dominated by its high$-l$ components.

Since molecular spectroscopy, the usual technique used to detect Rydberg molecules, is not applicable in the present scenario, a different detection scheme is desired. A method which can directly observe the wave function, rather than a more indirect observable, is additionally advantageous. Two possible detection techniques along these lines involve field ionization. In Stark photoionization spectroscopy, the electron is photoionized and detected on a distant screen. This maps the real-space electron wave function into Stark states, but unfortunately the theoretical description and extraction of the wave function's properties is too imposing for this to be a robust and clear method in the present context [294–296]. A related, but more straightforward, technique is ionization by half-cycle pulses [297, 298]. A half-cycle

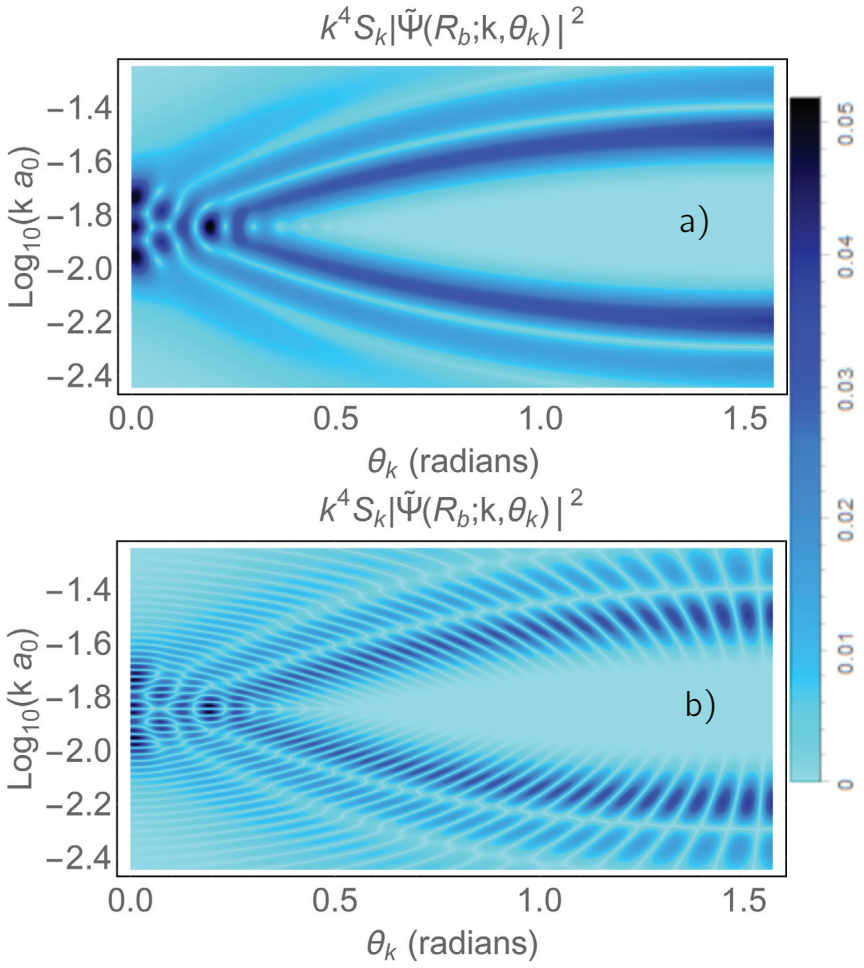

Figure 9.3. Momentum-space probability distributions for the $n = 70$ $b = 3$ trilobite dimer (a) and trimer (b). Both are symmetric about $\theta_k = \frac{\pi}{2}$ and, when multiplied by k^4, are logarithmically symmetric about $k = 1/n$. The scaling factor $S_k = (\theta_k + 0.1)$ was included to enhance the visibility of the distinctive features at large θ_k.

pulse along the z axis imparts a momentum kick to the Rydberg electron, and if the electron's increased energy is sufficient to overcome the ionization potential it

will be detected. A measurement of the electron current is therefore proportional to $\int_{k_z}^{\infty} \int_{k_x,k_y} |\Psi(k)|^2 \mathrm{d}^3k$, where k is the momentum of the electron. A very similar observable is obtained in Compton scattering [299]. k_z is determined by the momentum kick, so by varying this the probability density that the electron had momentum k_z

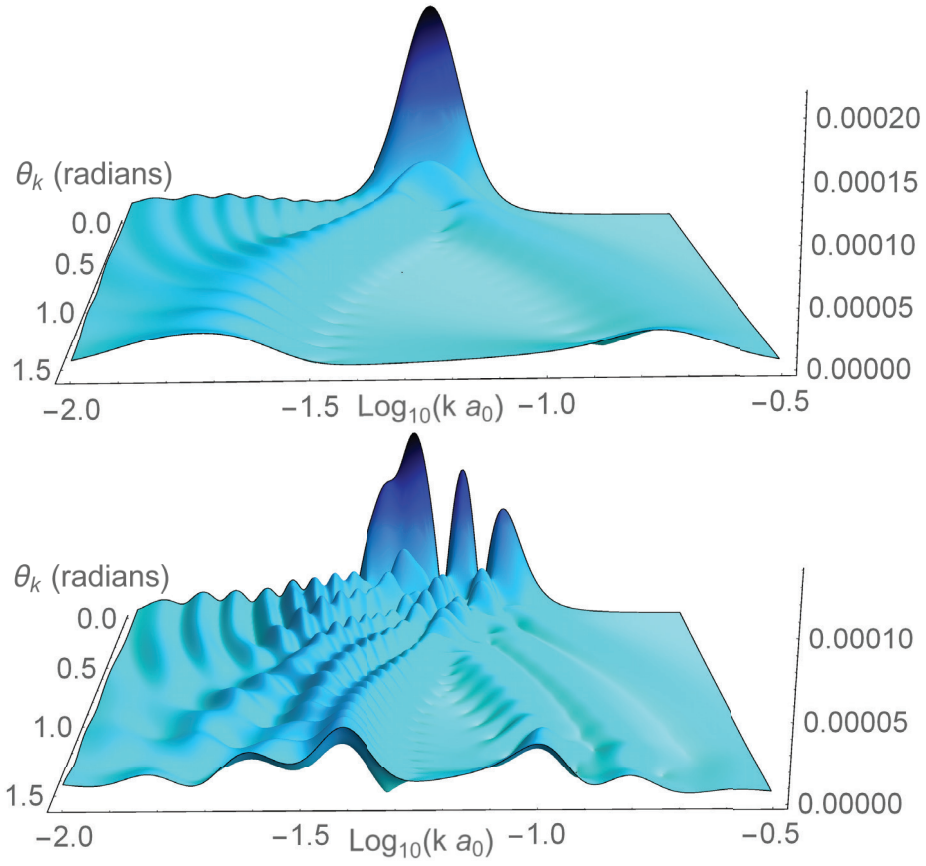

Figure 9.4. The quantity $k^2 F_T \quad R_b; k \quad$ for the $n = 30$ $b = 1$ and $b = 3$ trilobites. The scaling factor k^2 is added to improve visibility of small features. This function is also symmetric about $\theta_k = \frac{\pi}{2}$. $n = 30$ was chosen to connect back to the very first trilobite molecule prediction [40].

and any value of k_x and k_y can be obtained. Although the simplicity of this approach is attractive, much of the detailed structure of the wave function is averaged over and obscured.

Two methods measure the Rydberg wave function much more directly: electron momentum $(e, 2e)$ spectroscopy and x-ray diffraction. In $(e, 2e)$ spectroscopy an electron with momentum k_0 collides with the Rydberg electron, which has momentum k. Both elastically scatter into plane waves with momenta k_a and k_b, and are detected in coincidence. The triply-differential cross section for this process is [300–302]

$$\frac{d^3\sigma_{(e,2e)}}{d\Omega_a \Omega_b dE_b} = \frac{4k_a k_b}{k_0 |k_0 - k_a|^4} \left| \tilde{\Psi}(R_b; k) \right|^2, \tag{9.2}$$

where Ω_i is the solid angle in which electron i is detected, and E_b is the energy of electron b. This expression is valid provided that the electron-electron collision is fully elastic, requiring large momentum transfer $k_0 - k_a$, large momenta values throughout, and energies significantly higher than the ionization potential of the Rydberg electron [300, 302]. The experimental geometry determines the specific form of the kinematic factor $|k_0 - k_a|^{-4}$ and the relationship between k, k_a, and k_b. The direct proportionality to the electron's momentum density $\left| \tilde{\Psi}(R_b; k) \right|^2$ is a highly attractive feature for the desired detection scheme. We thus focus not on the specific experimental design but instead on the key features of the momentum density. Typically only spherically averaged cross sections are measured [302] since most samples are isotropic, but trilobite-like orbitals are particularly advantageous since they are aligned in the direction of the control fields, even after these fields are turned off.

A complementary technique is x-ray diffraction, characterized by the differential scattering probability [303]

$$\frac{d\sigma}{d\Omega} = \frac{d\sigma_{th}}{d\Omega} \left| |\Psi(R_b, \vec{r})|^2 e^{ik\cdot r} \mathrm{d}^3 r \right|^2, \tag{9.3}$$

where $\frac{d\sigma_{th}}{d\Omega}$ is the Thomson cross section. The differential cross section is no longer proportional to the momentum density, but to the Fourier transform of the electron density itself, creating another window into the electronic structure of these ghost orbitals. These two fundamental observables, $|\tilde{\Psi}(R_b;k)|^2$ and $F_T(R_b;k) = |\Psi(R_b;r)|^2\, e^{ik\cdot r}\mathrm{d}^3r$, are plotted for some illustrative cases in Figs. 9.3 and 9.4. As expected from Fourier analysis, the momentum-space wave functions in Fig. 9.3 mirror the symmetries and nodal structure present in the real-space wave functions, and therefore unambiguously determine the electronic character. Three clear ridges mirror the three nodes in the $b = 3$ trilobite, and the even-parity trimer possesses additional nodes overlapping these ridges showing the absence of odd-parity components. The symmetries in θ_k and k also relate to the symmetry of the real-space wave function. The Fourier-transformed electron density has many of these same features, although it is no longer symmetric about $k = 1/n$, and instead has a prominent feature near $k = 2/n$. It is also significantly smaller in magnitude and less clear to interpret, although the major nodal features corresponding to the trilobite lobes are still apparent. More details and examples of real and momentum space wave functions are shown in Appendix E.

Let us now delve into the time evolution of the system and control-theory algorithm in more detail. Our ability to prepare these exotic chemical bonds hinges on the fact that Rydberg electrons are strongly affected by external fields. These can be employed to manipulate the electronic wave function into classical wave-packets [22], circular states [304], or exotic giant-dipole configurations [305]. The enormous extent of Rydberg wave functions creates large transition dipole matrix elements, facilitating easy control even with weak field strengths. The Stark and quadratic Zeeman matrix elements scale as Fn^2 and B^2n^4, respectively, where F and B are electric and magnetic field amplitudes [12].

We describe the time evolution caused by these time-dependent field pulses using degenerate first-order perturbation theory. The electronic wave function is expanded into the degenerate stationary Rydberg states of a given n with time-dependent coefficients: $\Psi(r,t) = \sum_l c_l(t)\phi_{nl}(r)$. In a parallel field configuration m_l is still a good quantum number, so we consider only the $m_l = 0$ subspace. In a time period Δt_i^b when the electric field is zero, the Hamiltonian is $H_B = H_0 + \frac{B^2}{8} r^2 \sin^2\theta$. Likewise, when the electric field is nonzero for a time period Δt_i^f, $H_F = H_B + Fr\cos\theta$. In the degenerate subspace of a single n manifold, the action of H_0 is irrelevant and can be set to zero; the operators H_B and H_F are then diagonalized to obtain the diagonal eigenvalue matrices $\underline{b}$, $\underline{f}$ and eigenvector matrices $\underline{U_b}$, $\underline{U_f}$, respectively.

During each Δt the Hamiltonian is time-independent, so the evolution of the initial state is computed by iteratively acting on it with the unitary time evolution operator for each pulse until the final time is reached:

$$c_f = \underline{X_B}^\dagger \prod_{i=1}^{N} \underline{U_b} e^{-i\Delta t_i^b \underline{b}} \underline{U_b}^{-1} \underline{U_f} e^{-i\Delta t_i^f \underline{f}} \underline{U_f}^{-1} \quad \underline{X_B} c_0. \tag{9.4}$$

$X_b = \underline{U_b} e^{-i\Delta t_{\mathrm{ramp}} \underline{b}} \underline{U_b}^{-1}$ is the field ramp operator. We have represented the time-dependent coefficients in vector form; the goal is to match the engineered state c_f with the target state, c_T. Their similarity is characterized by the fidelity $\Phi = |\langle c_T | c_f \rangle|^2$. After choosing the field amplitudes and initial ramp times, determining $\underline{X_B}$, the only input needed to determine the final state are the $2N$ time periods, Δt_i^f and Δt_i^b.

The set of all possible pulse sequences $\{\Delta t_i^b, \Delta t_i^f\}$ form a highly multi-dimensional control landscape in which the fidelity $\Phi(\{\Delta t_i^b, \Delta t_i^f\})$ must be optimized. Numerical tests have shown that N scales as $\mathcal{O}(n)$. This nonlinear optimization problem is impervious to analytical solution or blind Monte Carlo simulation, but a gradient ascent algorithm starting with a random set of pulse durations finds optimal $\Delta t_i^{b,f}$ parameters giving local maxima in Φ remarkably efficiently. Unlike many problems

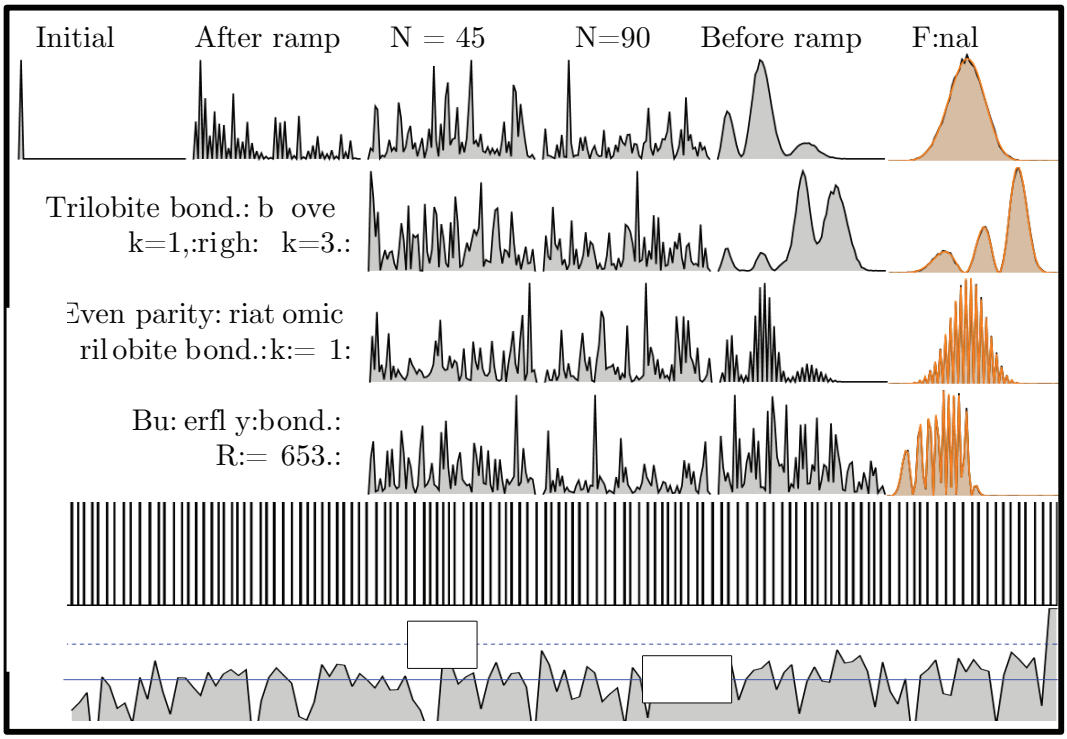

Figure 9.5. Details of the proposed scheme for the four orbitals shown in Fig 9.1. a) l-distributions as a function of time, spanning from $l = 0$ on the left to $l = 69$ on the right. The orange overlay in the final state shows the exact distribution. The orange overlay shows the exact distribution. The $b = 3$ trilobite is focused on in panels b and c: b) The field pulses responsible for this process. The electric fields are turned on in black regions and off in white regions. c) The fidelity, on a logarithmic scale, as a function of time.

where major effort is needed to numerically calculate the gradient [306], in the present

case the gradient is given analytically (without loss of generality here is the partial derivative with respect to Δt_j^f):

$$\frac{\partial \Phi}{\partial \Delta t_j^f} = \frac{\partial \vec{c_f}}{\partial \Delta t_j^f} \; c_T \quad c_T | c_f \; + \text{c.c.} \tag{9.5}$$

$$\frac{\partial \vec{c_f}}{\partial \Delta t_j^f} = \underline{X_B}^\dagger \prod_{i=1}^{N} \underline{U_b} e^{-i\Delta t_i^b \underline{b}} \underline{U_b}^{-1} \underline{U_f} \; -i\underline{f}^{\;\delta_{ij}} \, e^{-i\Delta t_i^f \underline{f}} \underline{U_f}^{-1} \; \underline{X_B} c_0.$$

After finding this gradient, the full set of parameters $\{\Delta t_i^O\}$ is shifted in the direction of the steepest change in the fidelity, $\Delta t_i^O \rightarrow \Delta t_i^O + \varepsilon \frac{\partial \Phi}{\partial \Delta t_i^O}$, where ε is a variable stepsize and O represents either f or b.

Numerical experiments reveal several generic features of the behavior of this gradient ascent approach and the optimal parameters it produces. First, every optimal pulse sequence is primarily determined by the distribution of values in the initial guess, typically drawn from a uniform distribution of experimentally realistic values. This implies that there are effectively infinitely many good pulse configurations. One of these pulse sequences is shown in Fig. 9.5b, and a full data table of this sequence along with others which create the other chemical bonds in Fig. 9.1 is given in the supplementary information. The non-uniqueness of the solutions implies that Φ is not convex, so there is no guarantee that a gradient ascent algorithm will discover global maxima. Surprisingly, our simulations found that, provided enough pulses (typically $N \approx 2n$) of adequate duration ($\sim$ 10s of ns) are used, almost all sequences thus obtained were optimal, satisfying $\Phi > 0.999$. Finally, methods that attempt to increase the fidelity monotonically with each pulse appear impossible. Fig. 9.5 c shows $\log_{10} \Phi$: at no time prior to the final step of evolution does the fidelity seem to increase above 0.01, nor does it increase monotonically in time.

These findings are corroborated by various results of optimal control theory [307]. The existence of multiple solutions has been well-known since early studies of quan-

tum control [308, 309], and quite general quantum proofs exist demonstrating that the topology of quantum control landscapes are very favorable to simple extrema search algorithms. Only globally maximal seams exist in a sufficiently large parameter space; local maxima do not exist [310–312]. Due to these general principles, it is justifiable to restrict the initial guess to realistic experimental values for the field strengths and durations, rather than directly implementing these constraints into the search algorithm. This works excellently given the incredible flexibility of possible solutions [308, 313]. The lack of local maxima, given the landscape is not overly constrained [310], guarantees that optimal solutions are found rapidly without needing more complicated genetic algorithms or stochastic optimizers.

The complex quantum pathways the wave function evolves along necessitate very stringent control over the field amplitudes and pulse timing. The experiment must be very well shielded from stray fields so that the control field amplitudes can be specified to better than 10 μV/cm and 1 mG. Rydberg atoms themselves can be used as highly sensitive field sensors [18, 314]. The pulse timing should be controlled to femtosecond precision to match the reported data in the supplementary information. These error bounds correspond to a 10% reduction in the fidelity from a theoretically optimal value. This sensitivity seems to stem from the cancellations that have to occur in the exponential factors of Eq. 9.4 and the large variation in field operator eigenvalues. It is therefore likely an intrinsic aspect of such high Rydberg states rather than a poorly informed optimal control theory approach, although it could be possible to construct an optimization cost function to penalize highly sensitive solutions. Additionally, these high sensitivities may require more precise theoretical methods to compute the time evolution as effects beyond first-order perturbation theory are near to this level of accuracy; the proof of principle demonstrated here will still persist in more sophisticated approaches.

The parameter ranges of this scheme were designed based on the following physical considerations.

Relativistic effects. The fine structure breaks the exact degeneracy of nl states with low l. The $70p_{1/2,3/2}$ ($70d_{3/2,5/2}$) levels are split by $\approx 0.25(0.085)$ MHz. Precession between different m_l states caused by the np splitting over the time scale of the experiment introduces undesirable decoherence. To avoid this problem a magnetic field of 100G is applied to access the Paschen-Back regime and eliminate this precession by energetically separating $m_l = 0$ levels.

Magnetic fields. These relatively large magnetic fields are also necessary since the quadratic Zeeman term is very small compared to the linear Stark shift. It is challenging to change fields of this strength quickly due to the self-inductance of the electronics. We have adopted the slew rate $10\text{G}/5\mu\text{s}$ of state of the art magnetic field coils developed to quench ultracold atomic species [315].

Pulse sequence and field strength parameters. There is considerable flexibility in the initially guessed pulse distribution. The simplest theoretical choice is simply to draw the initial distribution randomly from a region of experimentally realistic values. The range of these values should be limited to reduce the overall time. The optimized field pulses then closely mirror this initial distribution due to the incredible multiplicity of optimal configurations and their sensitivity. Sequences leading to very good fidelity can also be found with an initial configuration of equal-duration pulses, although with somewhat more difficulty since the parameter space is less robust. Setting $N = 130$ essentially guaranteed $\Phi > 0.999$ regardless of the initial distribution, while for $N = 120$ high fidelities $\Phi \approx 0.99$ were always achieved but $\Phi > 0.999$ was not. For N even as low as 70 $\Phi \approx 0.9$ reliably. Likewise the field amplitudes can be adjusted to better conform to a specific experiment. The magnetic field amplitude should be fairly large, as described above, while the electric field amplitude should

not be large enough that different Rydberg levels together can mix together. For $n = 70$ this restricts it to not far exceed the 0.1V/cm employed here.

Rydberg levels High principal quantum numbers are needed to ensure that the above constraints are sufficient, but also increase the theoretical complication and experimental limits on sensitivity. The benefits are contingent on various Rydberg scaling laws: the fine structure splitting decreases as $\mathcal{O}(n^{-3})$, magnetic field effects increase as $\mathcal{O}(n^4)$, and the natural and blackbody radiative decay rates decrease as $\mathcal{O}(n^{-3}) - \mathcal{O}(n^{-5})$ (depending on l) and $\mathcal{O}(n^{-2})$, respectively. The number of pulses and electric field influence increase as $\mathcal{O}(n)$ and $\mathcal{O}(n^2)$, respectively, and the electron's momentum decreases as $\mathcal{O}(n^{-1})$; the sensitivity to error and difficulty of detection are thus increased at high n. Additionally, first-order perturbation theory starts to become less accurate at higher n due to the decreasing (as $\mathcal{O}(n^{-3})$) separation between Rydberg manifolds. $n = 70$ functions in our exemplary calculations as a convenient middle ground, but the wide range of theoretical and experimental constraints mean that this choice is quite flexible depending on the circumstances.

Calculation details The specific field configurations for Fig. 9.5 are included in table 1 of the supplementary information. We chose $n = 70$, $B_{max} = 100$G, $F_{max} = 0.1$V/cm, and $N = 130$. Δt_i^b and Δt_i^f were chosen randomly from the ranges $\{200, 400\}$ and $\{20, 60\}$ns, respectively. The ability to of the gradient ascent algorithm within this scheme to find optimal solutions is surprisingly robust to variations of all these parameters. Scaling laws can also be used to vary the parameters. The system is invariant under the transformations $F \to \mathcal{F}$, $B \to B \quad \overline{\mathcal{F}/F}$, $\Delta t_i^O \to \Delta t_i^O(F/\mathcal{F})$, and $T_{\text{ramp}} \to T_{\text{ramp}}(F/\mathcal{F})^{3/2}$.

Orbital details The (unnormalized) final state coefficients are given by:

$$c^b_{nl,trilobite} = \phi_{nl0}(R_b) \tag{9.6}$$

$$c^b_{nl,butterfly} = \frac{\partial \phi_{nl0}}{\partial R_b} \tag{9.7}$$

$$c^b_{nl,even/oddparitytrimer} = \frac{(1 \pm (-1)^l)}{\sqrt{2}} c^b_{nl,x} \tag{9.8}$$

evaluated at the bond positions R_b which are determined for each state by finding the minima of $\sum_l |c^b_{nl,x}|^2$.

The momentum-space wave function for a trilobite-like orbital characterized by coefficients $c^b_{nl,x}$ is

$$\tilde{\Psi}(R_b; k) = \frac{\sum_{l=l_0}^{l=n-1} c^b_{nl,x} F_{nl}(k) Y_{l0}(\theta_k, \phi_k)}{\sqrt{\sum_{l=l_0}^{n-1} |c^b_{nl,x}|^2}}; \tag{9.9}$$

$$F_{nl}(k) = -(-i)^l \sqrt{\frac{2(n-l-1)!}{\pi(n+l)!}} n^2 2^{2(l+1)} l! n^l k^l \tag{9.10}$$

$$\times (n^2k^2+1)^{-l-2} C^{l+1}_{n-l-1}\left(\frac{n^2k^2-1}{n^2k^2+1}\right), \tag{9.11}$$

where C^j_i is the Gegenbauer polynomial of degree i and order j; these "radial" momentum space wave functions were calculated shortly after the solution of the quantum mechanical hydrogen atom [316]. The Fourier-transformed real-space electronic density is described in the supplementary information.

In this section we have presented a method to form and detect exotic ultra-long-range ghost chemical bonds consisting of just one atom. The electron, depending on the type of bond desired, can be either forced to localize very tightly on one or more positions in space, as in the trilobite molecules, or to spread out into an exotic fan-like structure, as in the butterfly molecule. A carefully controlled sequence of applied electric and magnetic fields is capable of emulating the Fermi pseudopotential responsible for the formation of Rydberg molecules by neutral perturbers.

These pulse sequences are designed efficiently using a gradient ascent algorithm, and excellent fidelity (99.9%) can be reached with typical laboratory fields and time scales. The stringent control requirements on the field amplitudes and pulse timings are certainly major experimental hindrances, requiring excellent shielding towards stray fields over the course of the experiment and accurate control of applied field strengths. The energy scales and system complexity studied here are a novel regime for optimal control theory, which is typically applied to smaller systems with only a few energetically accessible quantum states. One can envision even more exotic ghost states to investigate in the future, such as extended configurations like the trimer molecules shown here with several more "ghost" atoms spaced along a line, or even (if the $m_l = 0$ restriction is abandoned and the full degenerate Hilbert space of size n^2 is explored) polyatomic orbitals without cylindrical symmetry. The theory could be likewise extended to atoms with quantum defects, or as mentioned previously, to include nonperturbative field effects. The proposed detection methods are equally applicable to typical Rydberg molecules, and direct observations of their electronic densities, even time-resolved studies, could be implemented independently of the "ghost" molecule proposed here [317, 318].

9.2 Other alkali atoms

In recent years, alongside the growth of Rydberg molecules, the ultracold community has become very intrigued by mixtures of fermions and bosons in the quantum degenerate regime, which are now possible for a wide range of atomic species [319, 320]. Many fascinating experiments can now be performed. For example, the presence of one species can enhance the stability of the condensed phase of the other. Few-body physics is also enriched: recombination between species leading to unusual

few-body bound states such as Efimov trimers with favorable mass ratios [321–323]. The creation of ultracold polar molecules in their rovibrational ground state has become a very popular topic, and has resulted in the creation of nearly every bi-alkali combination. Since direct cooling of molecules is far harder than cooling atoms, a highly attractive alternative is then to begin with ultracold atoms, and photoassociate them into polar molecules. [229, 324–328].

This section presents two long-term aims motivated by these recent experimental developments. First, to calculate molecular properties of homonuclear Rydberg molecules in the light alkali atoms Li, Na, and K. These light alkali atoms have been almost completely ignored thus far in the Rydberg molecule community, but are the subject of recent interest [114]). Some preliminary calculations of the $n = 30$ potential energy curves are presented here using the phase shifts calculated in section 2.3.1. Secondly, we want to calculate properties of heteronuclear Rydberg molecules. The emphasis here is to find scenarios where the different atomic properties – their quantum defects, electron-atom scattering phase shifts, hyperfine splittings, and masses – conspire to bestow attractive properties onto these Rydberg molecules. Fortuitous degeneracies, either in the quantum defects [5, 154] or in the hyperfine/fine structure splittings [150, 161], have been explored already in homonuclear molecules; heteronuclear systems offer a greatly expanded parameter range to explore. These systems can also provide environments to study fundamental atomic properties, i.e. scattering lengths, shape resonance positions, ion-neutral scattering interactions, that are quite difficult to study otherwise. It is our goal that this broad survey of molecular and atomic properties will guide more involved future efforts to expand this field to a much wider parameter regime, and could provide means of studying chemical reactivity at much larger scales than experienced among ground state atoms and molecules.

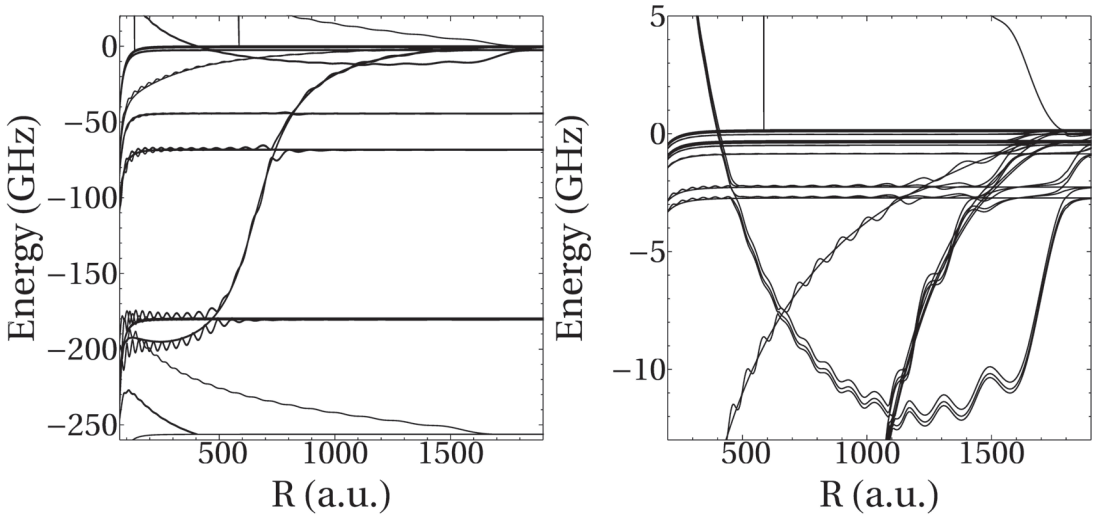

Figure 9.6. K_2 potential energy curves for $n = 30$. These potential curves resemble those of Rb_2 very closely due to the similarity of both the quantum defects and the scattering phase shifts between these two atoms, and differ primarily in the size of the hyperfine splitting. Vertical spikes are a numerical artifact of the p-wave potential.

The relevant Rydberg and ground state atom parameters were presented in tables 2.1 and 2.2. The theory detailed in chapter 6 was utilized, except the ${}^{J}P$ phase shifts were all set equal for Li, Na, and K since the spin-orbit splitting scales as Z^4, and is significantly smaller therefore for these atoms. Future work should, at least at the perturbative limit, calculate these splittings to confirm that they are too small to effect the physics of these molecules. Even these preliminary results suggest that there is a significant amount of interesting features in these Rydberg molecules beyond just replicating the same physics seen in Rb and Cs. The energy structure and phase shifts of K bear much similarity to Rb, as do its potential energy curves shown in Figs. 9.6 and 9.8a. As such, it should serve as a good benchmark for

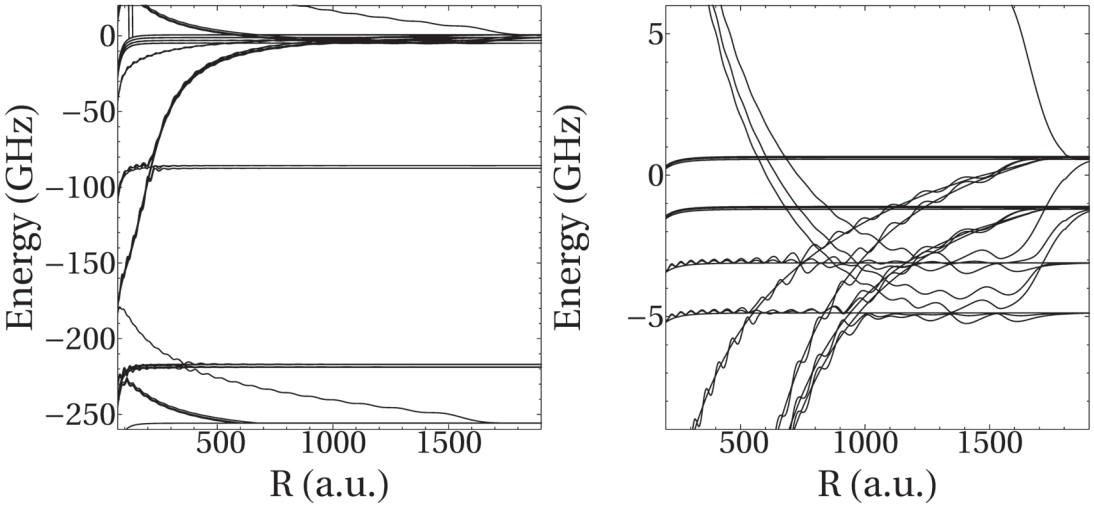

Figure 9.7. Na_2 potential energy curves for $n = 30$. The ^3P shape resonance is too broad to form the deep minima that support butterfly states, and the *nd* state mixes significantly into the trilobite potentials. Vertical spikes are a numerical artifact of the *p*-wave potential.

and confirm many of the observations made in rubidium. Its use in polyatomic or heteronuclear contexts is described below.

Sodium is somewhat more interesting for three reasons: its ^3P shape resonance is quite broad, and for $n = 30$ (and most likely all other n values) the formation of butterfly states is suppressed as the butterfly potential well does not descend to the *np* level, as it does in K, Rb, and Cs, until very small internuclear distances. This also means that it crosses the trilobite curve at a much smaller internuclear distance, avoiding the deep trilobite minima in contrast to heavier atoms. These trilobite wells are also interesting, as the *nd* quantum defect of sodium is very small. The *nd* state therefore mixes in with these trilobite potentials quite extensively, like the *ns* state of Cs. This could provide yet another means of accessing trilobite states

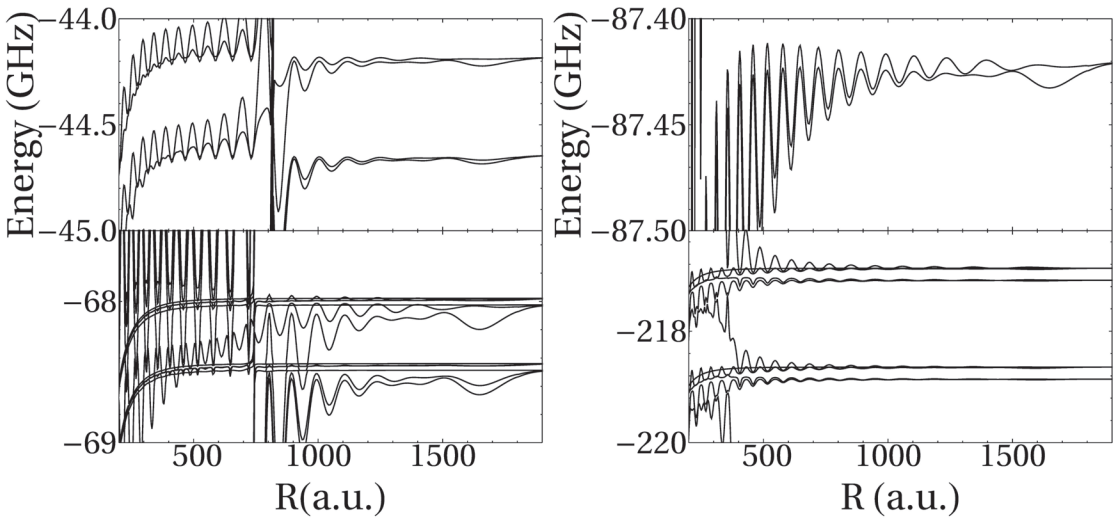

Figure 9.8. Left: $32s$ (top) and $29d$ (bottom) potential energy curves for potassium. Right: $32s$ (top) and $31p$ (bottom) potential energy curves for sodium.

experimentally. Finally, its ^{1}S scattering length is significantly larger than it is in heavier atoms, and this causes the singlet trilobite curve, climbing upwards from the hydrogenic manifold, to mix in with the np states. This mixing could open up a new trilobite regime, blue-detuned from the hydrogenic manifold and available in singlet, rather than triplet states, via a single photon transition near to the np states. These potentials are shown in Figs. 9.7 and 9.8b

Lithium's potential energy curves are quite featureless due to its almost vanishing np and nd quantum defects and tiny fine and hyperfine structures. Fig. 9.9 shows the potential energy curves for both isotopes of Li, which have markedly different hyperfine splittings. Li also does not exhibit butterfly potential wells. Future work will need to more systematically explore the energy levels of these homonuclear molecules

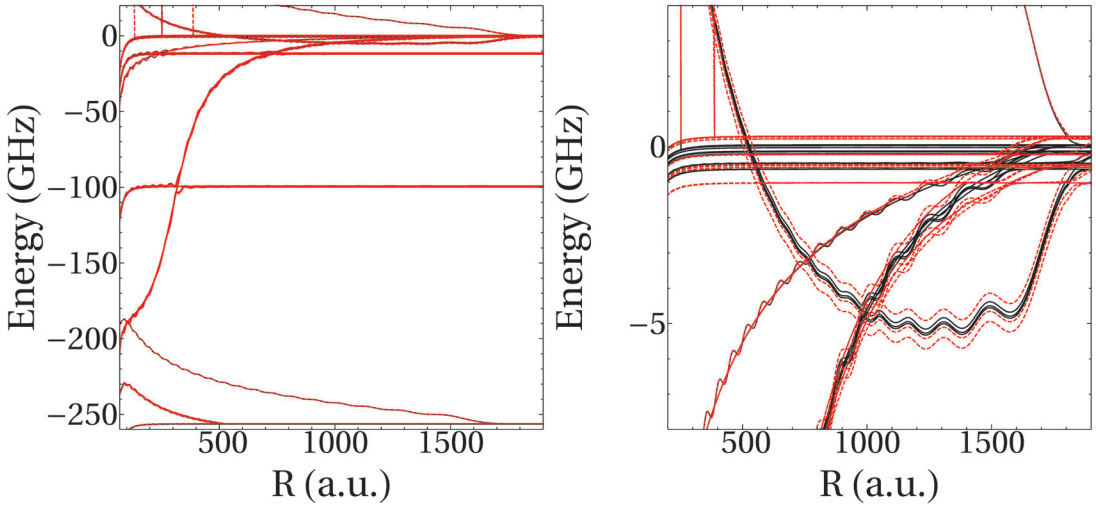

Figure 9.9. Lithium-lithium potential energy curves for $n = 30$. $^6Li_2$ (red) and $^7Li_2$ (black) are almost indistinguishable except for the larger hyperfine splitting of ^{7}Li. Vertical spikes are a numerical artifact of the p-wave potential.

in a search for interesting degeneracies and modifications to this potential structure as n changes.

Thus far no heteronuclear Rydberg molecules have been studied. Here we report on only a single example case, a KRb molecule. Both configurations – trading which atom is excited to the Rydberg state – are shown in Figs. 9.10 and 9.12. The spectra of these molecules closely resembles their homonuclear counterparts as the primary features depend most strongly on the scattering phase shifts. Although no interesting features of this heteronuclear molecule stand out, there is again a very large parameter space composed of all the parameters composing a Rydberg molecule – fine and hyperfine structure, quantum defects, scattering phases, and atomic masses – that must be explored in heteronuclear molecules to identify interesting regions.

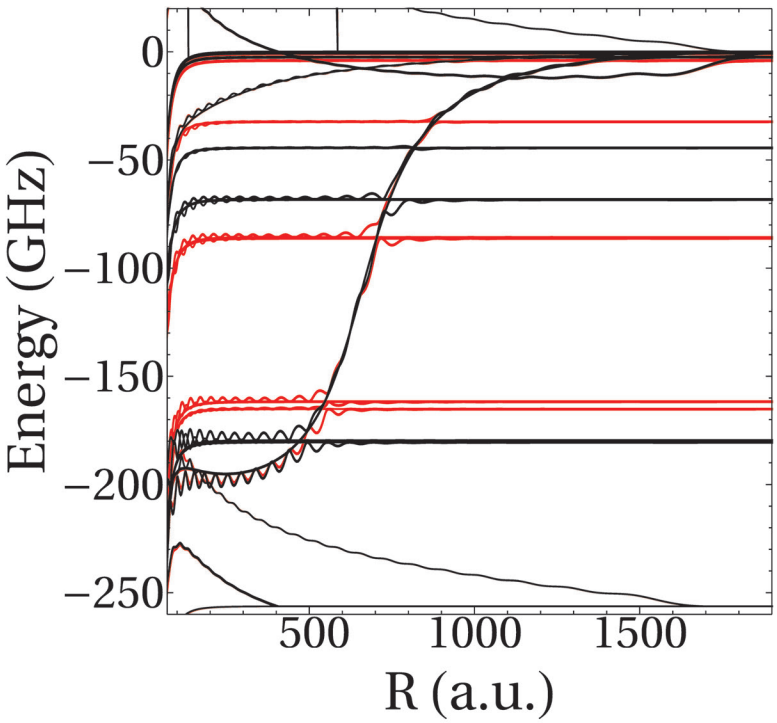

Figure 9.10. Potential energy curves for $^{87}Rb^{*}$ ^{39}K (red) and $^{39}K_2$ (black), in both cases relative to the $n = 30$ state. Vertical spikes are a numerical artifact of the p-wave potential.

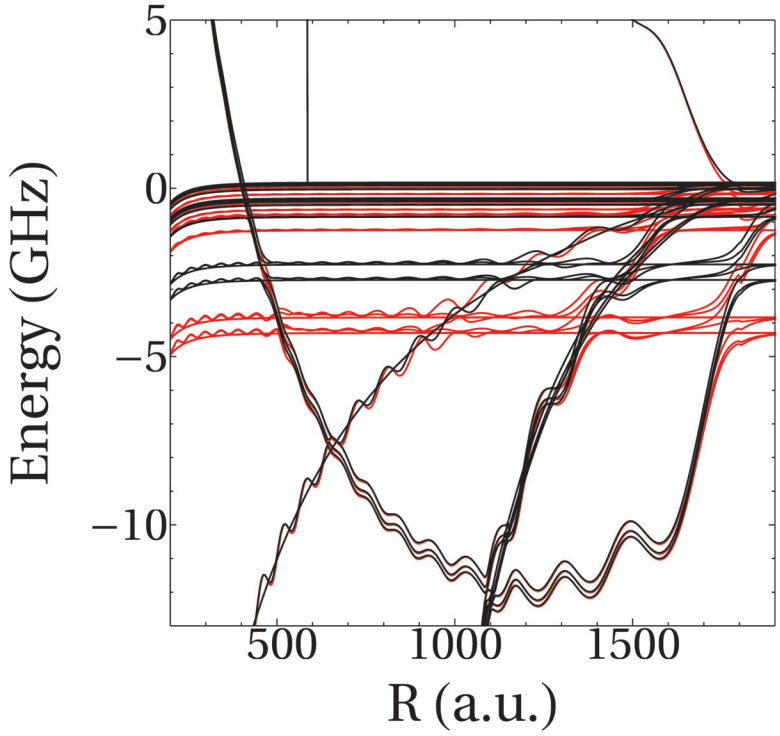

Figure 9.11. Trilobite potential energy curves for $^{87}Rb^{*}$ ^{39}K (red) and $^{39}K_2$ (black), in both cases relative to the $n = 30$ state. Vertical spikes are a numerical artifact of the p-wave potential.

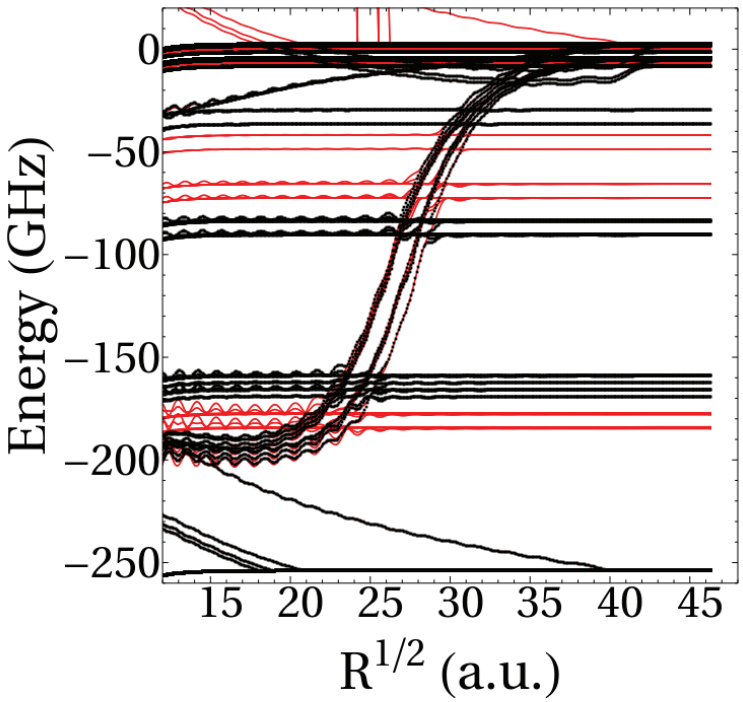

Figure 9.12. Potential energy curves for $^{39}K^{*}$ ^{87}Rb (red) and $^{87}Rb_2$ (black), in both cases relative to the $n = 30$ state. Vertical spikes are a numerical artifact of the p-wave potential.

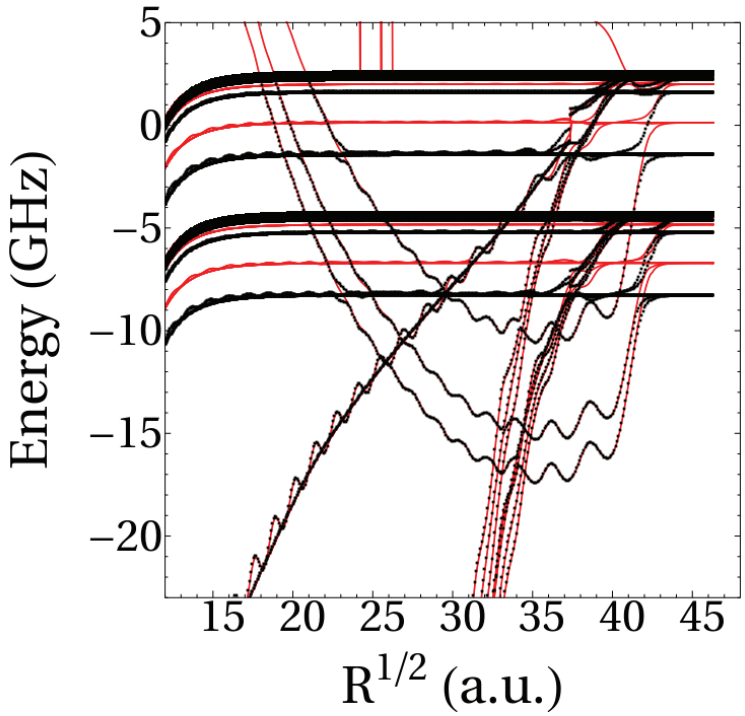

Figure 9.13. Trilobite potential energy curves for $^{39}K^*$ ^{87}Rb (red) and $^{87}Rb_2$ (black), in both cases relative to the $n = 30$ state. Vertical spikes are a numerical artifact of the p-wave potential.

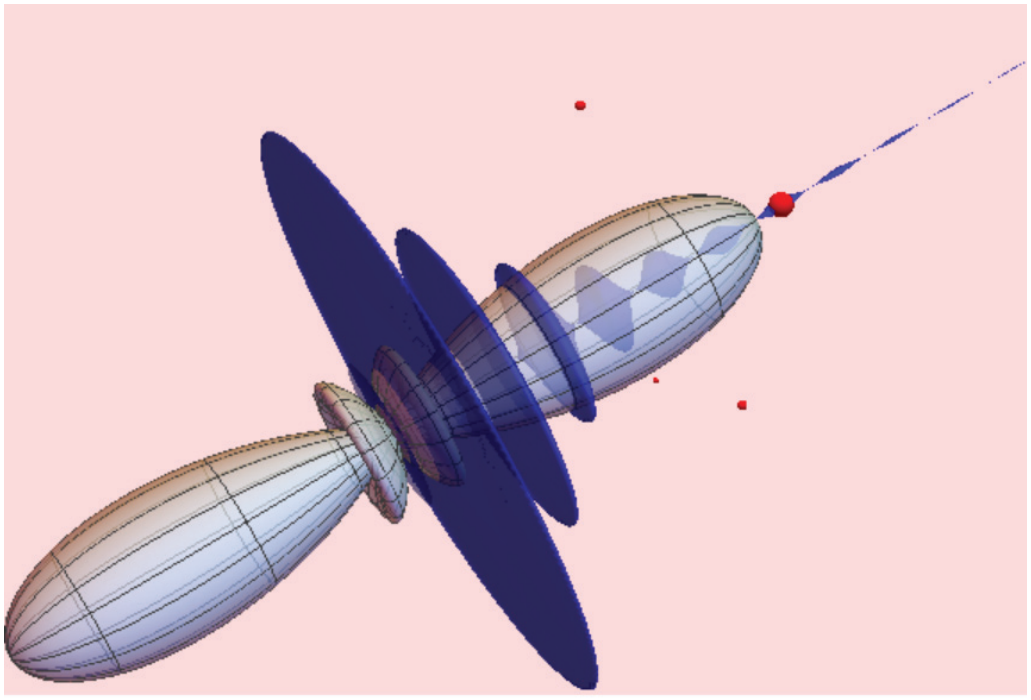

Figure 9.14. One possible system for future study discussed in Chapter 10: a long-range anionic molecule, formed from a ground state atom (red sphere) and a doubly excited H^- resonance state whose angular states hybridize to form a permanent dipole and whose electronic wave function is a Bessel function of imaginary order.

10. CONCLUSIONS AND OUTLOOK

The study of ultra-long-range Rydberg molecules has matured into a vibrant and dynamic field since its origin almost two decades ago. Substantial effort on the theoretical side has extended the scope of this field to include more interesting physics, but most exciting has been the tremendous experimental accomplishments within the last decade. We have focused on several aspects of these molecules in this present work. In the polyatomic direction, we developed a theory of polyatomic Rydberg molecules with arbitrary numbers of constituent atoms in a variety of configurations. We emphasized the construction of symmetric orbitals due to their ability to disentangle the complicated structure of the potential energy curves and to reveal the mathematical elegance of point group symmetries. Our inclusion of the p-wave interaction, of substantial importance in the heavy alkali atoms, is an important addition to the theory. Our further studies into the effects on states of low angular momentum and into the effects of disordered perturber placement have been substantial steps forward. Although the focus in this study has been on the breathing modes due to their relative simplicity, many of these extensions are readily applicable to polyatomic systems without this restriction. The hydrogen line broadening study presented is the first step in this direction, and similar ideas may be useful in interpreting Rb line shapes taken from very dense clouds. In the future, several exciting opportunities come to mind. First, the work presented here can be readily used to study the effects of symmetry breaking in these molecules. One could begin with a structural study of Rydberg trimers or tetramers, which would exhibit respectively Renner-Teller

and Jahn-Teller effects as they distort away from symmetric geometries. This could be applied more generally to non-adiabatic effects and conical interesections in the structure and dynamics of ultra-long-range Rydberg molecules. Finally, the ability to form Rydberg molecules in an optical lattice has been established [156], and this could lead to a wide range of fascinating work using highly symmetric polyatomic Rydberg molecules which span multiple lattice sites.

Secondly, we explored some of the novel possibilities stemming from the creation of these molecules in non-alkali atoms. Specifically, we predicted that Ca*-Ca polar trilobite molecules can be readily formed via two-photon excitation. We also examined the effects of Rydberg states that have significant character in Rydberg series converging to two spin-orbit split thresholds, and predicted that interesting potential energy curves exhibiting two dramatically different length scales can be obtained by exploiting this channel mixing. These molecules could therefore be photoassociated into states having radically different bond lengths at very similar energies. The dramatic recent successes at Rice University using Sr have shown that these experiments are promising, and we expect that the examples discussed in chapter 5 will spark further interest in complex, multichannel atomic species in the near future.

Third, we developed a complete theoretical picture for these Rydberg molecules including all their spin degrees of freedom, which has already been utilized in several theoretical and experimental studies. Future work here should focus on finding methods to improve the convergence of the diagonalization approach, or else to extend the Green's function or related methods to include these spin properties. The calculations for Rydberg molecules involving lighter alkali atoms and heteronuclear configurations presented in the previous chapter are also founded on this full theory. Eventually its extension to polyatomic homonuclear and heteronuclear molecules

would be desirable to uncover the rich and detailed physics in these complicated systems.

Fourth, we studied the interactions between polar Rydberg molecules, focusing on butterfly states due to their recent experimental observation. These results showed that the dipole-dipole interaction is enormous in these molecules, making them leading candidates for such studies. These sorts of calculations could easy be extended to other fascinating scenarios, such as the possible formation of bound tetramer states between two Rydberg molecules, or interactions between trilobite-like molecules and other bare Rydberg atoms. These same ideas, coupled with the polyatomic studies of chapter 4, could be relevant to Rydberg-Rydberg macrodimers and trimers.

The interplay of these molecular systems with external electric and magnetic fields is another interesting field of research with strong applications towards quantum control and manipulation. A particularly delicate example of this was shown in chapter 9, where electric and magnetic fields can be used to emulate the effect of a ground state atom on a solitary Rydberg atom.

We have also studied negative ion photodetachment in highly excited regimes. Our calculations are in excellent agreement with recent experimental work, and novel predictions for even higher excited states were made in addition to an improved interpretation of these previous observations. Further work is still required to fully understand the resonance structure of these partial cross sections and identify the physical causes of any resonant behavior, particularly to understand if it can be linked with the long-range physics of these systems. In the opposite regime, electron-atom interactions at very low energy was also studied in order to obtain very accurate scattering phase shifts of relevance to Rydberg molecules. To further combine these two systems, an interesting system to explore in greater detail is that of a doubly excited hydrogen anion near a perturber ion. Since, in the non-relativistic limit, the

degeneracy of hydrogenic states leads to a linear Stark effect, these doubly excited states are truly bound in a dipole potential which gives rise to Rydberg-like states whose sizes and lifetimes grow exponentially. The primary challenge to observing a type of "long-range anionic molecule" lies in the very short lifetimes of these doubly excited states. If sufficiently long-lived states can be found, this concept should give rise to novel bound states where two neutral objects, the excited hydrogen atom and a ground state pertuber, are bound together by a single electron.

APPENDIX

A. SYMMETRY-ADAPTED ORBITALS

We first present an example of how to calculate one matrix representation of a symmetry operation. The example molecule will have four atoms arranged in a tetrahedron, belonging to the point group T_d. The atoms are placed equidistant from the Rydberg core at the origin and, in order from A to D, at (θ, φ) values $(0,0), (b,0), (b, 2\pi/3), (b, 4\pi/3)$, where $b = \arccos(-1/3)$. According to equations (4.13-4.14) the θ, φ butterfly orbitals are thus parallel to the unit vectors $\sin\theta\hat{z} - \cos\theta\cos\varphi\hat{x} - \cos\theta\sin\varphi\hat{y}$ and $\sin\varphi\hat{x} - \cos\varphi\hat{y}$, respectively. Plugging in the actual values for these angles gives the four unit vectors for both orbitals:

$$\theta : -\hat{x}, \frac{\hat{x}}{3} + \frac{2\sqrt{2}}{3}\hat{z}, -\frac{\hat{x}}{6} + \frac{\hat{y}}{2\sqrt{3}} + \frac{2\sqrt{2}}{3}\hat{z}, -\frac{\hat{x}}{6} - \frac{\hat{y}}{2\sqrt{3}} + \frac{2\sqrt{2}}{3}\hat{z}.$$
$$\varphi : -\hat{y}, -\hat{y}, \frac{\sqrt{3}}{2}\hat{x} + \frac{\hat{y}}{2}, -\frac{\sqrt{3}}{2}\hat{x} + \frac{\hat{y}}{2}.$$

As the example symmetry operation we choose one of the C_3 operations corresponding to a rotation about the z axis by $\frac{2\pi}{3}$ radians. This cyclically rotates the three atomic labels not along the z axis, so that the symmetry operation for the trilobite orbital is

$$\begin{pmatrix} \psi_A \\ \psi_C \\ \psi_D \\ \psi_B \end{pmatrix} = \begin{pmatrix} 1 & 0 & 0 & 0 \\ 0 & 0 & 1 & 0 \\ 0 & 0 & 0 & 1 \\ 0 & 1 & 0 & 0 \end{pmatrix} \begin{pmatrix} \psi_A \\ \psi_B \\ \psi_C \\ \psi_D \end{pmatrix}.$$

The rotation matrix in coordinate space corresponding to this symmetry operation is

$$\begin{pmatrix} -\frac{1}{2} & -\frac{\sqrt{3}}{2} & 0 \\ \frac{\sqrt{3}}{2} & -\frac{1}{2} & 0 \\ 0 & 0 & 1 \end{pmatrix} \tag{A.1}$$

which then must act on the orbitals. For example the θ orbital originally at A, $-\hat{x}$, is rotated to become:

$$\begin{pmatrix} \frac{1}{2} \\ \frac{\sqrt{3}}{2} \\ 0 \end{pmatrix} = \begin{pmatrix} -\frac{1}{2} & -\frac{\sqrt{3}}{2} & 0 \\ \frac{\sqrt{3}}{2} & -\frac{1}{2} & 0 \\ 0 & 0 & 1 \end{pmatrix} \begin{pmatrix} -1 \\ 0 \\ 0 \end{pmatrix}. \tag{A.2}$$

The linear combination of θ and φ butterfly orbitals at A that equals $(\frac{1}{2}, -\frac{\sqrt{3}}{2}, 0)^T$ are then solved, giving

$$(\psi_A^\theta) = -\frac{1}{2}\psi_A^\theta + \frac{\sqrt{3}}{2}\psi_B^\varphi. \tag{A.3}$$

Likewise, the rotation matrix acting on the orbital ψ_B^θ rotates it to:

$$\begin{pmatrix} -\frac{1}{6} \\ \frac{1}{2\sqrt{3}} \\ \frac{2\sqrt{2}}{3} \end{pmatrix} = \begin{pmatrix} -\frac{1}{2} & -\frac{\sqrt{3}}{2} & 0 \\ \frac{\sqrt{3}}{2} & -\frac{1}{2} & 0 \\ 0 & 0 & 1 \end{pmatrix} \begin{pmatrix} \frac{1}{3} \\ 0 \\ \frac{2\sqrt{2}}{3} \end{pmatrix}. \tag{A.4}$$

The resultant vector is identified as the θ orbital at C, so the permutation of labels was sufficient here and there is no mixing of angular butterfly orbitals. In the end, the enlarged symmetry operation matrix is

$$\begin{pmatrix} -\frac{1}{2} & 0 & 0 & 0 & \frac{\sqrt{3}}{2} & 0 & 0 & 0 \\ 0 & 0 & 1 & 0 & 0 & 0 & 0 & 0 \\ 0 & 0 & 0 & 1 & 0 & 0 & 0 & 0 \\ 0 & 1 & 0 & 0 & 0 & 0 & 0 & 0 \\ -\frac{\sqrt{3}}{2} & 0 & 0 & 0 & -\frac{1}{2} & 0 & 0 & 0 \\ 0 & 0 & 0 & 0 & 0 & 0 & 1 & 0 \\ 0 & 0 & 0 & 0 & 0 & 0 & 0 & 1 \\ 0 & 0 & 0 & 0 & 0 & 1 & 0 & 0 \end{pmatrix}. \tag{A.5}$$

The presence of negative or fractional values on the diagonals is what contributes to the trace of $\hat{P}^j$, giving different decompositions.

The coefficients $\mathcal{A}_p^{(j,\alpha)}$ are given here for the example symmetries. The rows of each matrix correspond to a given irrep j labeled in the first column; each column thereafter corresponds to a diatomic orbital at R_p. For the octagon the labeling simply proceeds around the octagon; the first four columns of the cube correspond to the upper layer ordered counter-clockwise viewed from above; the final four correspond to the bottom layer ordered identically.

These coefficients are, for the octagonal molecule,

$$\mathcal{A}^{\mathbf{1,2,3}}_{\mathbf{C_{8v}}} = \begin{pmatrix} A_1 & 1 & 1 & 1 & 1 & 1 & 1 & 1 & 1 \\ B_2 & 1 & -1 & 1 & -1 & 1 & -1 & 1 & -1 \\ E_1 & 1 & a & 1 & 0 & -1 & -a & -1 & 0 \\ E_1 & -1 & 0 & 1 & a & 1 & 0 & -1 & -a \\ E_2 & 1 & 0 & -1 & 0 & 1 & 0 & -1 & 0 \\ E_2 & 0 & 1 & 0 & -1 & 0 & 1 & 0 & -1 \\ E_3 & -1 & a & -1 & 0 & 1 & -a & 1 & 0 \\ E_3 & -1 & 0 & 1 & -a & 1 & 0 & -1 & a \end{pmatrix}$$

$$\mathcal{A}^{\mathbf{4}}_{\mathbf{C_{8v}}} = \begin{pmatrix} A_2 & 1 & 1 & 1 & 1 & 1 & 1 & 1 & 1 \\ B_1 & 1 & -1 & 1 & -1 & 1 & -1 & 1 & -1 \\ E_1 & -1 & 0 & 1 & a & 1 & 0 & -1 & -a \\ E_1 & 1 & a & 1 & 0 & -1 & -a & -1 & 0 \\ E_2 & 0 & 1 & 0 & -1 & 0 & 1 & 0 & -1 \\ E_2 & 1 & 0 & -1 & 0 & 1 & 0 & -1 & 0 \\ E_3 & -1 & 0 & 1 & -a & 1 & 0 & -1 & a \\ E_3 & -1 & a & -1 & 0 & 1 & -a & 1 & 0 \end{pmatrix},$$

$a = \sqrt{2}$. As described in section 4.2 the θ-butterfly is decoupled for all co-planar molecules. For the cubic molecule,

$$\mathbf{A}^{\mathbf{1,2}}_{\mathbf{O_h}} = \begin{pmatrix} A_{1g} & 1 & 1 & 1 & 1 & 1 & 1 & 1 & 1 \\ A_{2u} & 1 & -1 & 1 & -1 & -1 & 1 & -1 & 1 \\ F_{1u} & 1 & -1 & 1 & -1 & 1 & -1 & 1 & -1 \\ F_{1u} & -1 & 0 & 1 & 0 & 1 & 0 & -1 & 0 \\ F_{1u} & 0 & 1 & 0 & -1 & 0 & -1 & 0 & 1 \\ F_{2g} & 1 & 1 & 1 & 1 & -1 & -1 & -1 & -1 \\ F_{2g} & 0 & -1 & 0 & 1 & 0 & -1 & 0 & 1 \\ F_{2g} & 1 & 0 & -1 & 0 & 1 & 0 & -1 & 0 \end{pmatrix}$$

$$\mathbf{A^3_{O_h}} = \begin{pmatrix}
E_1 & 1 & 1 & 1 & 1 & -1 & -1 & -1 & -1 \\
E_1 & 0 & 0 & 0 & 0 & 0 & 0 & 0 & 0 \\
E_2 & 1 & -1 & 1 & -1 & 1 & -1 & 1 & -1 \\
E_2 & 0 & 0 & 0 & 0 & 0 & 0 & 0 & 0 \\
F_{1g} & b & 0 & -b & 0 & b & 0 & -b & 0 \\
F_{1g} & 0 & b & 0 & -b & 0 & b & -b & 0 \\
F_{1g} & 0 & 0 & 0 & 0 & 0 & 0 & 0 & 0 \\
F_{1u} & 1 & 1 & 1 & 1 & 1 & 1 & 1 & 1 \\
F_{1u} & 0 & -1 & 0 & 1 & 0 & 1 & 0 & -1 \\
F_{1u} & 1 & 0 & -1 & 0 & -1 & 0 & 1 & 0 \\
F_{2g} & 1 & -1 & 1 & -1 & -1 & 1 & -1 & 1 \\
F_{2g} & -1 & 0 & 1 & 0 & -1 & 0 & 1 & 0 \\
F_{2g} & 0 & 1 & 0 & -1 & 0 & 1 & 0 & -1 \\
F_{2u} & b & 0 & -b & 0 & -b & 0 & b & 0 \\
F_{2u} & 0 & b & 0 & -b & 0 & -b & 0 & b \\
F_{2u} & 0 & 0 & 0 & 0 & 0 & 0 & 0 & 0
\end{pmatrix}$$

$$\mathbf{A^4_{O_h}} = \begin{pmatrix} E_1 & 0 & 0 & 0 & 0 & 0 & 0 & 0 & 0 \\ E_1 & 1 & 1 & 1 & 1 & -1 & -1 & -1 & -1 \\ E_2 & 0 & 0 & 0 & 0 & 0 & 0 & 0 & 0 \\ E_2 & 1 & -1 & 1 & -1 & 1 & -1 & 1 & -1 \\ F_{1g} & 0 & 1 & 0 & -1 & 0 & -1 & 0 & 1 \\ F_{1g} & 1 & 0 & -1 & 0 & 1 & 0 & -1 & 0 \\ F_{1g} & 1 & 0 & -1 & 0 & 1 & 0 & -1 & 0 \\ F_{1u} & 0 & 0 & 0 & 0 & 0 & 0 & 0 & 0 \\ F_{1u} & b & 0 & -b & 0 & b & 0 & -b & 0 \\ F_{1u} & 0 & b & 0 & -b & 0 & b & 0 & -b \\ F_{2g} & 0 & 0 & 0 & 0 & 0 & 0 & 0 & 0 \\ F_{2g} & 0 & b & 0 & -b & 0 & -b & 0 & b \\ F_{2g} & b & 0 & -b & 0 & -b & 0 & b & 0 \\ F_{2u} & 0 & -1 & 0 & 1 & 0 & -1 & 0 & 1 \\ F_{2u} & 1 & 0 & -1 & -0 & 1 & 0 & -1 & 0 \\ F_{2u} & 1 & -1 & 1 & -1 & -1 & 1 & -1 & 1 \end{pmatrix},$$

$b = \sqrt{3}$.

B. FURTHER DETAILS: POLYATOMIC RYDBERG MOLECULES

This appendix justifies the method discussed in Section 4.5, using a more formal derivation and a Hamiltonian of the form $H = H_0 + T + B + J$. H_0 is the Rydberg Hamiltonian, while T and B are general operators that can either represent two different perturbers or, as labeled here, trilobite and butterfly s-wave pseudopotentials. We can, without loss of generality, choose only two of these operators since the formalism developed in section 4.1 using the trilobite overlap matrix shows that these terms are essentially equivalent, so the generalization to include an arbitrary number of perturbers and all four partial wave terms is obvious from the set up here. J is any sort of additional operator, such as an external field. We diagonalize H in a basis of a single hydrogenic manifold for notational simplicity, although in a real calculation additional manifolds are included and the structure of the following equations scales appropriately. We reorder the basis in such a way as to clump eigenstates with vanishing quantum defects, the "high-l" states, in a block, and the "low-l" states in another block. This gives the matrix equation

$$\left[\begin{pmatrix} T_{hh} & T_{hl} \\ T_{lh} & T_{ll} \end{pmatrix} + \begin{pmatrix} B_{hh} & B_{hl} \\ B_{lh} & B_{ll} \end{pmatrix} + \begin{pmatrix} \epsilon I_{hh} & 0_{hl} \\ 0_{lh} & Q_{ll} \end{pmatrix} + \begin{pmatrix} J_{hh} & J_{hl} \\ J_{lh} & J_{ll} \end{pmatrix}\right] \begin{pmatrix} c_h \\ c_l \end{pmatrix} = E \begin{pmatrix} c_h \\ c_l \end{pmatrix}.$$

Here $= -\frac{1}{2n^2}$ is the hydrogenic energy level and $Q_{ll} = -\frac{1}{2(n-\mu_l)^2} I_{ll}$ are the quantum defect-shifted energy eigenvalues of the low-l states.

We next change the basis of the high-l coefficients to one defined:

$$c_h = (t_h, b_h, \underline{V}_{hh-2}) \cdot a_h,$$

where the $h \times h$ matrix defined there consists of the known trilobite and butterfly eigenvectors (or trilobite eigenvectors corresponding to different perturber locations, etc...), and the remaining columns are orthogonal to these vectors. Inputting this into our matrix equation, further partitioning the vector $a_h = (t_1, b_1, \vec{a}_{h-2})^\dagger$, and expressing the Fermi pseudopotential matrix elements using their separable form, we obtain:

$$\left[\begin{pmatrix} t_h t_h^\dagger t_h & t_h t_h^\dagger b_h & t_h t_h^\dagger V_{hh-2} & t_h \phi_l^\dagger \\ \phi_l t_h^\dagger t_h & \phi_l t_h^\dagger b_h & \phi_l t_h^\dagger V_{hh-2} & \phi_l \phi_l^\dagger \end{pmatrix} + \begin{pmatrix} b_h b_h^\dagger t_h & b_h b_h^\dagger b_h & b_h b_h^\dagger V_{hh-2} & b_h \psi_l^\dagger \\ \psi_l b_h^\dagger t_h & \psi_l b_h^\dagger b_h & \psi_l b_h^\dagger V_{hh-2} & \psi_l \psi_l^\dagger \end{pmatrix} \right.$$

$$\left. + \begin{pmatrix} \epsilon t_h & \epsilon b_h & \epsilon V_{hh-2} & 0_{hl} \\ 0_{l1} & 0_{l1} & 0_{lh-2} & Q_{ll} \end{pmatrix} + \begin{pmatrix} J_{hh} t_h & J_{hh} b_h & J_h h V_{hh-2} & J_{hl} \\ J_{lh} t_h & J_{lh} b_h & J_{lh} V_{hh-2} & J_{ll} \end{pmatrix} \right] \begin{pmatrix} t_1 \\ b_1 \\ a_{h-2} \\ c_l \end{pmatrix}$$

$$= \begin{pmatrix} E t_h & E b_h & E V_{hh-2} & 0_{hl} \\ 0_{l1} & 0_{l1} & 0_{lh-2} & I_{ll} \end{pmatrix} \begin{pmatrix} t_1 \\ b_1 \\ a_{h-2} \\ c_l \end{pmatrix}.$$

This equation cleans up substantially once we replace $\gamma_{11} = t_h^\dagger t_h$, $\gamma_{12} = t_h^\dagger b_h$, etc in preparation for the final answer. These are the eigenvalues and overlaps of the Fermi

pseudopotential matrices. We also eliminate terms which vanish due to orthogonality. This reveals:

$$\left[\begin{pmatrix} t_h\gamma_{11} & t_h\gamma_{12} & 0_{hh-2} & t_h\phi_l^\dagger \\ \phi_l\gamma_{11} & \phi_l\gamma_{12} & 0_{lh-2} & \phi_l\phi_l^\dagger \end{pmatrix} + \begin{pmatrix} b_h\gamma_{21} & b_h\gamma_{22} & 0_{hh-2} & b_h\psi_l^\dagger \\ \psi_l\gamma_{21} & \psi_l\gamma_{22} & 0_{lh-2} & \psi_l\psi_l^\dagger \end{pmatrix} \right.$$

$$\left. + \begin{pmatrix} \epsilon t_h & \epsilon b_h & \epsilon V_{hh-2} & 0_{hl} \\ 0_{l1} & 0_{l1} & 0_{lh-2} & Q_{ll} \end{pmatrix} + \begin{pmatrix} J_{hh}t_h & J_h h b_h & J_h h V_{hh-2} & J_{hl} \\ J_{lh}t_h & J_{lh}b_h & J_{lh}V_{hh-2} & J_{ll} \end{pmatrix} \right] \begin{pmatrix} t_1 \\ b_1 \\ a_{h-2} \\ c_l \end{pmatrix}$$

$$= \begin{pmatrix} Et_h & Eb_h & EV_{hh-2} & 0_{hl} \\ 0_{l1} & 0_{l1} & 0_{lh-2} & I_{ll} \end{pmatrix} \begin{pmatrix} t_1 \\ b_1 \\ a_{h-2} \\ c_l \end{pmatrix}.$$

The final step is to multiply the above by the matrix

$$\begin{pmatrix} t_h^\dagger & 0 \\ b_h^\dagger & 0 \\ V_{h-2h}^\dagger & 0 \\ 0 & I_{ll} \end{pmatrix}.$$

from the left. This then gives a matrix equation of the form:

$$\left[\begin{pmatrix} \gamma_{11}\gamma_{11} & \gamma_{11}\gamma_{12} & 0_{hh-2} & \gamma_{11}\phi_l^\dagger \\ \gamma_{21}\gamma_{11} & \gamma_{21}\gamma_{12} & 0_{lh-2} & \gamma_{21}\phi_l^\dagger \\ 0 & 0 & 0 & 0 \\ \phi_l\gamma_{11} & \phi_l\gamma_{12} & 0_{hh-2} & \phi_l\phi_l^\dagger \end{pmatrix} + \begin{pmatrix} \gamma_{12}\gamma_{21} & \gamma_{12}\gamma_{22} & 0_{hh-2} & \gamma_{12}\psi_l^\dagger \\ \gamma_{22}\gamma_{21} & \gamma_{22}\gamma_{22} & 0_{hh-2} & \gamma_{22}\psi_l^\dagger \\ 0 & 0 & 0 & 0 \\ \psi_l\gamma_{21} & \psi_l\gamma_{22} & 0_{lh-2} & \psi_l\psi_l^\dagger \end{pmatrix}$$
$$+ \begin{pmatrix} \epsilon\gamma_{11} & \epsilon\gamma_{12} & 0_{hh-2} & 0_{hl} \\ \epsilon\gamma_{21} & \epsilon\gamma_{22} & 0_{hh-2} & 0_{hl} \\ 0 & 0 & \epsilon I_{hh-2} & 0 \\ 0_{l1} & 0_{l1} & 0_{hh-2} & Q_{ll} \end{pmatrix}$$
$$+ \left.\begin{pmatrix} t_h^\dagger J_{hh} t_h & t_h^\dagger J_h h b_h & t_h^\dagger J_h h V_{hh-2} & t_h^\dagger J_{hl} \\ b_h^\dagger J_{hh} t_h & b_h^\dagger J_h h b_h & b_h^\dagger J_h h V_{hh-2} & b_h^\dagger J_{hl} \\ V_{h-2h}^\dagger J_{hh} t_h & V_{h-2h}^\dagger J_h h b_h & V_{h-2h}^\dagger J_h h V_{hh-2} & V_{h-2h}^\dagger J_{hl} \\ J_{lh} t_h & J_{lh} b_h & J_{lh} V_{hh-2} & J_{ll} \end{pmatrix}\right] \begin{pmatrix} t_1 \\ b_1 \\ a_{h-2} \\ c_l \end{pmatrix}$$
$$= \begin{pmatrix} E\gamma_{11} & E\gamma_{12} & 0_{hh-2} & 0_{hl} \\ E\gamma_{21} & E\gamma_{22} & 0_{hh-2} & 0_{hl} \\ 0 & 0 & EI_{hh-2} & 0 \\ 0_{l1} & 0_{l1} & 0_{hh-2} & I_{ll} \end{pmatrix} \begin{pmatrix} t_1 \\ b_1 \\ a_{h-2} \\ c_l \end{pmatrix}.$$

From this it is clear that, apart from the matrix operator for the external interaction which breaks the high$-l$ degeneracy, all the matrices are block diagonal and, removing the trivially zero components, are of the form

$$\begin{pmatrix} {}_i\gamma_{1i}\gamma_{i1} + \epsilon\gamma_{11} & {}_i\gamma_{1i}\gamma_{i2} + \epsilon\gamma_{12} & \gamma_{11}\phi_l^\dagger \\ {}_i\gamma_{2i}\gamma_{i1} + +\epsilon\gamma_{21} & {}_i\gamma_{2i}\gamma_{21} + \epsilon\gamma_{22} & \gamma_{21}\phi_l^\dagger \\ \phi_l\gamma_{11} & \phi_l\gamma_{12} & \phi_l\phi_l^\dagger + Q_{ll}. \end{pmatrix}$$

If all the low-l terms of this matrix are removed, can be set to zero since it is just an overall energy scale and, replacing these γ terms with the relevant trilobite overlap

matrices one obtains again the formalism of chapter 4. Keeping these couplings gives the same matrix elements as those developed in section 4.5.

Finally, we note that to include $\mathcal{N} > 1$ n manifolds we would simply lump all low-l states together into a larger sub-block, and include additional coupling terms for each manifold. Thus rather than having 2×2 matrices as in the above derivation, one would have matrices with dimension $2\mathcal{N} + 1$. For example, for two rather than one manifold the matrix terms would be replaced as follows:

$$\begin{pmatrix} T_{hh} & T_{hl} \\ T_{lh} & T_{ll} \end{pmatrix} \rightarrow \begin{pmatrix} T_{11} & T_{12} & T_{1l} \\ T_{21} & T_{22} & T_{2l} \\ T_{l1} & T_{l2} & T_{ll} \end{pmatrix},$$

where T_{11}, T_{22} are T_{hh} within manifolds 1 and 2 separately, T_{12} is a high-high coupling matrix between the two manifolds, and T_{1l}, T_{2l} couple the high-l states of each manifold to the total set of low-l states.

C. MQDT CLOSED-CHANNEL ELMINATION IN THE S-MATRIX FORMALISM

Alternatively, the MQDT calculation presented in chapter 5 can be accomplished with the S matrix formalism, starting with

$$M_{ii}\,(r) = f_i(r)\delta_{ii}\; - g_i(r)K_{ii}\,(r). \tag{C.1}$$

S is writted in terms of the in/outgoing wave functions:

$$\begin{aligned} M_{ii}\,(r) &= \frac{i}{\sqrt{2}}(-f^+ + f^-)\delta_{ii}\; - \frac{1}{\sqrt{2}}(-f^+ - f^-)K_{ii} \\ &= \frac{1}{i\sqrt{2}}(f_i^+(r)\delta_{ii}\; + if_i^+ J_{i\beta}I^{-1}_{\beta i}) - \frac{1}{i\sqrt{2}}(f_i^-\delta_{ii}\; - f_i^- iJ_{i\beta}I^{-1}_{\beta i}) \\ \Longrightarrow\; M_{ii}\,I_{i\,\beta} = F_{i\beta} &= \frac{1}{i\sqrt{2}}f_i^+(r)(I_{i\beta} + iJ_{i\beta}) - \frac{1}{i\sqrt{2}}f_i^-(r)(I_{i\beta} - iJ_{i\beta}). \end{aligned}$$

This is how we can rewrite our original solution, $F_{i\beta}(r)$, in terms of (f^+, f^-), and then manipulate this solution to obtain the scattering boundary conditions:

$$\begin{aligned} M_{ii}\,(r) &= F_{i\beta}(I_{i\beta} + iJ_{i\beta})^{-1} \\ &= \frac{1}{i\sqrt{2}}f_i^+(r) - \frac{1}{i\sqrt{2}}f_i^-(r)S_{ii}^\dagger\,. \end{aligned}$$

Notice that this then connects with the original relationship between $\underline{S}$ and $\underline{K}$:

$$\begin{aligned} S_{ii}^\dagger\; = (\underline{I} - i\underline{J})(\underline{I} + i\underline{J})^{-1} = \frac{\underline{I} - i\underline{J}}{\underline{I} + i\underline{J}} \cdot \frac{\underline{I}^{-1}}{\underline{I}^{-1}} &= \frac{\underline{1} - i\underline{K}}{\underline{1} + i\underline{K}} \\ \Longrightarrow\; \underline{S} &= \frac{\underline{1} + i\underline{K}}{\underline{1} - i\underline{K}}. \end{aligned}$$

Once again we partition the matrices into open/closed channel pieces to obtain:

$$\begin{bmatrix} M_{oo} & M_{oc} \\ M_{co} & M_{cc} \end{bmatrix} = \frac{1}{i\sqrt{2}} f^+(r) - \frac{1}{i\sqrt{2}} f^-(r) \begin{bmatrix} S^\dagger_{oo} & S^\dagger_{oc} \\ S^\dagger_{co} & S^\dagger_{cc} \end{bmatrix}$$

$$\underline{M}^{(-)}(r) = \underline{M} \begin{bmatrix} B_o \\ B_c \end{bmatrix} \implies M^-_{co} = \frac{1}{i\sqrt{2}}(-f^-_c S^\dagger_{co} B_o + (f^+_c(r) - f^-_c S^\dagger_{cc}) B_c).$$

The asymptotic expressions for $f^\pm$ are

$$f^\pm \to \propto e^{\pm i\beta} r^{-\nu} e^{\kappa r}. \tag{C.2}$$

Thus, at long range

$$\begin{aligned} M^-_{co} &= \frac{1}{i\sqrt{2}}(-e^{-i\beta} S^\dagger_{co} B_o + (e^{i\beta} - e^{-i\beta} S^\dagger_{cc}) B_c) \\ &= \frac{1}{i\sqrt{2}} e^{-i\beta}(-S^\dagger_{co} B_o - (S^\dagger_{cc} - e^{2i\beta}) B_c). \end{aligned}$$

Once again this constrains the elements B_c to eliminate the divergent terms:

$$B_c = -(S^\dagger_{cc} - e^{2i\beta})^{-1} S^\dagger_{co} B_o. \tag{C.3}$$

If there are no open channels then B_o vanishes and instead

$$(S^\dagger_{cc} - e^{2i\beta}) B_c = 0; \tag{C.4}$$

The bound state energies occur when $\det(S^\dagger_{cc} - e^{2i\beta}) = 0$ We can substitute this value back in to M^-_{co} to obtain the closed-channel coefficient

$$\begin{aligned} M^-_{co} &= \frac{1}{i\sqrt{2}}((f^+_c(r) - f^-_c S^\dagger_{cc}) B_c) \\ &= \frac{1}{i\sqrt{2}}(f^+_c(r) - f^-_c(r) e^{2i\beta}) B_c \\ &= \ -\frac{i}{\sqrt{2}} e^{-i\beta_i} f^+ + \frac{i}{\sqrt{2}} f^- e^{i\beta_i} \quad (-e^{i\beta_i} B_c) \\ &= W(r, \nu_i, l_i)(-e^{i\beta_i} B_c). \end{aligned}$$

D. B-SPLINES

B-splines were utilized to calculate the one-electron basis set for electron-atom scattering and negative ion photodetachment. This appendix gives some important details about how they work. First, one defines a set of knots, which define the regions where the B-splines are nonzero. A convenient choice for Coulombic potentials places these knots on a square root mesh. Extra knots must be placed at the boundaries to create the appropriate boundary conditions. Their *Mathematica* implementation uses the following logic:

- $O + 1$ knot points are placed at the boundaries, where O is the order of the splines. This ensures that the degree zero spline, which covers O knots, is completely zero, while the degree one(two) splines go to the first(second) non-boundary knots such that they are one(zero) at the boundary. In this way one can set either the wave function or its derivative to zero on the boundary, depending on the desired boundary conditions.

- All splines of degree 2 and higher are zero at the boundary (and analogously at the right boundary). Therefore, box boundary conditions require that only splines with $2 \leq$ degree $\leq N - 1$ are included.

- N is the total number of splines, and is equal to $K - O - 3$, where K is the number of knot points. Alternatively, if the initial knot points are distributed over X points (not counting the additional knots required at the boundaries), then $N = X + O$.

- Since the splines are non-orthogonal, a generalized eigenvalue problem $\underline{A}x = b\underline{O}x$ must be solved, where $\underline{O}$ is the overlap matrix. All matrices involving B-splines are conveniently sparse due to the compact support of the B-splines: the product of two splines of degree i and j times any other function is manifestly zero unless $|i - j| \leq O$.

To utilize these B-splines, we expand the one-electron wave-function into the spline basis set, $u_{nl}(r) = \sum_{i=2}^{i=N-1} c_i B_i^d(x)$, where $B_i(x)$ are the B-splines of degree i and order d, and the summation limits assume closed boundary conditions. Then, the Schrödinger equation becomes:

$$\underline{H_{ij}} c_j = E_{nl} \underline{O_{ij}} c_j \tag{D.1}$$

$$\underline{O_{ij}} = \int_{x_0}^{x_0} B_i^d(x) B_j^d(x) \mathrm{d}x \tag{D.2}$$

$$\underline{H_{ij}} = \int_{x_0}^{x_0} \frac{1}{2} \frac{d}{dx} B_i^d(x) \frac{d}{dx} B_j^d(x) + V(x) B_i^d(x) B_j^d(x) \mathrm{d}x, \tag{D.3}$$

where $V(x)$ is the potential energy, and the use of a Bloch operator to make the kinetic energy operator Hermitian is avoided by using Green's theorem. The limits of integration, x_0 and x_0, are determined just by finding the knot points determining where both B-splines are non-zero. Solution of Eq. D.1 gives the box states. For wave functions which fit inside the box, these solutions have negative eigenvalues and correspond to real electronic states, while positive energy solutions provide a pseudocontinuum basis.

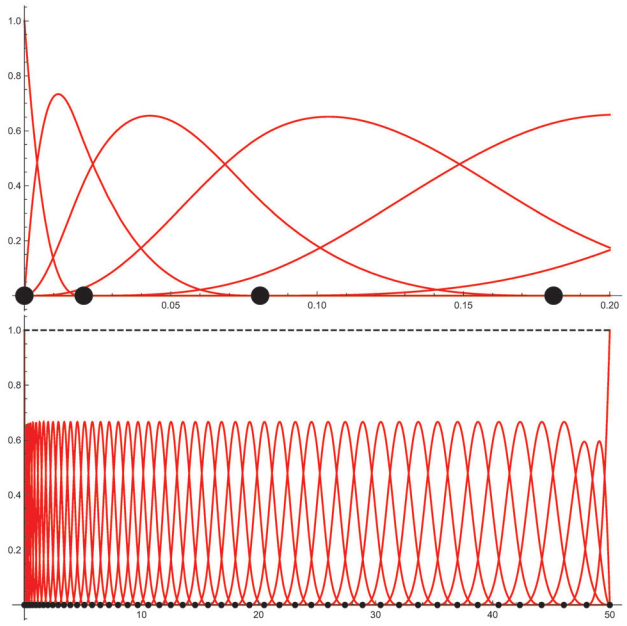

Figure D.1. Splines. The top panels shows splines near the left boundary, where in this case the degree one spline is included. To impose the boundary condition $\Psi(r = 0) = 0$ this spline must be removed from the basis. Black points show knot locations. Panel b shows all the splines used for the calculation; again the spline which is non-zero at the right boundary must be removed to satisfy box boundary conditions. The sum of all splines is unity.

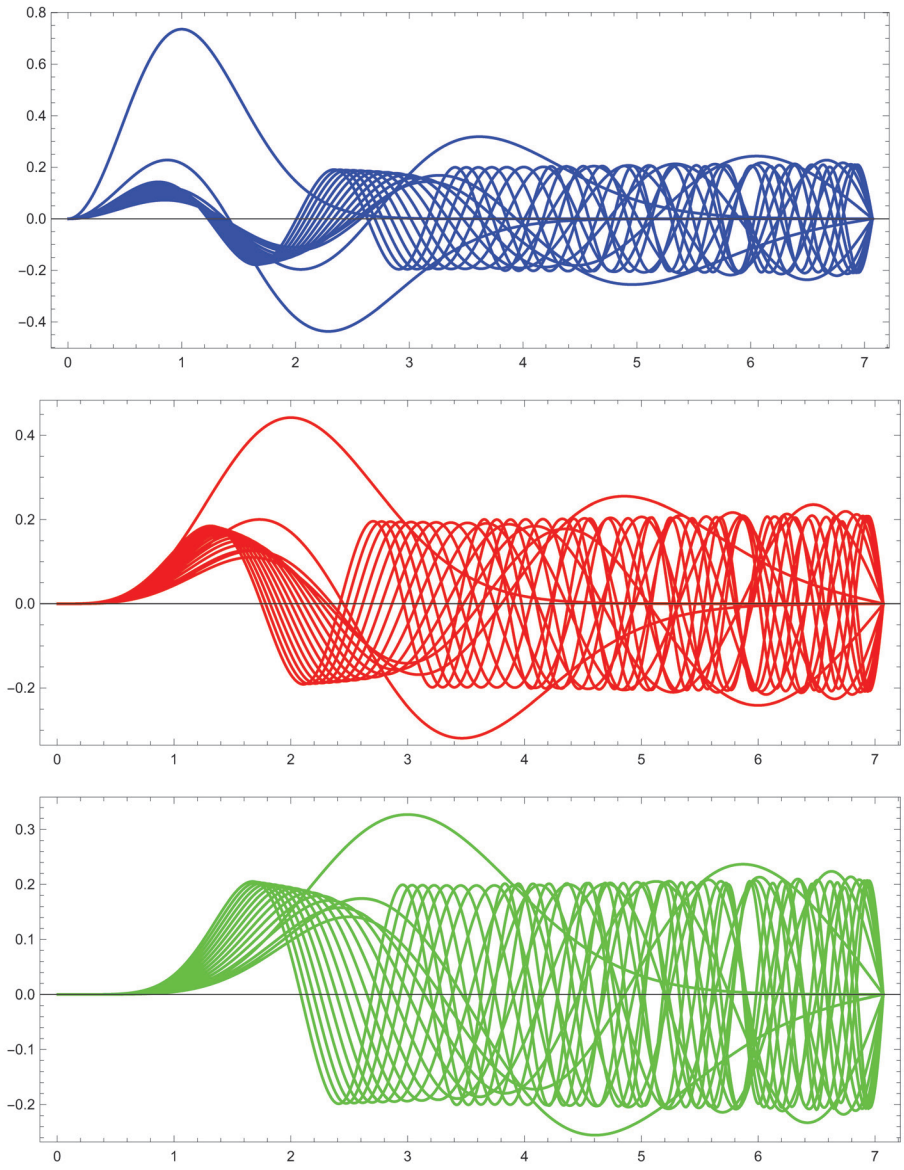

Figure D.2. A few examples of closed-channel orbitals used to create the two-electron basis for determining scattering phase shifts in potassium. From top to bottom: $l = 0, 1, 2$.

E. GHOST TRILOBITES: ADDITIONAL INFORMATION

The matrix elements necessary to calculate the time-evolution of the Rydberg state are:

$$l|\cos\theta|l \;=\; \sqrt{\frac{(l_<+1)^2}{(2l_<+1)(2l_<+3)}}\,\delta_{l,l\,\pm1} \tag{E.1}$$

$$l|\sin^2\theta|l \;=\; \frac{2(l^2+l-1)}{(2l+3)(2l-1)}\delta_{ll} \;-\; \sqrt{\frac{(l_<+2)^2(l_<+1)^2}{(2l_<+5)(2l_<+3)^2(2l_<+1)}}\,\delta_{l,l\,\pm2} \tag{E.2}$$

$$\begin{aligned} R^k_{nl,n\,l} \;&=\; \frac{2^{l+l\,+2}}{n^{l+2}n^{\,l\,+2}}\;\sqrt{\frac{(n-l-1)!(n\;-l\;-1)!}{(n+l)!(n\;+l\;)!}} \\ &\times \sum_{m,m\,=0}^{m=n-l-1}\binom{n+l}{n-l-1-m}\binom{n\;+l}{n\;-l\;-1-m} \\ &\times \frac{(k+m+m\;+l+l\;+2)!}{\frac{n+n}{nn}\;k+3+l+l\;+m+m}, \end{aligned} \tag{E.3}$$

where () are binomial coefficients. The "radial" momentum-space wave functions,

$$F_{nl}(k) = -(-i)^l\;\sqrt{\frac{2(n-l-1)!}{\pi(n+l)!}}n^2 2^{2(l+1)}l!n^l k^l(n^2k^2+1)^{-l-2}C^{l+1}_{n-l-1}\;\sqrt{\frac{n^2k^2-1}{n^2k^2+1}}\;\;, \tag{E.4}$$

possess a symmetry under the change of variables $nk = a^x$, where a is some constant. For simplicity, if a is e,

$$F_{nl}(x) = -(-i)^l\;\sqrt{\frac{2(n-l-1)!}{\pi(n+l)!}}n^2 2^{2(l+1)}l!n^l k^l e^{-2x}(\sinh(x))^{-l-2}C^{l+1}_{n-l-1}\,(\tanh(x))\,, \tag{E.5}$$

From inspection this function possesses a mirror symmetry (odd or even depending on the parity of n) about $x = 0$ when multiplied by e^{2x}. This is the reason for the symmetry about $k = 1/n$ of the function $|k^2\Psi(k)|^2$.

The Fourier transform of the electronic density is more involved than the calculation of the momentum wave functions. We proceed in the usual fashion, expanding the plane wave into spherical harmonics:

$$\begin{aligned}
\mathrm{d}^3 r e^{ik\cdot r}|\Psi(R_k,\vec{r})|^2 &= \sum_{l,k,p} \mathrm{d}^3 r c_l c_k 4\pi i^p j_p(kr) u_{nl}(r) u_{nk}(r) Y_{l0}(\hat{r}) Y^*_{k0}(\hat{r}) Y^*_{p0}(\hat{r}) Y_{p0}(\hat{k}) \\
&= 4\pi \sum_{l,k} c_l c_k \sum_{p=|l-k|}^{p=l+k} i^p \sqrt{\frac{(2l+1)(2p+1)(2k+1)}{4\pi}} \begin{pmatrix} l & p & k \\ 0 & 0 & 0 \end{pmatrix} \\
&\times^2 \quad \mathrm{d}r j_p(kr) u_{nl}(r) u_{nk}(r) Y_{p0}(\hat{k}).
\end{aligned}$$

Here c_l, c_k are the coefficients determining the orbital state. This radial integral can be evaluated in terms of hypergeometric functions following Eq. 40 of Ref. [317].

The following table shows the 130-pulse sequences used to make 99.9% molecular bonds corresponding to the first figure. Top row: the type of bond (trilobite, $k = 1, k = 3$; triatomic trilobite with $k = 1$; butterfly). Total time, including field ramps, in ns. The left column of each is the duration of the electric field pulse, while the right column is the interval in between electric field pulses. 130 pulses are used each time. Times are reported in ns.

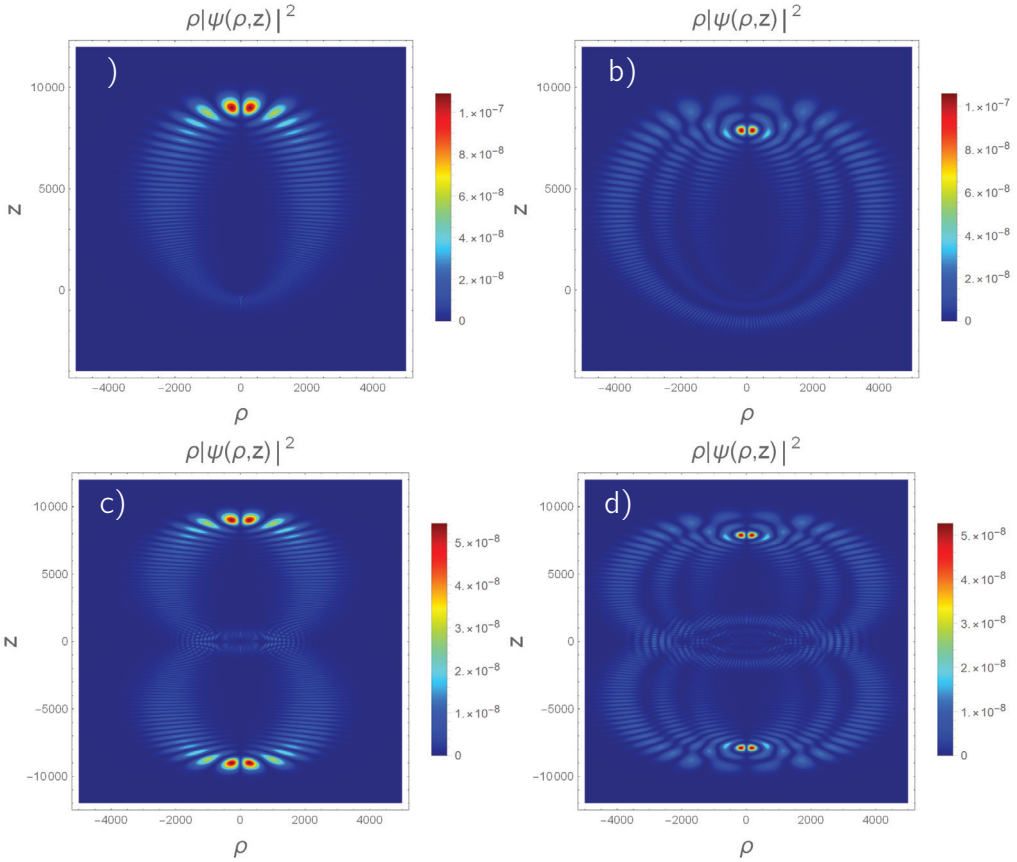

Figure E.1. Four real-space wave functions, plotted in cylindrical coordinates. a) $b = 1$ trilobite; b) $b = 3$ trilobite; c) $b = 1$ trilobite trimer; d) $b = 3$ trilobite trimer.

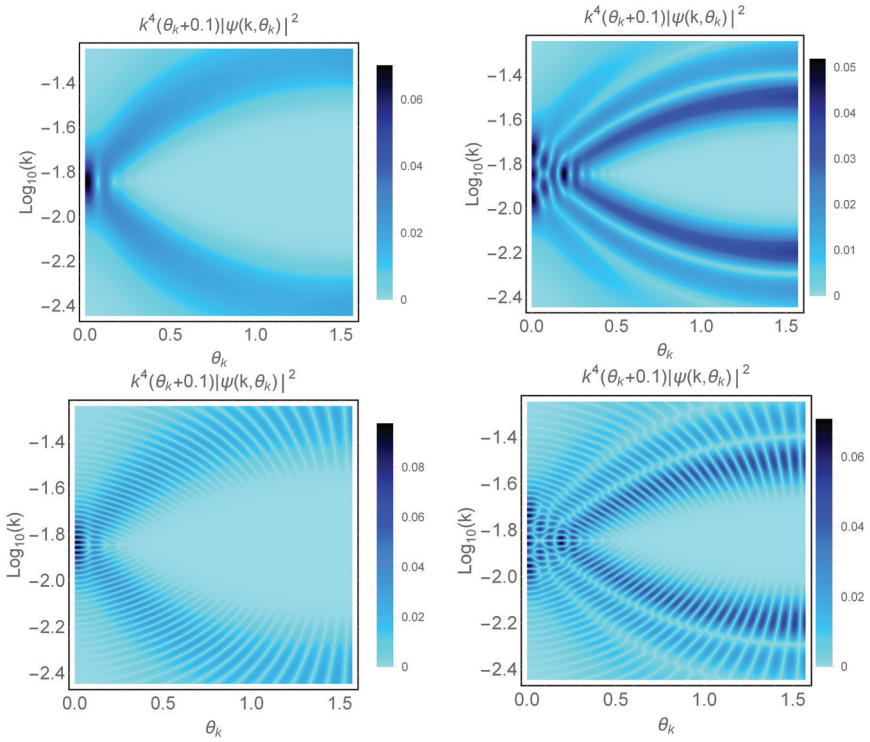

Figure E.2. Four momentum space wave functions, plotted in spherical coordinates. a) $b = 1$ trilobite; b) $b = 3$ trilobite; c) $b = 1$ trilobite trimer; d) $b = 3$ trilobite trimer.

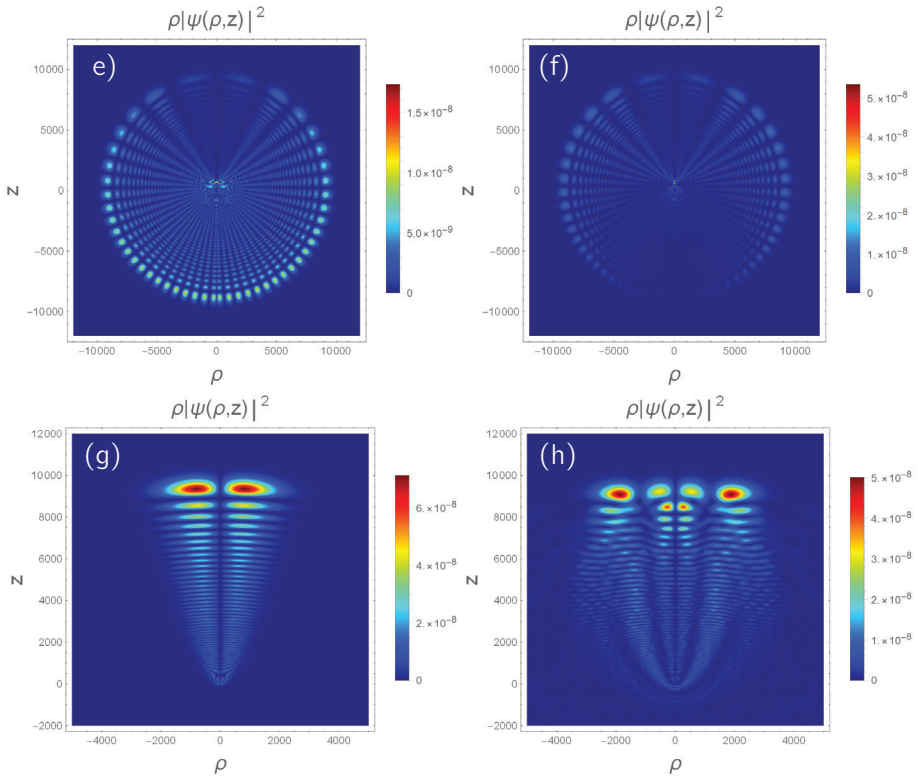

Figure E.3. Four real-space wave functions, plotted in cylindrical coordinates. e) $b = 48$ trilobite; f) butterfly; g) stark state; h) $b = 1$ trilobite, 84% match. .

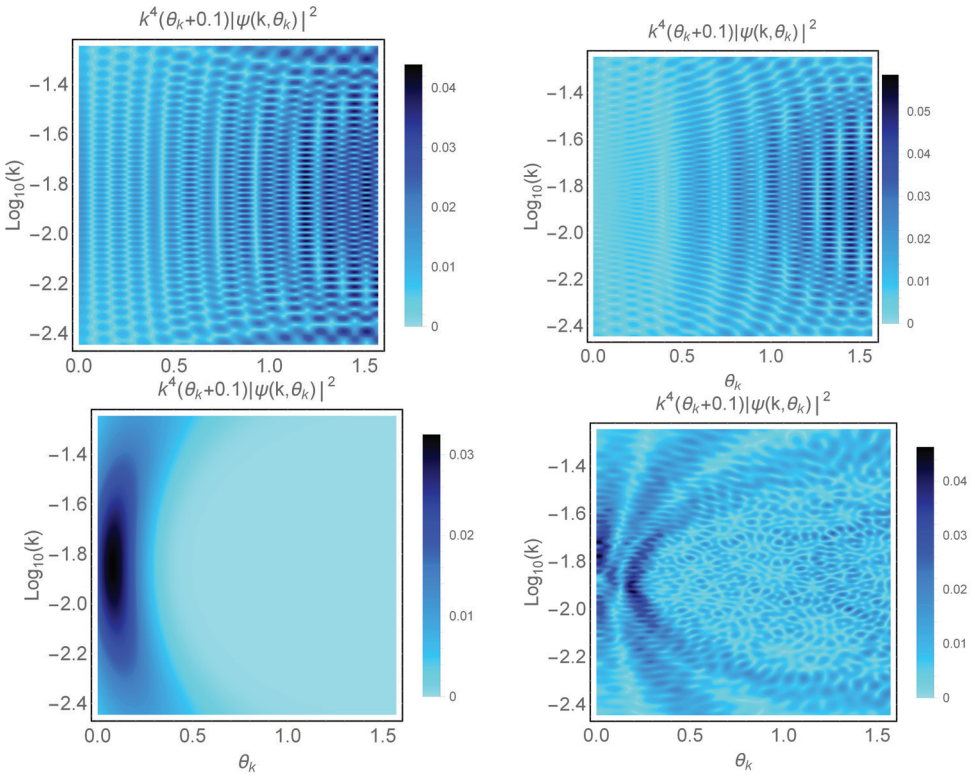

Figure E.4. Four momentum space wave functions, plotted in spherical coordinates. e) $b = 48$ trilobite; f) butterfly; g) stark state; h) $b = 1$ trilobite, 84% match.

$k=1$	(1-65)	(66-130)	143649	$k=3$	(1-65)	(66-130)	144631	trimer	(1-65)	(66-130)	144583	btfly	(1-65)	(66-130)	144578
36.0129	239.973	32.2792	224.897	30.6755	285.278	28.2444	295.56	35.4941	317.394	34.9943	371.849	60.3706	367.018	60.7922	228.261
47.4666	296.119	34.6906	224.662	59.6629	244.097	58.1024	266.409	41.2067	227.01	61.6375	330.277	39.8348	200.876	58.1241	242.571
30.0045	371.947	52.899	399.063	22.901	227.233	32.7547	254.69	37.1052	359.677	24.865	352.076	26.4902	305.972	38.5931	399.63
26.9364	305.557	32.3173	369.321	43.4052	329.984	57.4415	252.275	22.7512	274.308	53.14	250.2	59.5579	220.389	45.8705	378.874
48.2474	390.364	21.6446	326.888	46.8757	205.56	57.1991	327.417	43.174	316.964	45.5835	343.93	35.2915	219.911	42.8275	286.915
35.3907	286.297	49.5366	256.09	52.8709	362.685	30.79	381.279	52.2115	320.772	31.6169	316.027	28.1597	206.653	36.5052	366.661
30.4024	323.885	39.0652	315.117	36.9635	298.669	26.7545	357.504	44.5726	303.069	30.7177	327.868	54.4036	259.798	36.5816	335.232
56.3999	209.329	44.7074	381.198	20.7992	395.597	23.3285	395.421	30.6065	352.557	50.4794	213.035	24.8793	296.894	25.1104	357.093
45.9804	236.636	21.7709	326.225	39.8652	274.949	46.741	383.931	30.5509	315.958	52.9686	292.449	43.5578	313.587	40.7838	328.844
21.4295	335.036	57.9015	352.016	29.2127	373.025	56.8444	210.272	54.4517	295.954	30.9039	355.396	56.7162	245.521	35.0073	236.966
22.8669	367.902	54.4536	290.009	48.6238	397.661	32.1329	370.697	58.3629	329.656	38.9009	376.617	37.5066	220.36	19.574	365.431
32.0231	383.247	31.783	255.278	58.3326	345.844	21.8744	356.343	50.6946	376.125	55.3135	335.137	20.4112	393.853	35.8386	321.852
60.2675	265.296	48.1839	315.093	45.4129	202.377	47.0193	276.46	38.8064	228.696	49.6757	363.387	40.9484	363.069	45.881	268.174
38.8887	223.329	60.4721	250.07	51.7152	395.18	46.6587	288.208	32.8958	319.173	32.5454	251.306	51.8996	363.292	33.9069	373.105
58.0465	334.239	48.1055	212.31	22.0069	341.64	41.3305	210.498	50.8416	340.081	47.9297	280.926	39.7599	249.473	33.4779	207.189
57.5267	389.306	35.8335	217.65	26.2229	242.293	41.0315	299.244	49.1342	238.827	34.8307	273.306	57.2002	399.043	34.7687	222.04
23.5209	394.01	38.2097	201.5	50.2489	299.515	23.5623	219.671	30.9119	200.408	44.5811	278.972	32.0786	282.291	29.7687	305.958
54.5002	295.453	29.6287	285.938	54.3202	286.47	43.2787	296.826	22.971	226.089	35.117	337.097	32.5831	322.687	37.8944	305.699
39.4703	206.331	32.3441	258.172	56.3983	307.395	24.8648	379.713	24.3993	219.168	43.812	236.388	20.0271	361.559	47.3182	360.582
56.7084	256.443	30.9668	263.233	55.9024	259.512	29.4882	202.415	52.3659	334.999	28.1357	246.272	27.731	272.172	34.3291	340.796
28.0783	230.737	46.2487	379.572	31.1048	200.4	53.7477	385.433	22.6289	341.545	58.1248	365.036	35.2022	338.487	34.9558	330.768
27.4159	360.588	54.245	337.983	39.6045	336.299	58.7858	351.59	36.6224	348.738	55.4131	282.814	40.0481	338.553	36.2144	356.28
28.0018	209.663	51.2241	254.757	26.7141	204.882	56.6222	247.432	50.4774	308.945	48.6759	227.929	30.2489	326.799	36.7335	264.212
41.1562	375.336	54.7605	249.41	41.1233	273.923	46.0954	381.257	28.8492	242.746	29.9056	268.698	24.4098	216.463	37.3114	275.256
23.6961	269.633	45.594	358.763	32.4852	281.958	35.3781	388.049	40.7027	235.288	42.5593	229.814	37.4246	291.68	55.8091	232.417
44.193	239.039	21.8992	259.108	38.1478	384.26	48.7241	396.525	26.8742	378.235	35.1144	352.779	33.0148	326.247	44.7961	248.977
46.8809	266.353	26.2047	314.306	32.0011	217.978	31.4193	296.609	47.0053	242.595	55.8567	205.326	21.356	256.536	22.7177	360.936
27.4893	233.389	60.5374	213.329	55.9752	288.14	51.5617	357.951	56.9714	333.463	55.9697	277.301	58.0937	307.07	36.4336	375.12
59.4849	241.986	22.2376	380.693	59.7606	348.423	26.5195	371.158	37.708	392.821	28.0426	252.5	35.9571	239.647	45.9658	304.406
22.6778	288.645	23.7563	237.295	51.8483	352.026	34.3525	300.214	53.9524	229.21	39.4129	295.992	49.3244	278.39	30.0952	379.697
31.5342	215.259	38.1811	364.905	24.84	351.879	54.7173	234.761	37.2985	219.555	37.558	383.275	34.4936	291.086	41.2862	314.257
47.0625	292.209	20.9276	246.949	58.3077	268.378	31.1896	369.958	53.0096	238.627	36.2796	220.377	50.1296	297.785	40.6829	232.539
36.8888	382.182	29.8878	378.93	44.0284	278.645	44.8019	269.558	26.9275	247.854	58.1631	326.799	23.9885	365.504	38.6288	225.26
21.9193	280.661	24.6508	282.762	41.7882	298.654	31.932	220.334	54.7396	250.558	33.0521	318.584	51.5307	296.675	22.5173	342.054
20.2117	368.671	34.157	345.272	32.4352	262.323	23.4262	334.959	31.6746	364.349	42.9386	392.974	53.9926	233.198	40.3963	241.13
34.0221	384.654	27.9355	250.431	45.3283	316.765	22.251	235.589	46.3985	339.204	45.9787	238.165	39.6537	279.727	25.4145	289.824
43.1697	352.925	39.9112	305.71	58.4723	232.633	25.6947	327.89	26.5834	342.254	46.7611	259.763	50.0239	353.974	47.5152	216.052
32.9205	270.138	53.0118	375.556	57.6169	314.096	26.5022	277.831	48.5323	282.514	26.0348	330.627	27.7551	222.77	42.6354	267.576
37.0737	212.815	39.453	368.708	46.1446	285.484	52.1491	257.077	52.9682	337.359	25.494	303.908	37.3639	374.937	49.3535	312.226
43.3936	367.695	37.5166	364.99	26.4938	306.158	54.108	305.788	48.049	398.049	45.5871	228.933	39.1577	220.815	25.2979	246.669
55.2011	366.178	26.5726	309.188	45.6729	399.616	58.3289	297.998	25.9886	242.361	36.7109	227.367	55.7195	354.727	33.6709	268.085
27.6309	260.188	45.2975	263.423	42.7266	348.977	32.0211	208.119	48.9908	325.304	47.0478	287.425	39.606	278.581	42.3664	274.643
42.9364	333.198	36.1652	214.373	35.4476	213.432	36.2285	260.191	30.7462	286.924	54.5021	350.246	40.0968	216.426	39.8083	295.178
40.0133	259.606	28.0009	273.357	30.2824	274.801	43.815	346.334	37.7796	360.876	30.659	258.053	46.6367	301.11	39.2659	273.952
33.0666	218.466	22.2618	341.86	40.8836	346.152	50.3911	387.497	59.8862	332.371	47.8343	344.693	46.8011	239.983	22.707	337.213
54.7871	373.83	33.7303	399.873	41.4858	328.858	34.361	327.299	25.0457	351.478	24.1661	205.396	23.2958	298.147	23.9924	398.095
54.3451	397.18	22.9229	224.574	53.4793	384.304	27.7848	291.853	24.7318	292.757	49.4903	319.222	49.2207	319.552	29.7442	319.683
57.8814	328.957	46.1466	327.839	56.6214	216.886	36.1084	210.678	37.0623	271.255	26.2631	213.913	31.7887	300.338	53.9314	372.497
31.5916	346.092	53.2207	213.49	40.233	264.668	38.8696	301.498	51.1656	246.016	39.0814	269.016	56.8078	283.341	45.7196	326.861
24.6633	231.851	46.8305	234.938	47.705	242.544	34.5773	389.282	50.2561	352.668	45.4389	345.164	43.4683	365.088	40.0147	381.293
54.3504	261.233	50.3357	344.638	29.0366	231.35	46.7124	363.397	36.3142	265.519	39.3281	396.8	40.7234	362.227	52.517	348.404
32.1983	389.8	36.9001	331.687	21.2776	223.807	32.3433	329.799	41.0068	275.675	26.0152	377.603	49.116	310.698	55.5193	380.661
22.6872	274.048	29.8008	215.523	28.3009	381.216	45.6109	352.837	55.9664	386.452	52.1098	221.565	33.4176	330.421	51.5434	322.372
43.4619	358.925	50.3533	207.864	19.7572	305.762	46.3676	378.444	29.6656	316.855	43.691	309.508	35.0741	336.073	25.6841	326.033
28.8527	252.449	52.4104	221.434	56.604	202.659	28.8499	233.439	34.2256	390.769	49.2657	312.438	27.3429	212.455	24.8583	251.831
39.4534	305.38	52.7095	205.81	21.9487	236.969	59.5223	366.226	38.1006	283.029	25.9424	387.424	44.9696	387.841	25.2758	266.513
30.43	241.009	21.9003	237.052	55.7136	306.774	22.2856	350.021	51.914	309.416	19.6119	290.035	37.1665	381.029	56.1465	274.791
27.3553	332.955	34.6828	332.034	31.3573	365.94	36.114	285.159	34.6322	371.574	53.2117	380.421	25.9724	392.491	29.341	206.092
54.0787	245.303	32.9304	269.907	35.8464	263.302	52.1255	285.945	32.4816	212.59	51.8562	359.448	27.8902	311.855	43.1052	279.411
37.2938	295.502	40.6183	344.606	23.9831	216.722	23.9845	353.351	35.1543	382.07	43.5743	204.431	22.9743	391.437	58.5682	369.634
56.3689	237.913	26.4251	212.98	52.1499	310.168	46.6141	238.038	43.5145	258.071	38.2452	374.988	40.0114	250.353	21.3546	301.212
40.6591	359.133	57.6148	379.082	59.4687	292.52	41.9842	396.399	33.234	209.186	39.4088	262.242	59.7528	316.438	42.0565	381.647
34.8486	322.082	25.6399	396.547	43.7048	375.261	26.1372	330.203	43.1673	337.063	22.405	350.151	20.0563	394.524	22.1436	311.549
52.8148	250.462	31.7913	205.877	35.9426	363.576	39.6143	308.127	29.5018	340.9	49.5556	332.431	22.7972	352.624	41.8479	250.578
55.5378	314.747	49.2313	381.603	59.3795	210.514	22.9112	270.785	29.643	373.777	57.0129	283.93	25.3702	383.803	59.5442	203.046

Table E.1.

REFERENCES

REFERENCES

[1] M. T. Eiles, H. Lee, J. Pérez-Ríos, and C. H. Greene. Anisotropic blockade using pendular long-range Rydberg molecules. *Phys. Rev. A*, 95:052708, 2017.

[2] M. T. Eiles and C. H. Greene. Hamiltonian for the inclusion of spin effects in long-range Rydberg molecules. *Phys. Rev. A*, 95:042515, 2017.

[3] J. Pérez-Ríos, M. T. Eiles, and C. H. Greene. Mapping trilobite state signatures in atomic hydrogen. *J. Phys. B: At. Mol. Opt. Phys.*, 49:14LT01, 2016.

[4] M.T. Eiles, J. Pérez-Ríos, F. Robicheaux, and C. H. Greene. Ultracold molecular Rydberg physics in a high density environment. *Journal of Physics B: Atomic, Molecular and Optical Physics*, 49(11):114005, 2016.

[5] M. T. Eiles and C. H. Greene. Ultracold long-range Rydberg molecules with complex multichannel spectra. *Phys. Rev. Lett.*, 115:193201, 2015.

[6] N. Bohr. The spectra of helium and hydrogen. *Nature*, 92:231, 2014.

[7] N. Bohr. On the constitution of atoms and molecules. *Phil. Mag.*, 26:1, 2013.

[8] W. Ritz. Magnetische atomfelder und serienspektren. *Annalen der Physik*, 330(4):660–696, 1908.

[9] U. Fano and A. R. P. Rau. *Atomic Collisions and Spectra*. Academic, Orlando, 1986.

[10] M. Aymar, C. H. Greene, and E. Luc-Koenig. Multichannel Rydberg spectroscopy of complex atoms. *Rev. Mod. Phys.*, 68:1015, 1996.

[11] S. J. Buckman and C. W. Clark. Atomic negative-ion resonances. *Rev. Mod. Phys.*, 66:539, 1994.

[12] T. F. Gallagher. *Rydberg Atoms*. Cambridge University Press, Cambridge, England, 2005.

[13] A. Dalgarno. Rydberg states of atoms and molecules. Cambridge University Press, Cambridge, 1983.

[14] E de Prunelé. Coulomb and Coulomb-Stark Green-function approach to adiabatic Rydberg energy levels of alkali-metal-helium systems. *Phys. Rev. A*, 35:496, 1987. (erratum: 35 4864.).

[15] U. Fano. Unified treatment of perturbed series, continuous spectra and collisions. *J. Opt. Soc. Am.*, 65:979, 1975.

[16] M. Aymar. Rydberg series of alkaline-earth atoms Ca through Ba. The interplay of laser spectroscopy and multichannel quantum defect analysis. *Phys. Rep.*, 110:163, 1984.

[17] M. Aymar and M. Telmini. Eigenchannel R-matrix study of the $J = 0$ and $J = 2$ even parity spectra of calcium below the Ca^+ $3d_{3/2}$ threshold. *J. Phys. B: At. Mol. Opt. Phys.*, 24:4935, 1991.

[18] A. Facon, E-K Dietsche, D. Grosso, S. Haroche, J-M Raimond, M. Brune, and S. Gleyzes. A sensitive electrometer based on a Rydberg atom in a Schrödinger-cat state. *Nature*, 535:262, 2016.

[19] D. A. Harmin. Theory of the Stark effect. *Phys. Rev. A*, 26:2656, 1982.

[20] G. Alber and P. Zoller. Laser excitation of electronic wave packets in Rydberg atoms. *Phys. Rep.*, 199:231, 1991.

[21] G. Wunner, U. Woelk, I. Zech, G. Zeller, T. Ertl, F. Geyer, W. Schweitzer, and H. Ruder. Rydberg atoms in uniform magnetic fields: uncovering the transition from regularity to irregularity in a quantum system. *Phys. Rev. Lett.*, 57:3261, 1986.

[22] J. Parker and C. R. Stroud Jr. Coherence and decay of Rydberg wave packets. *Phys. Rev. Lett.*, 56:716, 1986.

[23] G. Pupillo, A. Micheli, M. Boninsegni, I. Lesanovsky, and P. Zoller. Strongly correlated gases of Rydberg-dressed atoms: quantum and classical dynamics. *Phys. Rev. Lett.*, 104:223002, 2010.

[24] D. E. Chang, V. Vuletić, and M.D. Lukin. Quantum nonlinear optics photon by photon. *Nature Photonics*, 8:685, 2014.

[25] M. Fleischhauer and M. D. Lukin. Dark-state polaritons in electromagnetically induced transparency. *Phys. Rev. Lett.*, 84:5094–5097, 2000.

[26] T. Peyronel, O. Firstenberg, Q-Y Liang, S. Hofferberth, A. V. Gorshkov, T. Pohl, M.D. Lukin, and V. Vuletić. Quantum nonlinear optics with single photons enabled by strongly interacting atoms. *Nature*, 488:57, 2012.

[27] M. Saffman, T. G. Walker, and K. Molmer. Quantum information with Rydberg atoms. *Rev. Mod. Phys.*, 82:2313, 2010.

[28] E. Urban, T. A. Johnson, T. Henage, L. Isenhower, D. D. Yavuz, T. G. Walker, and M. Saffman. Observation of Rydberg blockade between two atoms. *Nat. Phys.*, 5:110, 2009.

[29] M. D. Lukin, M. Fleischauer, R. Côté, L. M. Duan, D. Jaksch, J. I. Cirac, and P. Zoller. Dipole blockade and quantum information processing in mesoscopic atomic ensembles. *Phys. Rev. Lett.*, 87:037901, 2001.

[30] D. Møller, L. B. Madsen, and K. Mølmer. Quantum gates and multiparticle entanglement by Rydberg excitation blockade and adiabatic passage. *Phys. Rev. Lett.*, 100:170504, 2008.

[31] M. H. Anderson, J. R. Ensher, M. R. Matthews, C. E. Wieman, and E. A. Cornell. Observation of Bose-Einstein condensation in a dilute atomic vapor. *Science*, 269:198, 1995.

[32] K. B. Davis, M. O. Mewes, M. R. Andrews, N. J. van Druten, D. S. Durfee, D. M. Kurn, and W. Ketterle. Bose-Einstein condensation in a gas of sodium atoms. *Phys. Rev. Lett*, 75:3969, 1995.

[33] S. Kraft, F. Vogt, O. Appel, F. Riehle, and U. Sterr. Bose-Einstein condensation of alkaline earth atoms: Ca 40. *Phys. Rev. Lett*, 103:130401, 2009.

[34] S. Stellmer, K. M. Tey, B. Huang, R. Grimm, and F. Schreck. Bose-Einstein condensation of strontium. *Phys. Rev. Lett*, 103:200401, 2009.

[35] D. G. Fried, T. C. Killian, L. Willmann, D. Landhuis, S. C. Moss, D. Kleppner, and T. J. Greytak. Bose-Einstein condensation of atomic hydrogen. *Phys. Rev. Lett*, 81:3811, 1998.

[36] T. C. Killian, D. G. Fried, L. Willmann, D. Landhuis, S. C. Moss, T. J. Greytak, and D. Kleppner. Cold collision frequency shift of the $1S$- $2S$ transition in hydrogen. *Phys. Rev. Lett.*, 81:3807–3810, 1998.

[37] G. Herzberg. Rydberg molecules. *Annu. Rev. Phys. Chem.*, 38:27, 1987.

[38] Ch. Jungen and G. Herzberg. Rydberg series and ionization potential of the H_2 molecule. *Journ. Mol. Spec.*, 42:425, 1972.

[39] J. Wang, M. Gacesa, and R. Côté. Rydberg electrons in a Bose-Einstein condensate. *Phys. Rev. Lett.*, 114:243003, 2015.

[40] C. H. Greene, A. S. Dickinson, and H. R. Sadeghpour. Creation of polar and nonpolar ultra-long-range Rydberg molecules. *Phys. Rev. Lett.*, 85:2458, 2000.

[41] S. M. Farooqi, D. Tong, S. Krishnan, J. Stanojevic, Y. P. Zhang, J. R. Ensher, A. S. Estrin, C. Boisseau, R. Côté, E. E. Eyler, and P. L. Gould. Long-range molecular resonances in a cold Rydberg gas. *Phys. Rev. Lett*, 91:183002, 2003.

[42] C. Boisseau, I. Simbotin, and R. Côté. Macrodimers: ultralong range Rydberg molecules. *Phys. Rev. Lett.*, 88:133004, 2002.

[43] P. G. Harris, H. C. Bryant, A. H. Mohagheghi, R. A. Reeder, H. Sharifian, C. Y. Tang, H. Tootoonchi, J. B. Donahue, C. R. Quick, D. C. Rislove, W. W. Smith, and J. E. Stewart. Observation of high-lying resonances in the H^- ion. *Phys. Rev. Lett.*, 65(3):309, 1990.

[44] M. Halka, H. C. Bryant, E. P. Mackerrow, W. Miller, A. H. Mohagheghi, C. Y. Tang, S. Cohen, J. B. Donahue, A. Hsu, C. R. Quick, J. Tiee, and K. Rozsa. Observation of the partial decay into $H^0(n = 2)$ by excited H^- near the $n = 3$ and 4 thresholds. *Phys. Rev. A*, 44(9):6127, 1991.

[45] H. R. Sadeghpour and C. H. Greene. Dominant photodetachment channels in H^-. *Phys. Rev. Lett.*, 65(3):313, 1990.

[46] H. R. Sadeghpour, C. H. Greene, and M. Cavagnero. Extensive eigenchannel R-matrix study of the H^- photodetachment spectrum. *Phys. Rev. A*, 45(3):1587, 1992.

[47] A. O. Lindahl, J. Rohlen, H. Hultgren, I. Yu. Kiyan, D. J. Pegg, C. W. Walter, and D. Hanstorp. Threshold photodetachment in a repulsive potential. *Phys. Rev. Lett.*, 108:033004, 2012.

[48] C.-N. Liu. Photodetachment of K^-. *Phys. Rev. A*, 64:052715, 2001.

[49] J. Rohlen, A. O. Lindahl, H. Hultgren, R. D. Thomas, D. J. Pegg, and D. Hanstorp. Threshold behaviour in photodetachment into a final state with large negative polarizability. *Eur. Phys. Lett.*, 106, 2014.

[50] E. Jordan, G. Cerchiari, S. Fritzsche, and A. Kellerbauer. High-resolution spectroscopy on the laser-cooling candidate La^-. *Phys. Rev. Lett.*, 115:113001, 2015.

[51] G. Cerchiari, A. Kellerbauer, M. S. Safronova, U. I. Safronova, and P. Yzombard. Ultracold anions for high-precision antihydrogen experiments. *Phys. Rev. Lett.*, 120:133205, 2018.

[52] P. R. Bunker and P. Jensen. *Molecular symmetry and spectroscopy.* NRC Research Press, Ottawa, 1998.

[53] P. R. Bunker and P. Jensen. *Fundamentals of molecular symmetry.* 2004.

[54] Y.K. Ho. The method of complex coordinate rotation and its applications to atomic collision processes. *Physics Reports*, 99(1):1 – 68, 1983.

[55] A. U. Hazi and H. S. Taylor. Stabilization method of calculating resonance energies: Model problem. *Phys. Rev. A*, 1:1109–1120, 1970.

[56] V. A. Mandelshtam, T. R. Ravuri, and H. S. Taylor. Calculation of the density of resonance states using the stabilization method. *Phys. Rev. Lett.*, 70:1932–1935, 1993.

[57] E. Fermi. Sopra lo spostamento per pressione delle righe elevate delle serie spettrali. *Nouvo Cimento*, 11:157, 1934.

[58] C. H. Greene and M. Aymar. Spin-orbit effects in the heavy alkaline-earth atoms. *Phys. Rev. A*, 44:1773, 1991.

[59] M. Marinescu, H. R. Sadeghpour, and A. Dalgarno. Dispersion coefficients for alkali-metal dimers. *Phys. Rev. A*, 49:982, 1994.

[60] F. Robicheaux. Time propagation of extreme two-electron wavefunctions. *Journal of Physics B: Atomic, Molecular and Optical Physics*, 45:135007, 2012.

[61] K. W. Meyer, C. H. Greene, and B. D. Esry. Two-electron photoejection of He and H^-. *Phys. Rev. Lett.*, 78:4902–4905, 1997.

[62] D.A. Varshalovich, A. N. Moskalev, and V. K. Khersonskii. *THE GRAPHICAL METHOD IN ANGULAR MOMENTUM THEORY*, pages 412–451. WORLD SCIENTIFIC, 2013.

[63] S. Watanabe and C. H. Greene. Atomic polarizability in negative-ion photodetachment. *Phys. Rev. A*, 22(1):158, 1980.

[64] H. Le Rouzo and G. Raseev. Finite-volume variational method: First application to direct molecular photoionization. *Phys. Rev. A*, 29:1214–1223, 1984.

[65] C. H. Greene and L. Kim. Streamlined eigenchannel treatment of open-shell spectra. *Phys. Rev. A*, 38:5953–5956, 1988.

[66] S. Watanabe. Doubly excited states of the helium negative ion. *Phys. Rev. A*, 25(4):2074, 1982.

[67] C. Pan, A. F. Starace, and C. H. Greene. Parallels between high doubly excited state spectra in H^- and Li^- photodetachment. *J. Phys. B: At. Mol. Opt. Phys*, 27:L137, 1994.

[68] A.C. Allison. The numerical solution of coupled differential equations arising from the Schrödinger equation. *Journal of Computational Physics*, 6(3):378 – 391, 1970.

[69] E. T. Whittaker and G. N. Watson. *A Course of Modern Analysis*. Cambridge University, Cambridge, 1927.

[70] W. Li, I. Mourachko, M. W. Noel, and T. F. Gallagher. Millimeter-wave spectroscopy of cold Rb Rydberg atoms in a magneto-optical trap: Quantum defects of the *ns*, *np*, and *nd* series. *Phys. Rev. A*, 67:052502, 2003.

[71] J. Han, Y. Jamil, D. V. L. Norum, P. J. Tanner, and T. F. Gallagher. Rb nf quantum defects from millimeter-wave spectroscopy of cold ^{85}Rb Rydberg atoms. *Phys. Rev. A*, 74:054502, 2006.

[72] P. Goy, J. M. Raimond, G. Vitrant, and S. Haroche. Millimeter-wave spectroscopy in cesium Rydberg states. quantum defects, fine- and hyperfine-structure measurements. *Phys. Rev. A*, 26:2733, 1982.

[73] K. H. Weber and C. J. Sansonetti. Accurate energies of ns, np, nd, nf, and ng levels of neutral cesium. *Phys. Rev. A*, 35:4650, 1987.

[74] J. Mitroy, M. S. Safranova, and C. W. Clark. Theory and applications of atomic and ionic polarizabilities. *J. Phys. B: At. Mol. Opt. Phys*, 43:202001, 2010.

[75] H. Saßmannshausen, F. Merkt, and J. Deiglmayr. High-resolution spectroscopy of Rydberg states in an ultracold cesium gas. *Phys. Rev. A*, 87:032519–1, 2013.

[76] A. Tauschinsky, R. Newell, H. B. van Linden van den Heuvell, and R. J. C. Spreeuw. Measurement of ^{87}Rb Rydberg-state hyperfine splitting in a room-temperature vapor cell. *Phys. Rev. A*, 87:042522–1, 2013.

[77] E. Arimondo, M. Inguscio, and P. Violino. Experimental determinations of the hyperfine structure in the alkali atoms. *Rev. Mod. Phys.*, 49:31, 1977.

[78] A. Beckmann, K. D. Böklen, and D. Elke. Precision measurements of the nuclear magnetic dipole moments of ^{6}Li, ^{7}Li, ^{23}Na, ^{39}K and ^{41}K. *Zeitschrift für Physik*, 270(3):173–186, 1974.

[79] P. Goy, J. Liang, M. Gross, and S. Haroche. Quantum defects and specific-isotopic-shift measurements in ns and np highly excited states of lithium: Exchange effects between Rydberg and core electrons. *Phys. Rev. A*, 34:2889–2896, 1986.

[80] C-J Lorenzen and K. Niemax. Quantum defects of the $n\,^2P_{1/2,3/2}$ levels in ^{39}K I and ^{85} Rb I. *Physica Scripta*, 27(4):300, 1983.

[81] W. F. Holmgren, M C. Revelle, V. P. A. Lonij, and A. D. Cronin. Absolute and ratio measurements of the polarizability of Na, K, and Rb with an atom interferometer. *Phys. Rev. A*, 81:053607, 2010.

[82] E. Amaldi and E. Segrè. Effect of pressure on high terms of alkaline spectra. *Nature (London)*, 133:141, 1934.

[83] R. Stock, A. Silberfarb, E. L. Bolda, and I. H. Deutsch. Generalized pseudopotentials for higher partial wave scattering. *Phys. Rev. Lett.*, 94:023202, 2005.

[84] A. Derevianko. Revised Huang-Yang multipolar pseudopotential. *Phys. Rev. A*, 72:044701, 2005.

[85] K. Huang and C. N. Yang. Quantum-mechanical many-body problem with hard-sphere interaction. *Phys. Rev.*, 105:767–775, 1957.

[86] Z. Idziaszek and T. Calarco. Pseudopotential method for higher partial wave scattering. *Phys. Rev. Lett.*, 96:013201, 2006.

[87] A. Omont. On the theory of collisions of atoms in Rydberg states with neutral particles. *J. Phys. (Paris)*, 38:1343, 1977.

[88] E. P. Wigner. On the behavior of cross sections near thresholds. *Phys. Rev.*, 73:1002, 1948.

[89] N. Y. Du and C. H. Greene. Interaction between a Rydberg atom and neutral perturbers. *Phys. Rev. A*, 36:971, 1987. See also the erratum, *ibid.* **36**, 5467 (1987).

[90] N. Y. Du and C. H. Greene. Multichannel Rydberg spectra of the rare gas dimers. *J. Chem. Phys.*, 90:6347, 1989.

[91] I. L. Beigman and V. S. Lebedev. Collision theory of Rydberg atoms with neutral and charged particles. *Phys. Rep.*, 250:95, 1995.

[92] M. Tarana and R. Čurík. Adiabatic potential-energy curves of long-range Rydberg molecules: Two-electron R -matrix approach. *Phys. Rev. A*, 93:012515, 2016.

[93] A. S. Dickinson and F. X. Gadea. Undulations in potential curves analyzed using the Fermi model: LiH, LiHe, LiNe, and h_2 examples. *Phys. Rev.A*, 65:052506, 2002.

[94] X. Liu, Y. Yang, J. Zhao, L. Xiao, and S. Jia. An efficient method to study highly excited states at the ab initio level and application to ultralong rydberg csne molecules. *The Journal of Chemical Physics*, 139(5):054302, 2013.

[95] A. A. Khuskivadze, M. I. Chibisov, and I. I. Fabrikant. Adiabatic energy levels and electric dipole moments of Rydberg states of Rb_2 and Cs_2 dimers. *Phys. Rev. A*, 66:042709, 2002.

[96] M. I. Chibisov, A. A. Khuskivadze, and I. I. Fabrikant. Energies and dipole moments of long-range molecular Rydberg states. *J. Phys. B*, 35:L193, 2002.

[97] C. Bahrim and U. Thumm. Low-lying $^3P^o$ and $^3S^e$ states of Rb, Cs, and Fr. *Phys. Rev. A*, 61:022722, 2000.

[98] C. Bahrim, U. Thumm, and I. I. Fabrikant. Negative-ion resonances in cross sections for slow-electron-heavy-alkali-metal-atom scattering. *Phys. Rev. A*, 63:042710, 2001.

[99] M. Scheer, J. Thølgersen, R. C. Bilodeau, C. A. Brodie, H. K. Haugen, H. H. Andersen, P. Kristensen, and T. Andersen. Experimental evidence that the $6s6p^3p_j$ states of Cs^- are shape resonances. *Phys. Rev. Lett.*, 80:684, 1998.

[100] U. Thumm and D. W. Norcross. Evidence for very narrow shape resonances in low-energy electron-Cs scattering. *Phys. Rev. Lett.*, 67:3495, 1991.

[101] V. Bendkowsky, B. Butscher, J. Nipper, J. B. Balewski, J. P. Shaffer, R. Löw, T. Pfau, W. Li, J. Stanojevic, T. Pohl, and J. M. Rost. Rydberg trimers and excited dimers bound by internal quantum reflection. *Phys. Rev. Lett.*, 105:163201, 2010.

[102] H. Saßmannshausen, F. Merkt, and J. Deiglmayr. Experimental characterization of singlet scattering channels in long-range Rydberg molecules. *Phys. Rev. Lett.*, 114:133201, 2015.

[103] K. Bartschat and H. R. Sadeghpour. Ultralow-energy electron scattering from alkaline-earth atoms: the scattering-length limit. *J. Phys. B: At. Mol. Opt. Phys.*, 36:L9, 2003. see also: J. Yuan and Z. Zhang, Phys. Rev. A **42**, 5363 (1990).

[104] G. Haeffler, D. Hanstorp, I. Kiyan, A. E. Klinkmüller, U. Ljungblad, and D. J. Pegg. Electron affinity of Li: A state-selective measurement. *Phys. Rev. A*, 53:4127–4131, 1996.

[105] H. Hotop and W. C. Lineberger. Binding energies in atomic negative ions: II. *Journal of Physical and Chemical Reference Data*, 14(3):731–750, 1985.

[106] K. T. Andersson, J. Sandström, I. Y. Kiyan, D. Hanstorp, and D. J. Pegg. Measurement of the electron affinity of potassium. *Phys. Rev. A*, 62:022503, 2000.

[107] E. Karule. Elastic scattering of low-energy electrons by alkali atoms. *Physics Letters*, 15:137, 1965.

[108] D. W. Norcross. Low energy scattering of electrons by Li and Na. *J. Phys. B: At. Mol. Phys*, 5:1482, 1972.

[109] I. I. Fabrikant. Interaction of Rydberg atoms and thermal electrons with K, Rb, and Cs atoms. *J. Phys. B: At. Mol. Phys.*, 19:1527, 1986.

[110] A. L. Sinfailam and R. K. Nesbet. Variational calculations of electron-alkali-metal-atom scattering: elastic scattering by Li, Na, and K. *Phys. Rev. A*, 7:1527, 1987.

[111] D. L. Moores. The scattering of electrons by potassium atoms. *J. Phys. B: At. Mol. Phys*, 9:1329, 1976.

[112] A. R. Johnston and P. D. Burrow. Shape resonances in electron scattering from metal atoms. *J. Phys. B: At. Mol. Phys*, 15:L745, 1982.

[113] V. M. Borodin, I. I. Fabrikant, and A. K. Kazansky. Collisional broadening of Rydberg atoms perturbed by ground-state sodium atoms. *Z. Phys. D*, 27:45, 1993.

[114] T. Schmid, C. Veit, N. Zuber, R. Löw, T. Pfau, M. Tarana, and M. Tomza. Rydberg molecules for ion-atom scattering in the ultracold regime. *Arxiv: 1709.10488v1*, 2017.

[115] C. H. Greene. Photoabsorption spectra of the heavy alkali-metal negative ions. *Phys. Rev. A*, 42(3):1405, 1990.

[116] T. F. O'Malley, L. Rosenberg, and L. Spruch. Low-energy scattering of a charged particle by a neutral polarizable system. *Phys. Rev.*, 125:1300–1310, 1962.

[117] E. Karule. The spin polarization and differential cross sections in the elastic scattering of electrons by alkali metal atoms. *J. Phys. B: At. Mol. Phys*, 5:2051, 1972.

[118] V. S. Lebedev and I. I. Fabrikant. Inelastic and quasielastic collisions of Rydberg atoms with the heavy rare-gas atoms. *Phys. Rev. A*, 54:2888–2898, 1996.

[119] V. S. Lebedev and I. I. Fabrikant. Semiclassical calculations of the l-mixing and n,l -changing collisions of Rydberg atoms with rare-gas atoms. *Journal of Physics B: Atomic, Molecular and Optical Physics*, 30(11):2649, 1997.

[120] P. Valiron, A. L. Roche, F. Masnou-Seeuws, and M. E. Dolan. Molecular treatment of collisions between a Rydberg sodium atom and a rare-gas perturber. *J. Phys. B: At. Mol. Opt. Phys.*, 17:2803, 1984.

[121] E. L. Hamilton. *Photoionization, photodissociation, and long-range bond formation in molecular Rydberg states*. PhD thesis, University of Colorado, 2002.

[122] E. L. Hamilton, C. H. Greene, and H. R. Sadeghpour. Shape-resonance-induced long-range molecular Rydberg states. *J. Phys. B*, 35:L199, 2002.

[123] C. Fey, M. Kurz, P. Schmelcher, S. T. Rittenhouse, and H. R. Sadeghpour. A comparitive analysis of binding in ultralong-range Rydberg molecules. *New. J. Phys.*, 17:055010, 2015.

[124] D.A. Anderson, S. A. Miller, and G Raithel. Angular-momentum couplings in long-range Rb_2 Rydberg molecules. *Phys. Rev. A*, 90:062518, 2014.

[125] B. J. DeSalvo, J. A. Amen, F. B. Dunning, T. C. Killian, H. R. Sadeghpour, S. Yoshida, and J. Burgdörfer. Ultra-long-range Rydberg molecules in a divalent atomic system. *Phys. Rev. A*, 92:031403(R), 2015.

[126] M. Kurz. *Ultralong-range Diatomic Molecules in External Electric and Magnetic Fields*. PhD thesis, Hamburg University, 2014.

[127] V. M. Borodin and A. K. Kazansky. The adiabatic mechanism of the collisional broadening of Rydberg states via a loosely bound resonant state of ambient gas atoms. *J. Phys. B: At. Mol. Opt. Phys.*, 25:971, 1992.

[128] T. Niederprüm, O. Thomas, T. Eichert, C. Lippe, J. Pérez-Ríos, C. H. Greene, and H. Ott. Observation of pendular butterfly Rydberg molecules. *Nat. Commun.*, 7:12820, 2016.

[129] M. Schlagmüller, T.C. Liebisch, F. Engel, K. S. Kleinbach, F. Böttcher, U. Hermann, K. M. Westphal, R. Löw, S. Hofferberth, T. Pfau, J. Pérez-Ríos, and C. H. Greene. Ultracold chemical reactions of a single Rydberg atom in a dense gas. *Phys. Rev. X*, 6:031020, 2016.

[130] S. Markson, S. T. Rittenhouse, R. Schmidt, J. P. Shaffer, and H. R. Sadeghpour. Theory of ultralong-range Rydberg molecule formation incorporating spin-dependent relativistic effects: Cs(6s)-Cs(np) as case study. *ChemPhysChem*, 10:1002, 2016.

[131] O. Thomas, C. Lippe, T. Eichert, and H. Ott. Photoassociation of rovibrational Rydberg moleces. *arXiv:1802.04683*, 2018.

[132] T. Maier, H. Kadau, M. Schmitt, M. Wenzel, I. Ferrier-Barbut, T. Pfau, A. Frisch, S. Baier, K. Aikawa, L. Chomaz, M. J. Mark, F. Ferlaino, C. Makrides, E. Tiesinga, A. Petrov, and S. Kotochigova. Emergence of chaotic scattering in ultracold Er and Dy. *Phys. Rev. X*, 5:041029, 2015.

[133] F. Camargo, R. Schmidt, J. D. Whalen, R. Ding, G. Woehl, S. Yoshida, J. Burgdörfer, F. B. Dunning, H. R. Sadeghpour, E. Demler, and T. C. Killian. Creation of Rydberg polarons in a Bose gas. *Phys. Rev. Lett.*, 120:083401, 2018.

[134] W. Li, T. Pohl, J. M. Rost, Seth T. Rittenhouse, H. R. Sadeghpour, J. Nipper, B. Butscher, J. B. Balewski, V. Bendkowsky, R. Löw, and T. Pfau. A homonuclear molecule with a permanent electric dipole moment. *Science*, 334(6059):1110–1114, 2011.

[135] J.D. Jackson. *Classical Electrodynamics*. Wiley, New York, 1998.

[136] B. Granger, E. L. Hamilton, and C. H. Greene. Quantum and semiclassical analysis of long-range Rydberg molecules. *Phys. Rev. A*, 64:042508, 2001.

[137] C. H. Greene, E. L. Hamilton, H. Crowell, C. Vadla, and K. Niemax. Experimental verification of minima in excited long-range Rydberg states of Rb_2. *Phys. Rev. Lett*, 97:233002, 2006.

[138] M. Kurz and P. Schmelcher. Electrically dressed ultra-long-range polar Rydberg molecules. *Phys. Rev. A*, 88:022501, 2013.

[139] M. Kurz and P. Schmelcher. Ultralong-range Rydberg molecules in combined electric and magnetic fields. *J. Phys. B*, 47:165101, 2014.

[140] I. Lesanovsky, P. Schmelcher, and H. R. Sadeghpour. Ultra-long-range Rydberg molecules exposed to a magnetic field. *J. Phys. B: At. Mol. Opt. Phys.*, 39:L69, 2006.

[141] F. Hummel, C. Fey, and P. Schmelcher. Spin-interaction effects for ultralong-range Rydberg molecules in a magnetic field. *ArXiv: 1711.08748*, 2017.

[142] V. Bendkowsky, B. Butscher, J. Nipper, J. B. Balewski, J. P. Shaffer, R. Löw, and T. Pfau. Observation of ultralong-range Rydberg molecules. *Nature (London)*, 458:1005, 2009.

[143] B. Butscher, V. Bendkowsky, J. Nipper, J. B. Balewski, L. Kukota, R. Löw, T. Pfau, W. Li, T. Pohl, and J. M. Rost. Lifetimes of ultra-long-range Rydberg molecules in vibrational ground and excited states. *Journal of Physics B: Atomic, Molecular and Optical Physics*, 44(18):184004, 2011.

[144] A. Gaj, A. T. Krupp, P. Ilzhöfer, R. Löw, S. Hofferberth, and T. Pfau. Hybridization of Rydberg electron orbitals by molecule formation. *Phys. Rev. Lett.*, 115:023001, 2015.

[145] J. Tallant, S. T. Rittenhouse, D. Booth, H. R. Sadeghpour, and J. P. Shaffer. Observation of blueshifted ultralong-range Cs_2 Rydberg molecules. *Phys. Rev. Lett.*, 109:173202, 2012.

[146] F. Camargo, J. D. Whalen, R. Ding, H. R. Sadeghpour, S. Yoshida, J. Burgdörfer, F. B. Dunning, and T. C. Killian. Lifetimes of ultra-long-range strontium Rydberg molecules. *Phys. Rev. A*, 93:022702, 2016.

[147] J. D. Whalen, F. Camargo, R. Ding, T. C. Killian, F. B. Dunning, J. Pérez-Ríos, S. Yoshida, and J. Burgdörfer. Lifetimes of ultra-long-range strontium Rydberg molecules in a dense Bose-Einstein condensate. *Phys. Rev. A*, 96:042702, 2017.

[148] G. Raithel D. A. Anderson, S. A. Miller. Photoassociation of long-range *nd* Rydberg molecules. *Phys. Rev. Lett.*, 112:163201, 2014.

[149] F. Böttcher, A. Gaj, K. M. Westphal, M. Schlagmüller, K. S. Kleinbach, R. Löw, T. C. Liebisch andT. Pfau, and S. Hofferberth. Observation of mixed singlet-triplet Rb_2 Rydberg molecules. *Phys. Rev. A*, 93:032512, 2016.

[150] K. S. Kleinbach, F. Meinert, F. Engel, W. J. Kwon, R. Löw, T. Pfau, and G. Raithel. Photoassociation of trilobite Rydberg molecules via resonant spin-orbit coupling. *Phys. Rev. Lett.*, 118:223001, 2017.

[151] M. A. Bellos, R. Carollo, J. Banerjee, E. E. Eyler, P. L. Gould, and W. C. Stwalley. Excitation of weakly bound molecules to Trilobitelike Rydberg states. *Phys. Rev. Lett.*, 111:053001, 2013.

[152] R. A. Carollo, J. L. Carini, E. E. Eyler, P. L. Gould, and W. C. Stwalley. High-resolution spectroscopy of Rydberg molecular states of $^{85}\mathbf{Rb}_2$ near the $5s + 7p$ asymptote. *Phys. Rev. A*, 95:042516, 2017.

[153] A. Gaj, A. T. Krupp, J. B. Balewski, R. Löw, S. Hofferberth, and T. Pfau. From molecular spectra to a density shift in dense Rydberg gases. *Nat. Comm.*, 5:4546, 2014.

[154] D. Booth, S. T. Rittenhouse, J. Yang, H. R. Sadeghpour, and J. P. Shaffer. Production of trilobite Rydberg molecule dimers with kilo-Debye permanent electric dipole moments. *Science*, 348(6230):99–102, 2015.

[155] B. Friedrich and D. R. Herschbach. Spatial orientation of molecules in strong electric fields and evidence for pendular states. *Nature (London)*, 353:412, 1991.

[156] T. Manthey, T. Niederprüm, O. Thomas, and H. Ott. Dynamically probing ultracold lattice gases via Rydberg molecules. *New. J. Phys.*, 17:103024, 2015.

[157] N. Sándor, R. González-Férez, P. S. Julienne, and G. Pupillo. Rydberg optical Feshbach resonances in cold gases. *Phys. Rev. A*, 96:032719, 2017.

[158] O. Thomas, C. Lippe, T. Eichert, and H. Ott. Experimental realization of a Rydberg optical Feshbach resonance in a quantum many-body system. *arXiv:1712.05263*, 2017.

[159] H. Saßmannshausen, J. Deiglmayr, and F. Merkt. Long-range Rydberg molecules, Rydberg macrodimers and Rydberg aggregates in an ultracold Cs gas. *Eur. Phys. J. Special Topics*, 225:2891, 2016.

[160] K.S. Kleinbach, F. Engel, T. Dieterle, R. Löw, T. Pfau, and F. Meinert. An ionic impurity in a Bose-Einstein condensate at sub-microkelvin temperatures. *arXiv:1802.08587v1*, 2018.

[161] T. Niederprüm, O. Thomas, T. Eichert, and H. Ott. Rydberg molecule-induced remote spin flips. *Phys. Rev. Lett.*, 117:123002, 2016.

[162] B. Butscher, J. Nipper, J. B. Balewski, L. Kukota, V. Bendkowsky, R. Lw, and T. Pfau. Atom-molecule coherence for ultralong-range Rydberg dimers. *Nature Physics*, 6:970, 2010.

[163] I. Mirgorodskiy, F. Christaller, C. Braun, A. Paris-Mandoki, C. Tresp, and S. Hofferberth. Electromagnetically induced transparency of ultra-long-range Rydberg molecules. *Phys. Rev. A*, 96:011402, 2017.

[164] L. G. Marcassa and J. P. Shaffer. Chapter two - interactions in ultracold Rydberg gases. volume 63 of *Advances In Atomic, Molecular, and Optical Physics*, pages 47 – 133. Academic Press, 2014.

[165] J. P. Shaffer, S. T. Rittenhouse, and H. R. Sadeghpour. Ultracold Rydberg molecules. *arXiv:1802.06161v1*, 2018.

[166] H. Saßmannshausen and J. Deiglmayr. Observation of Rydberg atom macrodimers: Micrometer-sized diatomic molecules. *Phys. Rev. Lett.*, 117:083401, 2016.

[167] X. Han, S. Bai, Y. Jiao, L. Hao, Y. Xue, J. Zhao, S. Jia, and G. Raithel. Cs $62D_J$ Rydberg-atom macrodimers formed by long-range multipole interaction. *Phys. Rev. A*, 97:031403, 2018.

[168] J. B. Balewski, A. T. Krupp, A. Gaj, D. Peter, H. P. Büchler, R. Löw, S. Hofferberth, and T. Pfau. Coupling a single electron to a Bose-Einstein condensate. *Nature (London)*, 502:664, 2013.

[169] M. Schlagmüller, T.C. Liebisch, H. Nguyen, G. Lochead, F. Engel, F. Böttcher, K. M. Westphal, K. S. Kleinbach, R. Löw, S. Hofferberth, T. Pfau, J. Pérez-Ríos, and C. H. Greene. Probing an electron scattering resonance using Rydberg molecules within a dense and ultracold gas. *Phys. Rev. Lett.*, 116:053001, 2016.

[170] C. Fey, J. Yang, S.T. Rittenhouse, F. Munkes, M. Baluktsian, P. Schmelcher, H. R. Sadeghpour, and J. P. Shaffer. Observation of $Cs(nd)$ ultralong-range Rydberg trimers: effective three-body interactions. *arXiv:1803.09781v1*, 2018.

[171] T.C. Liebisch, M. Schlagmüller, F. Engel, H. Nguyen, J. Balewski, G. Lochead, F. Böttcher, K. M. Westphal, K. S. Kleinbach, T. Schmid, A. Gaj, R. Löw, S. Hofferberth, T. Pfau, J. Pérez-Ríos, and C. H. Greene. Controlling Rydberg atom excitations in dense background gases. *Journal of Physics B: Atomic, Molecular and Optical Physics*, 49(18):182001, 2016.

[172] R. Schmidt, J. D. Whalen, R. Ding, F. Camargo, G. Woehl, S. Yoshida, J. Burgdörfer, F. B. Dunning, E. Demler, H. R. Sadeghpour, and T. C. Killian. Theory of excitation of Rydberg polarons in an atomic quantum gas. *Phys. Rev. A*, 97:022707, 2018.

[173] R. Schmidt, H. R. Sadeghpour, and E. Demler. Mesoscopic Rydberg impurity in an atomic quantum gas. *Phys. Rev. Lett.*, 116:105302, 2016.

[174] T. Karpiuk, M. Brewczyk, K. Rzazewski, A. Gaj, J. B. Balewski, A. T. Krupp, M. Schlagmüller, R. Löw, S. Hofferberth, and T. Pfau. Imaging single Rydberg electrons in a Bose-Einstein condensate. *New J. Phys*, 17:053046, 2015.

[175] I. C. H. Liu and J. M. Rost. Polyatomic molecules formed with a Rydberg atom in an ultracold environment. *Eur. Phys. J. D*, 40:65, 2006.

[176] C. Fey, M. Kurz, and P. Schmelcher. Stretching and bending dynamics in triatomic ultralong-range Rydberg molecules. *Phys. Rev. A*, 94:012516, 2016.

[177] I. C. H. Liu, J. Stanojevic, and J. M. Rost. Ultra-long-range Rydberg trimers with a repulsive two-body interaction. *Phys. Rev. Lett.*, 102:173001, 2009.

[178] Perttu J. J. Luukko and Jan-Michael Rost. Polyatomic trilobite Rydberg molecules in a dense random gas. *Phys. Rev. Lett.*, 119:203001, 2017.

[179] J. A. Fernández, P. Schmelcher, and R. González-Férez. Ultralong-range triatomic Rydberg molecules in an electric field. *J. Phys. B: At. Mol. Opt. Phys.*, 49:124002, 2016.

[180] S. T. Rittenhouse and H. R. Sadeghpour. Ultracold giant polyatomic Rydberg molecules: coherent control of molecular orientation. *Phys. Rev. Lett.*, 104:243002, 2010.

[181] S. T. Rittenhouse, M. Mayle, P. Schmelcher, and H. R. Sadeghpour. Ultralong-range polyatomic Rydberg molecules formed by a polar perturber. *J. Phys. B: At. Mol. Opt. Phys.*, 44:184005, 2011.

[182] M. Mayle, S. T. Rittenhouse, P. Schmelcher, and H. R. Sadeghpour. Electric field control in ultralong-range triatomic polar Rydberg molecules. *Phys. Rev. A*, 85:052511, 2012.

[183] R. González-Férez, H. R. Sadeghpour, and P. Schmelcher. Rotational hybridization, and control of alignment and orientation in triatomic ultralong-range Rydberg molecules. *New J. Phys.*, 17:013021, 2015.

[184] J. Aguilera-Fernández, H. R. Sadeghpour, P. Schmelcher, and R. González-Férez. Electronic structure of ultralong-range rydberg penta-atomic molecules with two polar diatomic molecules. *Phys. Rev. A*, 96:052509, 2017.

[185] M. Chibisov, A. M. Ermolaev, F. Brouillard, and M. H. Cherkani. New summation rules for Coulomb wave functions. *Phys. Rev. Lett.*, 84:45, 2000. see also Cherkani, M. H., Brouillard, F., and Chibisov, M. ,*J. Phys. B.* **34** 49 (2001).

[186] R. Ma, E. M. Tai, P. M. Preiss, W. S. Bakr, J. Simon, and M. Greiner. Photon-assisted tunneling in a biased strongly correlated Bose gas. *Phys. Rev. Lett.*, 107:095301, 2011.

[187] R. A. Williams, S. Al-Assam, and C. J. Foot. Observation of vortex nucleation in a rotating two-dimensional lattice of Bose-Einstein condensates. *Phys. Rev. Lett.*, 104:050404, 2010.

[188] D. S. Lühmann, O. Jürgensen, M. Weinberg, J. Simonet, P. Soltan-Panahi, and K. Sengstock. Tunable gauge potential for neutral and spinless particles in driven optical lattices. *Phys. Rev. A*, 90:013614, 2012.

[189] K. Henderson, C. Ryu, C. MacCormick, and M.G. Boshier. Experimental demonstration of painting arbitrary and dynamic potentials for Bose-Einstein condensates. *New J. Phys.*, 11:043030, 2009.

[190] B. Zimmermann, T. Müller, J. Meineke, T. Esslinger, and H. Moritz. High-resolution imaging of ultracold fermions in microscopically tailored optical potentials. *New J. Phys.*, 13(043007), 2011.

[191] C. Schwartz. Electron scattering from hydrogen. *Phys. Rev.*, 24:1468, 1961.

[192] A. Quattropani, F. Bassani, and Sandra Carillo. Two-photon transitions to excited states in atomic hydrogen. *Phys. Rev. A*, 25:3079–3089, 1982.

[193] R. Joshi. Two-photon transitions to Rydberg states of hydrogen. *Physics Letters A*, 361(4):352 – 355, 2007.

[194] V. Florescu, S. Patrascu, and O. Stoican. Systematic study of 1s-ns and 1s-nd two-photon transitions of hydrogenlike atoms. *Phys. Rev. A*, 36:2155–2166, 1987.

[195] II Collins, G.W. *The Fundamentals of Stellar Astrophysics*. WH Freeman and Co., New York, 2003.

[196] H. Kuhn. Pressure shift and broadening of spectral lines. *Phil. Mag.*, 18:987, 1934.

[197] H. Kuhn. Pressure broadening of spectral lines and van der Waals forces. I. influence of argon on the mercury resonance line. *Proc. Roy. Soc. A*, 158:230, 1937.

[198] N. Allard and J. Kielkopf. The effect of neutral nonresonant collisions on atomic spectral lines. *Rev. Mod. Phys.*, 54:1103, 1982.

[199] T. Holstein. Pressure broadening of spectral lines. *Phys. Rev.*, 79:744, 1950.

[200] S. V. Stepkin, A. A. Konovalenko, N. G. Kantharia, and N. Udaya Shankar. Radio recombination lines from the largest bound atoms in space. *Monthly Notices of the Royal Astronomical Society*, 374(3):852–856, 2007.

[201] K. T. Lu and U. Fano. Graphic analysis of perturbed Rydberg series. *Phys. Rev. A*, 2:81, 1970.

[202] J. Sugar and C. Corliss. Atomic energy levels of the iron-period elements: potassium through nickel. *J. Phys. Chem. Ref. Data*, 14, Suppl. No. 2:1, 1985.

[203] J. Nunkaew and T. F. Gallagher. Microwave spectroscopy of the calcium $4snf \rightarrow 4s(n+1)d$, $4sng$, $4snh$, $4sni$, and $4snk$ transitions. *Phys. Rev. A*, 91:042503, 2015.

[204] M. Lu, N. Q. Burdick, S-H Youn, and B. L. Lev. Strongly dipolar Bose-Einstein condensate of dysprosium. *Phys. Rev. Lett.*, 107:190401, 2011.

[205] K. Aikawa, A. Frisch, M. Mark, S. Baier, A. Rietzler, R. Grimm, and F. Ferlaino. Bose-Einstein condensation of erbium. *Phys. Rev. Lett.*, 108:210401, 2012.

[206] Y. Takasu, K. Maki, K. Komori, T. Takano, K. Honda, M. Kumakura, T. Yabuzaki, and Y. Takahashi. Spin-singlet Bose-Einstein condensation of two-electron atoms. *Phys. Rev. Lett.*, 91:040404, 2003.

[207] F. Robicheaux, D. W. Booth, and M. Saffman. Theory of long-range interactions for Rydberg states attached to hyperfine-split cores. *Phys. Rev. A*, 97:022508, 2018.

[208] J. Hostetter, J. D. Pritchard, J. E. Lawler, and M. Saffman. Measurement of holmium Rydberg series through magneto-optical trap depletion spectroscopy. *Phys. Rev. A*, 91:012507, 2015.

[209] M. J. Seaton. Quantum defect theory. *Rep. Prog. Phys.*, 46:167, 1983. , and references therein.

[210] W. E. Cooke and C. L. Cromer. Multichannel quantum-defect theory and an equivalent n-level system. *Phys. Rev. A*, 32:2725, 1985.

[211] C. M. Brown, S. G. Tilford, and M. L. Ginter. Extended identifications of odd energy levels of Si I: Lu-Fano graphical analysis. *J. Opt. Soc. Am.*, 65:385, 1975.

[212] D. S. Ginter, M. L. Ginter, and C. M. Brown. Precise representation of the $J = 3^o$ energy levels of the $mpnd$ and $msmp^3$ configurations in SiI, GeI, and SnI using a perturbed coupledchannel model. *J. Chem. Phys*, 85:6530, 1986.

[213] D. S. Ginter and M. L. Ginter. Transitions to and threelimit, fourchannel representations for the $msmp^3$, $mpnd$ $J = 3^o$ levels in SiI and SnI. *J. Chem. Phys*, 85:6536, 1986.

[214] L. Kim and C. H. Greene. Two-electron excitations in atomic calcium. I. *Phys. Rev. A*, 36:4272, 1987. see also **38**, 5953 (1988).

[215] F. Robicheaux and C. H. Greene. Valence-shell photoabsorption spectra of C, Si, Ge, and Sn. *Phys. Rev. A*, 47:4908, 1993.

[216] C. L. Vaillant, M. P. A. Jones, and R. M. Potvliege. Multichannel quantum defect theory of strontium bound Rydberg states. *J. Phys. B: At. Mol. Opt. Phys.*, 47:155001, 2014.

[217] C. M. Lee and K. T. Lu. Spectroscopy and collision theory. II. the Ar absorption spectrum. *Phys. Rev. A*, 8:1241, 1973. C. H. Greene, J. Opt. Soc. Am. B **4**, 775 (1987).

[218] J. Neukammer and H. Rinneberg. Configuration interaction and singlet-triplet mixing probed by hyperfine structure of $6s14d\ ^1D_2$ and $^3D_{1,2,3}$ barium Rydberg states. *J. Phys. B: At. Mol. Opt. Phys.*, 15:3787, 1982.

[219] J-Q Sun and K. T. Lu. Hyperfine structure of extremely high Rydberg $msns\ ^1S_0$ and $msns\ ^3S_1$ series in odd alkaline-earth isotopes. *J. Phys. B: At. Mol. Opt. Phys.*, 21:1957, 1988.

[220] J-Q Sun, K. T. Lu, and R. Beigang. Hyperfine structure of extremely high Rydberg $msnd\ ^1D_2$, $^3D_1$, $^3D_2$ and $^3D_3$ series in odd alkaline-earth isotopes. *J. Phys. B: At. Mol. Opt. Phys.*, 22:2887, 1989.

[221] J.-W. Chen and M. J. Savage. $np \to d\gamma$ for big-bang nucleosynthesis. *Phys. Rev. C*, 60:065205, 1999.

[222] H. W. Hammer and D. R. Phillips. Electric properties of the Beryllium-11 system in Halo EFT. *Nuc. Phys. A*, 865:17, 2011.

[223] G. P. Lepage. How to renormalize the Schrödinger equation. *ArXiv:nucl-th/9706029v1*, 1997.

[224] U. Fano and G. Racah. *Irreducible tensorial sets.* Academic Press, New York, 1959.

[225] U. Fano and J. H. Macek. Impact excitation and polarization of the emitted light. *Rev. Mod. Phys.*, 45:553, 1973.

[226] C. H. Greene and R. N. Zare. Photofragment alignment and orientation. *Ann. Rev. Phys. Chem.*, 33:119, 1982.

[227] D. Dill and J. L. Dehmer. Electron-molecule scattering and molecular photoionization using the multiple-scattering method. *J. Chem. Phys.*, 61:692, 1974.

[228] C. Bahrim, U. Thumm, and I. I. Fabrikant. $^3S^e$ and $^1S^e$ scattering lengths for e^- + Rb, Cs, and Fr collisions. *J. Phys. B: At. Mol. Opt. Phys*, 34:L195, 2001.

[229] G. Quéméner and P. S. Julienne. Ultracold molecules under control! *Chem. Rev.*, 112:4949, 2012.

[230] M. H. G. de Miranda, A. Chotia, B. Neyenhuis, D. Wang, G. Quéméner, S. Ospelkaus, J. L. Bohn, J. Ye, and D. S. Jin. Controlling the quantum stereodynamics of ultracold bimolecular reactions. *Nat. Phys.*, 7:512, 2011.

[231] J. Pérez-Ríos, M. Lepers, R. Vixeau, N. Bouloufa-Maafa, and O. Dulieu. Progress toward ultracold chemistry: ultracold atomic and photonic collisions. *Journal of Physics: Conference Series*, 488:012031, 2014.

[232] A. Frish, M. Mark, K. Aikawa, F. Ferlaino, J. L. Bohn, C. Makrides, A. Petrov, and S. Kotochigova. Quantum chaos in ultracold collisions of gas-phase erbium atoms. *Nature (London)*, 507:475, 2014.

[233] D. DeMille. Quantum computation with trapped polar molecules. *Phys. Rev. Lett.*, 88:067901, 2002.

[234] Q. Wie, Y. Cao, S. Kais, B. Friedrich, and D. R. Herschbach. Quantum computation using arrays of N polar molecules in pendular states. *ChemPhysChem*, 17:1, 2016.

[235] J. L. Bohn, M Cavagnero, and C Ticknor. Quasi-universal dipolar scattering in cold and ultracold gases. *New J. Phys.*, 11:055039, 2009.

[236] Y. Wang, J. P. D'Incao, and C. H. Greene. Universal three-body physics for Fermionic dipoles. *Phys. Rev. Lett.*, 107:233201, 2011.

[237] M. A. Baranov, M. Dalmonte, G. Pupillo, and P. Zoller. Condensed matter theory for dipolar quantum gases. *Chem. Rev.*, 112:5012, 2012.

[238] I. Danshita and C. A. R Sá de Melo. Supersolid phases of dipolar bosons in optical lattices. *Phys. Rev. Lett.*, 103:225301, 2009.

[239] L. Santos, G. V. Shlyapnikov, and M. Lewenstein. Roton-maxon spectrum and stability of trapped dipolar Bose-Einstein condensates. *Phys. Rev. Lett.*, 90:250403, 2003.

[240] T. Lahaye, C. Menotti, L. Santos, M. Lewenstein, and T. Pfau. The physics of dipolar bosonic quantum gases. *Rep. Prog. Phys.*, 72:126401, 2009.

[241] T. Lahaye, J. Metz, B. Fröhlich, T. Koch, M. Meister, A. Griesmaier, T. Pfau, H. Saito, Y. Kawaguchi, and M. Ueda. d-wave collapse and explosion of a dipolar Bose-Einstein condensate. *Phys. Rev. Lett.*, 101:080401, 2008.

[242] S. Ronen, D. C. E. Bortolotti, and J. L. Bohn. Radial and angular rotons in trapped dipolar gases. *Phys. Rev. Lett.*, 98:030406, 2007.

[243] I. Tikhonenkov, B. A. Malomed, and A. Vardi. Anisotropic solitons in dipolar Bose-Enstein condensates. *Phys. Rev. Lett.*, 100:090406, 208.

[244] W. Lechner and P. Zoller. From classical to quantum glasses with ultracold polar molecules. *Phys. Rev. Lett.*, 111:185306, 2013.

[245] B. Gadway and B. Yan. Strongly interacting ultracold polar molecules. *J. Phys. B*, 49:152002, 2016.

[246] F. Cinti, P. Jain, M. Boninsegni, A. Micheli, P. Zoller, and G. Pupillo. Supersolid droplet crystal in a dipole-blockade gas. *Phys. Rev. Lett.*, 105:135301, 2010.

[247] K.-K. Ni, S. Ospelkaus, M. H. G. de Miranda, A. Pe'er, B. Neyenhuis, J. J. Zirbel, S. Kotochigova, P. S. Julienne, D. S. Jin, and J. Ye. A high phase-space density gas of polar molecules. *Science*, 322:231, 2008.

[248] J. W. Park, S. A. Will, and M. W. Zwierlein. Ultracold dipolar gas of fermionic ^{23}Na^{40}K molecules in their absolute ground state. *Phys. Rev. Lett.*, 114:205302, 2015.

[249] M. Guo, B. Zhu, B. Lu, X. Ye, F. Wang, R. Vexiau, N. Bouloufa-Maafa, G. Quéméner, O. Dulieu, and D. Wang. Creation of an ultracold gas of ground-state dipolar ^{23}Na^{87}Rb. *Phys. Rev. Lett.*, 116:205303, 2016.

[250] T. Takekoshi, L. Reichsöllner, A. Schindewolf, J. M. Hutson, C. R. LeSueur, O. Dulieu, F. Ferlaino, R. Grimm, and H.-C. Nägerl. Ultracold dense samples of dipolar RbCs moleucles in the rovibrational and hyperfine ground state. *Phys. Rev. Lett.*, 113:205301, 2014.

[251] H. Kadau, M. Schmitt, M. Wenzel, C. Wink, T. Maier, I. Ferrier-Barbut, and T. Pfau. Oberving the Rosensweig instability of a quantum ferrofluid. *Nature (London)*, 530:194, 2016.

[252] I. Ferrier-Barbut, H. Kadau, M. Schmitt, M. Wenzel, and T. Pfau. Obervation of quantum droplets in a strongly dipolar gas. *Phys. Rev. Lett.*, 116:215301, 2016.

[253] M. Lu, N. Q. Burdick, S.-H. Youn, and B. L. Lev. Strongly dipolar Bose-Einstein condesate of dysprosium. *Phys. Rev. Lett.*, 107:190401, 2011.

[254] T. Lahaye, T. Koch, B. Fröhlich, M. Fattori, J. Metz, A. Griesmaier, S. Giovnazzi, and T. Pfau. Strong dipolar effects in a quantum ferrofluid. *Nature (London)*, 448:672, 2007.

[255] T. J. Carroll, K. Claringbould, A. Goodsell, M. J. Lim, and M. W. Noel. Angular dependence of the dipole-dipole interaction in a nearly one-dimensional sample of Rydberg atoms. *Phys. Rev. Lett.*, 93:153001, 2004.

[256] S. Ravets, H. Labuhn, D. Barredo, T. Lahaye, and A. Browaeys. Measurement of the angular dependence of the dipole-dipole interaction between two individual Rydberg atoms at a Förster resonance. *Phys. Rev. A*, 92:020701, 2015.

[257] J. Deiglmayr, M. Aymar, R. Wester, M. Widemüller, and O. Dulieu. Calculations of static dipole polarizabilities of alkali dimers: prospects for alignment of ultracold molecules. *J. Chem. Phys.*, 129:064309, 2008.

[258] H. P. Büchler, E. Demler, M. Lukin, A. Micheli, N. Prokof'ev, G. Pupillo, and P Zoller. Strongly correlated 2D quantum phases with cold polar molecules: controlling the shape of the interaction potential. *Phys. Rev. Lett.*, 98:060404, 2007.

[259] S. Giovanazzi, A. Görlitz, and T. Pfau. Tuning the dipolar interaction in quantum gases. *Phys. Rev. Lett.*, 89:130401, 2002.

[260] L. F. Gonçalves and L. G. Marcassa. Control of Rydberg-atom blockade by dc electric-field orientation in a quasi-one-dimenional sample. *Phys. Rev. A*, 94:043424, 2016.

[261] J. M. Rost, J. C. Griffin, B. Friedrich, and D. R. Herschbach. Pendular states and spectra of oriented linear molecules. *Phys. Rev. Lett.*, 68:1299, 1992.

[262] M. Viteau, M. G. Bason, J. Radogostowicz, N. Malossi, D. Ciampini, O. Morsch, and E. Arimondo. Rydberg excitations in Bose-Einstein condensates in quasi-one-dimensional potentials and optical lattices. *Phys. Rev. Lett.*, 107:060402, 2011.

[263] H. Margenau. Van der Waals forces. *Rev. Mod. Phys.*, 11:1, 1939.

[264] A. Stone. *The theory of intermolecular forces*. Oxford University Press, 2 edition, 2013.

[265] G. C. Groenenboom, X. Chu, and R. V. Krems. Electronic anisotropy between open shell atoms in first and second order perturbation theory. *J. Chem. Phys.*, 126:204306, 2006.

[266] B. Bussery-Honvault, F. Dayou, and A. Zanchet. Long-range multipolar potentials of the 18 spin-orbit states arising from the C(^3P)+OH($X^2\Pi$) interaction. *J. Chem. Phys*, 129:234302, 2008.

[267] M. R. Flannery, D. Vrinceanu, and V. N. Ostrovsky. Long-range interaction between polar Rydberg atoms. *J. Phys. B. At. Mol. Opt.*, 38:S279, 2005.

[268] A. van der Avoird, P. E. S. Wormer, F. Mulder, and R. M. Berns. *Ab initio studies of the interactions in Van der Waals molecules*, pages 1–51. Springer Berlin Heidelberg, Berlin, Heidelberg, 1980.

[269] R. J. Le Roy. Long-range potential coefficients from RKR turning points: C_6 and C_8 for B($^3\Pi^+_{Ou}$)-State Cl_2, Br_2, and I_2. *Can. J. Phys.*, 52:246, 1974.

[270] A. T. Krupp, A. Gaj, J. B. Balewski, P. Ilzhöfer, S. Hofferberth, R. Löw, T. Pfau, M. Kurz, and P. Schmelcher. Alignment of D-state Rydberg molecules. *Phys. Rev. Lett.*, 112:143008, 2014.

[271] R. K. Kalia and P. Vahishta. Interfacial colloidal crystals and melting transition. *J. Phys. C*, 14:L643, 1981.

[272] R. Citro, E. Orignac, S. De Palo, and M. L. Chiofalo. Evidence of luttinger-liquid behavior in one-dimensional dipolar quantum gases. *Phys. Rev. A*, 75:051602, 2007.

[273] R. Citro, S. De Palo, E. Orignac, P. Pedri, and M. L. Chiofalo. Luttinger hydrodynamics of confined one-dimensional Bose gases with dipolar interactions. *New J. Phys.*, 10:045011, 2008.

[274] João D. Rodrigues, Hugo Terças, Luis F. Gonçalves, Luis G. Marcassa, and José T. Mendonça. Emergence of spatial order in highly interacting Rydberg gases. *Phys. Rev. A*, 97:022708, 2018.

[275] H. Fröhlich, H. Pelzer, and S. Zienau. Properties of slow electrons in polar materials. *Philosophical Magazine*, 31:221, 1950.

[276] N.B. Jörgensen, L. Wacker, K.T. Skalmstang, M. M. Parish, J. Levinsen, R. S. Christensen, G. M. Bruun, and J. J. Arlt. Observation of attractive and repulsive polarons in a Bose-Einstein condensate. *Phys. Rev. Lett.*, 117:055302, 2016.

[277] M.G. Hu, M. J. Van de Graaff, D. Kedar, J. P. Corson, E. A. Cornell, and D. S. Jin. Bose polarons in the strongly interacting regime. *Phys. Rev. Lett.*, 117:055301, 2016.

[278] E. S. Redchenko and Mikhail Lemeshko. Libration of strongly-oriented polar molecules inside a superfluid. *ChemPhysChem*, 17(22):3649–3654, 2016.

[279] R. Schmidt and M. Lemeshko. Rotation of quantum impurities in the presence of a many-body environment. *Phys. Rev. Lett.*, 114:203001, 2015.

[280] U. Fano. Effects of configuration interaction on intensities and phase shifts. *Phys. Rev.*, 124(6):1866, 1961.

[281] M. Gailitis and R. Damburg. The influence of close coupling on the threshold behaviour of cross sections of electron-hydrogen scattering. *Proc. Phys. Soc.*, 82:192, 1963.

[282] P. M. C. Morse and H. Feshbach. *Methods of theoretical physics*. Technology Press, 1946.

[283] B. P. Ruzic, C. H. Greene, and J. L. Bohn. Quantum defect theory for high-partial-wave cold collisions. *Phys. Rev. A*, 87:032706, 2013.

[284] J. Sandström, G. Haeffler, I. Yu Kiyan, U. Berzinsh, D. Hanstorp, D. J. Pegg, J. C. Hunnell, and S. J. Ward. Effect of polarization on photodetachment thresholds. *Phys. Rev. A*, 70:052707, 2004.

[285] O. H. Lindahl, J. Rohlén, H. Hultgren, D. J. Pegg, C. W. Walter, and D. Hanstorp. Observation of thresholds and overlapping resonances below the $10^2P_{1/2}$ and $^2P_{3/2}$ thresholds in the photodetachment of Cs^-. *Phys. Rev. A*, 88:053410, 2013.

[286] T. F. O'Malley. Effect of long-range final-state forces on the negative-ion photodetachment cross section near threshold. *Phys. Rev.*, 137:A1668, 1965.

[287] J. W. Farley. Photodetachment cross sections of negative ions: The range of validity of the Wigner threshold law. *Phys. Rev. A*, 40:6286, 1989.

[288] C.-N. Liu and Anthony F. Starace. Photodetachment of Na^-. *Phys. Rev. A*, 59(5):3643, 1999.

[289] M. Chibisov, A. M. Ermolaev, F. Brouillard, and M. H. Cherkani. New summation rules for Coulomb wave functions. *Phys. Rev. Lett.*, 84:45, 2000.

[290] J. W. Farley and W. H. Wing. Accurate calculation of dynamic Stark shifts and depopulation rates of Rydberg energy levels induced by blackbody radiation. Hydrogen, helium, and alkali-metal atoms. *Phys. Rev. A*, 23:2397–2424, 1981.

[291] T. F. Gallagher and W. E. Cooke. Interactions of blackbody radiation with atoms. *Phys. Rev. Lett.*, 42:835–839, 1979.

[292] F. Zhou and L. Spruch. Temperature-induced transition rates for some hydrogenic states. *Phys. Rev. A*, 49:718–725, 1994.

[293] I. I. Beterov, I. I. Ryabtsev, D. B. Tretyakov, and V. M. Entin. Quasiclassical calculations of blackbody-radiation-induced depopulation rates and effective lifetimes of Rydberg ns, np, and nd alkali-metal atoms with $n \leq 80$. *Phys. Rev. A*, 79:052504, 2009.

[294] S. Cohen, M. M. Harb, A. Ollagnier, F. Robicheaux, M. J. J. Vrakking, T. Barillot, F. Lépine, and C. Bordas. Photoionization microscopy of the lithium atom: Wave-function imaging of quasibound and continuum Stark states. *Phys. Rev. A*, 94:013414, 2016.

[295] L. B. Zhao, I. I. Fabrikant, M. L. Du, and C. Bordas. Test of the Stark-effect theory using photoionization microscopy. *Phys. Rev. A*, 86:053413, 2012.

[296] P. Giannakeas, F. Robicheaux, and C. H. Greene. Photoionization microscopy in terms of local-frame-transformation theory. *Phys. Rev. A*, 91:043424, 2015.

[297] F. Robicheaux. Pulsed field ionization of Rydberg atoms. *Phys. Rev. A*, 56:3358 (R), 1997.

[298] R. R. Jones. Creating and probing electronic wave packets using half-cycle pulses. *Phys. Rev. Lett.*, 76:3927, 1996.

[299] M. J. Cooper. Compton scattering and electron momentum determination. *Rep. Prog. Phys.*, 48:415, 1985.

[300] C.E. Brion, G. Cooper, Y. Zheng, I.V. Litvinyuk, and I.E. McCarthy. Imaging of orbital electron densities by electron momentum spectroscopy a chemical interpretation of the binary (e,2e) reaction. *Chemical Physics*, 270(1):13 – 30, 2001.

[301] M. A. Coplan, J. H. Moore, and J. P. Doering. (e,2e) spectroscopy. *Rev. Mod. Phys.*, 66:985–1014, 1994.

[302] C. E. Brion, G. Cooper, Y. Zheng, I. V. Litvinyuk, and I. E. McCarthy. Imaging of orbital electron densities by electron momentum spectroscopy - a chemical interpretation of the binary (e,2e) reaction. *Chemical Physics*, 270:13, 2001.

[303] R.W. James. *The Optical Principles of the Diffraction of X-rays*. Ox Bow, 1982.

[304] R. G. Hulet and D. Kleppner. Rydberg atoms in circular states. *Phys. Rev. Lett.*, 51:1430–1433, 1983.

[305] V. Averbukh, N. Moiseyev, P. Schmelcher, and L. S. Cederbaum. Transition from Rydberg to giant-dipole-moment states of hydrogen atoms in crossed fields: A suggestion for an experiment. *Phys. Rev. A*, 59:3695–3700, 1999.

[306] N. Khaneja, T. Reiss, C. Kehlet, T. Schulte-Herbrggen, and S. J. Glaser. Optimal control of coupled spin dynamics: design of NMR pulse sequences by gradient ascent algorithms. *Journal of Magnetic Resonance*, 172(2):296 – 305, 2005.

[307] C. Brif, R. Chakrabarti, and H. Rabitz. Control of quantum phenomena: past, present, and future. *New J. Phys*, 12:075008, 2010.

[308] M. Demiralp and H. Rabitz. Optimally controlled quantum molecular dynamics: a perturbation formulation and the existence of multiple solutions. *Phys. Rev. A*, 47:809, 1993.

[309] H. A. Rabitz, M. M. Hsieh, and C. M. Rosenthal. Quantum optimally controlled transition landscapes. *Science*, 303:1998, 2004.

[310] R. Chakrabarti and H. Rabitz. Quantum control landscapes. *International Reviews in Physical Chemistry*, 26(4):671–735, 2007.

[311] B. Russell, H. Rabitz, and R-B Wu. Control landscapes are almost always trap free: a geometric assessment. *J. Phys. A: Math. Theor.*, 50:205302, 2017.

[312] K. W. Moore and H. Rabitz. Exploring quantum control landscapes: Topology, features, and optimization scaling. *Phys. Rev. A*, 84:012109, 2011.

[313] J. M. Geremia, Wusheng Zhu, and Herschel Rabitz. Incorporating physical implementation concerns into closed loop quantum control experiments. *The Journal of Chemical Physics*, 113(24):10841–10848, 2000.

[314] L. Ma, D.A. Anderson, and G. Raithel. Paschen-Back effects and Rydberg-state diamagnetism in vapor-cell electromagnetically induced transparency. *Phys. Rev. A*, 95:061804, 2017.

[315] P. Makotyn. *Experimental studies of a degenerate unitary Bose gas.* PhD thesis, University of Colorado, 2014.

[316] B. Podolsky and L. Pauling. The momentum distribution in hydrogen-like atoms. *Phys. Rev.*, 34:109–116, 1929.

[317] H.-C. Shao and A. F. Starace. Imaging coherent electronic motion in atoms by ultrafast electron diffraction. *Phys. Rev. A*, 88:062711, 2013.

[318] G. Dixit, O. Vendrell, and R. Santra. Imaging electronic quantum motion with light. *Proceedings of the National Academy of Sciences*, 109(29):11636–11640, 2012.

[319] C. Silber, S. Günther, C. Marzok, B. Deh, Ph. W. Courteille, and C. Zimmermann. Quantum-degenerate mixture of fermionic lithium and bosonic rubidium gases. *Phys. Rev. Lett.*, 95:170408, 2005.

[320] M. Taglieber, A.-C. Voigt, T. Aoki, T. W. Hänsch, and K. Dieckmann. Quantum degenerate two-species fermi-fermi mixture coexisting with a Bose-Einstein condensate. *Phys. Rev. Lett.*, 100:010401, 2008.

[321] G. Roati, F. Riboli, G. Modugno, and M. Inguscio. Fermi-bose quantum degenerate ^{40}K−^{87}Rb mixture with attractive interaction. *Phys. Rev. Lett.*, 89:150403, 2002.

[322] G. Barontini, C. Weber, F. Rabatti, J. Catani, G. Thalhammer, M. Inguscio, and F. Minardi. Observation of heteronuclear atomic Efimov resonances. *Phys. Rev. Lett.*, 103:043201, 2009.

[323] J. Ulmanis, S. Häfner, R. Pires, E. D. Kuhnle, Y. Wang, C. H. Greene, and M. Weidemüller. Heteronuclear Efimov scenario with positive intraspecies scattering length. *Phys. Rev. Lett.*, 117:153201, 2016.

[324] L. D. Carr, D. DeMille, R. V. Krems, and J. Ye. Cold and ultracold molecules: science, technology and applications. *New J. Phys.*, 11:055049, 2009.

[325] K.-K. Ni, S. Ospelkaus, M. H. G. de Miranda, A. Pe'er, B. Neyenhuis, J. J. Zirbel, S. Kotochigova, P. S. Julienne, D. S. Jin, and J. Ye. A high phase-space-density gas of polar molecules. *Science*, 322(5899):231–235, 2008.

[326] J. G. Danzl, E. Haller, M. Gustavsson, M. J. Mark, R. Hart, N. Bouloufa, O. Dulieu, H. Ritsch, and H.-C. Nägerl. Quantum gas of deeply bound ground state molecules. *Science*, 321(5892):1062–1066, 2008.

[327] R. V. Krems. Cold controlled chemistry. *Phys. Chem. Chem. Phys.*, 10:4079–4092, 2008.

[328] T. M. Rvachov, H. Son, A. T. Sommer, S. Ebadi, J. J. Park, M. W. Zwierlein, W. Ketterle, and A. O. Jamison. Long-lived ultracold molecules with electric and magnetic dipole moments. *Phys. Rev. Lett.*, 119:143001, 2017.